UNIVERSITY OF LEEDS

An Alternative route for the production of alkali-activated cements

By

Yuyan Huang

Supervisors:

Professor Susan Bernal Lopez

Dr. Alastair T.M. Marsh

Dr. Samuel Adu-Amankwah

A thesis submitted in accordance with the
requirements for the degree of
Doctor of Philosophy

The University of Leeds
School of Civil Engineering
October 2023

Acknowledgements

My journey pursuing a PhD at Leeds holds special meaning for me, as it marked my first experience living abroad, in a foreign country. I am deeply grateful for the invaluable assistance, support, guidance, and the warmth extended to me by the individuals I had the privilege to meet during this time.

I would like to extend my heartfelt gratitude to my primary supervisor, Prof. Susan Bernal Lopez, for her unwavering guidance and support throughout my PhD journey. Her encouragement and kindness, especially during the Covid-19 lockdown, were deeply appreciated. Prof. Susan Bernal Lopez consistently provided me with the freedom and support needed for my research, offering valuable insights into experimental design. She actively encouraged my participation in conferences and provided opportunities for honing my presentation skills, offering constructive feedback on slide preparation. Additionally, she showed genuine concern for my financial well-being and offered me a part-time research assistant position to alleviate any financial burdens. Furthermore, she shared valuable advice on career development, drawing from her own experiences, which has been invaluable. I consider myself fortunate to have had Prof. Susan Bernal Lopez as my main supervisor. I would also like to express my sincere thanks to Dr. Sam Adu-Amankwah, who consistently offered kindness and support throughout my PhD journey. Additionally, my gratitude goes to Dr. Alastair T. M. Marsh, who was always readily available and supportive whenever I needed assistance. He played a pivotal role in helping me navigate the university and the school at the outset of my PhD. I greatly appreciate his patience and guidance, which encompassed aspects of research as well as life.

I would also like to give many thanks to our dedicated technician team, comprising Karen, Lucy, Stuart, Chris, Emma, Dave, and Morgan. Their invaluable assistance and unwavering support were instrumental in the successful completion of my experiments. I am especially thankful to our MUSE group, including Dr. Yuvaraj Dhandapani, Dr. Sreejith Krishnan, Dr. Alice Macente, and Dr. Bruno Fernandes, for their generous support in experiments particularly for utilizing SEM at later time. I would like to offer additional thanks to Zengliang, who devoted considerable time and effort in assisting me with SEM data collection over several whole days in the SEM lab. Being part of such a supportive group at Leeds has been an incredible stroke of luck. I am deeply grateful to all my friends, including Ning, Zhengyao, Xiaohong, Moro, and Jiangwei, for their forever companionship and encouragement during both joyful and challenging times.

Great thanks for the financial support of the UK Engineering and Physical

Finally, I want to express my heartfelt gratitude to my family, who have always provided me with warm support. I miss all of you immensely, particularly my grandmother, who sadly passed away in early 2020.

Abstract

Alkali-activated cements (AACs) are produced as a result of the chemical reaction between aluminosilicate precursors and alkaline activators. These cements have garnered considerable research attention due to their low-carbon binder credentials, representing a promising alternative to completely replace Portland cement in concrete production, which could contribute to reducing global carbon dioxide emission attributed to the construction sector. The commonly employed alkaline activators, including sodium hydroxide and silicates, play a substantial role in the carbon footprint associated with the manufacturing process of alkali-activated cements. Beyond environmental considerations, these activators also introduce safety concerns as they are corrosive substances. Its handling and use necessitate the expertise of skilled personnel to during the production of AACs, which is not always available in construction sites.

In the pursuit of more cost-effective as well as user-friendly methods for alkali-activated slag cement (AAS) production, this research centers in determining the viability of using metal carboxylates as alternative activators for the production of AAS. Results are benchmarked against sodium hydroxide activated slag systems, as they are some of the better understood AACs. This endeavour involves a comprehensive examination of metal carboxylates chemistry and identifying a suitable process so that these compounds can be used in a suitable way for AACs manufacturing. This included evaluating the feasibility of applying a sintering process (thermal treatment) to produce glasses with controlled solubility potential, and the characterization of the produced materials. It was hypothesized that such glasses might help overcoming some of the anticipated challenges when using the novel proposed activators, for example reducing their hygroscopicity. Various techniques, including X-ray diffraction (XRD) and differential scanning calorimetry (DSC) analysis, were applied to determine the potential glass-formability of the materials evaluated. pH measurements were conducted to determine the value of the solutions produced with produced thermally treated metal carboxylates to ensure such solutions can provide sufficient alkalinity to promote the dissolution of slag, and consequently be considered as suitable alkali-activators. After an extensive exploration of different metal carboxylates, it was identified that using sodium acetate (NaAc) or potassium acetate (KAc) were the most suitable potential activators evaluated.

In the next stage of the research the effectiveness of NaAc or KAc as activators was evaluated by blending solutions produced with them with blast furnace slag. The properties of AAS cements produced were compared to those of AACs produced with sodium hydroxide (NaOH) or potassium hydroxide (KOH). The fresh state properties of these materials including reaction kinetics and workability, were determined by isothermal calorimetry analysis and mini-slump test respectively. The setting time of the

evaluated binders was determined via the Vicat method. The evolution of phase assemblage (type and amount of reaction products forming) was monitored through various materials characterization techniques. A lower reaction degree was observed in acetates-activated slag cement; however, traces of calcium aluminosilicate hydrate (C-(A)-S-H) type gels, hydrotalcite-like phases, and calcium carbonates were identified in such systems, which are the main crystalline reaction products typically identified in AACs when conventional activators are used. This was a clear indicative that the acetates, although leading to a different reaction mechanism to conventional AACs, are effectively activating the slag. Significant structural differences in the C-(A)-S-H type phases forming in the acetates- or hydroxides-activated slag cements were detected through ^{29}Si MAS NMR spectroscopy, consistent with differences in chemical composition identified by SEM-EDS analysis. Compressive strength and pore size distribution of hardened pastes were determined, and no direct correlation between these properties was observed. Since acetates are used as additions in Portland blended concrete to reduced their permeability, in this research it was examined their effectiveness in reducing permeability in the produced AAS cements. The impermeability level was evaluated through water contact angle measurements. Finally, a mechanism of reaction of acetate-activated slag cement is proposed.

Although metal carboxylates were effective to promote the reaction of blast furnace slag to form hardened monoliths, NaAc-activated slag (NaAc-AAS) cement exhibits an extended reaction period in contrast to NaOH-activated slag (NaOH-AAS) cements, which undergo a rapid reaction process. In order to expedite the reaction kinetics of NaAc AACs, the effect of blended different concentrations of NaOH with NaAc (dosed at different ratios from 0% to 100%), was investigated by isothermal calorimetry. The effect of the blended activator in the phase assemblage evolution of the produced hybrid organic-inorganic AAS cements was determined by applying comparable analytical techniques to those adopted when using a single activator. Results revealed that the addition of NaOH effectively expedite the reaction kinetics, this being more noticeable at higher contents added. Compressive strength of cements pastes increased at higher NaOH contents in the activator.

In AAS systems the MgO content in slag has a pivotal effect in controlling the formation of secondary reaction products, particularly hydrotalcite-like phases. The formation of hydrotalcite-like phases enhances the CO_2 absorption capacity in some AAS cements, consequently leading to higher carbonation resistance. Magnesium acetate (MgAc), classified as a metal acetate and a source of MgO, was added to AACs. It was hypothesized that MgAc powder could act as an additional source of MgO to modify the phase assemblage of NaOH-AAS. The formation of hydrotalcite-like phases was evaluated in the modified cements by applying a multi-technique approach as described in other sections of the thesis. Unexpectedly the addition of MgAc hindered the formation of formation of crystalline hydrotalcite-like phases, although significant differences in the

phase assemblage or chemical composition of the main reaction products forming (e.g. a poorly crystalline C-A-S-H type phase) were not identified. Further studies are required to elucidate the effect of MgAc addition in AACs, as well as identifying other potential sources of MgO that can enhance the formation of hydrotalcite-type phases.

Publication from this thesis

Book chapters

Miranda de Lima L., Bernal S.A., Huang Y., Marsh A.T.M., Adesanya E.D., Lukkonen T., Yliniemi J., Ye G., Provis J.L. Chapter 3: Conventional precursors and activators. In Mechanical Properties of Alkali-Activated Concrete: State-of-the-Art Report, RILEM TC 294 MPA. Dordrecht: Springer Netherlands.

Krishnan S., Adesanya E.D., Chen B., Djobo J.N.Y., Huang Y., Marsh A.T.M., Nedelkovic M., Ye G., Yliniemi J., Yue Z., Bernal S.A. Chapter 4 'Non-conventional Precursors and Activators'. State of the Art Report, RILEM TC 294-MPA – Mechanical properties of alkali-activated concrete. Dordrecht: Springer Netherlands.

Journal publications

Huang Y., Marsh A.T.M., Adu-Amankwah S., Bernal S.A. Effect of the alkali cation in the structural evolution of acetate activated slag cements. *In preparation*.

Huang Y., Marsh A.T.M., Adu-Amankwah S., Bernal S.A. Effect of sodium acetate addition in the structure of alkali-hydroxide activated slag cements. *In preparation*.

Conference publications

Huang Y., Marsh A.T.M., Adu-Amankwah S., Bernal S.A. 'Alkali-activated slag cement with potassium acetate', on 41st Cement and Concrete Science Conference, Leeds, UK, September 2022.

Huang Y., Marsh A.T.M., Adu-Amankwah S., Bernal S.A. 'Alkali metal acetate-activated ground granulated blast furnace slag cements', 76th RILEM Week & International Conference on Regeneration and Conservation of Structures (ICRCS) 2022, Kyoto, Japan, September 2022.

Other conference presentations

Huang Y., Marsh A.T.M., Adu-Amankwah S., Bernal S.A. 'Effect of magnesium acetate addition on phase assemblage evolution of NaOH-activated slag cement', School of Civil Engineering 9th Annual Postgraduate Research Conference, Leeds, UK, April 2023.

Huang Y., Marsh A.T.M., Adu-Amankwah S., Bernal S.A. 'Synthesis and characterization of metal acetates as potential alkaline activators to produce low carbon cements', School of Civil Engineering Annual Postgraduate Research Conference, Leeds, UK, April 2021.

List of Abbreviations

OPC	Ordinary Portland Cement
AAMs	Alkali-Activated Materials
AAC	Alkali-Activated Cement
AAS	Alkali-Activated Slag Cement
GGBFS	Ground Granulated Blast Furnace Slag
OCAs	Organic Alkaline Carboxylate Activators
C-(A)-S-H	Calcium Aluminosilicate Hydrate
C-(N-)A-S-H	Calcium (Sodium) Aluminosilicate Hydrate
M-S-H	Magnesium Silicate Hydrate
ASR	Alkali-Silica Reaction
NaOH	Sodium Hydroxide
KOH	Potassium Hydroxide
Na_2SiO_3	Sodium Silicate
Na_2SO_4	Sodium Sulfate
Na_2CO_3	Sodium Carbonate
LiAc	Lithium Acetate
NaAc	Sodium Acetate
KAc	Potassium Acetate
RbAc	Rubidium Acetate
CsAc	Cesium Acetate
MgAc	Magnesium Acetate
CaAc	Calcium Acetate
NaPr	Sodium Propionate
NaBu	Sodium Butyrate
NaOc	Sodium Octanoate
CMA	Calcium Magnesium Acetate
LDH	Layered Double Hydroxide
LCA	Life-Cycle Assessment
w/b	Water-to-Binder
w/c	Water-to-Cement
A	Al_2O_3
C	CaO
H	H_2O
N	Na_2O
S	SiO_2
c	CO_2
Ca/Si	Calcium-to-Silicon
Al/Si	Aluminium-to-Silicon
CA	Water Contact Angle
SA	Sliding Angle
XRD	X-ray Diffraction

DSC	Differential Scanning Calorimetry
ATR-FTIR	Attenuated Total Reflection – Fourier Transform Infrared Spectroscopy
TG	Thermal Gravimetric Analysis
STA-MS	Simultaneous Thermal Analysis with Mass Spectrometry
Solid MAS NMR	Solid State Magic Angle Spinning Nuclear Magnetic Resonance
SEM-EDS	Scanning Electron Microscopy and Energy Dispersive X-ray Spectroscopy
BSE	Backscattered Scanning Electron
MIP	Mercury Intrusion Porosimetry

Table of Contents

List of Figures

List of Tables

Chapter 1 – Introduction

1.1 Background

The increase of global population promotes the continuously increasing need for infrastructure and consequently increasing the demand for construction materials [Provis, 2018, Andrew, 2018], particularly ordinary Portland cement (OPC) [Andrew, 2018, Pacheco-Torgal, 2014, Turner and Collins, 2013]. In spite of the technical benefits of OPC, its manufacturing process presently contributes to approximately 8% of worldwide human-caused CO_2 emissions, which is fourfold the CO_2 emissions of the aviation industry. This has motivated the development of a 'toolkit' of low-carbon cement alternatives that can be produced from resources (e.g. wastes, by-products) available in different regions [Passuello et al., 2017, Bernal et al., 2016].

Within low-carbon cements, alkali-activated cements (AACs) are considered as one of the most promising alternative binders for producing concrete [Mendes et al., 2021, Provis and Bernal, 2014b, Bernal et al., 2014b]. Their production has the potential to significantly reduce greenhouse gas emissions compared with OPC manufacturing [Juenger et al., 2011, Provis and Van Deventer, 2013, Provis, 2018]. AACs can develop performances that are not easily achieved by OPC, such as high mechanical strength at early curing ages, better resistance against fire, acids or sulphate attack, and excellent capability of immobilizing heavy metals [Juenger et al., 2011, Provis and Van Deventer, 2013, van Deventer et al., 2010]. These materials are being particularly accepted in the UK, and in recent years a British standard enabling the utilization of these materials has been developed.

Conventional AACs [Juenger et al., 2011, Provis and Van Deventer, 2013, Provis, 2018, Provis and Bernal, 2014b] are produced by the reaction of solid aluminosilicate precursors and alkaline activators, usually chemical solutions with high alkalinity which are corrosive and viscous. The handling, storing and transporting of large amounts of alkaline activating solutions such as sodium hydroxide/silicate are some of the main barriers to the industrial adoption of these materials [Provis and Van Deventer, 2013, Bernal et al., 2014a, Bernal et al., 2012]. Despite the potential advantages of using AACs in terms of both environmental impact and materials properties, these practical barriers mean that the industrial use of AACs remains low [Provis, 2018, van Deventer et al., 2010].

In recent years there has been an increased interest in using organic substances for tailoring the properties of alkali-activated cements. Such binders are often referred to as hybrid organic-inorganic geopolymer cements and present the advantage of reducing

the amount of alkaline activator that needs to be used for producing cements with desirable properties. However, most of the research in this topic has centered in using very small polymer contents to enhance the mechanical strength and other properties of the materials produced with them.

Metal carboxylates emerge as a promising alternative material with the potential for chemically activating slags. For the purpose of carboxylate solutions to be used as activators they have to fulfil two fundamental requirements of an activator: to provide metal cations for charge-balancing reaction phases forming in the binder, and provide sufficient alkalinity for the precursors to dissolve [Palomo et al., 1999, Luukkonen et al., 2018, Amer et al., 2021b]. Metal carboxylates can form glasses after melting and quenching. The advantage of glass formation is that properties are not limited by specific phases, and a range of properties such as solubility can be achieved by tailoring their chemical composition. Such versatility in controlling the release alkalinity with time (upon mixing with water) is desirable, because this allows control of the alkali-activation process.

Metal acetates are commonly used as alkali-derived airfield deicers for concrete pavements as these compounds are less corrosive than chloride-based deicers [Kotwica and Malich, 2021], however, this approach has proved ineffective, unlike chloride-based deicers that exhibit high effectiveness at a lower cost. Moreover, environmental conditions, such as temperature, imposed limitations on the practical application of the method. For example, sodium and potassium acetate addition increased the degree of alkali-silica reaction (ASR) [Kotwica and Malich, 2021] [Giebson et al., 2010]. The influence of magnesium acetate and calcium acetates on the ASR reaction is different. Magnesium acetate addition results in concrete damage, but little deterioration was observed in concretes when calcium acetate was used as a deicer [Lee et al., 2000]. An argument was existed on whether higher Mg/Ca ratio is beneficial for concrete deterioration [Lee et al., 2000, Dunn and Schenk, 1980b] . Zinc acetate added in the fresh mix prior concrete could slow down the corrosion in concrete [Maliekkal et al., 2018]. Moreover, potassium acetate could work at a very low temperature as the deicer and less corrosive compared to conventional NaCl deicer [Sajid et al., 2022]. Another application of sodium acetate in construction is its use as a protective concrete coating on freezing and hot temperature of -25°C and 60 °C. The concrete with the 2% addition (by mass of cement) of sodium acetate exhibited a significant reduction on the water adsorption rate and remarkable increase on the compressive strength [Al-Kheetan et al., 2020a]. The application of metal carboxylates in concrete has garnered attention, prompting further exploration for diverse applications, including their potential utilization as alkaline activators. However, a notable gap exists as none of these studies specifically addressed the utilization of metal acetates in cement production. Furthermore, the application of alkaline carboxylate activators (OCAs) remains unexplored in cement production, and there are no published studies on metal

carboxylates for the manufacturing of AACs. This underscores the novelty and significance of this research in filling the existing gaps in the literature.

Alkali carboxylate glasses have been used for fertilizers manufacturing [Patil et al., 1968, Blair et al., 1992]. Melting metal carboxylates do not need high temperatures (typically < 400 °C), so the melting process will not consume too much additional energy. Using the novel activators bring the possibility to modify the properties of produced AAS cements, representing an important step forward in developing specialized materials for different infrastructure needs.

Ground granulated blast furnace slag (GGBFS) is one of precursors employed in AAC production. This is due to its high reactivity in alkaline media, and the enhanced mechanical properties and durability developed by AAC produced with it. The exclusive use of GGBFS as the sole precursor in this research was deliberate. GGBFS has been extensively studied over the years in the context of AAC, rendering it an ideal reference material. This choice allows for a comprehensive evaluation of the efficacy of metal carboxylate as potential activators and their impact on the properties of AAC produced by them.

The research hypothesis proposed in this study is that it is feasible to utilize metal carboxylates as alkaline activators in AACs, and the materials produced could yield novel and advantageous properties compared with other conventional AACs. The results of the study substantiate this hypothesis by demonstrating that metal carboxylates, specifically metal acetates, can effectively serve as alternative activators, influencing the phase assemblage and properties of AAC. However, challenges and areas for further exploration have emerged. These include the need for a more in-depth understanding of the reaction mechanisms between metal carboxylates and precursors and assessing the long-term durability and performance of AAC produced with metal carboxylate activators. Addressing these challenges will not only enhance the comprehension of the underlying processes but will also contribute to the practical applicability and broader adoption of metal carboxylates in sustainable cementitious materials. This research is the first of its kind, and therefore is lying the foundations for further research in this area, with the goal of optimizing the micro- and macro structure and consequently the performance of these novel cements.

1.2 Aim and Objectives

The overarching aim of this PhD research is to develop an alternative activation route for the production of alkali-activated cements by employing organic carboxylates as alternative alkaline activators. The efficacy of these organic activators was systematically assessed in comparison to conventional hydroxides. The impact on the

resulting AAC was thoroughly analyzed, encompassing aspects such as reaction kinetics, microstructure, mechanical and physical properties, and the developing conceptual reaction mechanisms explaining how the activation process proceeds in these novel cements. Additionally, the structural evolution of AAC of MgAc added materials was also determined.

Four sub-objectives are delineated to help achieve the overall aim of this PhD project:

Obj1. Synthesize and characterize organic alkaline carboxylate activators (OCAs) based on metal carboxylates.

Obj2. Evaluate alkali-activated slag cements produced with OCAs, including determination of the fresh state properties, phase assemblage evolution, physical and mechanical properties in comparison to those of AAC produced with conventional alkali hydroxide activators.

Obj3. Elucidate the effect of partial replacement of sodium hydroxide by sodium acetate in the reaction kinetic, phase assemblage evolution and hydrophobic properties of blended alkali activated slag cements.

Obj4. Determine the effect the addition of magnesium acetate in AAC on the reaction kinetics and phase assemblage evolution.

1.3 Research Scope and Strategy

The research scope of this study encompassed the exploration of metal carboxylates, specifically metal acetates, as alternative alkaline activators in cement production, with a primary focus on AAC. GGBFS was selected as the sole precursor material, leveraging its extensive prior research as a reference point. The investigation sought to understand the influence of metal carboxylate activators on the phase assemblage, microstructure, and properties of AAC, with the aim of providing the scientific evidence required to make an informed decision to recommend this novel activator route or not for the development of future AACs.

The research strategy employed a systematic and comprehensive approach. Initially, an extensive literature review was conducted to establish the theoretical framework and identify existing gaps. Experimental methodologies involved the preparation of activating solutions using metal carboxylates, particularly metal acetates. The most promised acetates (considering the pH achieved in solutions produced with them) were selected to be blended with blast furnace slag. Reference cements produced with similar metal cations and dosed in comparable quantities to those produced with

acetates were produced for comparative purposes. An extensive analysis of the pastes produced was conducted utilized a variety of analytical techniques, such as X-ray Diffraction (XRD), Scanning Electron Microscopy (SEM), and various mechanical and physical property tests, to determine the properties and behaviour of AAC produced with metal carboxylate activators. The research strategy aimed to integrate theoretical understanding with practical experimentation to address the overarching research questions and objectives.

1.4 Thesis outline

The thesis includes 8 chapters including: Introduction; Literature Review; Materials and Methodology; and four chapter of experimental results, and Conclusion and Future Research. A brief overview of the contents of each chapter is given below.

Chapter 2 presents an overview of the chemistry of GGBFS, reaction kinetics and phase assemblages of AAC. The advantages and limitations when using conventional alkaline activators, as well as the challenges and barriers for the widespread adoption of AAC, are discussed, in order to justify why alternative alkaline activators are needed. Previous studies on metal carboxylates, and their applications in the cementitious materials, are also presented, emphasizing the novelty of the present research thesis.

Chapter 3 encompasses a detailed exploration of properties of GGBFS and metal carboxylates. Additionally, it delves into the grades and sources of the chemical carboxylates and metal hydroxides employed throughout the study. The methodologies for sample preparation are meticulously outlined, providing a comprehensive understanding of the processes applied. Furthermore, the chapter offers intricate technical insights into the characterization methods utilized in the analysis of the produced materials tested in this study.

Chapter 4 presents the investigation on organic metal carboxylates to form glasses as alternative activators, as a way to control the dissolubility rate. A series of single, binary, ternary and quaternary systems composed of different thermally treated metal carboxylates were investigated to understand the effect of the cation type, anion type and number of components on the potential of glass-formation on the current used conditions for the evaluated systems. Results demonstrate that thermal treated NaAc and KAc yielded high enough pH solutions to be explored further as alternative activators for the production of AACs.

Chapter 5 discusses the evaluation on the effectiveness of using NaAc or Kac for producing AAC, their effect on the property of the produced AAC. Results are compared with those of reference pastes produced with hydroxide-based activators.

This covers fresh-state properties, phase assemblage evolutions, microstructure, porosity, as well as hydrophobic properties. Results reveal that NaAc/KAc exhibit different reaction kinetics compared to NaOH/KOH, but could be used as alternative activators, and the materials produced develop impermeability properties. In order to overcome the prolonged reaction process observed in AACs produced by NaAc suggests NaOH could be used as an accelerator. To explore this, a modified activator composition was proposed, involving the partial substitution of NaOH with NaAc. The primary objective of this approach is to moderate the overall reaction process of AAC, thereby addressing the challenge of rapid setting associated with NaOH-AAC and the slow setting of NaAc-AAC. The outcomes of this modification are detailed in Chapter 6. Recognizing that the content of MgO significantly influences the phase assemblage evolution, particularly the formation of hydrotalcite-like phases, an external MgO source was sought. This motivation led to the utilization of magnesium acetate (MgAc). The structural evolution findings resulting from this approach are presented in Chapter 7.

Chapter 8 summarizes the main findings from Chapter 4 to Chapter 7, explains the significance of this research for both improving scientific understanding and developing low-carbon cementitious materials, and lastly gives recommendations for future research and potential for industrial adoption.

Chapter 2 – Literature review

2.1 Introduction

This literature review endeavors to present a concise overview of the established AAC manufactured using various activators, with GGBFS as a precursor. Subsequently, the review aims to delve into the potential of metal carboxylates to overcome the limitations associated with current activation methods.

Considerable research efforts have been dedicated to the study of alkali-activated materials (AAMs) over the past decades, driven by the potential to minimize impact to environment and improve durability in contrast to Ordinary Portland Cement (OPC) [van Deventer et al., 2010, Juenger et al., 2011, Provis et al., 2015]. The advancement of AAMs holds promise in addressing the requirements of infrastructure development and the broader built environment [Provis and Bernal, 2014b, Guo et al., 2023]. Precursors [Juenger et al., 2011] widely employed in alkali-activated cements (AACs) are natural materials, such as treated clay [Scrivener et al., 2018a] or feldspars [Oestrike et al., 1987] and industrial by-products like blast furnace slag generated during iron-making [Provis and Van Deventer, 2013] or fly ash (generated during coal-combustion) [Almalkawi et al., 2019]. They show superior performance characteristics over traditional OPC in terms of chemical and temperature resistance [Garcia-Lodeiro et al., 2015]. AACs are a low-carbon, high-performance substitutes of conventional cements for many applications, and are gaining more industrial acceptance as a solution contributing to decarbonize the construction sector.

Conventionally studied AAC mixtures contain both liquid phase (activator) and solid phase (aluminosilicate precursors) materials. Alkaline activators such as sodium silicates or hydroxides with strong corrosive and viscous properties require special attention during handling, and should be used by taking strict protective measures, which is very unfavorable for current construction practices especially for on-site casting [Provis et al., 2015, Provis and Bernal, 2014b].

Varieties of AACs have undergone development and investigation over time, categorizing them into two primary groups according to precursors' chemical composition, which can be presented in the oxide system of $CaO-SiO_2-Al_2O_3$. They are (1) high Ca and (2) low Ca systems, that differs in the mechanism as described in Figure 2.1 [Provis and Van Deventer, 2013]:

(1) High Ca-$(Na, K)_2O-CaO-Al_2O_3-SiO_2-H_2O$ system: In this system, materials like blast furnace slag which content of silica and calcium oxide exceed 70% of the total, are activated under appropriately suitable alkaline conditions [Bakharev et al., 2000,

Provis and Van Deventer, 2013, Bakharev et al., 1999]. Then the main reaction product is an aluminum substituted calcium silicate hydrate (C-(A)-S-H) type gel, similarly to the hydration product forming in OPC with Al-containing supplementary cementitious materials [Provis and Van Deventer, 2013].

(2) Low Ca-(Na, K)$_2$O-Al$_2$O$_3$-SiO$_2$-H$_2$O system: Precursors in this system mainly include aluminum and silicon as well as CaO but exhibit a lower content, like metakaolin or type F fly ash. After the alkali-activation, the main product forming during the process is an alkaline aluminosilicate hydrate ((N, K)-A-S-H) type gel with a structure of three-dimension. It can also be referred to as a geopolymer or inorganic polymer [Palomo et al., 1999, Palomo et al., 2004, Provis et al., 2009].
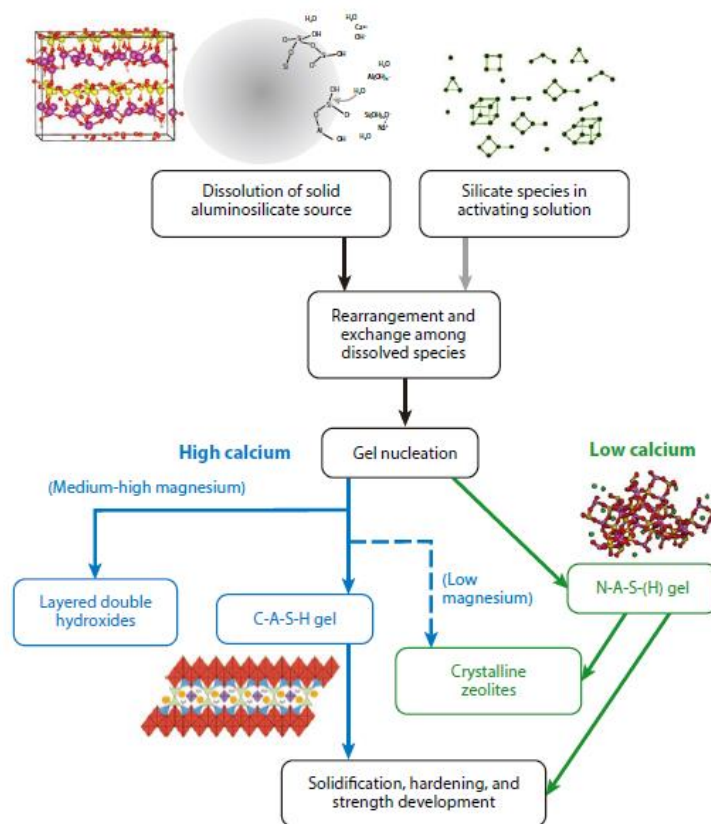
Figure 2.1 Different routes for high calcium and low-calcium systems. Adapted from [Provis and Van Deventer, 2013]

Due to the great variety of precursors that can be used for producing these cements, including agricultural ashes, metallurgical slags among others [Provis et al., 2015], it is necessary to discuss how their chemistry influences their microstructure and properties, this being linked to their reactivity affected by different activator types and amount used, changeable curing condition adopted. As it has previously been explained, this PhD project will focus on using blast furnace slag (a high Ca system) as a precursor - these are the most well-understood precursors for manufacturing alkali-activated cements,

and therefore the most suitable for use in developing a novel activator. Hence, the subsequent section will offer a comprehensive overview of the current state of knowledge concerning alkali-activated slag cements.

2.2 Alkali-activated slag cements

This section focused on choosing GGBFS as the precursor for manufacturing AACs, on the aspect including GGBFS's chemistry, the reaction kinetics as well as phase assemblage evolution is discussed.

2.2.1 GGBFS

The GGBFS powder contains a substantial glassy component, typically ranging from 80% to 90% of the material, and this glassy phase exhibits inherent hydraulic properties. Figure 2.2 [Pacheco-Torgal, 2014] is a schematic structure of the glassy slag. In the molten glassy structure of slag, silicon atoms are bridged together by bridging oxygen to form a network space, in which network changing body ions (such as Ca^{2+}, Mg^{2+}, etc.) are irregularly distributed in this space [Garcia-Lodeiro et al., 2015, Provis and Bernal, 2014a]. When the molten glass body undergoes rapid cooling, the network structure at this time is fixed, building a network that extends uniformly in each direction, and the structure is manifested as short-range order and long-range disorder [Zanotto and Mauro, 2017].
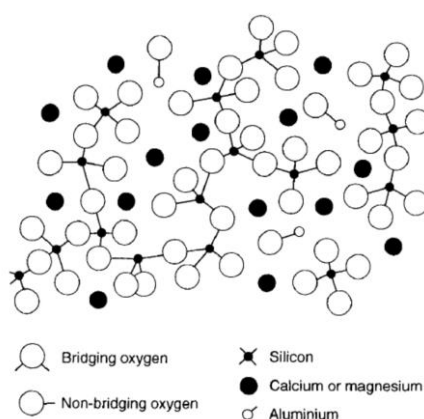
Figure 2.2 Slag exhibits glassy structure. Reproduced from [Pacheco-Torgal, 2014]

GGBFS primarily comprises SiO_2, Al_2O_3, CaO and MgO, alongside trace elements like Fe_2O_3, MnO, TiO_2, P_2O_5, among others. A ternary diagram illustrating the CaO-SiO_2-Al_2O_3 in the composition is presented in Figure 2.3 [Pacheco-Torgal, 2014]. Typically, GGBFS consists of 30-50% CaO, 27-42% SiO_2, 5-20% Al_2O_3, and 1-18% MgO [Bernal et al., 2014a, Provis and Van Deventer, 2013]. When considering OPC, GGBFS contains lower CaO levels but higher SiO_2 content [Provis et al., 2015].

GGBFS's potential reactivity in alkali activation hinges primarily on its internal structure [Provis and Bernal, 2014a]. The vitreous structure of GGBFS is closely tied to its chemical composition, exerting a substantial influence on its hydraulic reactivity. The role of MgO within this context is contingent upon the concentrations of CaO and Al_2O_3 in the slag [Ben Haha et al., 2011b, Ben Haha et al., 2012]. Notably, TiO_2 content only becomes influential when exceeding 4% [Pacheco-Torgal, 2014].
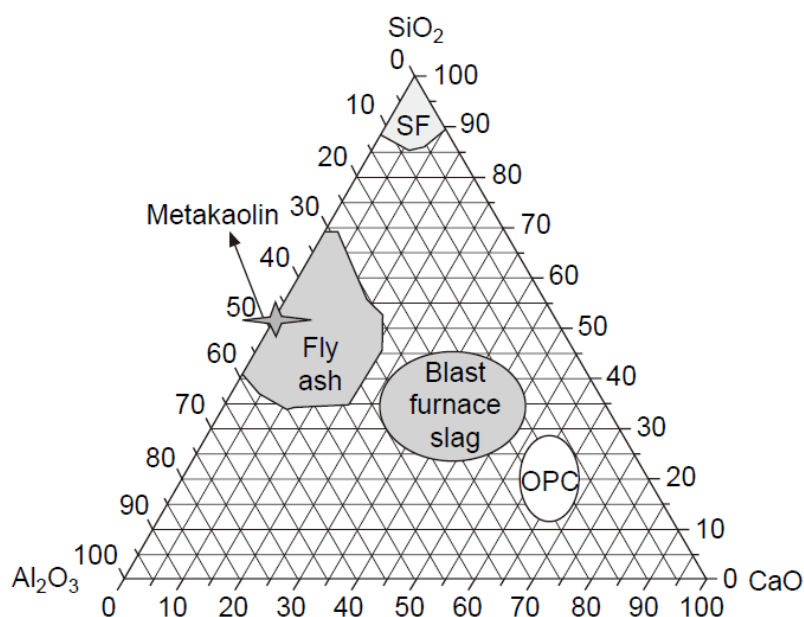
Figure 2.3 Raw materials in the composition range of $CaO-SiO_2-Al_2O_3$
for preparing alkali-activated cement. Reproduced from [Pacheco-Torgal, 2014]

The level of vitrification and reactivity of GGBFS exhibits an upward trend with higher CaO content within the slag. Nevertheless, when CaO content within the slag becomes excessively high, the viscosity of the molten slag decreases, rendering it more susceptible to crystallization during cooling [Provis et al., 2015, Provis and Van Deventer, 2013]. This process leads to reduced glassy components and, subsequently, decreased reactivity [Garcia-Lodeiro et al., 2015, Imen Yamina et al., 2021]. Typically, the content of SiO_2 in the slag surpasses that of CaO and Al_2O_3. The higher viscosity of molten SiO_2 is generally advantageous for glassy body formation to some extent. However, an excessive SiO_2 content may result in crystallization during cooling, yielding alkaline calcium silicate and high-silica glass, thereby diminishing reactivity [Garcia-Lodeiro et al., 2011, Silva et al., 2007]. Al_2O_3 exists within the slag in both four-coordination and six-coordination forms [Silva et al., 2007]. The prevailing belief is that six-coordinate Al contributes positively to reactivity, whereas four-coordinate Al exerts an adverse impact [Ben Haha et al., 2012]. MgO functions as a network modifier within the slag's glassy component, and its presence augments the reactivity of the slag's glass body [Ben Haha et al., 2011b, Zhang et al., 2022]. The presence of

MgO in a cement system is contingent upon its binding within non-reactive phases such as merwinite [Chen et al., 2010]. This is particularly advantageous for ensuring the stability of autoclaved Portland cement-slag blends, but proves detrimental when present as a more reactive periclase form [Jin et al., 2015].

Alkali activation is a promising valorization and management route of wastes and by-products in the construction industry. The primary distinction between AACs and OPC lies in the fact that the hydration reactions of OPC occur immediately upon mixing with water, whereas alkali activation necessitates the incorporation of alkalis to initiate the reaction. Provis et al. [Provis, 2018] outlined that the activator could be any compound, but needs to supply alkali cations, while elevating the pH value of the forming solution as a alkali source, and enhancing solid dissolution. The key role of activators in AAS is to promote slag dissolve into small structural units, and then polycondensate as the reaction proceeds to form a short-range ordered gel structure. Hence, the choice of an appropriate alkali activator plays a pivotal role in the advancement of AACs, as it can strongly affect the characteristics and performance of AACs.

The following section will discuss various alkaline activators, which commonly encompass alkali hydroxides and concentrated alkali silicates. Additionally, the potential use of alkali carbonates and sulfates for alkaline activation will be explored.

2.2.2 Conventional alkaline activators

Aluminosilicates are commonly activated by alkali hydroxides in the form of aqueous solutions. This choice is primarily attributed to the fact that both precursor dissolution and gel formation are processes that take place at the interfaces between liquid and solid phases, and both processes necessitate the presence of water [Duxson et al., 2005, Provis, 2018].

Sodium hydroxide is the most commonly used hydroxide solution as an alkali activator [Shi et al., 2019, Luukkonen et al., 2022]. While potassium hydroxide has specific applications, the widespread use of lithium, rubidium, and cesium hydroxides is restricted because of their higher cost together with scarcity [Provis and Bernal, 2014a, Shi et al., 2019]. Alkali hydroxides are typically manufactured through the electrolysis of chloride salts [Provis et al., 2015]. However, this process involves some energy consumption and results in associated CO_2 emissions during AACs manufacture. The extent of emissions attributed to the process depends on factors such as whether chlorine is also generated during the process and whether it is a valuable product or a by-product [Bernal et al., 2014a].

Studies indicate that NaOH demonstrates a higher ability for the release of silica and alumina monomer compared to KOH [Halasz et al., 2007]. In the presence of soluble silicates associated with Na or K, the polymerization process accelerates when compared to the use of alkaline hydroxide alone [Alhawat et al., 2022]. When alkali hydroxide activators are incorporated into AAC mix designs, their higher concentrations can be considered as a potentially hazardous substance concerning occupational health and safety [Provis et al., 2015, Provis and Bernal, 2014a]. The preparation of concentrated hydroxide solutions can lead to a significant increase in temperature due to the exothermic nature of their dissolution, posing challenges for industrial production. High-concentration hydroxide solutions are more susceptible to efflorescence, primarily because of their greater permeability when compared to silicates [Longhi et al., 2019]. Considering that the degree of reaction accomplished by the binder prior to curing is typically limited, the resulting open microstructure allows for the presence of mobile, alkali-rich pore solutions. Surplus alkali can interact with atmospheric CO_2, resulting in the creation of white carbonate or bicarbonate crystals. These formations may present potential hazards to the structural stability of the material [Jun et al., 2023, Longhi et al., 2019]. It's important to note that efflorescence is more likely to occur with sodium hydroxide than with potassium hydroxide.

In addition to the aforementioned alkali hydroxide solutions, alkali-silicate solutions offer an alternative activation method. Sodium or potassium are the most widely utilized alkali metal cations in alkali-silicate solutions [Shi et al., 2019]. Alkali silicate is commonly generated by melting carbonate and silica to form a glass, which is then dissolved in water to yield a viscous, adhesive solution often referred to water glass [Provis et al., 2015, Duxson et al., 2005]. Among alkali-silicate solutions, sodium silicates, in particular, are the second most widely used for the alkali activation of slag [Bernal et al., 2014a, Provis and Bernal, 2014a]. Soluble silica plays a pivotal role in this process as it significantly influences processability, solidification, and mechanical strength [Garcia-Lodeiro et al., 2015, San Nicolas et al., 2014]. Moreover, it impacts the composition of the gel and the microstructure of the resulting material [San Nicolas et al., 2014, Bernal et al., 2010].

The use of different conventional activators in alkali-activated materials demonstrates varied effects on the properties and suitability of these materials. Sodium hydroxide (NaOH) [Zhang et al., 2017, Redden and Neithalath, 2014, Lu and Poon, 2018] exhibits high alkalinity, facilitating the solubilization of silica and alumina, resulting in strong compressive strength and optimal geopolymerization. Potassium hydroxide (KOH) [Richardson and Li, 2018] with its larger cation size, enhances polycondensation reactions, leading to a denser geopolymer network and increased compressive strength. Sodium silicate provides additional SiO_2 [Yliniemi et al., 2015], maintaining high alkalinity and contributing to improved compressive strength while preserving a denser microstructure. Mixed solutions, such as NaOH + Na_2SiO_3 or KOH + K_2SiO_3 or with other combination [Zaharaki et al., 2016, Nazari and Sanjayan, 2015,

Zawrah et al., 2016, Manjunath et al., 2019], demonstrate synergistic effects, leading to higher compressive strength, improved microstructure, and self-sealing capabilities. The choice of conventional activator significantly influences the performance of alkali-activated materials, emphasizing the need for careful consideration based on specific material and application requirements.

Table 2.1 A summary of conventional alkaline activators focus on suitability

Activator Type	Precursors	Effects on the properties of AAC	Suitability of the product	References
Sodium Hydroxide (NaOH)	Metakaolin+ fly ash + slag/GGBFS	• Produces geopolymer with good mechanical strength. • Sodium hydroxide results in uniform morphology and dense gel phase in geopolymers. • Geopolymers activated with NaOH tend to have better mechanical, thermal, and morphological behavior.	Promotes high compressive strength, with variations in morphology based on precursor. Optimal for geopolymerization.	[Zhang et al., 2017, Redden and Neithalath, 2014, Lu and Poon, 2018]
Potassium Hydroxide (KOH)	Metakaolin+ fly ash + slag/GGBFS	• Promotes higher compressive strength compared to NaOH. • Favorable for the formation of geopolymers with a dense polycondensation reaction.	Favors dense polycondensation reaction, enhances geopolymer network formation, and increases compressive strength.	[Richardson and Li, 2018]
Sodium Silicate (Na$_2$SiO$_3$)	Metakaolin, fly ash, GGBFS, ladle slag	• Addition increases degree of condensation and mechanical strength. • Combining sodium silicate with sodium hydroxide results in geopolymers with greater strength and	Enhances compressive strength, aids in condensation, but may result in lower crystalline formation. Maintains a denser microstructure.	[Yliniemi et al., 2015]

		denser microstructures.			

| Mixed Solution (e.g., NaOH + Na_2SiO_3) | Metakaolin+ fly ash + slag/GGBFS | • Higher compressive strength observed with mixed solution in alkali-activated materials.
• SiO_2/Na_2O ratio= 1-2, preferred for greater strength and denser microstructures.
• Potassium-based (K-based) compounds advantageous for refractoriness and reduced efflorescence.
• Sodium-based (Na-based) compounds more commonly used due to cost and availability, despite higher associated energy and CO2 emissions. | • Favors denser polycondensation, increases geopolymer network, and enhances compressive strength for K-based systems.
• Promotes higher compressive strength, improves microstructure, and provides self-sealing capabilities for Na-based compounds. | [Zaharaki et al., 2016, Nazari and Sanjayan, 2015, Zawrah et al., 2016, Manjunath et al., 2019] |

2.2.3 Alternative alkaline activators

Near-neutral salts, mainly composed of sodium sulfate (Na_2SO_4) and sodium carbonate (Na_2CO_3), which can be sourced from natural deposits or as by-products from various industrial processes, have demonstrated the capacity to activate GGBFS [Mobasher et al., 2014a, Mobasher et al., 2016, Akturk et al., 2019]. Sodium carbonate can be derived from trona mining or through the Solvay process [Steinhauser, 2008]. Similarly, sodium sulfate can be obtained from mined mirabilite, Na-rich brines, or as

by-products of HCl production and silica pigment manufacturing [Bernal, 2016, Rashad et al., 2013a]. The production process of neutral salts-activated cement offers notable benefits, including reduced handling hazards associated with highly alkaline solutions and decreased environmental impact. Moreover, the cost-effectiveness of these neutral salts surpasses that of Na_2SiO_3 and NaOH [Bernal, 2016]. Nevertheless, current research indicates that the strength of AAS activated by these neutral salts is constrained among all curing time from early to later ages, and the product requires an extended period to achieve the necessary hardening with better workability for commercial construction applications [Clark and Brown, 2000].

Sodium carbonate-activated slag cements have demonstrated remarkable mechanical properties and durability, making them an attractive option for various construction applications. Their reaction process follows a similar path to sodium hydroxides after the carbonates were exhausted, resulting in high compressive strength and reduced porosity [Bernal et al., 2015b]. Notably, challenges like long setting times and delayed compressive strength development have been effectively addressed by various methods, such as incorporating slag types exhibit higher MgO in the composition, or adding layered double hydroxides (CLDH) [Ke et al., 2016]. On the other hand, sodium sulfate-activated slag binders offer a suitable solution for nuclear waste management due to lower pH values and less heat release [Rashad et al., 2013b]. Sodium sulfates/carbonates can reduce the hazards associated with highly alkaline solutions and minimize environmental impact [Rashad et al., 2013b, Mobasher et al., 2014b]. The costs of these neutral salts are competitive when related to traditional activators for example Na_2SiO_3 and NaOH [Mobasher et al., 2014b, Bernal et al., 2015c].

In summary, near-neutral sodium carbonate/sulfate activation of slag cements offers several advantages in terms of durability, environmental impact, and cost-effectiveness. However, challenges related to setting times, early strength development, and potential energy consumption should be carefully considered in their adoption.

Given that the conventional activation process is based upon the properties and requirements of the activators typically used (alkali hydroxides and silicates), there has been a move towards investigating alternative sources of alkalinity which are compatible with conventional concrete production processes. Whilst not all of the sources investigated are applicable to slag, they offer precedents for how novel alkali sources can be adapted for AAC production.

The investigation into alternative activators for alkali-activated materials unveils promising pathways for sustainable and cost-effective solutions. Diverse studies have probed the suitability and effects of various activators, including rice husk ash (RHA), waste glass, potassium hydroxide (KOH) with silica fume, and agricultural by-products (Olive and almond-shell biomass ash). These alternative activators, when paired with

suitable precursors like fly ash, blast furnace slag, or metakaolin, have demonstrated substantial potential. RHA-based solutions [Mejía et al., 2014, Tong et al., 2018], while exhibiting commendable compressive strength slightly lower than commercial sodium silicate, illustrate a feasible alternative. Waste glass [Tchakouté et al., 2016, Tchakouté et al., 2017], serving as an activator, yields impressive mechanical performance, outperforming RHA-based solutions. Potassium hydroxide with silica fume [Villaquirán-Caicedo, 2019] as an alternative activator shows enhanced compressive strength and favorable microstructural characteristics, indicating equivalence to conventional activators. Activators derived from olive biomass ash (OBA) [Alonso et al., 2019, de Moraes Pinheiro et al., 2018, Font et al., 2017] and almond-shell biomass ash (ABA) [Soriano et al., 2020] showcase promising results, with OBA demonstrating efficiency comparable to commercial KOH. These findings underscore the suitability of different alternative activators, shedding light on their effects in terms of environmental benefits and reduced production costs. Additionally, the observed potential of these activators to enhance the mechanical properties of alkali-activated materials suggests a viable path for sustainable and economical construction practices.

Table 2.2 A summary of alternative activators focus on the suitability

Activator Type	Precursors	Effects on the properties of AAC	Suitability of the product	References
Rice Husk Ash (RHA) + NaOH	Blast furnace slag and metakaolin	- Compressive strength around 42 MPa at 7 days.	Demonstrates feasibility as an alternative activator, with moderate compressive strength. Reduces production costs substantially.	[Mejía et al., 2014]
Rice Husk Ash (RHA) + NaOH	Fly ash, blast furnace slag (60% FA)	- Similar mechanical performance to commercial sodium silicate. Shorter setting times, suggesting more readily available silicates in RHA-derived solution. Compressive strength around 60 MPa at 28 days.		[Tong et al., 2018]
Waste Glass + NaOH	Fly ash and blast furnace slag	- Compressive strength values ranged from 22.9 MPa (7 days) to 39.7 MPa (56 days). Higher strength compared to RHA-based solution. Higher amounts of soluble Si ions in glass	Impressive mechanical performance, outperforming RHA-based solutions. Demonstrates potential for sustainable construction practices.	[Tchakouté et al., 2016]

		waste solution confirmed by FTIR.		
Potassium Hydroxide (KOH) + Silica Fume	Portland cement and blast furnace slag	- Mechanical strength increase with 50% replacement of commercial activator by alternative. Strength values higher than 60 MPa at 7 days. Microstructural analysis showed predominant amorphism.	Indicates equivalence to conventional activators, with enhanced compressive strength and favorable microstructural characteristics.	[Villaquirán-Caicedo, 2019]
Olive Biomass Ash (OBA)	Blast furnace slag, coal ash	- Alkali-activation of blast furnace slag with OBA showed satisfactory mechanical performance close to commercial KOH. Alkali-activation of coal ash impracticable.	Demonstrates efficiency comparable to conventional activators, particularly in cost reduction.	[Alonso et al., 2019]
Olive Biomass Ash (OBA)	Blast furnace slag and coal ash	- High efficiency of OBA-based activator in terms of mechanical performance. OBA-based mortars showed better mechanical behavior compared to KOH-activated mortars.		[de Moraes Pinheiro et al., 2018, Font et al., 2017]
Almond-Shell Biomass Ash (ABA)	Blast furnace slag	- Almond-shell biomass ash as an activator promoted higher compressive strength and the formation of C–S–H/C(K)-A-S-H gels.	Shows promising results, enhancing compressive strength and contributing to gel formation.	[Soriano et al., 2020]

Red mud [Li et al., 2021, Hertel and Pontikes, 2020, Qaidi et al., 2022], a by-product of alumina refining, offers an economical alternative with the potential to strengthen the properties of AACs. Advantages include its pozzolanic reactivity, which can enhance mechanical performance and mitigate environmental issues associated with red mud disposal [Qaidi et al., 2022, Ye et al., 2016]. However, the high alkalinity requirement for its activation and challenges in controlling the setting times can be limiting factors [Choo et al., 2016]. Nonetheless, variations in composition, alkali content, and combustion processes require stringent quality control.

Overall, these alternative activation routes present promising solutions for sustainable cementitious materials. The advantages lie in their potential to utilize industrial and environmental by-products, reduce waste, and lower the carbon footprint of construction. Nevertheless, challenges like variations in feedstock composition, potential high costs, and specific technical requirements need to be addressed to ensure consistent performance.

2.2.4 Reaction kinetics of AAS

Numerous variables have the potential to affect the reaction kinetics of AAS. Subsequent discussion focused on particular emphasis placed on the activator type, specifically sodium hydroxide, sodium silicate, and potassium hydroxide.

In a study involving GGBFS with varying MgO contents activated by sodium silicate (Na_2SiO_3)[Bernal et al., 2014c], distinct reaction kinetics were observed. The hydration process displayed an initial pre-induction phase, as indicated by the first peak, which transpired in less than 1.5 hours. This was succeeded by the formation of reaction products during a phase characterized by rapid acceleration and deceleration, constituting the second peak. This is primarily resulted by the generation of C-(A)-S-H type gels [Bernal et al., 2014a, Provis and Bernal, 2014a]. Interestingly, samples have smaller amount of Al_2O_3 and large MgO amount experienced an extended induction period. Specifically, GGBFS with the Al_2O_3 in a smaller amount but MgO content (exceeding 7%) displayed accelerated reaction kinetics [Bernal et al., 2014c]. However, it is worth noting that a different trend was discovered by Ben Haha et al. [Ben Haha et al., 2011b]. In their research, the first peak in the reaction was observed between 2 and 4 hours, and the subsequent second peak occurred during the acceleration and deceleration process after 2 days, specifically in AAS cements with higher MgO content of 11% and 13%, respectively. The concentration of Al_2O_3 will modulate the consequences of different levels of MgO on reaction kinetics, potentially offering a method to customize the formation of secondary reaction products. Sodium hydroxide (NaOH)-AAS cements exhibit a distinctive behavior compared to silicate-activated slag cements [Bernal et al., 2014a, Provis and Bernal, 2014a, Provis and Van Deventer, 2013]. They do not undergo an extended dormant period. Instead, there is an initial peak appeared at the very early time once the reaction began, followed by another big peak occurred from 1h to 24 h [Ben Haha et al., 2011b, Ben Haha et al., 2012]. AAS were produced using a 5 mol/L potassium hydroxide (KOH) solution and cured for 18 years [Richardson and Li, 2018]. The findings [Richardson and Li, 2018] demonstrate that the main reaction products observed from the samples are C-(A)-S-H type gels and Mg-Al layered double hydroxide (LDH) with a consistent Mg/Al ratio of 2.6, which remains unchanged over the curing period. In general, potassium hydroxide (KOH) tends to

enhance fluidity [Omur et al., 2022] and promote strength development [Omur et al., 2022, Jun et al., 2020], while sodium hydroxide (NaOH) has the effect of reducing shrinkage [Omur et al., 2022].
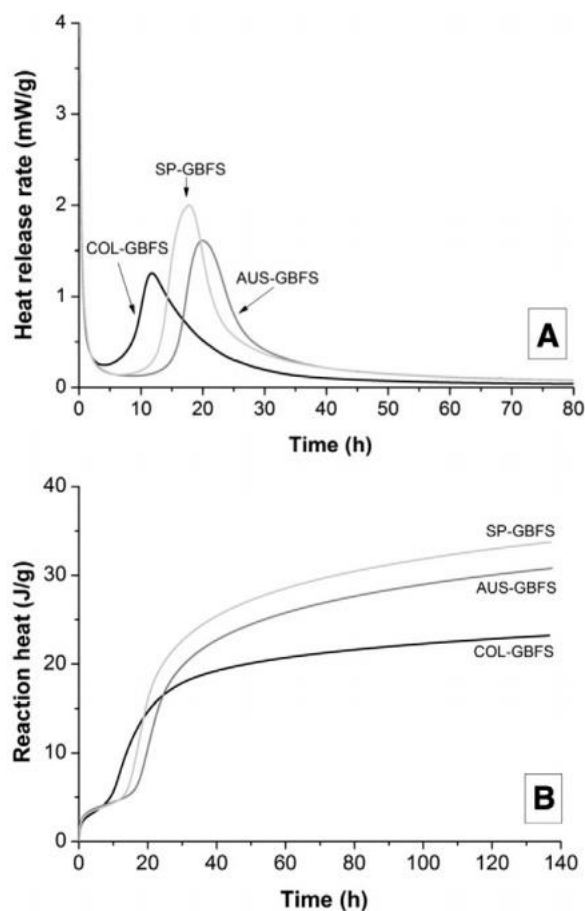
Figure 2.4 (A) Rate of heat release and (B) cumulative reaction heat of sodium silicate-activated GBFS exhibit varying MgO content in the composition of GBFS. COL-GBFS: GBFS with 1.17% MgO, AUS-GBFS: GBFS with 5.21% MgO, and SP-GBFS: GBFS with 7.44% MgO. Adapted from [Bernal et al., 2014c]

2.2.5 Phase assemblage evolution of AAS

When considering AACs, the chemistry and amount of reaction products that emerge are significantly shaped by factors such as oxide composition of slag, activator with varying metal cations and ions, activator dosage, and various curing conditions employed. The formed main reaction products in AAS can be summarizing [Pacheco-Torgal, 2014, Garcia-Lodeiro et al., 2015, Provis and Bernal, 2014a]:

(1) The principal reaction product is a hydrated calcium aluminosilicate gel (C-(A)-S-H), characterized by a lower Ca/Si ratio (Ca/Si = 0.9-1.2). Interestingly, this ratio does not exhibit significant variations compared to the gel formed in OPC;

(2) Secondary reaction product-hydrotalcite ($Mg_6Al_2CO_3(OH)_{16}\cdot4H_2O$) is stable in both NaOH and water glass activated slag systems. Hydrotalcite is a natural mineral phase with a unique structure, made up of a layered structure consisting of brucite ($Mg(OH)_2$) sheets with intercalated H_2O molecules as well as CO_3^{2-} ions. These crystals, typically on a submicroscopic level, are scattered throughout the C-(A)-S-H gel.

(3) C_4AH_{13} crystal phases have been discovered in NaOH-AAS system. These products manifest in the shape of thin flakes, measuring approximately 0.1-0.2 mm in thickness and with a diameter of roughly 1.5 mm. In addition, other scholars simultaneously observed carbonate phases, including C_4AcH_{11} and $C_8Ac_2H_{24}$, in NaOH-AAS and $Ca(OH)_2$-AAS (A equals to Al_2O_3, N equals to Na_2O, S represents SiO_2, H means H_2O, C is CaO, c equals to CO_2).

Calcium (sodium) aluminosilicate hydrate, C-(N-)A-S-H type gel, represented the main reaction product in both high-Ca and low-Ca system, which owing a tobermorite-like structure with disorder, shown as Figure 2.5 [Myers et al., 2015].
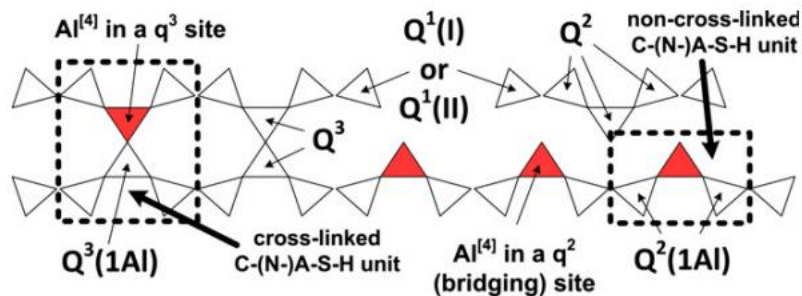
Figure 2.5 A schematic diagram presented the structure of C–(N-)A–S–H type gels. Aluminate species are presented by red tetrahedra, and silicate species as presented as white tetrahedra. Adapted from [Myers et al., 2015].

The composition of slag strongly affects the growth on structure by the formed solid phases in AAS [Bernal et al., 2014c, Le Saoût et al., 2011, Ben Haha et al., 2011b, Ben Haha et al., 2012]. The content of Al_2O_3 in slag materials has a pronounced impact on C-(A)-S-H type gels formed in AACs. Observations were conducted on GGBFS with varying Al_2O_3 content (7-17%). It was noted that the increased presence of Al_2O_3 led to notable changes in the formed hydrotalcite, particularly in the Mg/Al ratio within the AAS system. This leads to an enhanced integration of aluminum into the C-(A)-S-H type gels, ultimately facilitating the occurrence of strätlingite shown in Figure 2.7 [Ben Haha et al., 2012]. This relationship is particularly evident when occurring higher alkalinity [L'Hôpital et al., 2015, Schneider et al., 2001]. On the other hand, slag with various amount of MgO has an effect in controlling the available Al within the system,

which significantly influences the concentrations of secondary products such as hydrotalcite [Jin et al., 2015]. GGBFS owing smaller amount of MgO, as documented in previous studies [Ben Haha et al., 2011b, Bernal et al., 2014c], expedites the initial reaction stages, albeit at the cost of diminishing the overall degree of reaction attained. This promotes C-(A)-S-H type gels developed has a higher aluminum absorption, longer chain lengths, and reduced crosslinking in the later stages of the process. AAS with lower MgO content (<5%) tend to favor zeolites, particularly gismondine, while higher amount of MgO promotes more hydrotalcite formed shown in Figure 2.6 [Bernal et al., 2014c]. The intricate interplay between slag composition, the resultant secondary phases, the C-(A)-S-H type gels with varying structural features and different chemistry behind underscores the complexity of AAS and their response to varying Al_2O_3 and MgO content. Table 2.3 provides a concise overview of the impact of MgO content on the phase assemblage evolution in AAS based on varying slag compositions.

Table 2.3 The content of Al_2O_3 on phase assemblage evolution

Al_2O_3 Content	Impact on Phase Assemblage Evolution	Reference
7-17%	• Notable changes in hydrotalcite, particularly in Mg/Al ratio within AAS system. • Enhanced integration of aluminum into C-(A)-S-H type gels, facilitating strätlingite formation.	[Ben Haha et al., 2012]. [L'Hôpital et al., 2015, Schneider et al., 2001]
Varying	MgO content affects Al availability, influencing concentrations of secondary products like hydrotalcite. • Lower MgO expedites initial reaction stages but diminishes overall degree of reaction. AAS with <5% MgO favors zeolites • Higher MgO promotes hydrotalcite formation.	[Jin et al., 2015] [Ben Haha et al., 2011b, Bernal et al., 2014c]
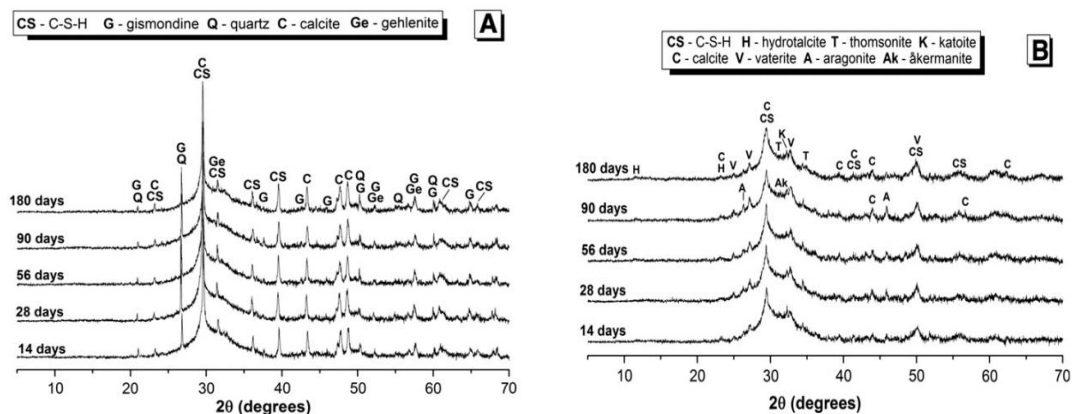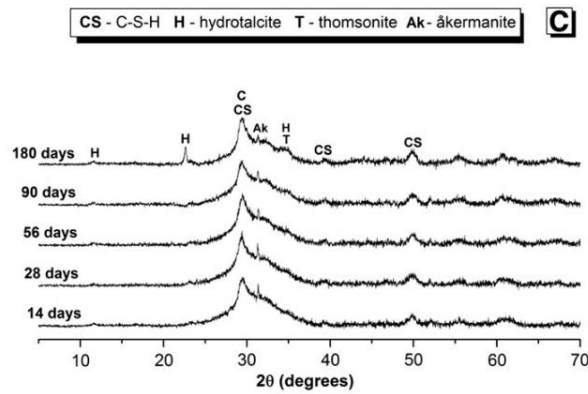
Figure 2.6 XRD patterns of alkali-silicate slag cements with different MgO content (A) 1.17% MgO, (B) 5.21% MgO, and (C) 7.44% MgO. Adapted from [Bernal et al., 2014c]
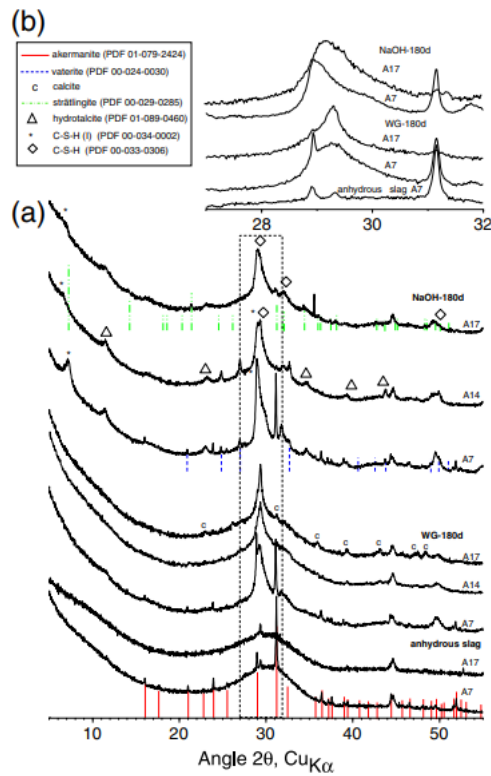
Figure 2.7 XRD patterns of anhydrous slag and AAS cements curing after 180 days at (a) the range of 5-55°, and (b) the range of 25-32°. A7-slag with 7% Al_2O_3, A17- slag with 17% Al_2O_3, WG-water glass. Adapted from [Ben Haha et al., 2012] .

2.3 Research gap and motivation

GGBFS has variable chemical composition, so it is necessary to add appropriate alkalis and adjust the mix design based on a given slag's composition. The above operations have very high requirements on the technical level of the operator, and high-

level technicians are not common. The promotion and application of this technology relies on skilled and experienced technicians and has not continued to increase with the growth of market demand for "green" building materials.

There are also questions around whether it is feasible to produce the typical activators (alkali hydroxides and silicates) at the scale required to meet any significant proportion of global demand for cements. Each year, the chlor-alkali process yields approximately 60 Mt of NaOH, with limited prospects for expanding production due to constrained demand for chlorine worldwide as a by-product in the world [Khale and Chaudhary, 2007]. Thus, there is a demand for alternative activators which are both scalable and have a sufficiently low environmental impact.

Furthermore, it is widely recognized that GGBFS undergoes dissolution when combined with alkaline activators, leading to a reaction process with kinetics and the type and quantity of reaction products formed that are often challenging to predict [Amer et al., 2021b].

The existing research on alternative activators for alkali-activated cements has primarily focused on well-established solutions, such as sodium sulfate (Na_2SO_4), sodium carbonate (Na_2CO_3), sodium aluminate, red mud, and calcium oxide (CaO). While these activators have shown promise, there remains a notable research gap in understanding and controlling the intricate reaction processes and kinetics associated with these activators, particularly when applied to GGBFS. The existing alternatives exhibit dissolution behaviors in the presence of alkaline activators, leading to challenges in predicting the kinetics and the nature of the reaction products.

The motivation behind seeking new alternative activators stems from the need to address these uncertainties and gain better control over the reaction process. By exploring novel alternative activators, there is an opportunity to tailor the composition and characteristics of the activators, thereby influencing the reaction kinetics and the resulting products. This approach aims to provide a more nuanced and customizable activation method for producing AAC, enhancing the understanding and predictability of their performance.

2.4 Promising alternative alkaline activators

In the case of metal carboxylate salts, a potential route to achieve some level of control over the solubility behavior of these salts is to produce glasses, rather than use them in their crystalline form [Zanotto and Mauro, 2017]. Glasses formation gives the resultant material homogeneous properties, which means non-stoichiometric compositions can be formed. The properties can, in principle, be tailored and not limited

to the values of the individual compounds [Angell, 1990, Zanotto and Mauro, 2017]. Therefore, a range of properties such as solubility can be controlled by tailoring glass composition, compared with materials in their crystalline form.

The releasing of alkalinity over time after mixing with water is the most desirable property for a solid activator, as it allows control kinetics of reaction of the alkali-activation process. Thus, glasses formed by metal carboxylate have the potential to fulfill all the requirements for a novel activator for use in manufacturing of AACs. As discussions will be elaborated upon in subsequent sections, the low melting point (typically <400°C) of metal carboxylate salts means that manufacture of these glasses would not be as energy-intensive as other manufacturing routes.

In this section, the glass formation ability, the solubility of the glasses composed of metal carboxylates, and the application of metal carboxylates in cementitious materials are presented and discussed.

2.4.1 Utilization of metal carboxylates in cementitious materials

Metal carboxylates have the potential on glass-forming through the casting process, which means that their properties, particularly their solubility and/or composition can be tailoring depending on the type of metal carboxylate used. Following an extensive literature review, it was evident that there is a lack of studies or references regarding the use or addition of metal carboxylates in AAS systems. Nonetheless, the utilization of acetates in OPC-based cementitious materials has been subject to a paucity of research investigations or in other construction materials, which will be summarized in this section.

Metal acetates are commonly employed as deicers for concrete pavements in airfield applications [Abed et al., 2023, Giebson et al., 2010]. The impact of different deicers, such as magnesium acetate (MgAc), calcium acetate (CaAc), and calcium magnesium acetate (CMA), owing varying Mg: Ca ratios on the deterioration of cementitious materials has been explored [Sajid et al., 2022]. Their findings have highlighted that the primary cause of deterioration is that generated non-cementitious magnesium silicate hydrate (M-S-H), which results in the peeling of aggregates and cement paste [Sajid et al., 2022]. Notably, the addition of MgAc and CMA resulted the precipitation of M-S-H, brucite, and calcite, while CaAc produced only calcite [Antolik et al., 2023]. Therefore, a lower Mg: Ca ratio has been recommended to mitigate deterioration, a conclusion in line with Lee's study [Lee et al., 2000]. Their research also implies that the occurrence of magnesium in acetate solutions can result in concrete damage, with the damage rate correlating with the percentage of magnesium in the mixtures. CaAc, on the other hand, resulted in minimal deterioration, suggesting that

higher Mg: Ca ratios potentially cause severe damages and can result in premature concrete degradation.

However, this contrasts with the findings of Dunn and Schenk [Dunn and Schenk, 1980a], who argue that a higher ratio can be advantageous for deicing purposes, citing the greater solubility and reduced freezing point depression exhibited by magnesium acetate. Recommendations are made on using CMA with an Mg: Ca ratio of 7:3 as a deicer to minimize concrete frost damage on airport pavements aligning with the results of Dunn and Schenk [Dunn and Schenk, 1980b]. Deicing solutions containing magnesium, such as CMA, have been shown to induce significant degradation of the paste. This degradation is a result of the formation of brucite and M-S-H phases, although these solutions are generally less corrosive than chloride-based deicers [Tsang et al., 2016, Peterson, 1996]. However, CMA does not offer the same cost-efficiency as chloride-based deicers, and its use is constrained by temperature-related constraints.

Sodium acetate (NaAc) and potassium acetate (KAc) have emerged as alternative acetate-based deicers in studies [Shi et al., 2009, Antolik et al., 2023]. While they exhibit more significant expansions of alkali-silica reaction (ASR) compared to conventional sodium chloride deicers, they demonstrate lower corrosiveness than sodium chloride, making them a viable option for use in specific extreme conditions [Kotwica and Malich, 2021, Feng et al., 2023]. KAc, in particular, operates efficiently at very low temperatures, benefiting the environment similar to calcium magnesium acetate (CMA) at -15°F [Sajid et al., 2022]. However, it should be noted that prolonged exposure of concrete to KAc as a deicer can result in more damage compared to sodium chloride (NaCl) [Xie et al., 2020, Wang et al., 2006]. Microstructural analysis has revealed that areas inside concrete specimens after treated with KAc deicer, the interfacial transition zone (ITZ) appeared potassium sulfate crystals and higher values of porosity [Silva et al., 2014]. The presence of potassium acetate leads to structural changes in pastes and a subsequent increase in pH levels, releasing substantial amounts of hydroxide ions. This process initiates with potassium acetate, followed by the formation of calcium-potassium compounds and ultimately potassium sulfate [Silva et al., 2014]. Nonetheless, it is essential to highlight that KAc exhibits fewer detrimental impacts on asphalt than CMA, resulting in its enhanced crack resistance, which can lead to additional stress and cracking within intermediate temperature ranges of 0-60°C [Mirzababaei et al., 2023]. Table 2.4 summarizing the effect of different kinds of metal acetates as deicers on various aspects of concrete and the mechanisms behind their impact can be outlined:

Table 2.4 A summarized overview of the impact and mechanisms of different metal acetates as deicers on concrete

Deicer Type	Impact on Concrete	Mechanism Behind Impact	Reference
MgAc	Precipitation of M-S-H, brucite, and calcite	Generation of non-cementitious magnesium silicate hydrate	[Sajid et al., 2022] [Antolik et al., 2023].
CaAc	Precipitation of calcite	Minimal deterioration	[Antolik et al., 2023].
CMA	Precipitation of M-S-H, brucite, and calcite	Potential for significant degradation	[Tsang et al., 2016, Peterson, 1996]
NaAc	Significant expansions of alkali-silica reaction (ASR)	Lower corrosiveness compared to NaCl	[Shi et al., 2009, Antolik et al., 2023]
KAc	Significant expansions of ASR, efficient at low temperatures	Structural changes, release of hydroxide ions, formation of potassium sulfate	[Xie et al., 2020, Wang et al., 2006], [Silva et al., 2014], [Mirzababaei et al., 2023].

Metal acetates also find applications as organic admixtures, as demonstrated in the following instances. In a study by Zhang et al. in 2018 [Zhang et al., 2018a], KAc solution was used as an intermediate admixture subjected to freeze-thaw cycles for the purpose of assessing frost endurance of roller compacted concrete (RCC) containing rubber particles and steel fibers. The research findings indicated that, with a 25% (by weight) KAc solution, the maximum cumulative mass loss reached 155.17 g/m2 after 300 cycles. In another assessment, Cao et al. [Cao et al., 2021] explored the impact of CaAc solution on the performance of OPC at various concentrations (1%, 2%, and 3%). When a 2% CaAc solution was utilized, it significantly facilitated the cement hydration process, resulting in the production of more ettringite and portlandite crystals as curing ages extended to 28 days (Figure 2.8). Consequently, there was a remarkable boost on the compressive strength of mortars when incorporating a 2% CaAc solution, yielding a 23.34% and 15.43% increase compared to systems lacking CaAc, after curing for 3 and 28 days, respectively. Furthermore, research by [Abed et al., 2023] suggests that a 5.1% CaAc content is the optimal value as an admixture for concrete using a water-to-cement (w/c) ratio equals to 0.48.
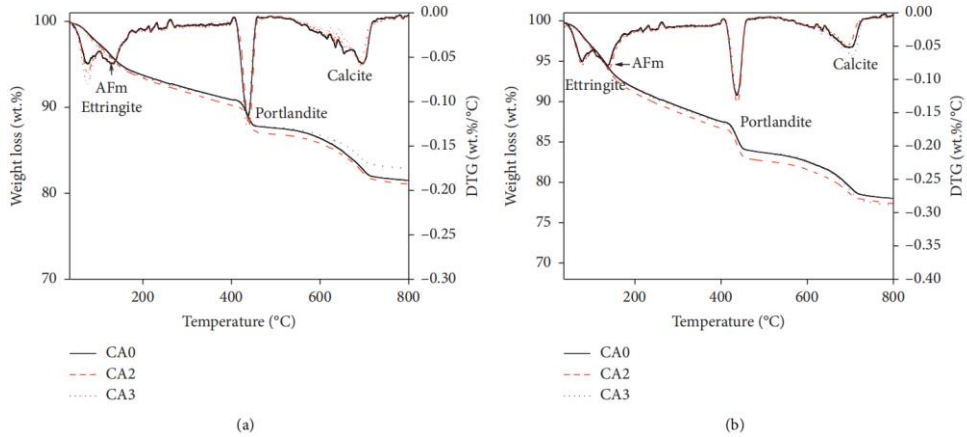
Figure 2.8 Weight loss results for OPC with varying CaAc content curing after (a) 3 days and (b) 28 days. Reproduced from [Cao et al., 2021]

In the conducted study [Lyu et al., 2022], who also produced AAS and the selection of admixture was CaAc, with concentrations ranging from 0% to 2% (by weight). These mixtures were prepared by combining CaAc with water glass and sodium hydroxide at a Ms ratio of 1.2. The investigation revealed that the reaction kinetics in AAS, which included 2% CaAc, was significantly hindered, resulting in a decline in compressive strength, as depicted in Figure 2.9, after cured 28 days [Lyu et al., 2022]. Nonetheless, it's worth noting that the compressive strength still exceeded 90 MPa. This could potentially resulted a microstructure exhibit a lower density, as evidenced in Figure 2.10 [Lyu et al., 2022]. There were no notable variations in the morphology since the main reaction products remained similar. Hence, it can be inferred that there exists an optimal CaAc dosage for producing AAS.
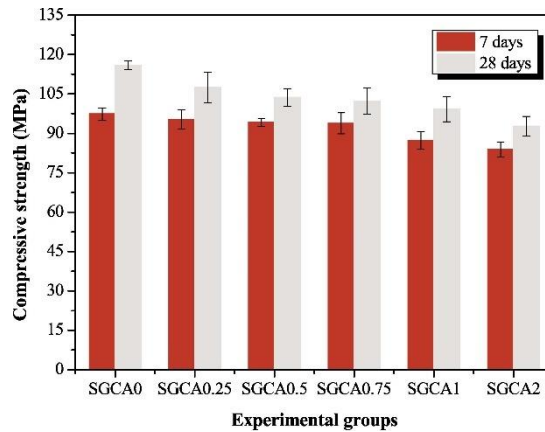
Figure 2.9 Compressive strength of AAS, SGCA0=SG (slag)+ CA0 (content of 0% CaAc), adopted from [Lyu et al., 2022]
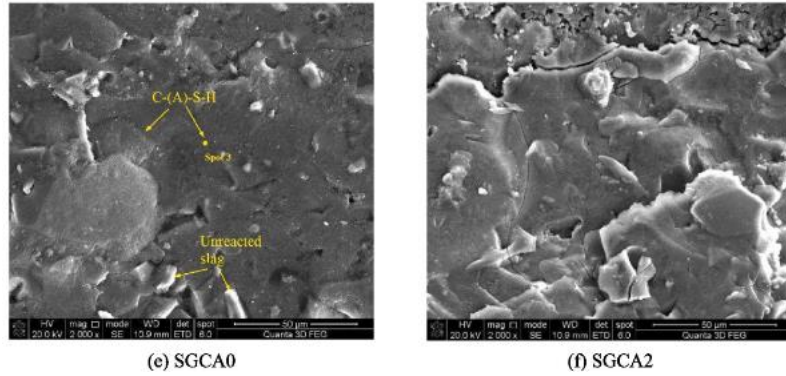
(e) SGCA0   (f) SGCA2

Figure 2.10 SEM images of AAS with various content of CaAc, (e) SGCA0-slag with 0% CaAc and (f) SGCA2- slag with 2% CaAc. Adapted from [Lyu et al., 2022]

Zinc acetate, when combined with trisodium citrate (TSC) to create TSC-zinc acetate, serves as an effective retarder, slowing down the corrosion of steel rebar in concrete interstitial solutions containing chloride [Maliekkal et al., 2018]. The effect on the formation of hydrated magnesium carbonates (HMCs) of MgAc regarded as an organic admixture was investigated according to Nguyen et al. [Nguyen et al., 2022]. Their research, depicted in Figure 2.11, elucidated a reaction pathway involving brucite in the MgAc solution. This pathway demonstrated that MgAc solution promotes large amounts of nucleation sites generated, resulting in an increased degree of reaction. It was observed that the initial nucleation sites necessary for the growth of HMCs become active after the complexes between Mg^{2+} and acetate ligands are disrupted, facilitating the establishment of bonds between Mg^{2+} and CO_3^{2-}. These findings align with previous research [Dung and Unluer, 2017], which explored the role of MgAc as a hydration agent to enhance the brucite content within Mg-based cement. This leading to form a denser microstructure and improving mechanical properties.
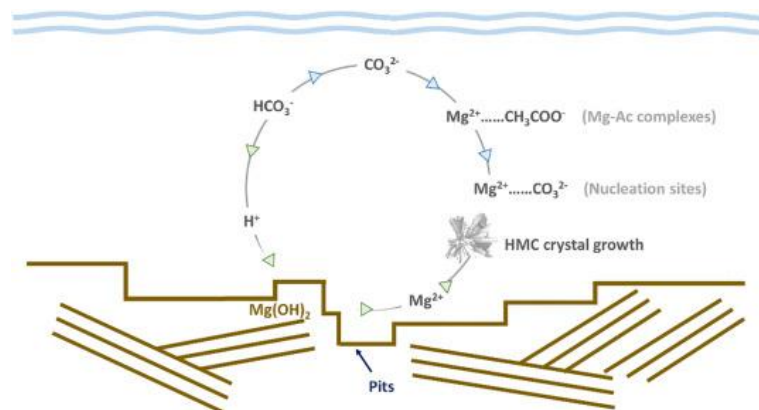
Figure 2.11 A reaction pathway of brucite in MgAc solution. Reproduced from [Nguyen et al., 2022]

Table 2.5 provides a summarized overview of the impact and mechanisms of

different metal acetates as admixtures on cementitious materials based on the above description.

Table 2.5 A summarized overview of the impact and mechanisms of different metal acetates as deicers on concrete

Admixture Type	Impact on Cementitious Materials	Mechanism Behind Impact	Reference
KAc	Frost endurance assessment in RCC	Increased cumulative mass loss after freeze-thaw cycles	[Zhang et al., 2018a]
CaAc	Improved cement hydration, increased ettringite and portlandite crystals	Facilitated cement hydration process, enhanced compressive strength	[Cao et al., 2021]
CaAc	Hindered reaction kinetics in AAS, decline in compressive strength	Optimal dosage required for AAS production	[Lyu et al., 2022]
Zinc Acetate (TSC-zinc acetate)	Effective retarder for slowing down steel rebar corrosion	Slows down the corrosion of steel rebar in chloride-containing solutions	[Maliekkal et al., 2018]
MgAc	Enhances brucite content, increases nucleation sites, denser microstructure	Promotes nucleation sites, improves microstructure and mechanical properties	[Nguyen et al., 2022] research [Dung and Unluer, 2017]

The protective material composed of acetates such as NaAc [Jahandari et al., 2023, Al-Kheetan et al., 2020a], CaAc [Du et al., 2023, Lu et al., 2023, Jiao et al., 2018b, Gao et al., 2022] and MgAc [Omar et al., 2022] in crystalline form could increase the impermeability of the concrete. The key mechanism involves these crystalline systems leveraging the available water to foster crystal growth within the concrete matrix [Jahandari et al., 2023, Teng et al., 2014]. This growth process effectively closes off potential pathways through which moisture could penetrate the concrete structure [Al-Kheetan and Rahman, 2019, Al-Otoom et al., 2007]. A notable advantage of crystalline technologies lies in their capacity to enable self-sealing when concrete develops cracks [Xue et al., 2021]. As water infiltrates these fissures, it triggers the growth of new crystals, effectively sealing the cracks and restoring the concrete's water-resistant properties [Al-Kheetan et al., 2020a, Jahandari et al., 2023]. Consequently, concrete incorporated with self-sealing capabilities undergoes a transformation into a highly effective water barrier, significantly enhancing its overall resilience and performance. A comprehensive depiction of the interaction process between NaAc and concrete is illustrated in Figure 2.12, the effectiveness was assessed through the examination of waterproof concrete under extreme (freezing and high) temperature variations [Al-Kheetan et al., 2020a].
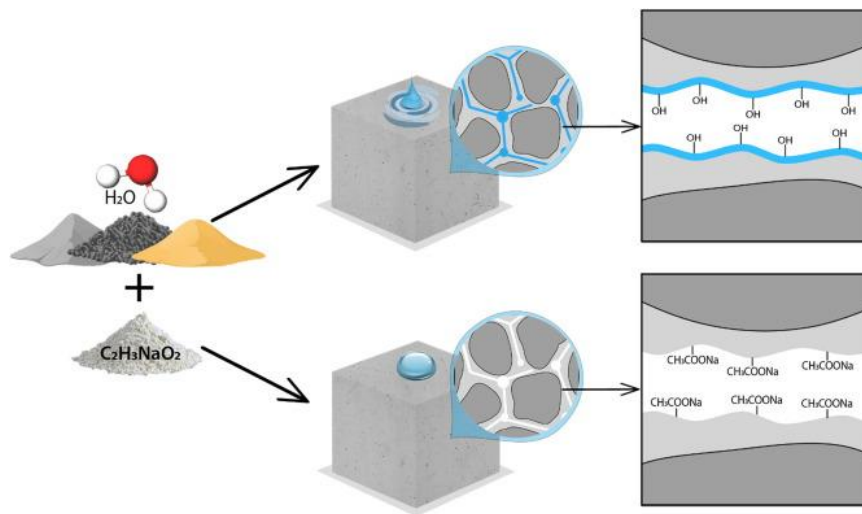
Figure 2.12 Process of how the material with hydrophobic property formed. Reproduced from [Al-Kheetan et al., 2020a]

A study specifically focused on NaAc demonstrated its effectiveness in reducing water adsorption rates and enhancing compressive strength under severe temperature conditions encompassing -25 °C and 60 °C [Al-Kheetan et al., 2020a]. The optimized concentration of NaAc was found to be 4%, aligning with earlier research [Al-Kheetan and Rahman, 2019]. Additionally, varying proportions of NaAc affected permeability [Kushartomo and Prabowo, 2019] differently in concrete with varying strength levels, highlighting the importance of concentration and curing conditions [Al-Kheetan et al., 2021]. Table 2.6 summarizes the impact of different concentrations of NaAc on water adsorption rates, compressive strength, and permeability in concrete, providing a quick reference to the findings of the studies mentioned.

Table 2.6 Effect of Different Concentrations of Sodium Acetates as Protective Materials on Cementitious Materials:

Concentration (NaAc)	Effect on Water Adsorption Rate	Effect on Compressive Strength	Reference
2%	79% decrease compared to control	Notable improvement	[Al-Kheetan et al., 2020a]
4%	Substantial 64% enhancement	Optimized concentration	[Al-Kheetan et al., 2020a],[Al-Kheetan and Rahman, 2019].
3%	Lower permeability in low-strength concrete	Varying results based on strength levels	[Kushartomo and Prabowo, 2019]
6%	Lowest permeability observed	Impact on permeability in different environments	[Al-Kheetan et al., 2021].

The utilization of metal acetates in cementitious materials serves various purposes and exhibits diverse effects. Metal acetates, including NaAc, CaAc, and MgAc, find application as deicers, protective materials, and admixtures in concrete. As deicers, they have been explored for airfield pavements, demonstrating effectiveness in mitigating frost damage while considering factors like Mg: Ca ratios. When used as protective materials in crystalline form, metal acetates enhance concrete impermeability by fostering crystal growth, providing self-sealing capabilities to repair cracks and significantly improving water resistance. As admixtures, metal acetates impact concrete properties such as compressive strength, hydration processes, and microstructure. NaAc, in particular, has been studied for its role in reducing water adsorption rates and enhancing compressive strength under severe temperature conditions. The concentration of metal acetates is a crucial factor influencing their effectiveness, with optimal concentrations determined based on specific applications and desired outcomes. Overall, the utilization of metal acetates in cementitious materials showcases their versatility and potential for improving various aspects of concrete performance. The examination of acetates' applications in cementitious materials, combined with our limited understanding of glass-forming systems, suggests the feasibility of utilizing metal acetates for casting potential glass-forming systems. This, in turn, opens up the possibility of discovering unique applications, including their use as surface protective materials.

2.4.2 Metal carboxylates and glass-forming ability

Metal carboxylates are a family of salts, which consist of a carboxylate anion group bonded with a metal cation. Various metal carboxylate compounds are possible, depending on the length (number of carbon backbones) of the carboxylic acid chain (e.g. acetate, propionate, butyrate and octanoate) and the identity of the metal cation (e.g. Li, Na, K) [Blair et al., 1992]. For instance, the molecular diagrams of several sodium metal carboxylates are described as Figure 2.13.

(a)   (b)   (c)   (d)
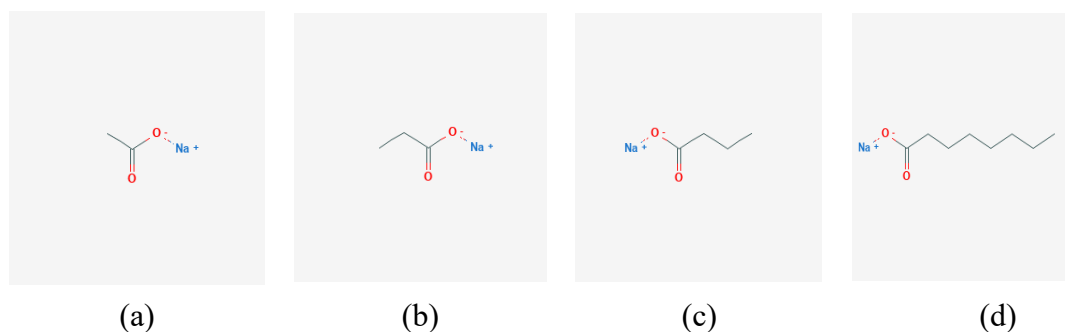
Figure 2.13 Structural framework of (a) sodium acetate, (b) sodium propionate, (c) sodium butyrate and (d) sodium octanoate (drawn from Chemdraw Software)

Before discussing the potential suitable conditions for manufacturing metal carboxylate glasses, it is essential to define the key terminology of glass science, and explaining the underlying thermodynamic and kinetic phenomena which explain glass-forming ability. According to Zanotto and Mauro [Zanotto and Mauro, 2017], a glass is a substance that does not crystallize during the cooling process and is not in equilibrium. It exhibits the characteristics of glass transition. The structural characteristics of a glass closely resemble those of its original supercooled liquid state, as they relax spontaneously to the supercooled state and will crystallize in an infinite time [Zanotto and Mauro, 2017]. The glass transition is a phenomenon marked by abrupt shifts in various thermodynamic properties of the glass, including heat capacity and thermal expansion, when a glass changes from a solid state to a supercooled liquid state as heated [Bennett et al., 2016].

The diagram presented in Figure 2.14 (a) and (b) [Zanotto and Mauro, 2017, Jiang and Zhang, 2014] is a key chart to understand the nature and essence of glasses. The plot illustrates the enthalpy developed with the temperature starting from absolute zero to melting point shown in Figure 2.14 (b) [Jiang and Zhang, 2014]. As is evident that supercooled liquids hold a higher value of energy and volume than that of the crystalline states at the temperature range of T_g-T_m [Jiang and Zhang, 2014, Lu and Liu, 2003, Lu and Mauro, 2017]. T_g represents the glass transition temperature of the liquids, and T_m denoted that the melting point of the crystalline solids. This confirms that the most frequently employed method to obtain glass is by rapidly cooling the liquid to the melting point (T_m), thus bypassing the crystallization temperature of the liquid. This rate also destroys the equilibrium in the liquid and rearranges the structure, depicted in Figure 2.14 (b) [Lu and Liu, 2003, Lu and Mauro, 2017]. The cooling rate of the liquid could influence the glass transition temperature T_g, which higher transition temperature could be generated by quick cool as $T_{g''}$, $T_{g'}$ and T_g [Jiang and Zhang, 2014].

As the cooling rate is a factor affecting T_g, therefore modifying the cooling rates could result in a series of supercooling curves [Jiang and Zhang, 2014, Lu and Liu, 2003, Lu and Mauro, 2017]. Figure 2.14 (a) has shown the changes of specific heat (ΔC_p) as a function of temperature of crystalline and vitreous solids owing the same composition. The same reduction in C_p was noted above the melting temperature T_m in both crystalline and vitreous solids [Lu and Mauro, 2017, Zanotto and Mauro, 2017]. When a crystal forms at Tm, C_p undergoes a sharp drop, aligning with the lower value characteristic of crystalline solids. Subsequent cooling results in a pronounced linear decline of C_p, approaching temperatures near absolute zero, in accordance with the Debye three-T relation. [Jiang and Zhang, 2014, Zanotto and Mauro, 2017]. However, if crystallization is not occurring at T_m, there will be a different situation. Firstly, further

cooling will lead the continuous decrease of C_p, and the melts turn into "undercooled liquid". In addition, when the temperature reached T_{g+}, C_p starts to decrease from the inflection at temperature T_g to the temperature T_{g-} by an increasing slope as it is close to that hold by a crystalline solid at this point [Jiang and Zhang, 2014]. The phase of the melt changes into glasses during this temperature interval. If continuation applied on cooling, C_p maintaining a value near, albeit slightly above, that of the crystalline solid, decreased at a slight faster rate as a result. It is clearly suggested that the glass exhibits more energy than crystals and is in a metastable condition. The temperature range of T_{g+}-T_{g-} definitely shown the glass transition (also referring as "softening range") [Jiang and Zhang, 2014, Zanotto and Mauro, 2017]. It could be concluded that glass formation is much easier to occur owing a smaller energy gap between the glass and the crystal composed of same composition.

From Figure 2.14, it can be noticed that in order to generate a glass, the liquid must be cooled sufficiently fast from above the liquid's temperature to the glass transition temperature, and not intersect the crystallization curve. The bigger internal energy gap between crystals of the same composition and the glass, the easier the crystalline solid phase will form, which makes it more difficult to form glass [Cavagna, 2009, Narasimham and Rao, 1978].

As depicted in Figure 2.14(b), it is evident that the thermodynamically stable liquids only exist above the T_m and never crystallize [Zanotto and Mauro, 2017]. Supercooled liquids exist between T_m and T_g. They are metastable and must overcome thermodynamic barriers for crystal nucleation and crystallization occurs over a specific duration. shown as red arrow [Zanotto and Mauro, 2017, Lu and Mauro, 2017]. Glasses exist below T_g which are thermodynamically unstable and can naturally relax back towards any supercooled liquid at a non-zero temperature (the grey arrow in Figure 2.14). The glass transition occurs at T_g depended on the rate of heating, the glass changes to supercooled liquids at T_g. The typical heating rate to measure Tg is 10 K/min [Zanotto and Mauro, 2017, Bartholomew and Lewek, 1970]. At any temperature higher or lower than T_g, any supercooled liquids or glass will relax and then eventually crystallize with sufficient times (shown in Figure 2.14 (b)). Crystals are solids that have well-organized atomic structures at various ranges and are thermodynamically stable below T_m [Zanotto and Mauro, 2017, Jiang and Zhang, 2014].
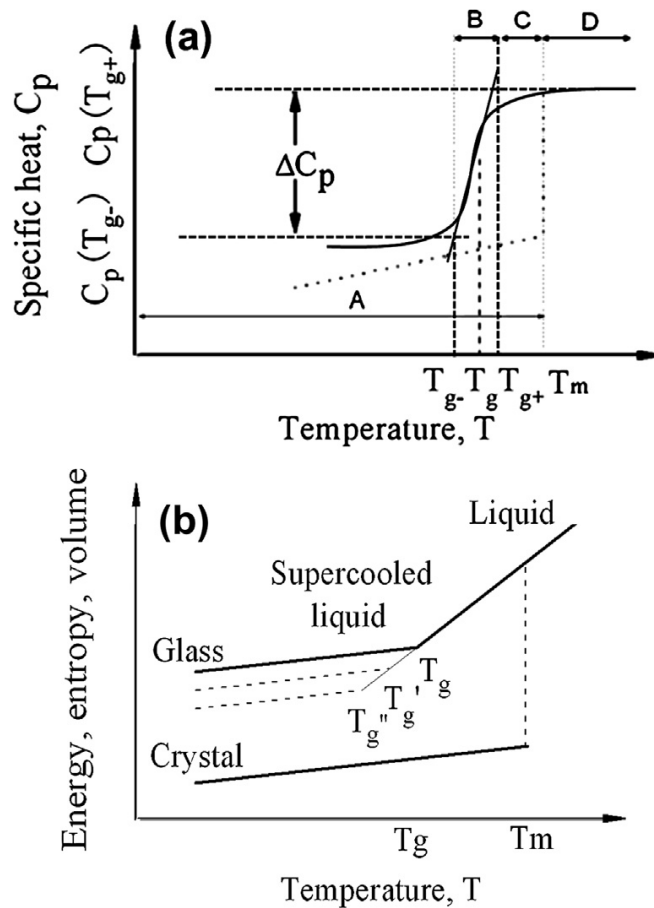
Figure 2.14 Schematic plot of the materials in different states, (a) Change in specific heat over a range of high temperatures for crystalline and vitreous solids. A – crystalline solid; B – $(T_g\text{-}T_{g+})$ glass transition temperature range; C – $(Tm\text{-}T_{g+})$ undercooled liquid glass melt; D – liquid melt. (b) First-order thermodynamic properties of energy, entropy or volume for glass changed with temperature [Jiang and Zhang, 2014, Zanotto and Mauro, 2017].

For binary or multiple-component systems, phase diagrams are commonly used to understand the glass-forming composition [Wang et al., 2010, Lu and Liu, 2003, Lu and Mauro, 2017]. From thermodynamic view, glass-forming ability is related to the free liquid-solid Gibbs free energy difference ΔG ($\Delta G = \Delta H - T\Delta S$), which ΔG works in the role of a thermodynamic motivator [Lu and Liu, 2003, Lu and Mauro, 2017]. For supercooled liquid regions, the relatively low ΔG could be effectively to prevent crystallization and thus favor the glass formation. Entropy, practically refer to the melting entropy ΔSm has been confirmed by several studies [Lu and Liu, 2003, Lu and Mauro, 2017, Zanotto and Mauro, 2017] to have a substantial impact to the glass-forming process. For small supercooling liquids, the approximation of $\Delta G \approx \Delta Sm\Delta T$, which highly emphasizes lower ΔSm (or $d\Delta G/dT$) working as the small thermodynamic driving force for glass formation [Wang et al., 2010].

To conclude, appropriate cooling rate and free ΔG influence the capacity of glass-forming. Moreover, glass-forming systems are composed of different components, such as single component, binary systems and multiple components system [Wang et al.,

2010, Chen, 1976, Chen and Turner, 1980]. The thermodynamics in mixtures is more complicated than that in single glass-forming systems. Eutectic composition was introduced to systems composed of double components on glass-forming ability [Wang et al., 2010, Rawson, 1967, Li, 2005], which is much relevant to our studies. Glass will form in the regions of the eutectic composition, as shown in Figure 2.15, which was corresponded to Rawson law in binary or multi-component systems [Rawson, 1967, Wang et al., 2010, Tan et al., 2003]. The reason is that eutectic composition has comparable higher viscosity at liquids and relatively minimum temperature range of super-cooling thus easy for glass forming [Rawson, 1967, Wang et al., 2010].
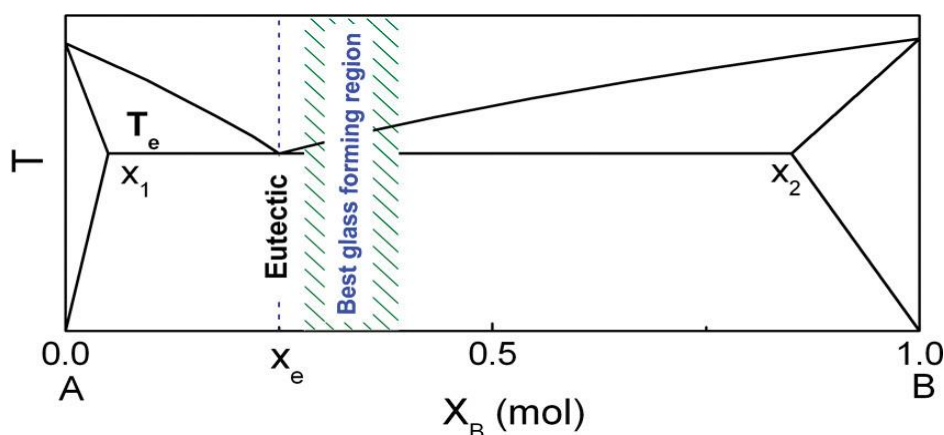
Figure 2.15 Schematic diagram to show glass forming in composition in binary system [Wang et al., 2010]

It could be concluded that eutectic composition has a higher potential for glass-forming ability in binary systems. In addition, off-eutectic composition is beneficial for glass forming in binary systems composed of alloys [Kurtuldu and Löffler, 2020]. Although it is only simple binary glass systems composed of alloys, it would facilitate the understanding of basic knowledge on glass-forming ability, providing a primary unit in complex systems with multiple components.

2.4.3 Various glass-forming systems

Glass-forming materials fall into several distinct groups. These groups encompass inorganic glass oxides like silicate and nitrate glass, low-temperature chalcogenide glasses containing elements such as Se, S, and Te [Portier, 1989], fluoride glasses [Nazabal et al., 2012], metallic glasses, and ionic salt glasses [Angell, 1990]. Metal carboxylates are categorized within the domain of ionic salt glasses. Unlike inorganic glass systems, ionic salt glasses are not viewed as binary mixtures of oxides. Instead, they consist of components with salt-like properties [Blair et al., 1992]. This category

encompasses nitrates [Rawson, 1967], sulfates [Narasimham and Rao, 1978], chlorides, carbonates, and acetates [Blair et al., 1992].

Ionic salts capable of forming glass structures typically comprise metal salts of simple organic anions like formate (HCO_2^-) and acetate ($CH_3CO_2^-$), which belong to the carboxylate group [Blair et al., 1992]. The tendency of ionic salts to form glass structures is linked to their ability to create desired composite structures. Within ionic glasses [Calahoo and Wondraczek, 2020], cations serve various roles, including major anion cluster formation and secondary anion cluster bridging. Generally, larger cations with high electrostatic field strength have the ability to hold ion clusters together, as seen with NO_3^-. Smaller cations (e.g., Li) or those with lower field strength (e.g., K) act as covalent bonds that limit movement [Calahoo and Wondraczek, 2020, Hadjiivanov et al., 2021]. For instance, nitrate ions are symmetrical and can easily transfer to cations with large field strengths or radii [Hayes et al., 2015]. In contrast, acetate anions are primarily bonded through carboxylic oxygens, making them less effective as bridges between cations. Once coordinated, their positions are unlikely to change [Rich and Maréchal, 2008]. The formation of clusters depends on field strength and is significantly influenced by steric factors [Han et al., 2023]. Consequently, regardless of the anion-to-cation ratio, the glass's stability increases as cation field strength rises. This factor is essential to consider when designing mixtures with equal mass or equal numbers for overall charge-balancing in ionic salts.

In the crystalline state, a key objective is to maintain a long-range order by adjusting bond angles, interatomic distances, and site occupancies [Friesner et al., 2006]. This helps achieve a specific symmetry and minimizes bulk free energy. However, when it comes to glass, the primary focus shifts to minimizing local free energy, which may entail a different bonding arrangement compared to crystals [Tanaka et al., 2019]. To enhance glass formation ability, increasing the number of components in the composition is crucial to reduce the driving force for crystallization, ultimately closing the gap in Gibbs free energy [Blair et al., 1992]. Another approach involves expanding the atom arrangement [Blair et al., 1992] by utilizing various carboxylates in different combinations. This kinetic rationale underlies the approach adopted in this project.

Acetate ions belong to a category of oxyanions, and they can serve as unidentifiable, chelated, or bridged ligands, as illustrated in Figure 2.16. Structurally, they share similarities with nitrate ions, but they exhibit a tendency to form glasses across a wider range of compositions compared to nitrates. However, despite the extensive research conducted on molten nitrate melts and the formation of nitrate glasses, there has been limited attention given to the molten state of acetates and the formation of acetate glasses [Blair et al., 1992].
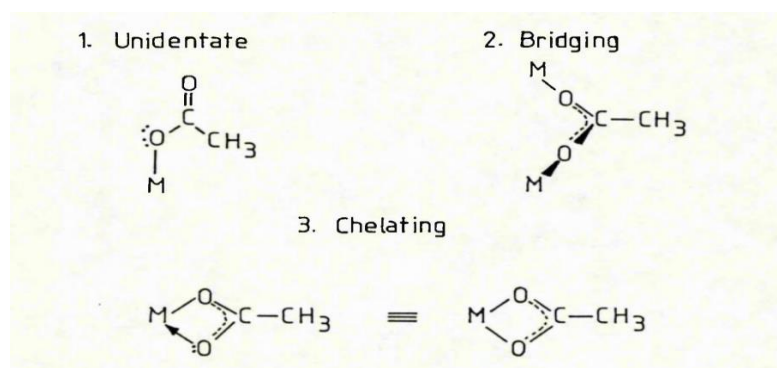
Figure 2.16 Unidentate, bridging and chelating ligands in acetate, adapted from [Blair et al., 1992]

2.4.4 Studies on glass-forming of metal carboxylates

In earlier investigations on alkali metal carboxylate glasses, Bartholomew and Lewek [Bartholomew and Lewek, 1970] made a significant discovery involving glass-forming substances that involved mixtures of univalent and divalent acetate salts melted and quenched, akin to the process used for nitrate glasses. They [Bartholomew and Lewek, 1970] employed a controlled atmosphere dry box to prevent the hygroscopic nature of nitrate glasses and employed X-ray techniques to confirm the formation of glass from molten materials. Their exploration of metal acetate systems for glass formation revealed several one-component acetate glass-forming systems, including lithium and lead acetates, which formed glasses at a slower quenching rate. Significantly, the range of metal cations capable of forming glasses from melts containing two acetates was broader than what was previously known for nitrate systems [Angell, 1990]. The acetate mixture compositions that have been extensively studied encompass potassium acetate-lead acetate in the range of 21 to 71 mol%, sodium acetate-lithium acetate spanning 0-67 mol%, and potassium acetate-cadmium acetate within the range of 40-75 mol%. They also found that terminal lead and lithium acetates could form glass, although determining their precise limits was challenging. The speed of quenching molten materials and the quantity of raw materials involved played a crucial role in the melting-quenching process, with the quenching rate dictating the glass formation potential. In the context of glass structure, the extension of covalent bonds within the ions during melting inhibits the formation of a closely packed structure, causing it to deviate from an ideal state-a concept initially proposed by [Angell, 1968]. This concept can predict the arrangement of ions in close proximity with zero configurational entropy.

Duffy and Ingram [Duffy and Ingram, 1969] concurred with this notion, finding the expectation of glass formation in acetate systems to be quite plausible. The propensity for glass formation often depended on the specific combination of components, similar to what occurs with nitrate mixtures, such as the interplay between

zinc chloride and potassium bisulfate. An interesting observation was that molten potassium acetate alone could not be successfully quenched into glass, but when combined with metal cations, including Li^+, Na^+, and K^+, it yielded a wide array of ion combinations. A spectroscopic analysis [Ingram et al., 1972] was undertaken to compare various transition-metal ions in acetic acid, acetate glass, and melt, as well as nitrate glass. This study aimed to identify the available sites within the mixture and to discern any modifications in the environment resulting from the quenching process as the material changed from melt to glass. The study [Bartholomew and Lewek, 1970] revealed that glass could be produced by quenching a melt comprising specific metal acetates, such as lithium sodium (Li: Na=4:3), sodium calcium (Na: Ca=1:1), and potassium calcium (K: Ca=1:1) (molar ratios indicated in parentheses). This extended the range of compositions that molten acetates could quench into glasses. In addition to lead acetate, it was found that a combination of sodium acetate and lithium acetate, as well as mixtures of monovalent and divalent cation acetates, could also form glasses. The systems capable of forming ionic glasses were summarized through Table 2.7.

Table 2.7 A table summarized acetates glass-forming systems, adapted from [Bartholomew and Lewek, 1970]

Number of components in composition	Acetates glass-forming systems in molar ratio
Single	Li-acetates
	Pb-acetates
Binary	K-acetate-Pb acetate, 21% to 71%
	Na-acetate-Li-acetate, 0-67 mol%
	K-acetate-Li-acetate
	K-acetate- cadmium (Cd) acetate, 40-75 mol%
	terminal Pb and Li-acetate
	Li-acetate-Na-acetate (4: 3)
	Na-acetate-Ca-acetate (1: 1)
	Na-acetate-Ca-acetate (1: 1)
	a mixture of monovalent and divalent cation acetates

Numerous types of acetate glasses exist, including hydrous trivalent rare earth (La) acetate glasses, as well as mixed monovalent cation (Li, Na, and K) and trivalent cation (B^{3+}, P^{3+}) acetate glasses. Despite the high melting point of anhydrous CH_3^- and CF_3^- acetates, glasses of these materials can still be formed if they contain water (H_2O). The presence of water is crucial as it aids in bridging between cations and reduces the melting point, thus preventing decomposition. To confirm the formation of glasses, Ingram et al. [Ingram et al., 1972] employed a differential thermal analyzer, revealing that glass transitions occurred above room temperature, indicating that these materials form glasses rather than supercooled liquids. It's worth highlighting that the

hygroscopic nature of glass is influenced by the vessel material, with Pyrex vessels exhibiting a catalytic effect compared to fused quartz vessels, which can accelerate the onset of decomposition [Bell et al., 1994b]. Therefore, Pyrex vessels are not suitable for casting acetate glasses. Spectral analysis further revealed significant variations in the properties of acetate glasses. These research findings demonstrate that spectral analysis can assist in identifying the bonds between metal cations and carboxylate ions, which are characterized by their ionic nature.

2.4.5 Investigations on solubility of metal carboxylates

Research on the solubility of metal carboxylate glasses has been relatively limited compared to their glass-forming capacity. Key insights into this matter include the solubility behavior in water, which is contingent upon the metal ion and the chain length of the carboxylate [Hurst and Fortenberry, 2015, Akanni et al., 1984]. Electronegativity [Little and Jones, 1960] is a relative metric used to gauge an atom's strength in attracting electrons when it engages in covalent bonding. Variations in electronegativity between metal cations and oxygen, as outlined in Table 2.8, result in an ionic character of the bond between the metal cation and carboxylate anion [Ternstrom, 1964]. It was emphasized that the greater the difference in electronegativity, the more polarized the electron distribution [Ouellette and Rawn, 2015]. Ingram et al [Ingram et al., 1972] noted the presence of covalent bonding in lead acetate glasses, unlike the ionic structure found in other acetate glasses at room temperature, highlighting the interplay of ionic and covalent bonding in glass structures. In the case of ionic compounds, a stronger ionic polarization indicates a bond with more covalent elements and fewer ionic elements, leading to lower solubility. Ion charge, ion radius, and ion electronic configuration influence the degree of ion polarization, with higher charge numbers, smaller cation radius, and larger anion radius resulting in a greater degree of ionic polarization [Hurst and Fortenberry, 2015]. In essence, it can be inferred that metal carboxylates with a more covalent ionic character exhibit reduced solubility.

Table 2.8 A summary table of electronegativity values of the metal cations used, adapted from [Ternstrom, 1964]

Metal cations	Electronegativity values
Li	0.98
Na	0.93
K	0.82
Rb	0.82
Cs	0.79
Mg	1.31
Ca	1.00

Awad et al. [Awad et al., 2004] highlighted the pivotal role of alkyl chain length in influencing interactions between carboxylates and lead (II). Consequently, variations in the carboxylate chain length were designed based on these insights. At room temperature, hydrogen bonds are formed by a combination of a water molecule, the hydroxyl hydrogen atom of the carboxylate, and a lone pair of electrons bridging the two oxygen atoms. However, as the length of the carbon chain increased, the lengthier alkane "tail" in the molecule extended between the water molecule, disrupting the hydrogen bond. The extended non-polar hydrocarbon chain exerted dominance over the ion's physical properties, causing a decline in solubility with increasing chain length. In this scenario, the weakened hydrogen bonds were substituted by the considerably less potent Van der Waals dispersion forces [Leiserowitz, 1976]. Consequently, carboxylates with lengthier chain structures exhibited reduced solubility when dissolved in water. This reduction in solubility occurred as the chain length of the carboxylates increased, leading to the enlargement of covalent compounds within the ionic bonding structure.

In their study, Giebson et al. [Giebson et al., 2010] conducted solubility tests of potassium-acetates (K-acetates) solutions including CH_3COOK or $HCOOK$ inside the glovebox. Solutions of K-acetates at different concentrations (0.05, 0.3, 1.5, and 2.5 mol/L) were blended with an excess of solid gypsum and placed in sealed, airtight plastic vials. These vials were then stored at 20°C for 24 hours. The pH level of the solution is presented in Figure 2.17. Upon adding CH_3COOK or $HCOOK$, the initial pH of the saturated $Ca(OH)_2$ solutions rapidly rose as shown in Figure 2.17. Examination of the resulting solutions also indicated a heightened Ca concentration [Giebson et al., 2010].
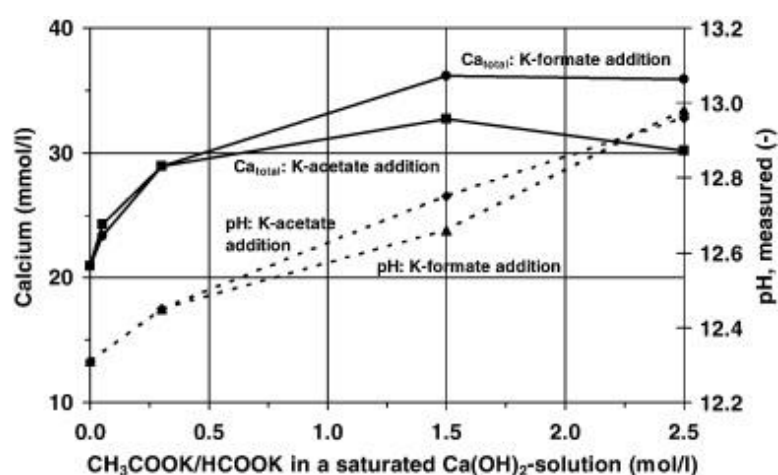
Figure 2.17 Ca concentration and pH value in a saturated $Ca(OH)_2$ solution with $CH_3COOK/HCOOK$, adapted from [Giebson et al., 2010]

The research landscape on the solubility of metal carboxylates is relatively limited, with existing studies primarily focusing on a constrained set of metal ions recognized for their potential glass-forming ability. However, it is crucial to emphasize that various factors affected the glass formation process, for example, acetates made up of varying alkali or alkaline metal cations, and the ionic nature of these interactions. Casting samples with different combinations of metal acetates owing various solubility when mix with water, is one of the objectives of the present thesis, with the aim of potentially govern the reaction kinetics of AACs or modify their chemical composition.

2.5 Concluding remarks

Alkali-activated materials represent a promising class of construction materials with unique properties and environmental benefits. The effect of slag composition on alkali-activated slag cements has been extensively studied, revealing that the chemical composition of slag significantly influences the properties of the produced AAC. Conventional alkaline activators, including hydroxides and silicates, have been widely used, showcasing advantages such as effective activation of precursors but also posing disadvantages like high carbon footprint and cost. In response to these challenges, alternative alkaline activators, such as RHA, biomass ash, red mud and other ashes, have been investigated. Despite their potential, there is a research gap in understanding the nuanced effects of these alternative activators on alkali-activated materials.

The motivation behind exploring metal carboxylates as potential activators lies in their capacity to moderate the reaction process, offering a tailored approach to enhance the properties of alkali-activated slag cements. Thus, to contributing to more sustainable and economically viable solutions in the realm of alkali-activated materials.

Chapter 3 – Materials and Methodology

3.1 Introduction

This chapter describes the materials, sample preparation and different techniques to investigate the properties of the product.

3.2 Materials

3.2.1 GGBFS

The precursor employed in this study were two commercial GGBFS provided by ECOCEM®, with oxide compositions detailed in Table 3.1. The slag 1 had a specific surface area, as determined by BET analysis, of 1.25 m²/g, and its particle size distribution with an average d_{50} was 10.75 μm determined by the laser diffraction presented in Figure 3.1. Throughout the experiments described in Chapter 5, the ECOCEM® slag 1 was consistently utilized. However, partway through the planned experiments the material was exhausted. It was then necessary to use a different slag (slag 2) from the same supplier for conducting the experiments reported in Chapters 6 and 7. Due to the inadequate quantity of Slag 1, a substitution was made with Slag 2 possessing a comparable oxide composition. The specific area and d_{50} of the slag 2 were 1.48 m²/g and 12.15 μm, respectively.

Table 3.1 Oxide composition (wt.%) of GGBFS measured by X-ray fluorescence spectroscopy. (LOI is the loss on ignition at 900 °C)

GGBFS type	Chemical composition									
	SiO_2	Al_2O_3	CaO	MgO	K_2O	Na_2O	Fe_2O_3	SO_3	TiO_2	LOI
Slag 1	36.30	9.70	43.85	6.28	0.3	0.26	0.37	1.48	0.59	0.87
Slag 2	35.84	9.59	42.68	7.25	0.48	0.33	0.68	2.1	0.68	0.37
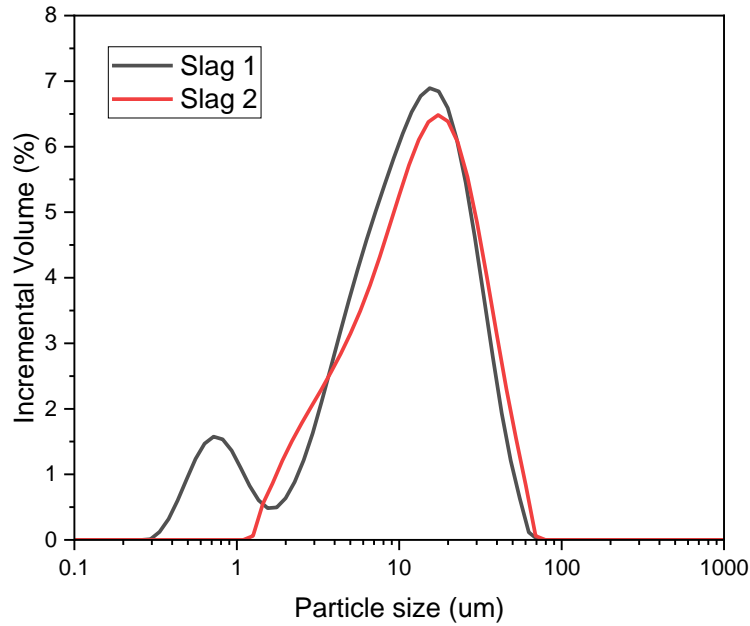
Figure 3.1 Particle size distribution curves for the two slags

3.2.2 Metal carboxylates and metal hydroxides

As potential alkali-activators a variety of metal carboxylates, featuring diverse metal cations and carboxylate groups, were employed in the development of alternative alkaline activators. The alkali metal (Group I) cations that were explored included Li^+, Na^+, K^+, Rb^+ and Cs^+, while the alkaline earth metal (Group II) cations examined were Ca^{2+} and Mg^{2+}. The carboxylate groups under investigation encompassed acetate (-CH_3COO), propionate (-CH_3CH_2COO), butyrate (-$CH_3CH_2CH_2COO$) and octanoate (-$C_7H_{16}COO$).

While numerous metal carboxylates exhibit varying combinations of metal ions and carboxylate groups, only a limited selection is readily accessible for commercial purposes. To ensure the practical achievement of the project's objectives, it was thus determined not to synthesize any metal carboxylates but instead rely exclusively on those procurable from chemical suppliers. The assortment of metal carboxylates employed in this investigation is presented in Table 3.2, along with their reported purity from the supplier and the two pertinent values associated with the melting and quenching processes: melting temperature and thermal decomposition temperature. All metal carboxylate salts utilized were procured from Alfa Aesar. Unless explicitly specified, all salts were provided in their dehydrated state. Owing to the susceptibility of certain salt compounds to transform into their hydrated forms under standard atmospheric conditions, some salts were delivered as hydrates. For these particular salts, the values documented in Table 3.2 for melting temperature and thermal decomposition

temperature pertain to their anhydrous state, i.e., after undergoing dehydration during the heating process. In the instance of sodium propionate and calcium acetate hydrate, two distinct temperatures are provided for the decomposition process, as at 440°C, calcium acetate might undergo a melting phase, which can potentially influence the decomposition process, as detailed by Judd et al. [Judd et al., 1974]. For sodium propionate, the first temperature corresponds to the decomposition of sodium propionate into sodium carbonate, while the second denotes the decomposition of sodium carbonate into sodium oxide [Masłowska and Więdłocha, 2000].

Table 3.2 Abbreviations, chemical formulae and key temperature values of metal carboxylates used (The purity was provided by the supplier).

Abbreviation	Full name	Formula	Purity (%)	Melting pointing (°C)	Thermal decomposition temperature (°C)
LiAc	Lithium Acetate Dihydrate	$CH_3COOLi \cdot 2H_2O$	99	286 [Halmos et al., 1970]	320 [Halmos et al., 1970]
NaAc	Sodium Acetate	CH_3COONa	99	324 [Halmos et al., 1970]	380 [Halmos et al., 1970]
KAc	Potassium Acetate	CH_3COOK	99	292 [Halmos et al., 1970]	390 [Halmos et al., 1970]
RbAc	Rubidium Acetate	CH_3COORb	99.8	246 [Information，]	380 [Information，]
CsAc	Cesium Acetate	CH_3COOCs	99	194 [Information]	380 [Information]
MgAc	Magnesium Acetate Tetrahydrate	$CH_3COO(0.5Mg) \cdot 2H_2O$	98	80 [Information]	350 [McAdie and Jervis, 1970]
CaAc	Calcium Acetate Hydrate	$CH_3COO(0.5Ca) \cdot H_2O$	99	440,437 [Judd et al., 1974]	440,437 [Judd et al., 1974]
NaPr	Sodium Propionate	CH_3CH_2COONa	99	287 [Duruz et al., 1971]	400,697 [Masłowska and Więdłocha, 2000]
NaBu	Sodium Butyrate	$CH_3CH_2CH_2COONa$	98	250-253 [Information]	The temperature is unknown

NaOc	Sodium Octanoate	$C_7H_{16}COONa$	96	225 [Information]	The temperature is unknown

In Chapter 5, the effectiveness of metal carboxylates was assessed by using sodium hydroxide (Honeywell, 98%) and potassium hydroxide (Honeywell, 98%) as benchmark activators. Chapter 6 involved the use of NaAc with substitution for NaOH as blended activators in alkali-activated slag (AAS) production. Additionally, MgAc, sourced from the supplier and detailed in Table 3.2, was considered an alternative MgO source to influence the evolution of phase assemblage in Chapter 7.

3.3 Sample preparation

3.3.1 Preparation of thermally treated metal carboxylates

Three frequently employed techniques for glass manufacturing include chemical vapor deposition (CVD), the sol-gel process, and melt-quenching method [Axinte et al., 2017]. The choice of the melt-quenching method was made due to its well-established status and extensive utilization in glass preparation. The procedure developed for the experiments of this thesis was inspired from the methods described in the existing literature [Duffy and Ingram, 1969], as well as the work conducted at the University of Aberdeen in 2011 [Macphee and Hansen, 2011], where they had already pioneered the development of metal carboxylate-based glasses, adjusted to the available equipment.

The protocol for producing metal carboxylate activators is illustrated in details as shown in Figure 3.2. When preparing a melt with multiple metal carboxylates, they underwent manual mixing for a duration of 3 minutes to ensure a homogeneous blend before the heating process. Fused quartz beakers were utilized in accordance with the recommendation provided by Bell et al. [Bell et al., 1994a], as opposed to soda-lime glass or pyrex, to minimize any adverse effects of vessel materials on the initiation of the decomposition temperature of metal carboxylates. Subsequently, the beaker containing the metal carboxylates was placed inside a static furnace set at an appropriate temperature, typically 350°C for most cases. The choice of temperature was determined by referencing the melting and decomposition temperature values detailed in Table 3.3. For most carboxylate salts, maintaining the temperature around 340-350°C within the furnace proved sufficient for achieving melting without inducing thermal decomposition.

After situating the beaker in the furnace, intermittently accessed the furnace by per minute to assess if the solids had fully melted or commenced thermal decomposition.

Once a visual inspection confirmed the complete melting of the solids, the beaker was carefully removed from the furnace. Subsequently, the melt was rapidly quenched by pouring it into a pre-cooled aluminum mold, which had a diameter of 2.5 cm and a thickness of 3 cm, as depicted in Figure 3.3. Prior to casting, the mold was cooled using ice sourced from a -20°C freezer. The choice of quenching conditions was determined by the following considerations:

1) Ensuring that the mold facilitates rapid cooling of the liquids to encourage glass formation.

2) Utilizing a cylindrical mold shape to facilitate the consistent solidification of the cast liquids.

3) Selecting a volume that ensures the melted liquids do not exceed the capacity of the mold.

Photographs were taken of the cast samples. A desiccator full of silica gel desiccant was used for sample after casting storge in case to prevent adsorption of atmospheric moisture, as these materials are known to be highly hygroscopic [Lin et al., 2023].
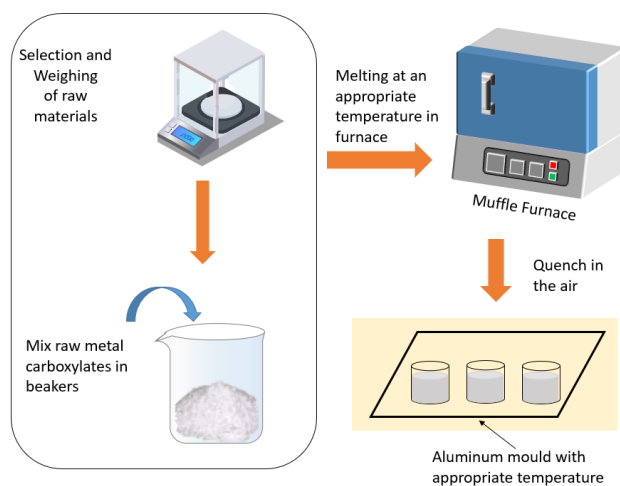
Figure 3.2 Protocol for casting metal carboxylates by a melt-quenching method.
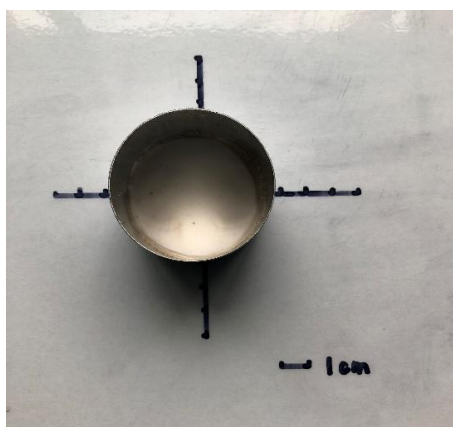
Figure 3.3 Photo of the cylindrical aluminum mould used for casting samples.

The glass-forming ability of the various blends was assessed through visual inspection of the transparency/opacity of samples after thermal treatment, XRD, and TG-MS. After synthesized products, their solubility in water was investigated by pH measurements. The two sets of results (glass-forming ability and solubility) were then used to identify the optimum compositions for metal carboxylates that can be used as potential activators for producing AAS cements.

3.3.2 Preparation of alkali-activated slag pastes

AAS pastes were produced by a regular water to binder ratio (w/b = 0.3) and a invariable 4 wt.% Na_2O activator dosage with respect to the mass of GGBFS. The ratio of w/b = 0.3 aligns with the typical range employed in AAS, which typically spans from 0.3 to 0.5, as documented in the literature [Sun et al., 2022, Zhang et al., 2021]. Similarly, a dosage of 4 wt.% Na_2O relative to the mass of slag, as this is a commonly adopted value for alkaline activators [Tong et al., 2021, Zhang et al., 2021].

In Chapter 5, activating solutions were meticulously prepared by dissolving NaOH, KOH, NaAc, or KAc separately into distilled water. Moving to Chapter 6, alkaline solutions were crafted by adding the solute (commercial NaOH pellets and NaAc after thermal treatment in different molar ratio) together into distilled water to formulate the alkaline solutions, and the desired activation conditions. In Chapter 7, a similar approach was employed, with MgAc and NaOH mixed together then dissolved in distilled water. The combination of these two solutions was then utilized in the production of alkali-activated slag (AAS) cements. Furthermore, MgAc underwent a grinding and sieving process, being reduced to a powder with an average particle size of 74 μm, aligning it with the particle size of the GGBFS used in this project. This step was taken to ensure comparability in particle sizes between MgAc and GGBFS. To guarantee thorough dissolution and achieve room temperature, all solutions were left undisturbed for a minimum of two hours. This standardized approach was implemented to ensure the completeness of dissolution and maintain consistency across the experimental procedures.

AAS pastes were produced by the high-shear mixer, starting with a 3-minute-low speed (139rpm), then changed to a 2-minute-high speed at 591 rpm. Centrifuge tubes with 15 mL were used for AAS pastes casting, then stored and placed in a water-bath under 20°C curing for all ages evaluated including 3 days, 7 days, 28 days, 250 days, and 360 days.

The reaction kinetics underwent assessment using isothermal calorimetry and the workability was evaluated by mini-slump test. The evolution of phase assemblage in different AAS cements was examined across various curing time through X-ray diffraction, infrared spectroscopy, thermogravimetry, ^{29}Si MAS NMR and SEM-EDS. The mechanical and physical properties were monitored including compressive strength test, pore size distribution and wettability measurement.

3.3.3 Preparation of samples for powder-based characterization techniques

At different curing ages, samples were extracted from the water bath and subsequently transferred from centrifuge tubes. These samples were manually ground using an agate mortar and pestle, ensuring thorough grinding, and then passed through a 74 μm sieve to obtain a powder for subsequent testing. Immediate testing of the powdered samples followed the grinding process, and any remaining powder was securely stored in a vacuum desiccator. This meticulous procedure aimed to maintain the integrity of the samples and provide a consistent basis for analysis and evaluation throughout the study.

3.4 pH measurements

The measurement of pH quantifies the level of acidity or alkalinity of an aqueous solution at a specific temperature [Karastogianni et al., 2016]. pH is expressed mathematically by Eq. 3.1, which represents the negative logarithm of the concentration of hydrogen ions. In this equation, pH is equal to the logarithm (base 10) of the inverse of the hydrogen ion concentration (C), provided by moles per liter (c). [Karastogianni et al., 2016].

$$\text{pH} = -\log_{10} [\text{H+}] \qquad \text{Eq. 3.1}$$

In an aqueous solution, the product of the hydrogen ion concentration and the hydroxyl ion concentration remains constant [Karastogianni et al., 2016, Cameron, 2012]. The pH values ranging from 0 to 14, and distilled water is considered neutral with pH equals to 7. pH values vary depending on the ratio of hydrogen ions (H^+) to hydroxyl ions (OH^-), serving as an indicator of whether a solution is acidic or basic (refer to Figure 3.4). While pH < 7 suggests acidity, pH >7 denotes alkalinity. Lower pH values correspond to greater acidity, while higher values signify increased alkalinity [Cameron, 2012].

Figure 3.4 pH scale from [https://www.elevise.co.uk/gacc4a.html]
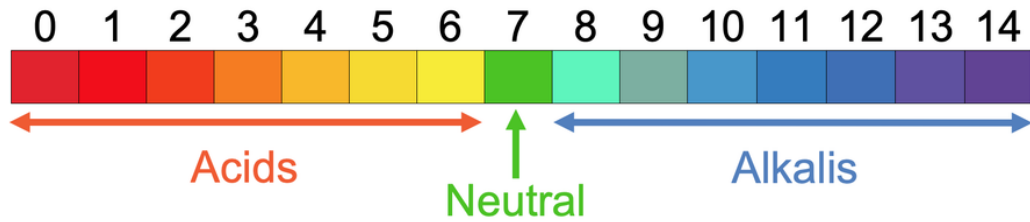
A pH meter operates on a potentiometric principle [McLean, 2017], measuring the voltage of an electrochemical cell to ascertain a solution's pH level, it is subsequently correlated with the temperature sensor.

The pH values of solutions, created by dissolving cast metal carboxylates in distilled water, were monitored at various time intervals using the pH meter. This measurement serves to quantify the alkalinity of solutions produced with different carboxylate-based and/or hydroxide-based activators. Furthermore, observing the pH at different time intervals aids in comprehending the dissolution rate. Once an alkaline solution is obtained, it can serve as an alternative alkaline activator for slag activation.

3.5 Reaction kinetics and fresh state properties

In each of the following sub-sections, a brief explanation is given about the different techniques used in this study, providing information about how each technique works, the specific type of information each technique provides, and a rationale for how each one helps develop the understanding of the materials evaluated in this research. Details of measurement conditions can be found in the Materials and Methods section of per thesis Chapter.

3.5.1 Isothermal calorimetry

Isothermal conduction calorimetry, as depicted in Figure 3.5, involves measuring the heat released by a small sample (S) using a sensor to test heat flow. This heat is conducted and goes into a heat exchanger within a thermos-stated environment [Wadsö, 2010]. It is a valuable technique for studying the exothermic nature of certain chemical reactions, providing insights into reaction kinetics [Ben Haha et al., 2011a, Gebregziabiher et al., 2016]. In this setup, both references and samples are put in the

calorimeter, then the recorded data comprises the difference between the thermal signals obtained from the two. The reference serves the crucial role of mitigating potential external factors' effects, and it is chosen based on its matching heat capacity without instigating any thermal reactions [Gijbels et al., 2020, Liu et al., 2019]. The calorimeter's data output is essentially the discrepancy between the sample signal and the reference signal.

In cement applications, isothermal calorimetry is employed to investigate the kinetics of formation of reaction products. For alkali-activated cements, distilled water is selected as the reference material with a heat capacity of 4.18 J/g/K [Bentz, 2007], while the heat capacity of slag is 0.73 J/g/K [Kockal, 2016]. It is essential to ensure that the overall heat capacity among samples and references closely match on total.
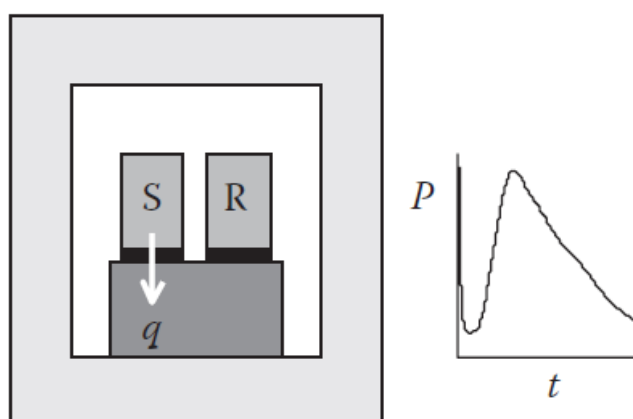
Figure 3.5 Schematic illustrations of an Isothermal Calorimetry [Scrivener et al., 2018b]. S: sample; R: reference; P: thermal power; t: time.

The heat released of AAS pastes during the reaction was measured by a TAM air (TA Instruments, U.S.) isothermal calorimeter with 8 twin-channels. The heat flow and cumulative heat produced during the reaction were obtained. After mixing, 9 grams of fresh paste for each mix was poured into a glass vial and rapidly put into the calorimeter. AAS pastes were tested at 20 ± 0.02 °C for over 28 days. Reference samples are composed of quartz and distilled water (9 g in total). In order to have a comparable result, duplicated samples were tested for each mix evaluated. The paste weight (including water) was used to calculate the normalized heat release.

3.5.2 Setting time

The setting time of AAS composed of initial and final setting time is measured through a Vicat apparatus, coupled with a 1.13 mm diameter needle (Figure 3.6), according to BS EN 196-3 [2016]. The fresh pastes were prepared and then setting time measurements was started. The initial setting time of AAS concludes when the needle reaches a depth of 4 mm ± 1 mm from the bottom plate. Subsequently, the time that the ring attachment could not leave traces on the specimen means final setting. When nearing the initial setting time, measurements should be taken every 1 minute. Similarity applied for the final setting time approaches. The setting behavior of AAS are notably responsive to ambient temperature and relative humidity [Zhu et al., 2020, Fernández-Jiménez and Puertas, 2001]. Hence, it is crucial to select suitable conditions for conducting setting time examinations. The Vicat apparatus was put into a curing room which temperature is approximately 20 °C with high relative humidity for the measuring setting time.
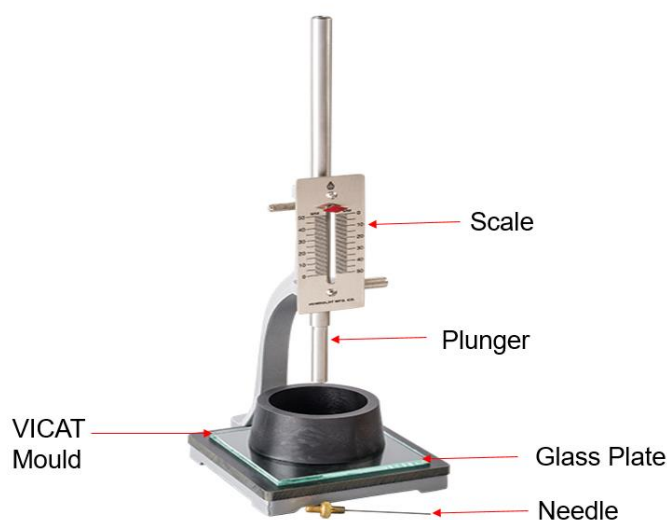
Figure 3.6 A Vicat apparatus instrument

3.5.3 Workability determined via the mini-slump test

The flowability of freshly prepared AAS pastes was tested by a mini-slump test [Tan et al., 2017], the procedure and the equipment used are identical to those previously described for casting AAS pastes (Section 3.2.2). The test apparatus consisted of a steel cylindrical container and a 2×2 cm^2 squares poly (methyl methacrylate) flat plate with markings. Steel cylindrical container approximately 5 cm

in diameter and 10 cm high. Approximately 70g of fresh (freshly mixed) pastes is required each time. During the test, fill the cylindrical container with fresh mixture and then lift the container as slowly as possible to reduce the impact of inertia. After the paste has completely fallen off the container, test the diameter of the paste on the flat plate. The same paste should be tested at least three times to ensure the reliability of the data.

3.6 Evolution of phase assemblage

3.6.1 Mineralogical analysis

X-ray powder diffraction (XRD) is an analytical approach primarily on identifying materials with crystalline structure and can provide information on unit cell dimensions [Liu et al., 2019, Blair et al., 1992]. All atoms will scatter the incident X-rays, but it is only in crystalline materials that the scattering will achieve constructive interference, and very small and highly disordered crystals will diffract weakly [Tänzer et al., 2015, Blair et al., 1992]. Incident X-rays are used with wavelength similar to the distance between atoms in the crystal [Blair et al., 1992]. The well-defined distances between the atom planes in crystals can be determined by the constructive interference (i.e. diffraction) that occurs due to elastic scattering of X-rays by nuclei [Patil et al., 1968]. This diffraction phenomenon is defined as Bragg's Law, Eq. 3.2, here n illustrates the reflection; λ represents the X-ray wavelength; d equals to the distance between lattice planes; θ is the incidence angle.

$$n\lambda = 2d\sin\theta \qquad \text{Eq. 3.2}$$

Considering that the metal carboxylate activators were produced through melting and quenching processes, it was anticipated that any crystallization during this process would result in high nucleation rates and the formation of small crystals. It is possible that crystalline phases exist but may not diffract with sufficient intensity to be discernible on the XRD pattern. As a result, XRD analysis provides a general indication of the "extent of crystallinity" in the carboxylates sample, rather than a straightforward binary answer of presence or absence for crystals existed.

A Bruker D8 X-ray powder diffractometer was used to analyze the metal carboxylates after thermal treatment, and the obtained powder samples of AAS cements cured for different ages. The radiation was CuKα with a wavelength of 0.1541 nm (40 kV). The 2θ range evaluated was 5 to 60° for AAS and 5 to 45° for thermally treated metal carboxylates, exhibit a step size of 0.033º at a rate of 3 s/step. All the diffractograms were executed under the room temperature. Highscore software and

ICDD database was utilized for crystalline phase identification.

3.6.2 Spectroscopic analysis of reaction products forming

Attenuated total reflection (ATR) is a characterization technique frequently employed in conjunction with FTIR, allowing for direct testing of cement paste samples without the need for additional preparation [Ramer and Lendl, 2006]. Attenuated total reflection – Fourier transform infrared spectroscopy (ATR- FTIR) can also be employed for in-situ non-stop testing, facilitating continuous monitoring the structural adjustments in AAS [Ke et al., 2018a]. The fundamental principle of ATR, as depicted in Figure 3. 7, involves the propagation of an evanescent wave through the phenomenon of total internal reflection. The IR beam traverses an ATR Zinc Selenide crystal, which typically possesses refractive index values ranging from 2.38 to 4.01 at 2000 cm^{-1}. It then penetrates the sample to a depth of just a few microns (0.5 μ-5 μm). Variations in signal within the optical path are recorded and processed via Frontier Transform in combination with background subtraction [Ramer and Lendl, 2006]. The ATR FTIR spectrum exhibits distinct absorption bands, each associated with the characteristic vibrations of various chemical bonds and groups [Liu et al., 2019, Tänzer et al., 2015].
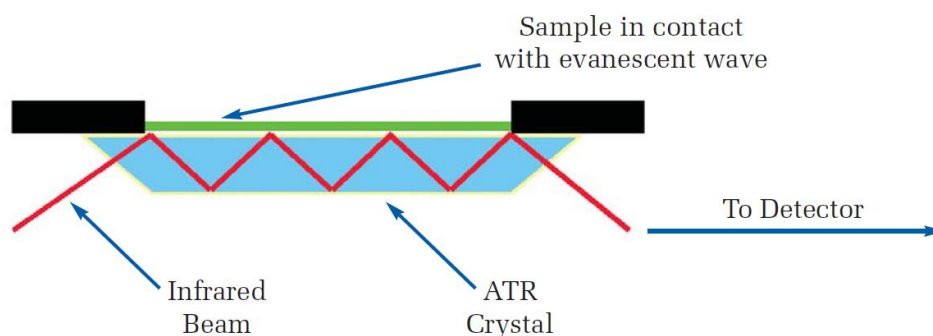
Figure 3.7 A multiple system of ATR-FTIR spectroscopy [https://www.perkinelmer.com/uk/]

The evolution of the evaluated AAS were monitored through a PerkinElmer Polymer ID-Analyzer with an ATR attachment spectrometer over. Collecting the spectra in a range between 600 and 2000 cm^{-1} wavenumbers at a resolution of 4 cm^{-1}, and collecting a minimum of 16 scans per measurement. Powder samples at different curing time were analyzed, immediately after manual grinding and sieved pass through 74 μm without solvent exchange.

3.6.3 Thermogravimetry analysis

Simultaneous thermal analysis is a combination of thermal gravimetric analysis (TGA) and differential scanning calorimetry (DSC) [Gijbels et al., 2020, Niu et al., 2010]. In Figure 3.8 (b), the STA measurement setup is clearly illustrated, featuring a furnace and integrated sensors for the reference and sample crucibles [Scrivener et al., 2018b], enabling temperature changes to be recorded. The reference side typically consists of an empty pan made of the same material as the sample containers [Van Humbeeck, 1998]. As depicted in Figure 3.8 (a), the reference side heats faster than the sample side, which is governed by the heat capacity of the sample. The green line (representing the reference side) develops more rapidly than the red line (indicating the sample side). These two lines run in parallel until a reaction occurs within the sample, such as melting, decomposition, or re-crystallization, during constant heating. For instance, the time point t1 in Figure 3.8 (a) can be regarded as a DSC signal, signifying the occurrence of such reactions. The change in temperature (ΔT) is also recorded, and the area under the peak A (depicted in blue) is considered the transition enthalpy (J/g).

(a)   (b)
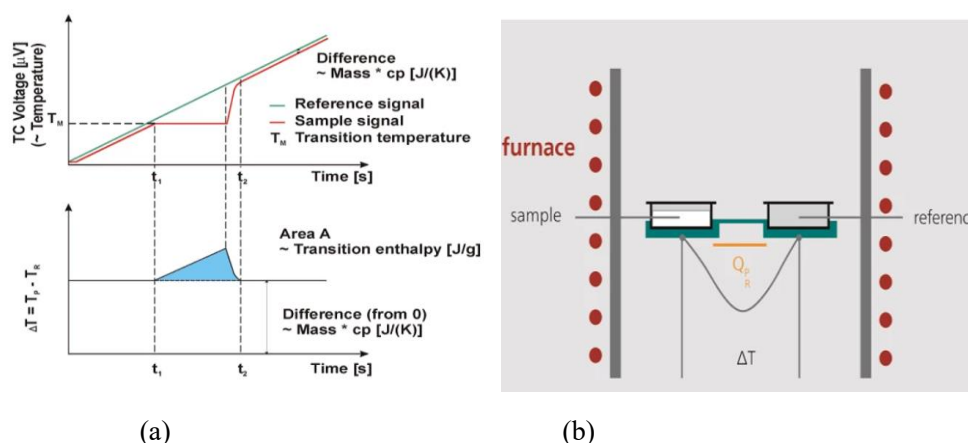
Figure 3.8 (a)The principle of the DSC calculation and (b) the schematic program of the equipment [https://analyzing-testing.netzsch.com]

DSC was employed to quantify temperatures and heat changes associated with thermal transformations within materials under examination. For thermally treated metal carboxylates, DSC findings can identify the melting point and the transition from a glass state to a super-cooled liquid in cast samples [Landoll and Holtzapple, 2013, Blair et al., 1992].

TGA monitors the alteration in the mass of samples as the temperature fluctuates over time [Niu et al., 2010]. Hence results of TGA can show the decomposition temperature of the cast carboxylates after quenching, associated with the mass loss

[Landoll and Holtzapple, 2013]. Mass spectrometry (MS) is an analytical technique employed for determining the mass-to-charge ratio of ions, making it suitable for the identification of evolved gases [Van Uitert et al., 1971, Aleixo et al., 2005]. This information can be correlated with the reactions taking place within the sample during the heating process.

The accuracy of a STA measurement affected through numerous sensors, like the heating rate, crucible types (open or closed), sample weight, and the drying method employed for sample storage prior to testing. These factors have been comprehensively documented in the references [Van Humbeeck, 1998, Janković et al., 2020].

TTG was conducted on a mass of 26 mg samples, encompassing metal carboxylates after thermal treatment in Chapter 4, 28-day reacted AAS samples in Chapter 5, and all samples reacted at different curing ages for Chapter 6 and 7. Using a Netzsch STA 49 F5 simultaneous thermal analyzer, which heat rate is 10°C per minute, between 30°C and 1000°C under nitrogen (N_2) atmosphere. A gas flow of 60 mL/min is used to avoid carbonation occurred. Collecting the isotherms at temperature starting from 30° to finally 1000°C for 10 min during the experiment.

3.6.4 Nanostructure of AAS cements

Nuclear magnetic resonance (NMR) spectroscopy works by recording the interaction of radio frequency (Rf) electromagnetic radiation with molecular nuclei in strong magnetic fields, thus providing comprehensive data regarding the structure, dynamics, reaction states, and chemical environment of molecules [Gao et al., 2017]. Most atomic nuclei are charged and can spin [Akitt and Mann, 2017]. Atomic nuclei subjected to an external magnetic field undergo an energy transfer from the basic state to higher energy levels, at wavelengths in harmony with corresponding radio frequencies. Emissions may take place at frequencies identical to the energy when the spin reverts to its basic level [Akitt and Mann, 2017].

One of the most important analysis of solid MAS NMR in AAS should be ^{29}Si MAS NMR [Cherki El Idrissi et al., 2018, Alharbi et al., 2020, Walkley and Provis, 2019], which is a powerful tool to determine the characteristics of the reaction products being generated, mainly for characterizing the nano-structural features of the C-(A)-S-H type gels [Cong et al., 2019, Walkley and Provis, 2019, Alharbi et al., 2020]. It is useful in providing unique information for the structural characterization of silicates, which the detected peaks in the spectra corresponded to silicon environments owing different orders [Bernal et al., 2014c, Wang and Scrivener, 2003].

The solid-state MAS NMR spectra were collected by a Bruker Avance III HD

spectrometer with a 400 MHz magnet (magnetic field 9.4 T). ^{29}Si MAS NMR spectra were conducted on 79.5 MHz of operating frequency, with a zirconia rotor used in a 7 mm probe rotating at 6 kHz, and deployed a 90° pulse, which endured for 5.5 μs, along with a 40 s of the relaxation delay and requiring at least 2048 scans. Reference for ^{29}Si shifts was external samples named tetramethylsilane (TMS).

3.6.5 Microstructure analysis

The scanning electron microscope (SEM) employs a concentrated electron beam to produce various signals at the surface of solid specimens [Alharbi et al., 2020, Amer et al., 2021a]. Among these signals are backscattered electrons (Figure 3.9), which result from interactions between electrons and the sample. Backscattered scanning electron (BSE) can provide valuable insights into the sample, including details about its external morphology (texture), chemical composition, as well as the crystalline structure and orientation of its constituent materials [Scrivener, 2004]. Typically, the data collected are located on selected areas owing by a sample surface, and their changes are visualized in two-dimensional images. Energy dispersive X-ray spectroscopy (EDS) is particularly valuable for obtaining semi-quantitative information about chemical compositions[Alharbi et al., 2020, Coudert et al., 2021]. For AAS, the employed EDS analysis help determine the elemental compositions of the forming products [Bernal et al., 2015a, Criado et al., 2018].
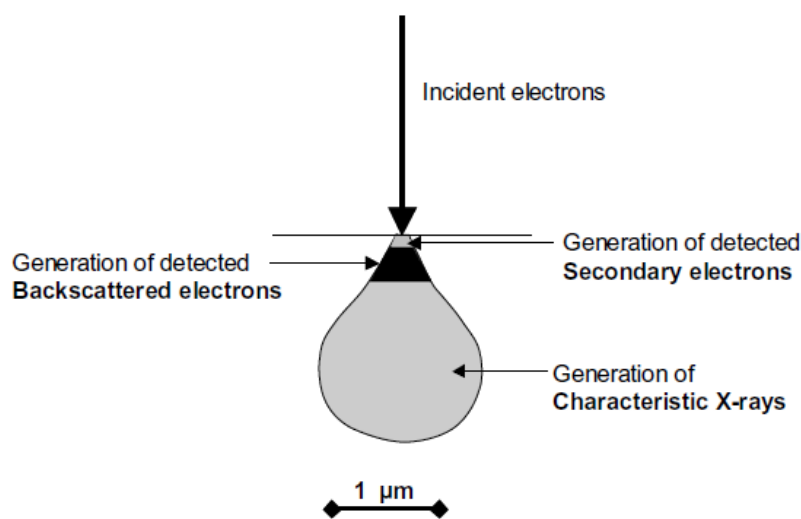
Figure 3.9 Schematic diagram of signals generation in the scanning electron microscope (SEM) [Scrivener, 2004]

The preparation process for BSE samples involves the following four steps: (1) Cutting: Slices of approximately 5 mm thickness were obtained using an Isomet cutter. The samples were not using IPA bathing as acetates are sensitive to IPA. However, a wash with IPA was performed to remove any residual water on the sample surface after cutting. (2) Resin Impregnation: Buehler resin was accurately measured and used to impregnate the samples. Subsequently, placing the resin-embedded samples in an oven at 40 °C overnight for samples hardened properly, following recommended guidelines by the resin supplier. (3) Grinding: SiC paper with grit sizes of P600, P1200, and P2500 was utilized until the desired appearance of the sample was achieved. (4) Polishing: A sequence of different diamond pastes manifest particle sizes including 6, 3, 1, and 0.25 μm was employed for the polishing step. After each application of diamond paste, the sample was cleaned using cotton.

For each sample, at various ages and formulations, over 60 points (EDS spots) were selected based on SEM images taken at a 2000x magnification. SEM in backscattered electron mode (BSE) coupled with energy-dispersive x-ray spectroscopy (EDS) was employed for understanding the microstructural and chemical variations in the specimens evaluated, as a function of the activator type used. A Zeiss Evo 15 scanning electron microscope, operating at a voltage of 20kV was used for image analysis. The pastes were meticulously evaluated at distinct time points: after 180 days with gold coating for Chapter 5, after 360 days with carbon coating for Chapter 6, and after 28 days with carbon coating for Chapter 7. Elements maps including calcium, aluminum, magnesium, sodium or potassium, silicon, carbon was collected.

3.7 Mechanical and physical properties

3.7.1 Compressive strength

Compressive strength representing a material's capacity to endure axial compressive forces. In the assessment of compressive strength for alkali-activated cement pastes [Martinez-Lopez and Ivan Escalante-Garcia, 2016, Al-Kheetan et al., 2020c, Divvala and M, 2021, Abdollahnejad et al., 2020, Yang et al., 2012, Ben Haha et al., 2011b, Nunes et al., 2019, Xie et al., 2020], cubic specimens measuring $25 \times 25 \times 25$ mm³ were employed. The plastic wrap was applied for covering and sealing the mould, and curing them in a fog room (95% relative humidity) for all curing gages. An Instron 3382 with different attachments was employed for the strength test, which has a loading rate 50N/s for the compressive tests, according to BS EN 196-1:2016 clause 9.1 [2016]. These cubic paste samples were positioned on the testing machine's

platform, without any filler material placed between the cube and the steel platens owing to the compression testing equipment, as depicted in Figure 3.10.
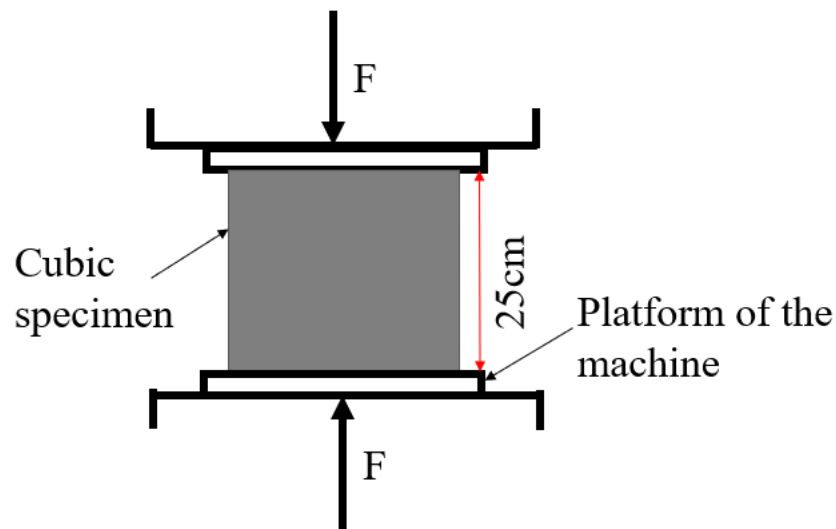
Figure 3.10 A diagram described the compressive strength measurement

3.7.2 Pore size distribution

Mercury Intrusion Porosimetry (MIP) is a robust technique used for evaluating porosity and the distribution of pore sizes [Shi et al., 2018, Longhi et al., 2019]. This porosimeter utilizes a chamber, as depicted in Figure 3.11, that subjects the specimen to elevated pressure to introduce mercury into its pore spaces. As the pressure gradually rises, mercury initially occupies the larger pores before infiltrating the smaller ones, enabling the characterization of both porosity and pore size distribution [Ismail et al., 2013].
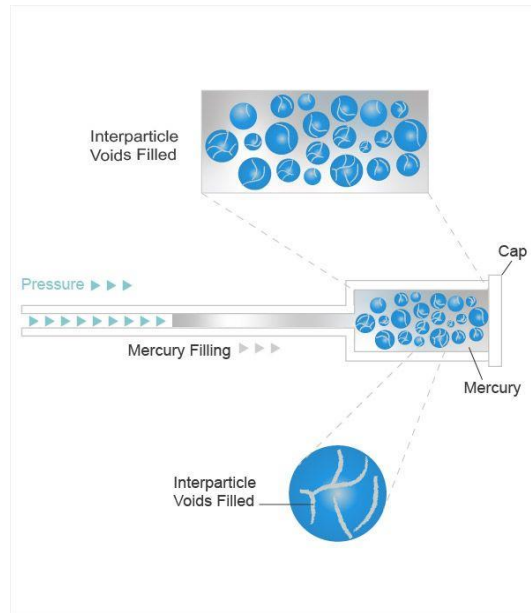
Figure 3.11 Schematic figure illustrates the principles of MIP (adapted from
[https://www.particletechlabs.com/analytical-testing/gas-adsorption-and-porosimetry/mercury-intrusion])

The MIP technique relies on the nonwetting characteristic of mercury [Berodier et al., 2016]. Mercury is a nonwetting liquid, as indicated by a contact angle θ greater than 90°, necessitating the application of an external pressure P to balance the pressure differential across the mercury meniscus within the pores. The Washburn Equation (Eq. 3.3) establishes a connection correlates the applied pressure with pore diameter, utilizing key physical properties of mercury, which include the contact angle correlates mercury with the material, as well as surface tension [Berodier et al., 2016].

$$P = -\frac{2\gamma\cos(\theta)}{r}$$
Eq. 3.3

Where γ records the surface tension of mercury; θ represents the contact angle; r is equal to the capillary radius. The pressure range is approximately 1-60,000 psi provided by the instrument, which enables the measurement of pores at the range of 250 μm to 0.003 μm (3 nm) [Berodier et al., 2016].

AACs exhibit a range of pore sizes spanning from the micron to the nanoscale [Li et al., 2019b]. Among the various techniques employed for characterizing the intricate pore structure owing by AACs, MIP is one of the most frequently utilized methods [Liang and Yao, 2023, Zhang et al., 2023]. MIP results provide valuable information regarding pore size distribution and porosity, offering insights into microstructural changes, such as C-(A)-S-H type gels generated, as well as their relationship with compressive strength.[Zhang et al., 2023, Jiang et al., 2022b].

The pore structure including pore size distribution of samples curing at 28 d was

determined by Mercury Intrusion Porosimetry (MIP). It was tested through a MicroActive AutoPore V 9600 Version 1.02 employed various pressure modes. Prior to testing, the water that might be present in the samples need to be removed. In this study cylindrical samples with an aspect ratio of 1:1 was cut and then quartered. The small specimens were placed in a 60 mL beaker, covered with ethanol and sealed for 5-6 h. Samples were needed to be removed from the beaker, and then placed into a vacuum desiccator before testing for one week. The mass of 0.855g is needed per test. Experiments were conducted by the Penetrometer 11 exhibit 5 cc on the head size, a value of 1.13 on stem volume, mercury was induced which rate is 0.1-61000 psia under 20°C and a contact angle was set at 130°.

3.7.3 Wettability assessment

Water contact angle measurement is a characterization technique that assesses the dynamic response to water on the material's surface [Yao et al., 2021]. Water contact angle (CA) refers to the angle that a liquid interface meets a solid surface (Figure 3.12) [Yao et al., 2021]. Values for contact angle can be used to categorize hydrophilicity and hydrophobicity of surfaces: hydrophilic (CA below 90°), hydrophobic (CA exceed 90°), over-hydrophobic (CA between the angle range of 120°-150°) and super-hydrophobic (CA between the angle range of 150°-180°, sliding angle (SA) below 10°) [Yao et al., 2021].
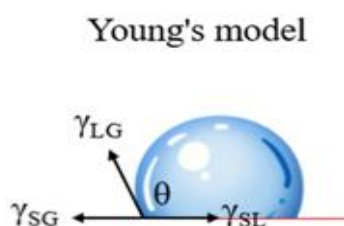
Figure 3.12 Schematic diagram illustrates contact angle for a liquid drop on a smooth surface from Young's model adopted from [Yao et al., 2021]

Young's model [Yao et al., 2021, Zhao et al., 2022] is employed to analyze the surface wettability of materials. This model relies on the premise of an ideally smooth and flat surface, as illustrated in Figure 3-11(b), and Young's model listed by Eq. 3.4 is as follows:

$$Cos\theta = \gamma_{SG} - \gamma_{SL} / \gamma_{LG} \qquad\qquad Eq.\ 3.4$$

Where, γ_{SL} is representing the interfacial tensions within the solid-liquid, γ_{LG} refers to the interface tensions of liquid–gas, and γ_{SG} is the interface tensions according to solid–gas system; θ can be described as the angle formed by the liquid-solid interface.

Water contact angle measurements provide a visual indication of the hydrophobicity or hydrophilicity of alkali metal acetate-activated cements. Moreover, the contact angle, as determined by Equation 3-4 [Yao et al., 2021], can quantitatively assess the hydrophobicity of a solid surface in contact with a liquid. Previous studies demonstrate that acetates can impermeabilize concretes [Kushartomo and Prabowo, 2019, Al-Kheetan et al., 2020c]. In this study it was decided to determine the level of potential impermeabilization that can be achieved by the acetate activators by determining the wettability potential of the pastes produced. Figure 3.13 illustrates the KSV equipment used for contact angle measurements, where a water drop is dispensed via a needle onto the surface of the samples. Images are automatically collected for each water contact angle measurement.
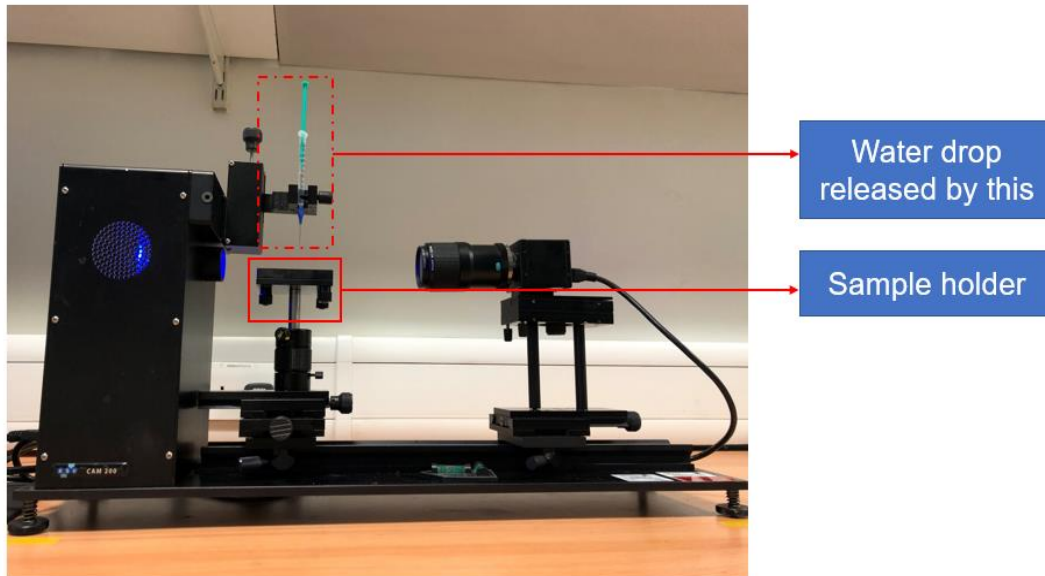
Figure 3.13 Photograph of the KSV for contact angle tester at University of Leeds

Samples were taken from 15 mL centrifuge tubes and cut into 2 mm disks using a Isomet high precision saw. Afterwards the disk was polished, using SiC paper to flatten the surface and reduce potential roughness induced by cutting, which can influence the contact angle detected. After a flat surface was obtained, samples were kept in a vacuum desiccator before testing.

Chapter 4 – Production and characterization of organic alkaline carboxylate activators (OCA)

4.1 Introduction

Metal carboxylates are organic ionic salts made up of two components: a metal cation, and a carboxylate group anion [Chen et al., 2021]. Alkali carboxylates glasses could be produced with them, which was used for fertilizers manufacturing in agriculture [Zainul Armir et al., 2021]. They could also be applied in infrastructure, which one of the commonly utilization is alkali-derived airfield deicers for concrete pavements [Kotwica and Malich, 2021]. The alkali-derived airfield deicers composed of metal carboxylates was less corrosive than conventional chloride-based deicers [Kotwica and Malich, 2021]. For example, sodium acetate, potassium acetate and magnesium acetate play different roles as alkali-derived airfield deicers. The degree of alkali-silica reaction (ASR) was increased when sodium and potassium acetate was used [Kotwica and Malich, 2021] [Giebson et al., 2010]. The effect of magnesium acetate and calcium acetates on the ASR is unclear [Lee et al., 2000] [Dunn and Schenk, 1980a]. Zinc acetate has been applied in concrete as well as a retarder which slow down the corrosion [Maliekkal et al., 2018]. In addition, potassium acetates has been used as deicers when exposed to serve environments such as very low temperature [Sajid et al., 2022]. The cost-effectiveness of alkaline organic deicers is not high compared with conventional chloride-based deicers, and their application is restricted by the environment conditions. When concrete is exposed to freezing or high temperatures, its properties can be improved by sodium acetate, as small doses seem to increase the compressive strength [Al-Kheetan et al., 2020a]. Although there are several studies investigating the utilization of metal carboxylates in concrete, the use of such organic alkaline carboxylate as alkaline activators (OCAs) has not been explored to manufacture alkali-activated slag cements.

Using organic alkaline carboxylate activators (OCAs) as glassy activators to potential provide a way to control their dissolution rate was evaluated. The OCAs produced are mainly composed of metal carboxylates. A series of single, binary, ternary and quaternary systems of metal carboxylates were investigated aiming to explore the impact of the cation type, anion type and number of components. Melting behavior was studied first to discover practical constraints around melting, including charring. Visual inspection of the glasses produced, XRD and DSC analysis of the cast samples was

conducted to evaluate the glass-forming potential of the different compositions evaluated. pH measurements were undertaken to assess solubility behavior and determine the suitability of the dissolved metal carboxylates as potential alkali-activators.

4.2 Thermal treatment

4.2.1 Mix preparation design

A detailed description of the properties of the metal carboxylates used in this study are provided in Section 3.1.2 and 3.2.1 of Chapter 3. Evaluations made on the effect of metal cation radius, Group I and Group II metal cations, and carboxylate chain length on the glass formation ability, single component metal carboxylates were grouped into three categories including single system, binary system and ternary and quaternary systems listed in Table 4.1.

For single system, the exploration range covered metal acetates from LiAc to CsAc, also MgAc and CaAc, as well as sodium carboxylates depending on the different carboxylate chain length. When the number of components is >1, the equimolar ratio of each component was applied in the design. A NaAc-KAc mixture was evaluated as NaAc and KAc were commonly used within the literature. To verify the effect of carboxylate chain length, the binary mixture was composed of the sodium carboxylates with shorter carboxylate chain length and longer chain length.

Ternary mixtures were also produced by adding CaAc or MgAc with binary mixture of NaAc-KAc shown in Table 4.1, and different combinations of sodium carboxylates with various carboxylate chain length. Finally, quaternary system was designed by mixing both MgAc and CaAc into binary NaAc-KAc mixtures.

The binary, ternary and quaternary mixtures were heated at 350°C to prepare a melt, as was done for the single component systems following the approach used by Batholomew and Lewek [Bartholomew and Lewek, 1970]. A total of 18 metal carboxylate mixes listed in Table 4.1 were produced, using a total of 5g solid metal carboxylate precursors per melting batch.

Table 4.1 Design of mixtures for equimolar ratio components of metal carboxylate

Composition parameter varied within series			Sample ID
Vary: number of components	Single system	Vary: Alkali metal (Group I) cation	LiAc
			NaAc
			KAc

		RbAc
		CsAc
	Vary: Alkaline earth metal (Group II) cation	MgAc
		CaAc
	Vary: Length of carboxylate group anion	NaPr
		NaBu
		NaOc
Binary system	Vary: Alkali metal (Group I) cation	NaAc-KAc
	Vary: Length of carboxylate group anion	NaAc-NaPr
		NaBu-NaOc
Ternary system	Vary: Alkaline earth metal (Group II) cation	MgAc-NaAc-KAc
		CaAc-NaAc-KAc
	Vary: Length of carboxylate group anion	NaAc-NaPr-NaBu
		NaPr-NaBu-NaOc
Quaternary system	Vary: Mix of alkali metal (Group I) cation and alkaline earth metal (Group II) cation	CaAc-MgAc-NaAc-KAc

4.2.2 Characterization of as-received metal carboxylate salts

The as-received metal carboxylate precursors were first characterized by XRD and thermal analysis, in accordance with the procedures outlined in Section 3.2.1 of Chapter 3, for the analysis of metal carboxylates after melting and quenching.

Figure 4.1 and Figure 4.2 depicts the XRD patterns of the metal carboxylates precursors. In addition to searching for database patterns for the anhydrous metal carboxylates, their hydrates were also searched for. Because metal carboxylates are highly hygroscopic [Lin et al., 2023], it is plausible that hydrates may be present in the as-received materials. It can be seen from Figure 4.1 (a), major peaks were assigned to metal carboxylates in all the as-received precursors except for Rubidium acetate, as Rubidium acetate completely mismatches with patterns in powder diffraction file (PDF) #00-028-0873 and #00-037-0599. No patterns in the ICDD PDF database were available for Rubidium acetate hydrate. Sodium acetate and potassium acetate have similar peak position occurring in the 2θ range of 8-10°. Slight differences in the peak reflections are identified between NaAc and KAc. It could be seen that the peaks positions of as-received CaAc monohydrate matches that in PDF#00-019-0199 and similarly applied for MgAc tetrahydrate with the PDF#00-011-0729 in Figure 4.1 (b).
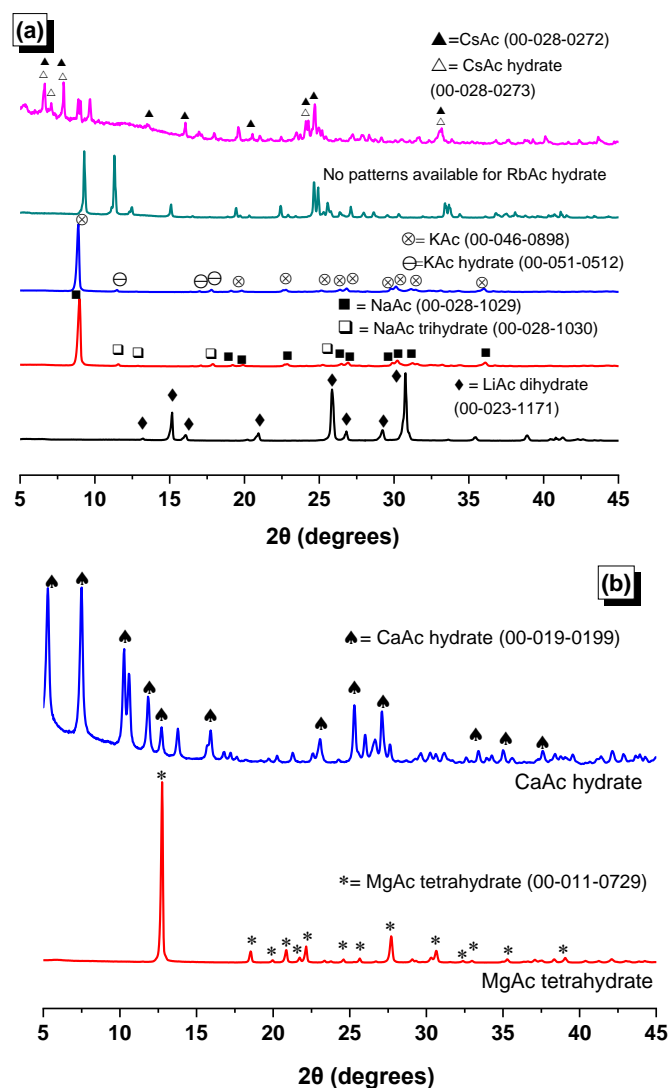
Figure 4.1 Cu-α XRD of (a) metal acetate from LiAc to CsAc precursors and (b) MgAc and CaAc precursors.

The peak positions identified in the X-ray diffractograms in the as-received NaAc match the patterns in PDF #00-028-1029 of NaAc and the patterns in PDF #00-028-1030 of NaAc trihydrate obtained from Figure 4.2. The peaks in the pattern for as-received NaBu is consistent with that in PDF #00-001-0015. It is observed that the main diffraction peak is shifting to lower diffraction angles as the carboxylate chain lengths increases. This implies a larger lattice spacing, suggested that a larger unit cell exists if the crystalline structure is the same. It is worth noting that no PDF file was found in the ICDD database that could be matched to the NaOc.
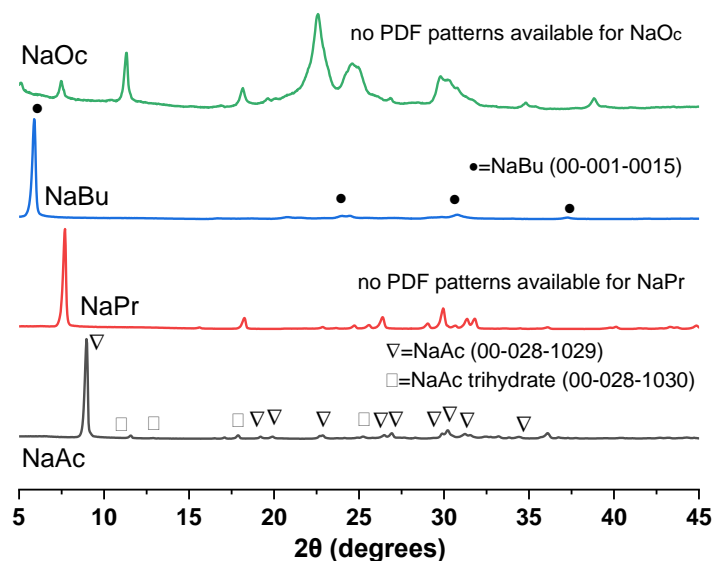
Figure 4.2 Cu-α X-ray diffractograms of as-received sodium carboxylate precursors

4.2.3 Temperature evaluation on thermal treatment

Thermal treatment by Muffle furnace was utilized to change the as-received crystalline metal carboxylates into possible glasses. In order to determine a suitable temperature for melting metal carboxylates, thermal analysis under a flow of N_2 atmosphere was used to investigate the decomposition temperature of the as-received metal carboxylates. A heating programme of 30-1000°C was used. The mass loss associated with decomposition of the metal acetate in Figure 4.3 (a) is lower for the Group I alkali metals with higher ionic radius as expected shown in Figure 4.4. The onset of decomposition is identified at a similar temperature for all as-received Group I metal acetates, around the temperature of 450°C, except for LiAc whose decomposition was observed at 350°C. From Figure 4.3 to Figure 4.4, the precursors have the same anion (i.e. acetate CH_3COO^-) and the metal cation is varied within Group I (i.e. Li^+, Na^+, K^+, Rb^+, Cs^+). Melting temperature (as identified by endotherms) from sodium acetate to cesium acetate decreases as ionic radius of the alkali metal increases. This trend did not apply for lithium acetate dihydrate. LiAc dihydrate loses water at temperatures below 200°C [Tobón-Zapata et al., 2000]. It is also noted from Figure 4.4, decomposition temperature (step change happened above the temperature of 350°C) in all these metal acetates are very similar.
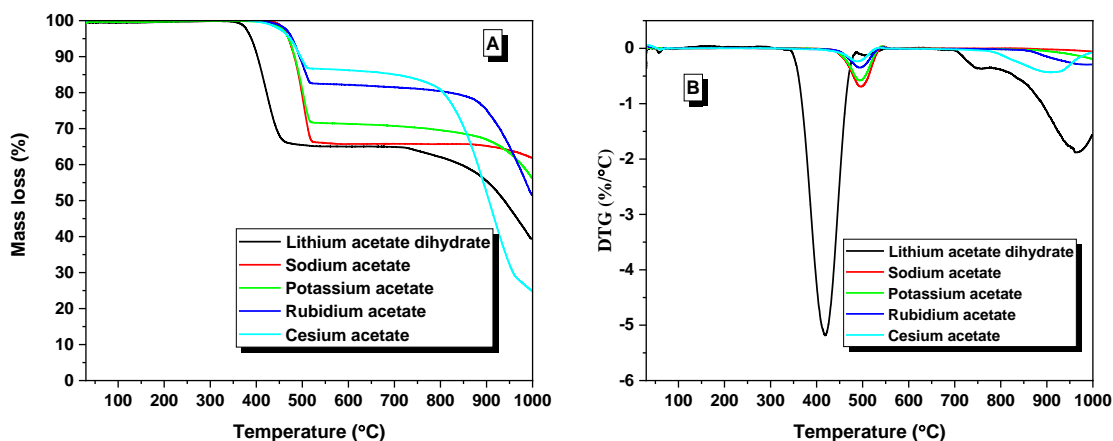
Figure 4.3 Themogravimetry results of as-received Group I metal acetate precursors as a function of the metal cation, (a) Mass loss and (b) DTG curves.
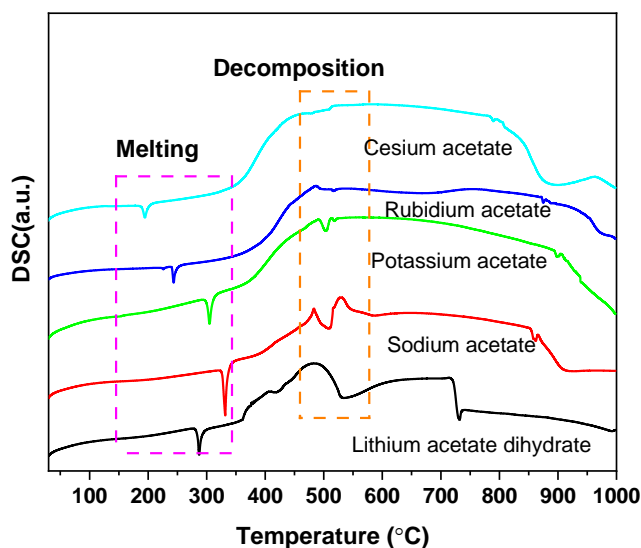
Figure 4.4 DSC curves of as-received Group I metal acetate precursors

The mass loss associated with decomposition of the metal acetate in Figure 4.5 (a) is different for the Group II alkaline earth metal cations of Ca^{2+} and Mg^{2+} shown in Figure 4.6. The thermal behaviour of magnesium acetate tetrahydrate and calcium acetate hydrate exhibit significant difference. For magnesium acetate tetrahydrate, the melting temperature and decomposition temperature were so close around 350°C seen from Figure 4.6, which makes it difficult to select the temperature of 350°C for melting magnesium acetate tetrahydrate. For calcium acetate hydrate, the onset melting temperature seems to above 400°C, while the decomposition temperature shown in Figure 4.6 is around 800°C. In general, the temperature of 350°C is not suitable for melting magnesium acetate tetrahydrate and calcium acetate hydrate which metal cations assigned to Group II alkaline earth metal cations.
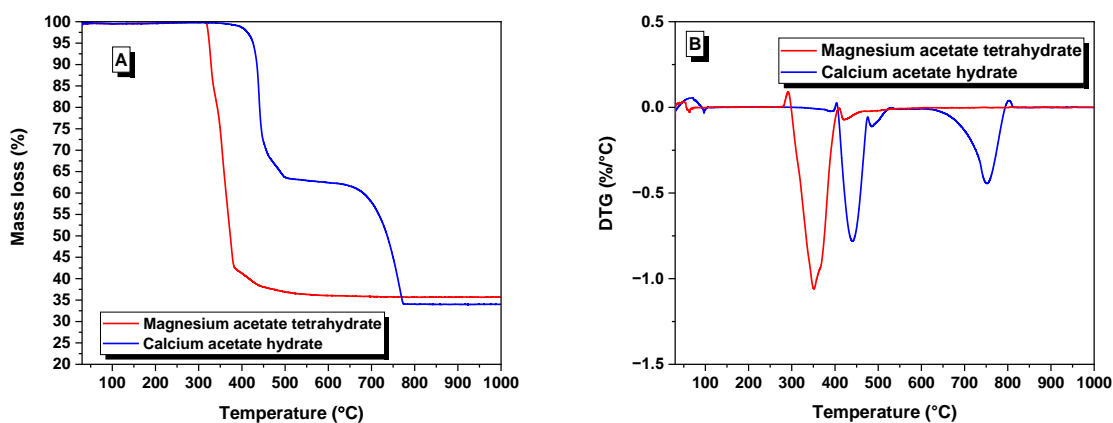
Figure 4.5 Themogravimetry results of as-received Group II metal acetate precursors as a function of the metal cation, (a) Mass loss and (b) DTG curves.
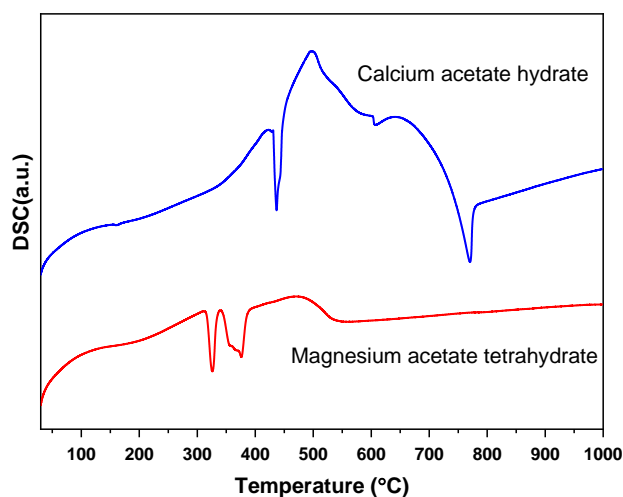
Figure 4.6 DSC curves of as-received Group II metal acetate precursors

Different pre-heating step was used for sodium carboxylates with different carboxylate chain lengths in order to get a clearer measurement of the melting temperature, without potential overlap from dehydration mass loss. In Figure 4.7, curves assigned to sodium propionate (pre-heating at 250°C), sodium butyrate (pre-heated at 200°C) and sodium octanoate. DSC results (Figure 4.8) show that the melting temperature reduced as the carboxylate chain length increases. The onset of decomposition is identified at a similar temperature for all as-received sodium carboxylates at around 450°C considering the DSC results (Fig. 4.8), independently of the chain length. However, as the chain length of the carboxylate increased, the mass loss associated with their decomposition increased (Fig. 4.7). Therefore, the temperature of 350°C is considered suitable for melting sodium carboxylates with different carboxylate chain length.
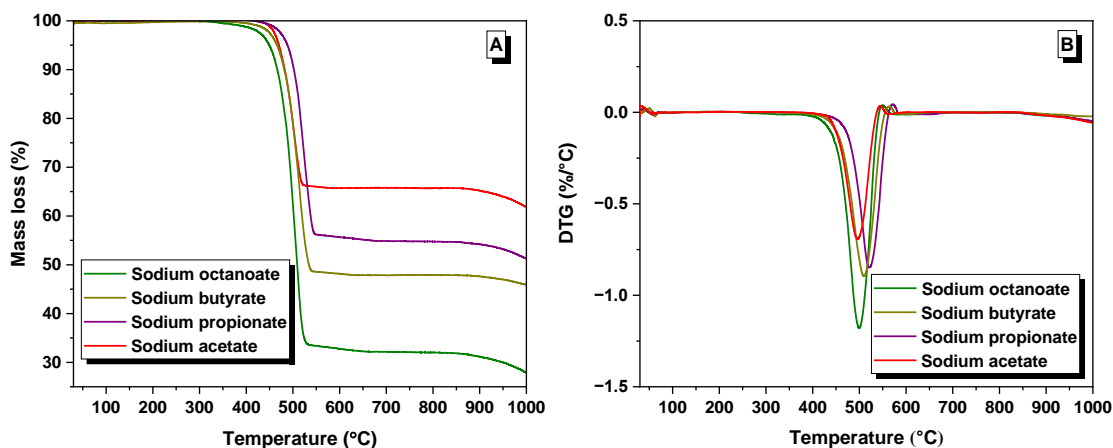
Figure 4.7 Thermogravimetry curves of as-received sodium carboxylate precursors as a function of the carboxylate chain length, (a) Mass loss and (b) DTG curves.
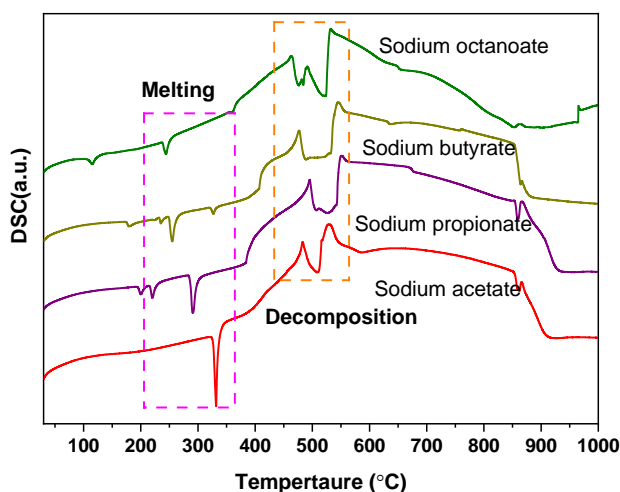
Figure 4.8 DSC curves of as-received sodium carboxylate precursors as a function of carboxylate chain length

Given that the temperature of 350°C was appropriately not reaching the decomposition temperature of most metal carboxylates, it was decided to use this temperature value for the thermal treatment of metal carboxylates. The following section will investigate the influence of the thermal treatment process on different composite systems with various mix design.

For solids, there is no remarkable difference existed in entropy (ΔS) between pure and impure solids as solids are constrained in atomic motion shown in Figure 4.9. Comparatively, there is a greater difference in entropy between pure and impure liquids, because of the potential for greater disorder and greater entropy in impure liquids [Zhang, 2022]. Therefore, pure material holds a higher T_m than the impure material, as illustrated in Figure 4.10. T_m decreases as the composition becomes more blended with another solid [Zhang, 2022, Kurtuldu and Löffler, 2020]. In the impure solid mixtures, the minimum melting temperature needed at a certain composition of components, is named the eutectic point (Figure 4.23 a). This concept could be utilized to likely explain

when the number of component in composition changed from single system to multiple/ternary system in both cast metal acetates and cast sodium carboxylates from thermodynamic view as there is no existing literature studied the melting point of the blended metal acetates.
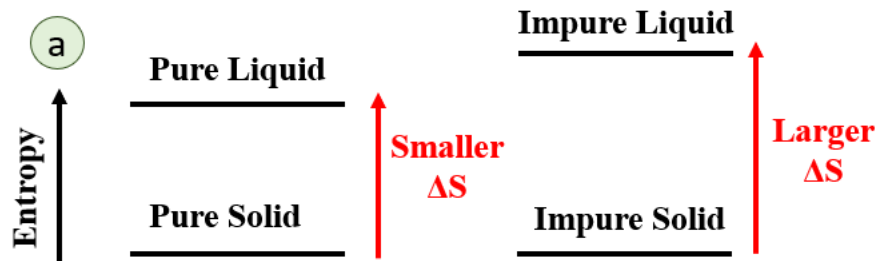
Figure 4.9 The entropy changes during melting process [Zhang, 2022]
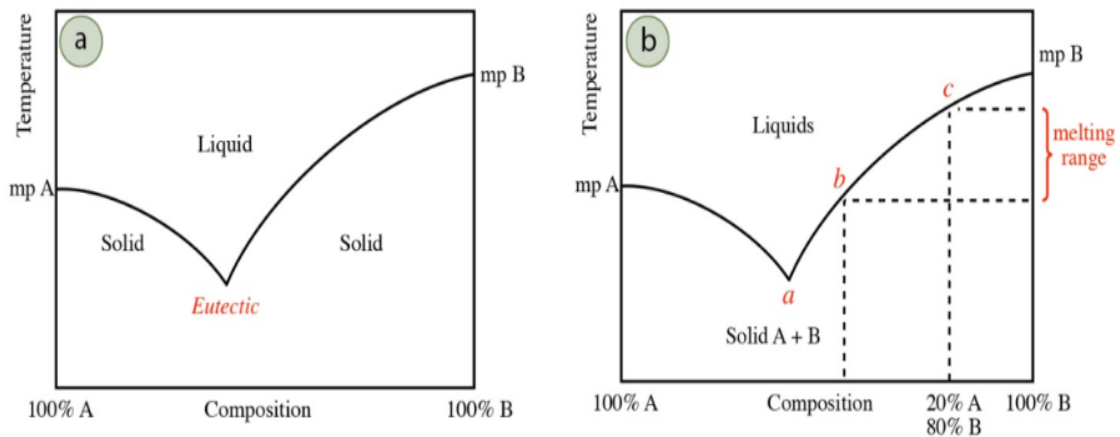
Figure 4.10 The melting process of pure and impure material [Zhang, 2022]

4.3 Results and discussion

4.3.1. Observations on the melting process and visual characteristics of cast samples

4.3.1.1 Single component systems

The metal acetates studied in this section were chosen to investigate the effect of different metal cations (Group I and Group II, Table 4.1). In addition, LiAc will be covered separately later on.

Figure 4.11 (a)-(d) shows the cast samples of single acetates, from NaAc to CsAc. The appearance of the cast NaAc is shown in Figure 4.11 (a) - its colour is white and the surface of the cast is rough and uneven. For KAc, the colour of cast KAc is a bit darker but owing a smooth surface compared to the cast NaAc. Figure 4.11 (c) and Figure 4.11 (d) illustrated the obtained cast products of RbAc and CsAc. Figure 4.11 (d) presented a rough surface of the cast RbAc with a brown color. The colour of the cast sample is related to the charring or burned during the melting process. CsAc seems to have the smooth appearance seen from Figure 4.11 (d) compared to RbAc in Figure 4.11 (c).
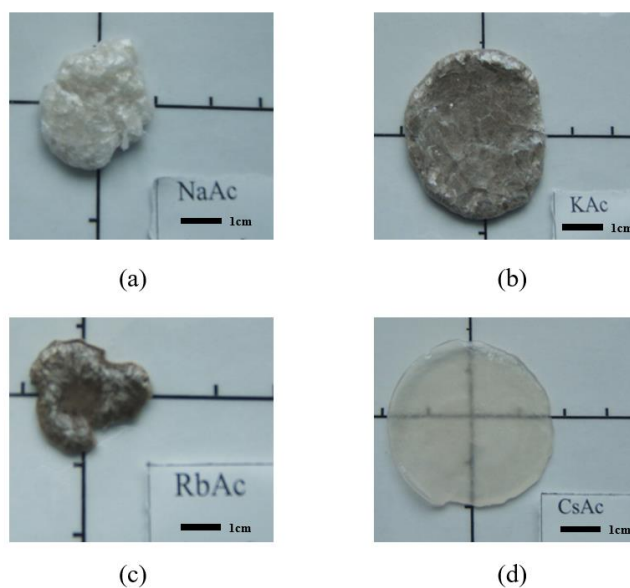
Figure 4.11 Photographs of cast samples of (a) NaAc, (b) KAc, (c) RbAc and (d) CsAc

Figure 4.12 illustrated the calculation of the melting time of the metal carboxylates during the melting process. As shown in Figure 4.12, an error of 1 minute was set as the furnace was opened per minute to be checked whether the metal carboxylates were melted or not.

Melting process (calculated by the time spent /min)

Start 1 2 3 4 5 To be continued

Melting time = 5 min

Error comes from the solids partially melted to fully melted into liquids within 1 min
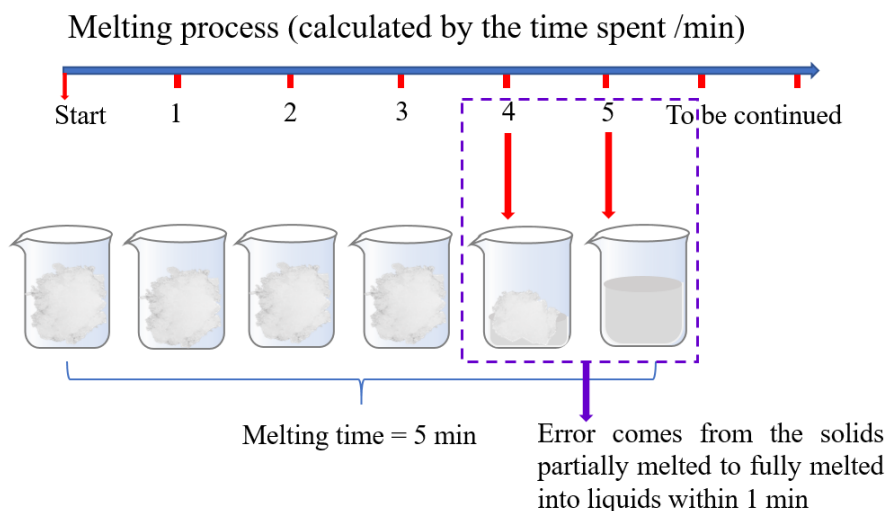
Figure 4.12 Schematic diagram of the the melting time was calculated

Melting is a crucial shift from solid to liquid due to rising temperature and enhanced particle motion, as depicted in Figure 4.12 [Zhang, 2022]. It occurs at the material's melting point, transitioning from a solid to a liquid, achieving equilibrium. This phase transition stabilizes when the Gibbs free energy change (ΔG) reaches zero.

$$\Delta G = \Delta H - T\Delta S \quad \text{Eq. 4.1 [Zhang, 2022]}$$

$$T = \Delta H/\Delta S \quad \text{Eq. 4.2 [Zhang, 2022]}$$

Here, ΔH means the required enthalpy energy alteration required for melting each mole of ionic crystal; T signifies the melting temperature; ΔS denotes the entropy shift [Zhang, 2022].
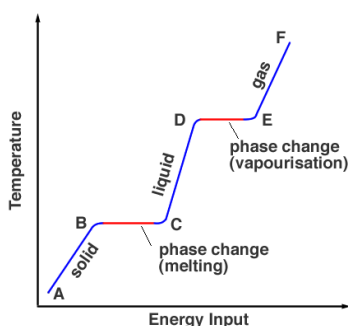
Figure 4.13 The heat curve of solid to liquid and gas (adopted from [Zhang, 2022])

The correlation between melting time of different Group I metal acetate precursors as a function of ionic radius of the Group I metal cations is illustrated in Figure 4.12. The time required for melting reduced as the radius of the Group I alkali metal cations increased. This is because in order to make solids melt, lattice bonds need to be broken which means the energy greater than the lattice enthalpy needs to be put into the system

[Zhang, 2022, Halmos et al., 1970]. The lattice energy corresponding to Group I alkali metal cations exhibits a reciprocal connection with the ionic radius of the cations [Halmos et al., 1970, Ingram et al., 1972]. Ions hold a smaller ionic radius required more energy. Therefore, the needed energy for breaking the lattice bonds reduces as the ionic radius of metal cations increases. The standard (p° = 0.1 MPa) molar enthalpies of formation in the crystalline state of Group I alkali metal acetates at T = 298.15 K, were listed as [Aleixo et al., 2005]:

$$\Delta H \ (NaAc) = (711.01 \pm 0.51) \ kJ/mol$$

$$\Delta H \ (KAc) = - (722.36 \pm 0.49) \ kJ/mol$$

$$\Delta H \ (RbAc) = - (722.31 \pm 1.09) \ kJ/mol$$

$$\Delta H \ (CsAc) = - (726.10 \pm 1.07) \ kJ/mol$$

Thus, when heating at the same temperature of 350°C, the shortest time was needed for melting CsAc in all these four materials.
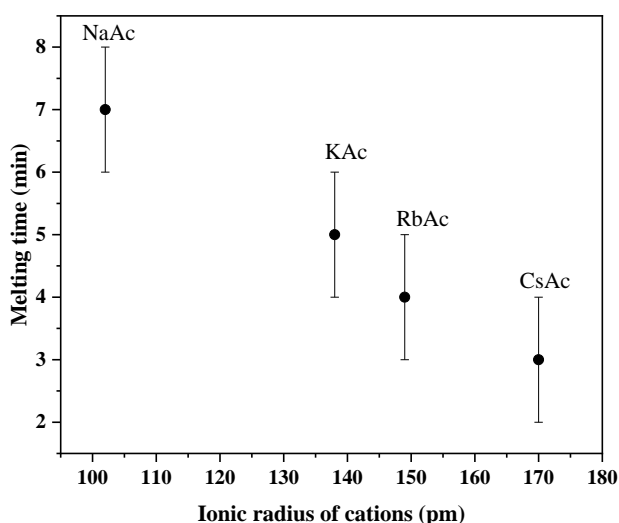
Figure 4.14 Melting time of NaAC, KAc, RbAc and CsAc.

LiAc is not included in Figure 4.11, as it could not be melted at the temperature of 350°C, and after 13 minutes of exposure to this temperature it had begun to thermally decompose. In order to identify an alternative melting temperature that could avoid thermal decomposition, LiAc was heated at individual 300°C, 350°C, 380°C and 420°C. The observations of LiAc during the heating process at varying temperature are summarized in Figure 4.15. It is evident that at the temperature below 350°C (inclusive), LiAc only partially underwent melting, and also showed some agglomeration, in a time duration of 13-19 minutes, which is a long period for melting compared to other metal acetates. However, LiAc fully melted quickly within 5 minutes at 380°C. The time for LiAc to melt reduced to 4 minutes as the temperature of furnace increased to 420°C.

This demonstrated one possible method that works effectively on reducing the time for LiAc to melt is to employing a higher temperature in the furnace such as 420°C.

Furnace temperature (°C)

300	350	380	420

Observations

After 6 min, it was partially melted, 19 min later it agglomerated at the bottom of the beaker.	After 4 min it was partially melted. 13 min later, it seems burnt, and a brown/ black sample was obtained.	After 5 min, the sample was melted.	After 2 min it was partially melted, after 4 min at this temperature the colour changed.
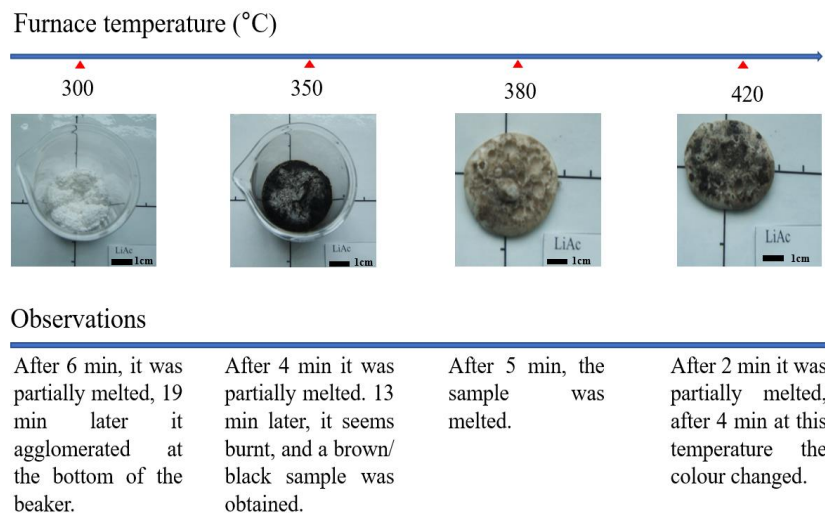
Figure 4.15 Schematics for the changes of LiAc when exposed to different temperatures

The Group II alkali earth metal acetates included magnesium acetate (MgAc) and calcium acetate (CaAc). MgAc could not be successfully melted after 17 minutes at the temperature of furnace at 350°C. The furnace temperature of 350°C was not suitable for melting MgAc, as the decomposition temperature of MgAc is 350°C [Halmos et al., 1970, Van Uitert et al., 1971]. Therefore, it was decided to decrease the temperature of the furnace to see if lower temperatures would enable MgAc to melt and avoid decomposition. Temperatures of 220°C, 250°C and 300°C were chosen. Figure 4.14 presents a schematic diagram of MgAc at the mentioned temperature range and the observations were also summarized. For MgAc, it was observed that a temperature of 220 °C was still too high to attempt to melt this acetate. In general, the heated MgAc was charred and agglomerated at all the temperatures tested shown in Figure 4.16.

Furnace temperature (°C)

220	250	300

Observations

After 3 min, the sample was charring and agglomerated.	After 2 min, charring happened to the sample and agglomerated.	After 2 min, the sample was charring and agglomerated.
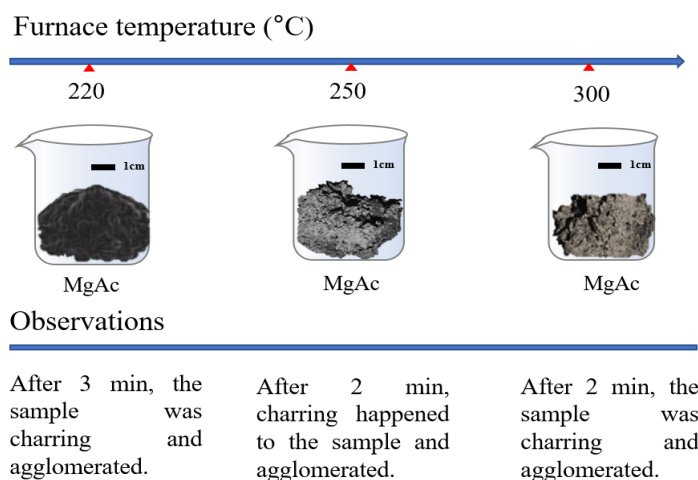
Figure 4.16 Schematic diagram of MgAc at various temperature

As calcium acetate is highly hygroscopic, only hydrates are available from commercial chemical suppliers. Similar to MgAc, CaAc also could not be melted at 350°C after 23 minutes. When melting CaAc at the temperature of 350°C, it became charred and agglomerated at the bottom of the beaker, but did not melt in the air. It was different compared to the DSC results shown in Figure 4.6, which suggested no melting or charring at 350°C under N_2 atmosphere. This may due to the presence of oxygen, which could enable charring at a low temperature. Therefore, the melting temperature was modified and decreased to 220°C, 250°C and 300°C respectively. The changes during these three different temperatures observed in CaAc are summarised in Figure 4.17. Conversely, to that of MgAc, CaAc did not show any variations at all the tested temperatures, which may indicate that higher temperature was needed for CaAc melting. The melting temperature of calcium acetate hydrate and the literature values for the melting temperature and are very close. Therefore, it is difficult to find the appropriate temperature for melting CaAc.

Furnace temperature (°C)

220	250	300

Observations

| After 22 min, the sample did not melted at all and no charring happened. | After 20 min later, it was still not melted and no charring occurred. | After 16 min later, it was still not melted and no charring occurred. |
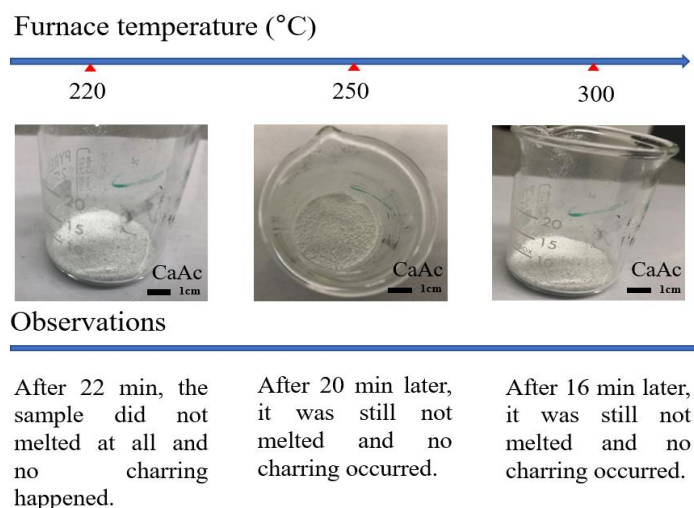
Figure 4.17 Changes of CaAc when exposed to different temperatures

From all the results of alkaline earth metal (Group II) acetates illustrated in Figure 4.14 and Figure 4.15, clearly that 350°C on furnace and the temperature range of 220°C-300°C evaluated in this study when attempting to melt the acetate precursors (exactly MgAc and CaAc) is not appropriate. This poses a limitation to preparing melts of Group II alkali earth metal acetates prior to casting as the suitable heating temperature is not known.

Figure 4.18 (a)-(d) shows the cast sodium carboxylates with various carboxylate chain length. The obtained product of NaPr after quenching is shown in Figure 4.16 (b). It is light grey in colour and the large individual grains are clearly visible from the

appearance compared to NaAc shown in Figure 4.16 (a). When exposing NaBu to 350°C presented in Figure 4.15 (c), the product obtained was darker and much rougher than the melted NaPr. NaOc is different from the other acetates tested, because it did not melt at the temperature of 350°C and seems to be burnt due to the darker appearance under the current temperature conditions. Instead, it changed into a black solid that seemed burned, shown in Figure 4.16 (d). From Figure 4.16 (a) to Figure 4.16 (d), it is evident that the color owing by the obtained product becomes darker which may due to the chain length of the carboxylate increases [Massarotti and Spinolo, 1979].
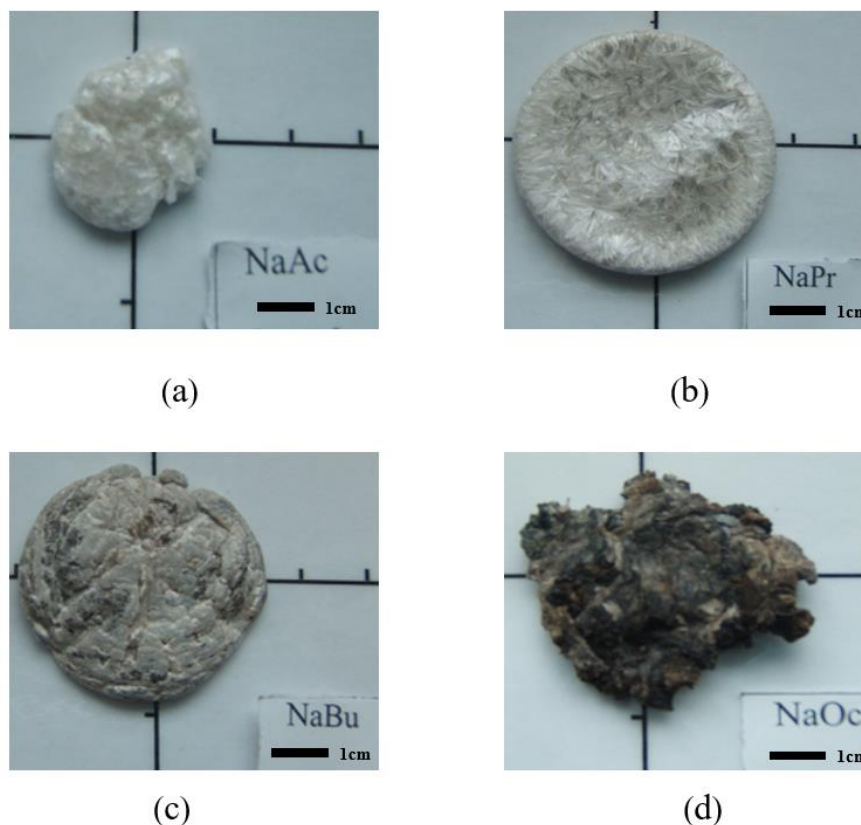
Figure 4.18 Photographs of cast samples with different carboxylate chain length, where (a) NaAc (b) NaPr, (c) NaBu and (d) NaOc

Figure 4.19 shows the melting time of different sodium carboxylates with varying carboxylate chain length. It seems to show that the melting time reduced as the carboxylates group length increased, from 7 minutes for NaAc to 4 minutes for NaBu, except NaOc as its melting time could not be determined.

Sodium carboxylates are considered ionic solids and the strength of electrostatic attraction is important to intramolecular as well as intermolecular bonding due to their permanent non-directional charges [Binnemans, 2005, Michels and Ubbelohde, 1972]. The melting points of ionic solids are commonly high, because the strong Coulombic forces produced between positive and negative ions were needed to be overcome in the melting process. However, metal carboxylates could not be treated as a simple ionic

solid (e.g. NaCl) in practice. It may be partly distributed by the anion which is a molecule, thus the bonding will likely not be totally ionic in character. A study [Binnemans, 2005] applied to Group I metal carboxylates owing longer chains n (number of CH_3) > 6 suggested that the melting point of the carboxylate chain length decreases with increasing carboxylate chain length. This could be related to the fact that the compounds with shorter chain length owing more closely packed groups. It is also reasonable to assume similar trend would apply for the materials with shorter chain length.

Michels [Michels and Ubbelohde, 1972] mentioned that the layers of charged carboxylate-groups should exert a major influence on the crystal packings designated for Group I metal carboxylates, making contact with adjacent cations and separating them from the alkane "tail" of the anion. A model of 'electrostatic sandwich' of carboxy-groups and cations was determined and to be expected to occur in salts with the shorter chain length.

Although it seems there is no exact explanation to answer how carboxylate chain length affects the melting time based on the above-mentioned findings for sodium carboxylates. However, this implies that a longer anion (carboxylate) chain length leads to a less compact structure, resulting in weaker intermolecular forces and lower lattice enthalpy. Therefore, a lower melting temperature was obtained and shorter melting time as a result.
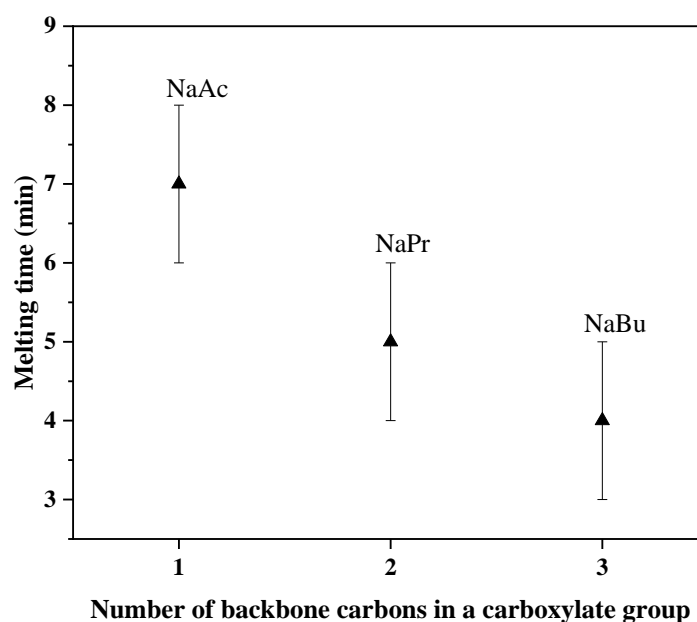
Figure 4.19 Melting time of NaAc, NaPr and NaBu for heating at 350°C.

In general, the melting time at 350°C of Group I alkali metal acetates decreases as ionic radius of alkali metal cation increases, except for LiAc. In addition, when carboxylate group chain length increased, the melting time reduced. The two Group II

alkali earth metal acetates, CaAc and MgAc, have limitations for casting single-component systems due to their charring behaviour. NaOc also has restrictions compared with other sodium carboxylates because of its charring behaviour. Charring occurred in single acetate systems, but it is not yet known what would happen if two components with charring behaviour are blended. Therefore, further investigation is needed to explore the melting and quenching behaviour of a range of metal carboxylate combinations.

4.3.1.2. Binary system of metal carboxylates

Figure 4.20 (a)-(c) shows the photographs of the cast (which means after thermal treatment) samples composed of two metal carboxylate components. The colour of appearance is white in the cast NaAc-KAc in Figure 4.20 (a) and the surface is not smooth - it seems lighter in appearance than the individual cast NaAc in Figure 4.11 (a) and individual cast KAc in Figure 4.11 (b). Figure 4.20 (b) and Figure 4.20 (c) shows the casting results of binary system composed of sodium carboxylates differ with carboxylate group length. The colour of cast NaAc-NaPr in Figure 4.20 (b) is lighter than NaBu-NaOc in Figure 4.20 (c). The surface of the cast NaBu-NaOc in Figure 4.20 (c) is rough and uneven. Compared with individual cast NaBu in Figure 4.18 (c) and cast NaOc in Figure 4.18 (d), the color of blend NaBu-NaOc is darker than that of the individuals.

(a)

(b)

(c)
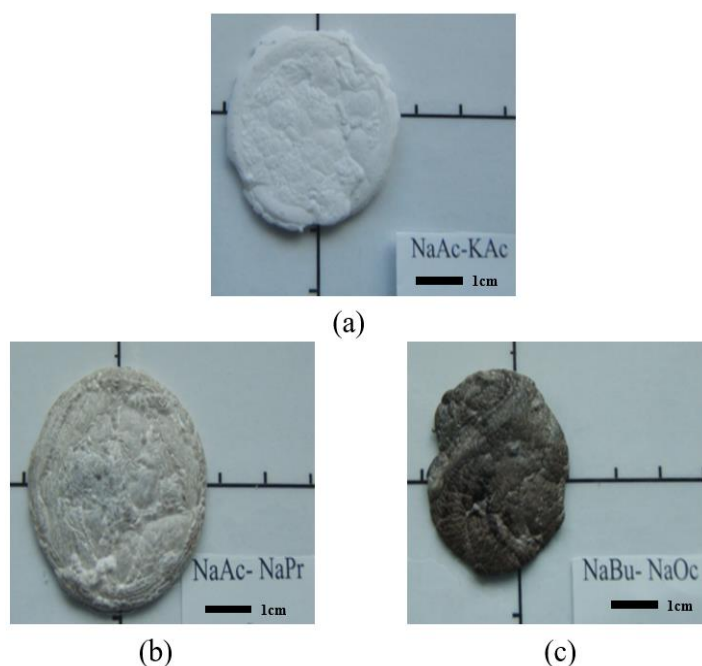
Figure 4.20 Photographs of cast samples (a) NaAc-KAc, (b) NaAc-NaPr and (c) NaBu- NaOc

Obtaining the cast NaOc in a single-component system is currently unavailable,

the solid existed seen from Figure 4.18 (d) seemed burnt. But there is no charring occurred in the process of casting NaBu-NaOc, demonstrated that it may be suggested to do the casting process in the composition of binary system are better to avoid charring.

4.3.1.3. Ternary and quaternary systems of metal carboxylates

Figure 4.21 (a) and (b) show the photographs of cast NaAc-NaPr-NaBu and NaPr-NaBu-NaOc – these two combinations differ in their average carboxylate group chain length. Evidently from Figure 4.21 (a) and (b), the color of NaPr-NaBu-NaOc seems darker. The surface appearance of both these cast samples is not smooth. The colour of the cast NaAc-NaPr-NaBu (Figure 4.21 (a)) is darker than the binary system of NaAc-NaPr presented in Figure 4.20 (b). While the colour of the cast NaPr-NaBu-NaOc shown in Figure 4.21 (b) is not as dark as that of NaBu-NaOc in Figure 4.20 (c) as observed.
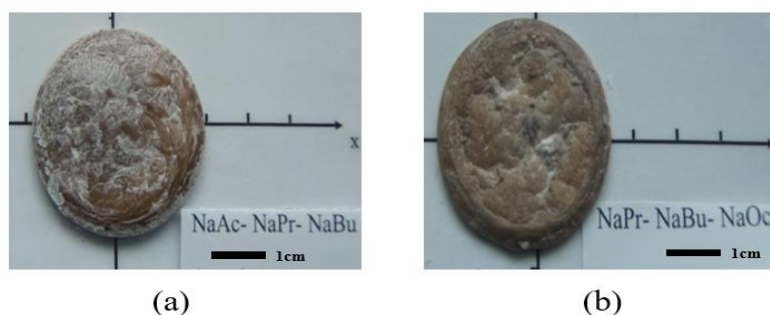
Figure 4.21 Photographs of cast samples (a) NaAc-NaPr-NaBu and (b) NaPr-NaBu-NaOc

The casting results of ternary and multiple combinations of metal acetates are presented in Figure 4.22 (a)-(c). The ternary system MgAc -KAc-NaAc is shown in Figure 4.22 (a), which has a largely transparent appearance. For CaAc -KAc-NaAc in Figure 4.22 (b), Observations of that it is also largely transparent. Photograph of casting results of CaAc-MgAc-KAc-NaAc is shown in Figure 4.22 (c), which is partly transparent. The color of CaAc-MgAc-KAc-NaAc in Figure 4.22 (c) seems darker. The colour of CaAc-MgAc-KAc-NaAc in Figure 4.22 (c) is darker than that of CaAc -KAc-NaAc in Figure 4.22 (b) and MgAc -KAc-NaAc shown in Figure 4.22 (a). It could be related to the addition of MgAc and CaAc - further explanation will be addressed later in the melting time section.
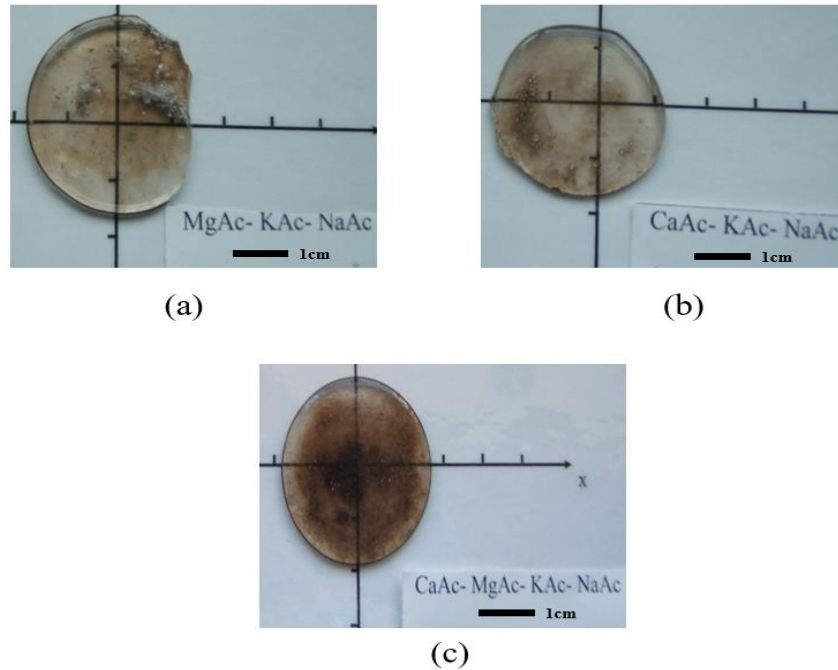
Figure 4.22 Photographs of cast samples (a) MgAc -KAc-NaAc, (b) CaAc -KAc-NaAc and (c) CaAc-MgAc-NaAc-KAc

Figure 4.23 shows that the melting time of NaAc-KAc was 9 min. It is noted that the melting time of NaAc-KAc was longer than that of either individual cast NaAc (7 min) or KAc (5min). The melting times of MgAc -KAc-NaAc and CaAc -KAc-NaAc systems were 8 min and 9 min, respectively. But, the melting process for MgAc -KAc-NaAc was 1 minute shorter compared to the binary system of NaAc-KAc.

The melting time of CaAc-MgAc-KAc-NaAc was up to 10 minutes. Compared with the ternary system MgAc -KAc-NaAc, the melting time of the four-component system CaAc-MgAc-KAc-NaAc was 2 minutes longer, from 10 min to 8 min. This seems to be the influence of the additional CaAc. In theory, as Ca^{2+} has a larger ionic radius than Mg^{2+}, the electrostatic attraction would be weaker, giving a reduced lattice energy, and resulting in a decreased melting point [Binnemans, 2005]. The melting point would be reduced as a result in theory. But it is difficult to make a direct comparison of ionic radius in the system composed of multiple components. Additionally, nothing happened for the individual cast CaAc at this heating temperature. Therefore, it is difficult to conclude the reason for prolonged melting time when we change the composition from MgAc-KAc-NaAc to CaAc-MgAc-KAc-NaAc. Similarly, 1 minutes longer was observed from CaAc -KAc-NaAc to CaAc-MgAc-KAc-NaAc. The difference in composition was additional MgAc. This is also a complicated system that cannot be explained only from the ionic radius aspect, nothing was found in the literature to compare against.
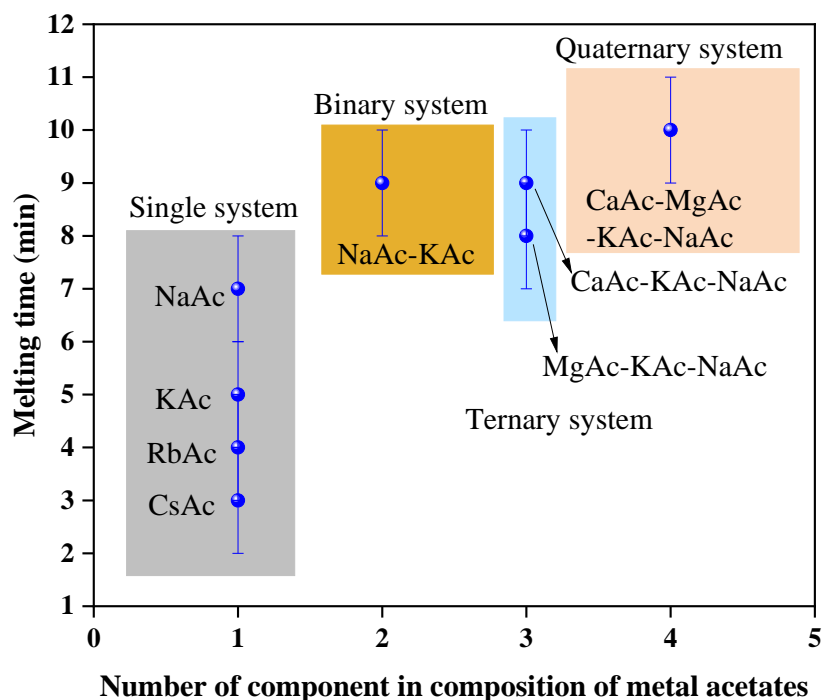
Figure 4.23 Melting time of single system, binary system and multiple system composed of cast metal acetates (5 g of precursors was used for all these melts)

The melting time of cast sodium carboxylates is shown in Figure 4.24, varying the number of components. It was divided into three colored areas including the single system (grey color), binary system (yellow color) and the ternary system (purple color). In binary system from Figure 4.24, the melting time of NaAc-NaPr is 6 min, and the melting time of NaBu-NaOc is 14 min, 8 minutes longer than that of the former. The difference of melting time between these two samples at the temperature of 350°C possibly was due to average carboxylate length. But as we discussed previously, it is hard to compare the carboxylate chain length in the number of components of non-single system. In addition, individual NaOc could not be melted as charring was unavoidable according to Portier et al [Portier, 1989], but NaBu-NaOc could be successfully melted. Generally, it is hard to tell the influence of NaOc on the melting behavior of binary system at current situation.

The melting time of NaAc-NaPr-NaBu and NaPr-NaBu-NaOc was shown in Figure 4.21, 8 min and 12 min, respectively. Compared with NaAc-NaPr binary system, the time of melting process of NaAc-NaPr-NaBu is longer than binary systems, from 8 min to 6 min. In contrast, the reverse was observed in NaPr-NaBu-NaOc ternary system, 2 minutes shorter than that of NaBu-NaOc binary system. All the discussions above suggested that the number of components in sodium carboxylates influenced the time of melting process, which would possibly due to the chain lengths.
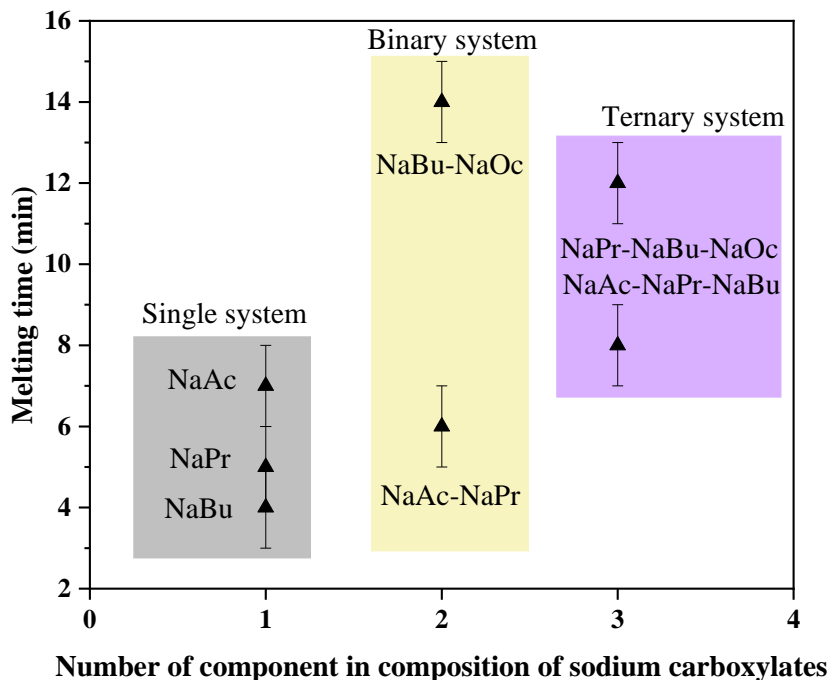
Figure 4.24 Melting time of single system, binary system and ternary system composed of cast sodium carboxylates (5 g of precursors was used for all these melts)

4.3.2 Characterization of cast metal carboxylate samples

4.3.2.1. Single acetate precursors and cast samples

Figure 4.25 (a) and (b) respectively displayed the XRD patterns of cast NaAc and KAc. Strong crystalline peaks occurred in the XRD patterns of the cast samples, the increase in peaks intensity could suggest that the melting and quenching are leading to additional ordering of the acetate, rather than inducing the potential amorphisation. It could be seen from Figure 4.25 (b), there is also strong crystalline peaks existed at the 2θ range of 8-10° assigned to KAc (PDF# 00-046-0898). Structural information within crystalline solids can be reflected by the X-ray diffraction patterns of atoms [Zanotto and Mauro, 2017, Jiang and Zhang, 2014]. Amorphous materials such as glass, on the other hand, without long-range ordered periodic arrays existed, so it is not possible to see them in XRD patterns [Jiang and Zhang, 2014]. Therefore, if the material shows strong crystalline peaks in its X-ray diffraction pattern like the cast NaAc and cast KAc presented in Figure 4.25 (a) and (b), this suggests that they little potential on glass-forming ability.
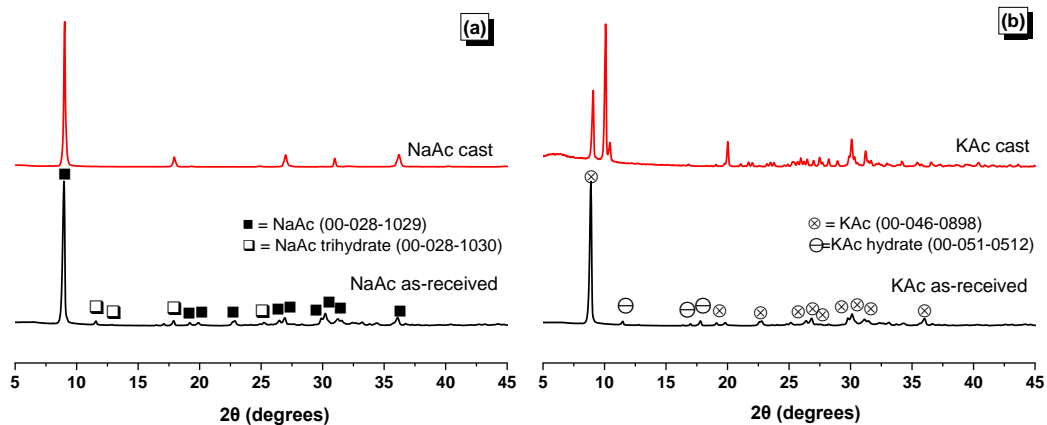
Figure 4.25 XRD patterns of (a) NaAc and (b) KAc. Where NaAc as-received = the precursor; NaAc cast = the cast sample after melting and quenching. KAc as-received = the precursor; KAc cast = the cast sample after melting and quenching.

Figure 4.26 shown the XRD patterns of cast NaPr and NaBu respectively, both of which have strong crystalline peaks. The fact that the intensity of the peaks increases with thermal treatment suggest that this treatment is potentially inducing further ordering of the crystalline solid metal carboxylates relative to their as-received form [Jiang and Zhang, 2014], and that these compounds have little potential to form glasses under the quenching conditions used in this study. This possibly contribute to influence the peak intensity of the diffraction patterns in the cast NaPr and the cast NaBu.
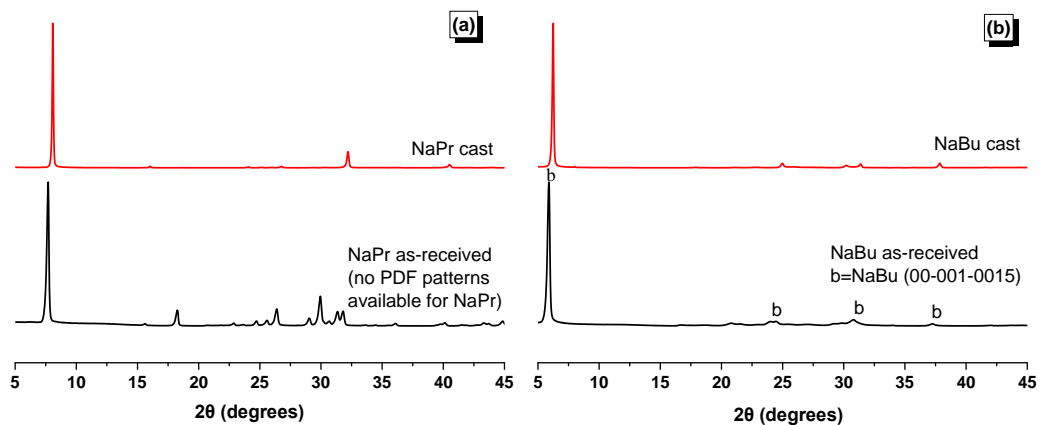
Figure 4.26 XRD patterns of the cast (a) NaPr and (b) NaBu

The results suggest that single systems of cast NaAc and cast KAc have low glass forming ability under the quenching conditions evaluated. The low potential of glass-forming ability concluded considering two aspects, firstly as seen in the photographs (Figure 4.9) of the cast NaAc and cast KAc the resulting solids were not transparent, secondly there is strong crystalline peaks existed in the XRD patterns of both cast NaAc and KAc. In addition, the non-transparent appearance observed in the photographs of the cast and still strong crystalline peaks occurred demonstrated less potential of glass

forming for the single systems of cast NaPr and NaBu. To conclude, low glass-forming ability was possibly existed in the cast NaAc, KAc, NaPr and NaBu under the current quenching process used.

4.3.2.2. Binary systems of metal carboxylate

For the cast binary system composed of NaAc and KAc, the XRD pattern is shown in Figure 4.27. Strong crystalline peaks appeared in the XRD patterns of the cast NaAc-KAc, suggesting that crystalline potassium acetate existed in the cast NaAc-KAc sample.

In addition, strong crystalline peaks existed in very similar position to dominant peaks for NaAc (PDF#00-028-1029) at the 2θ range of 8-10°. This indicates that crystalline phases are present in the cast NaAc-KAc, suggesting that NaAc-KAc has little potential to form glasses under these quenching conditions. Moreover, there is a new peak (i.e. at 7-8,10-11 of 2θ) occurring but not assigned to any phases detected in either of the precursors or founded on the ICDD database when doing an elemental search.
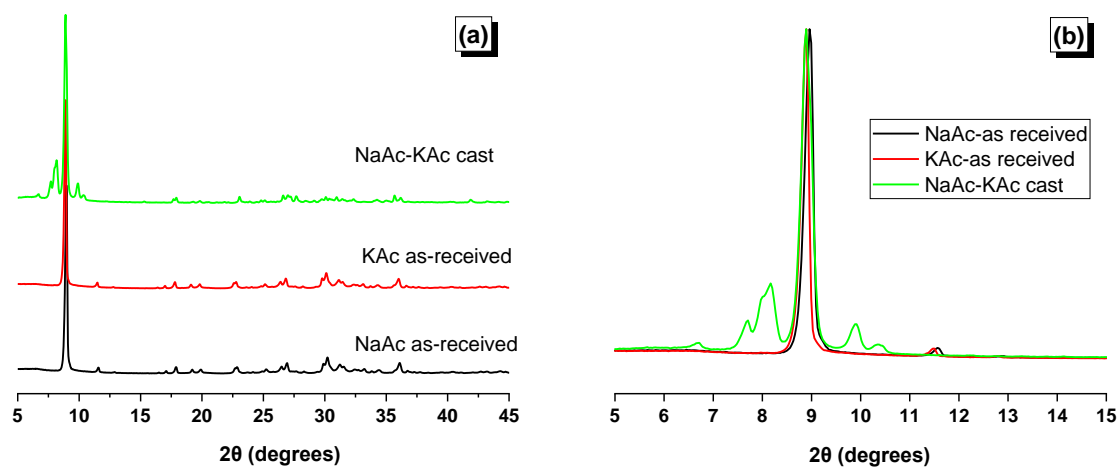
Figure 4.27 XRD patterns of NaAc-KAc cast (a) at 2θ range of 5-45° and (b) at 2θ range of 5-15°.

Using differential scanning calorimetry (DSC) to test temperatures and heat changes linked to heat transitions resulting from the cast metal carboxylates composed of binary to multiple components. DSC results can identify the melting point T_m and relaxation of a glass to a super-cooled liquid [Jiang and Zhang, 2014] [Zheng et al., 2019]. A schematic DSC curve for a glass is shown in Figure 4.27. As it was discussed in previous sections, from the thermodynamic point of view, melting refers to a first order phase transition, where discontinuous change occurred in enthalpy (i.e. absorbs

latent heat). Glass transition is a second order phase transition, at which the continuous change existed in enthalpy (i.e. no latent heat) [Zheng et al., 2019, Jiang and Zhang, 2014]. The specific heat capacity C_p, is defined by the following Equation 4-1:

$$\left(\frac{\partial H}{\partial T}\right)_p = C_p \qquad \text{Equation 4-1}$$

Therefore, the DSC output signal is proportional to Cp. A peak for a first order transition representing melting was expected in the DSC output signal, and a step change for a second order transition representing the glass transition T_g was also to be expected if a glass is present illustrated in Figure 4.28 [Zheng et al., 2019]. T_g is a kinetic phenomenon which relies on the cooling rate in quenching and the rate of heating in DSC [Zheng et al., 2019].
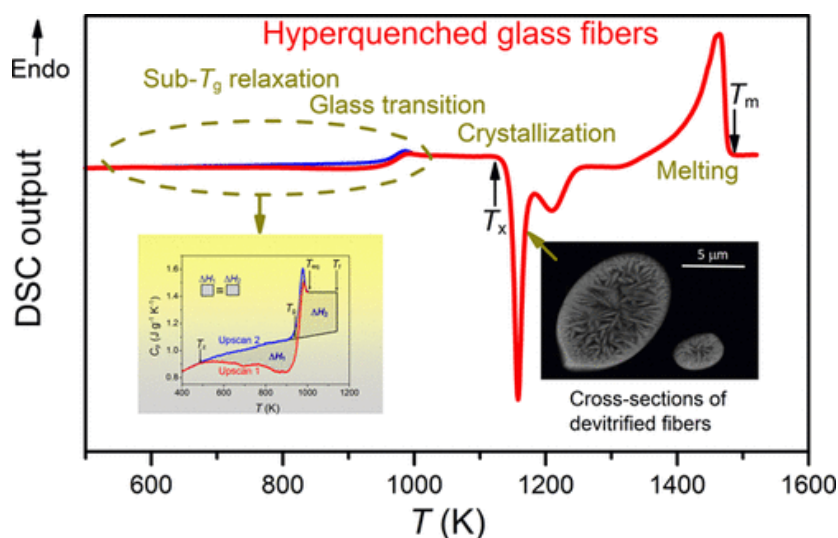
Figure 4.28 Schematic plot of DSC output, where T_x referred to the temperature that crystallization occurred; T_m represented the temperature solids melted [Zheng et al., 2019].

Figure 4.29 (a) shows the DSC curve of NaAc-KAc cast sample, and the mass spectrometry of the cast NaAc-KAc is shown in Figure 4.29 (b). There is no glass transition in the cast NaAc-KAc DSC curve shown in Figure 4.29 (a), suggesting that no glass state materials existed in this cast sample. This is consistent with the XRD patterns of the cast NaAc-KAc shown in Figure 4.27 where strong crystalline peaks are observed, demonstrating that there was no glass formation. In Figure 4.29 (b), the mass spectra for H_2O and CO_2 as a function of temperature during DSC testing shows two major events occurring at temperatures around 100 °C and between 400 and 600 °C. There is no known literature discussed the melting point of the blended cast NaAc-KAc in DSC curves, however, it can be assumed that the decomposition of acetates will not be too dissimilar to that of thermal decomposition of acetic acid, which can be described according to Eq. 4.3 and Eq. 4.4 [Blake and Jackson, 1968]. This could be partially

contributed to the occurrence of CO_2 and H_2O, which observed from the MS data shown in Figure 4.29 (b).

$$CH_3CO_2H \rightarrow CH_2CO + H_2O \qquad \text{Eq. 4.3 [Blake and Jackson, 1968]}$$

$$CH_3CO_2H \rightarrow CH_4 + CO_2 \qquad \text{Eq. 4.4 [Blake and Jackson, 1968]}$$
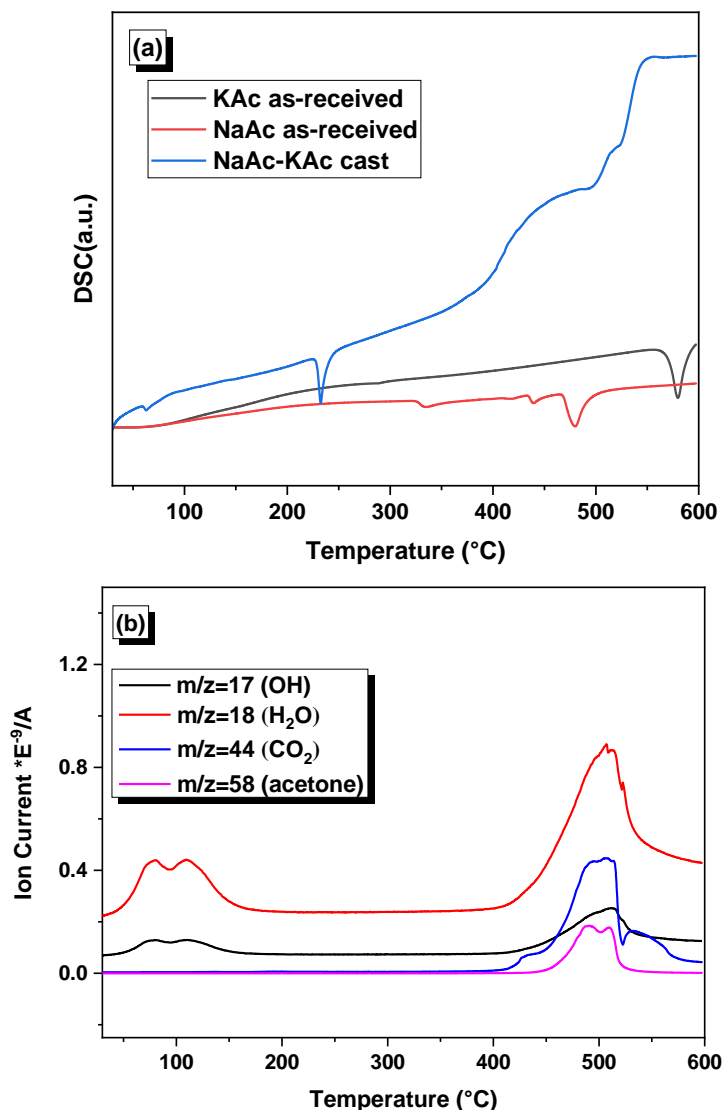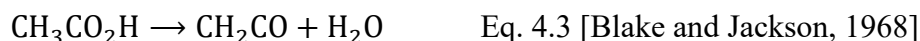
Figure 4.29 The cast NaAc-KAc with (a) DSC output signal; (b) mass spectra of 17 (OH), 18 (H_2O) and 44 (CO_2) and 58 (acetone)

The cast NaAc-NaPr exhibit strong crystalline peaks shown in Figure 4.30 (a). And for the cast NaBu-NaOc presented in Figure 4.30 (b), a new crystalline phase was identified as wegscheiderite ($Na_5(CO_3)(HCO_3)_3$) with the PDF #00-015-0653 at the 2θ position of 9.35°. No previous studies on quenched metal carboxylates were found for this phase. According to the current used ICDD database, there is no standard PDF for NaPr and NaBu precursors for providing related information.

Since the XRD pattern of as-received NaOc contains diffraction peaks with much lower intensity compared to the XRD pattern of as-received NaBu, it is difficult to compare the binary system of the cast NaBu-NaOc directly to as-received (not thermally treated) NaBu and NaOc. There is no evident trend found in the XRD patterns regarding the phases formed and the intensity of the crystalline peaks changed with the carboxylate chain length in the binary systems of NaAc-NaPr and NaBu-NaOc. Cast samples exhibit crystalline peaks in the XRD results indicate that these binary systems have relatively low glass-forming potential under these quenching conditions.
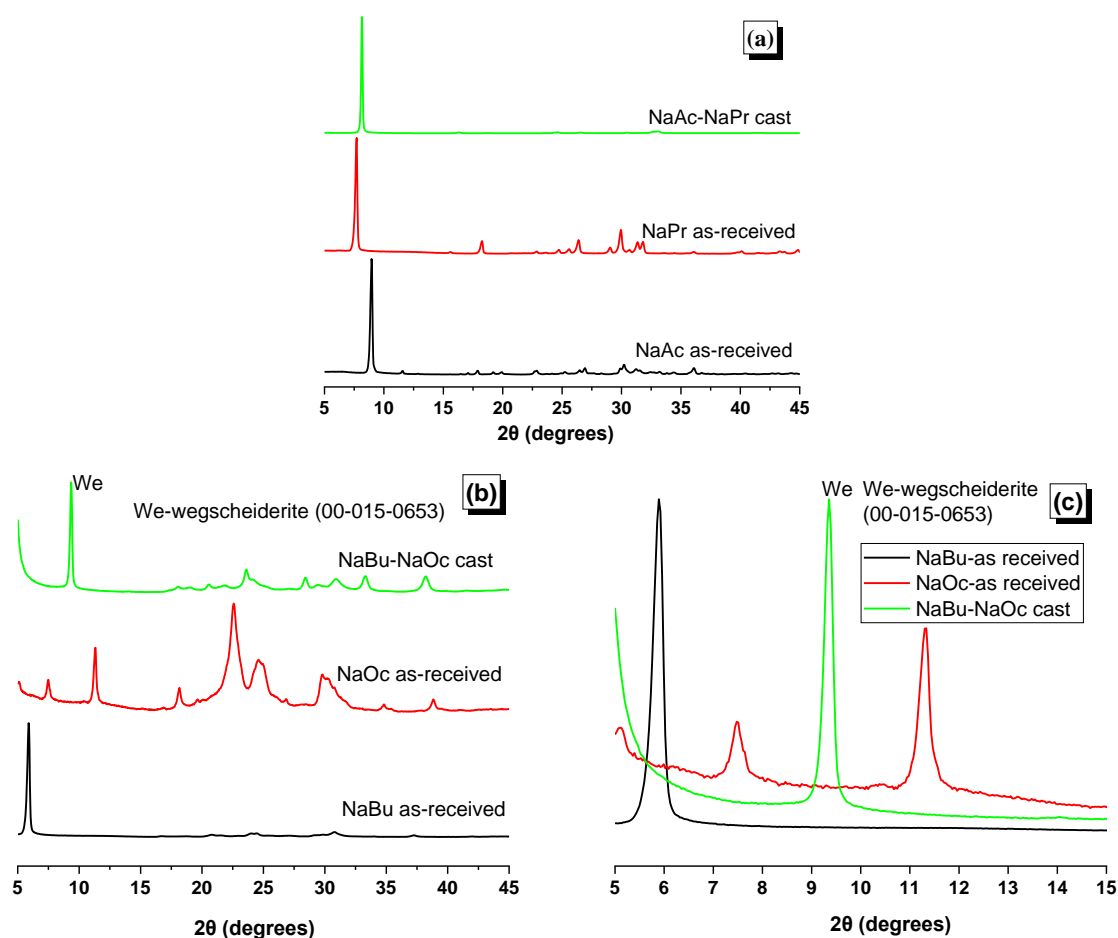
Figure 4.30 XRD patterns of the cast (a) NaAc-NaPr and (b) NaBu-NaOc at 2θ range of 5-45° and (c) NaBu-NaOc at 2θ range of 5-15°.

It can then be concluded that strong crystalline peaks present in the XRD patterns among the evaluated cast carboxylates composed of binary systems (NaAc-KAc, NaAc-NaPr and NaBu-NaOc), indicates relatively low glass-forming potential under the quenching conditions evaluated in this study.

4.3.2.3. Ternary and quaternary systems of metal carboxylates

No strongly diffracting peaks were detected in the XRD patterns for the cast MgAc-KAc-NaAc and CaAc-KAc-NaAc in Figure 4.31 (a) and (b). Instead, there is an X-ray amorphous hump occurring at the 2θ range of 5-12° in the patterns of cast MgAc-KAc-NaAc and CaAc-KAc-NaAc. The X-ray amorphous hump suggest that samples which have ternary compositions like these have no crystalline phases. However, very small crystallites could not be ruled out at the same position compared to that in the precursor. But it is uncertain that whether this hump will be in the same position/range for glasses, or phases that have potentially crystallized from the melt of cast NaAc and KAc.
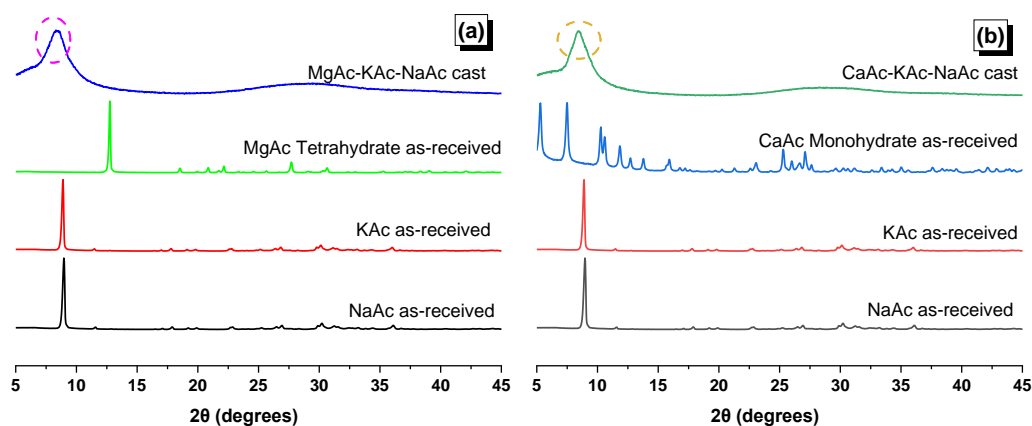
Figure 4.31 XRD patterns of the cast (a) MgAc-KAc-NaAc and (b) CaAc-KAc-NaAc (The dashed area in purple and orange color represents the X-ray amorphous hump).

Figure 4.32 shows the (a) DSC curves and (b) mass spectrometry curves for cast MgAc-KAc-NaAc. It can be seen that there is no step change referring to the glass transition T_g in the DSC curve for cast MgAc-KAc-NaAc. Similar water decomposition was observed on the temperature range around 100°C. A distinct water loss occurred at 170°C which was assigned to the semi-structural water loss, with a higher binding energy. Although there are no direct studies on the decomposition of MgAc-KAc-NaAc, the appearance of water and carbon dioxide existed on the MS curve shown in Figure 4.31 (b) suggested the potential reaction resulted by Equation 4-2 and 4-3.

In general, no order step change which would suggest glass-formation is seen from DSC curves shown in Figure 4.32 (a). In addition, an X-ray amorphous hump suggested no crystalline phases was existed in the XRD patterns in Figure 4.31 (a). Moreover, the photograph of the cast MgAc-KAc-NaAc (Fig. 4.20 (a)) shows that the cast sample is transparent even though with opaque areas. All these observations could be the evidence to support that the cast MgAc-KAc-NaAc on the quenching condition used have high potential on the glass-forming ability.
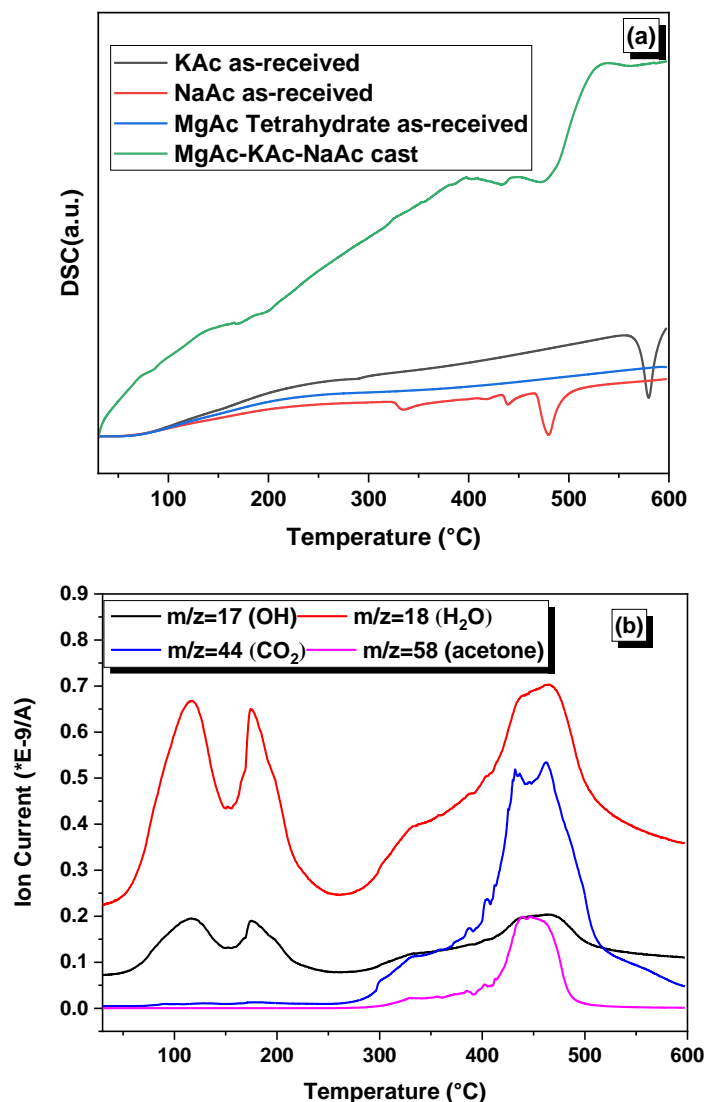
Figure 4.32 (a) DSC output signal for MgAc-KAc-NaAc; (b) mass spectra for 17 (OH), 18 (H_2O) and 44 (CO_2) and 58 (acetone)

In the DSC curve of cast CaAc-KAc-NaAc in Figure 4.33 (a), a small step change occurred at the temperature around 170°C which is attributed to semi-structural water loss, similarly to the cast MgAc-KAc-NaAc. Other step changes appeared are not known due to the lack of related melting temperature of the ternary system of CaAc-KAc-NaAc cast. Given the XRD results illustrated in Figure 4.31 (b) show an X-ray amorphous hump, it can be inferred that the ternary system composed of the cast CaAc-KAc-NaAc have potential of glass-forming ability under the adopted conditions evaluated.
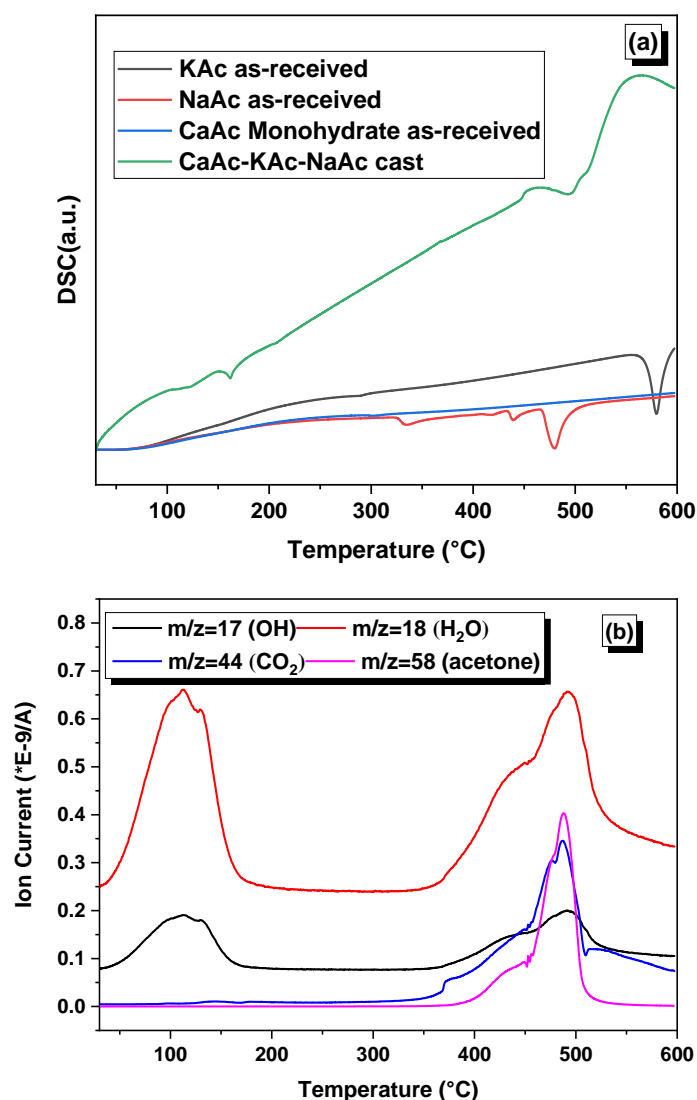
Figure 4.33 Figure for cast CaAc-KAc-NaAc, where (a) DSC output signal; (b) mass spectra of 17 (OH), 18 (H_2O) and 44 (CO_2) and 58 (acetone)

XRD results of the cast NaAc-NaPr-NaBu and NaPr-NaBu-NaOc ternary systems were depicted as Figure 4.34 (a) and (b). It is expected that as carboxylate chains get longer, the dominant 2θ peak position decreases i.e. lattice spacing increases. However, the dominant 2θ peak position in the XRD patterns of cast NaAc-NaPr-NaBu does not follow this trend seen from Figure 4.34 (a), and differences are existed compared to individual as-received salts from NaAc to NaBu. For the cast NaPr-NaBu-NaOc in Figure 4.33 (b), it is clearly to see that the low angle peaks compared to that of the two as received NaBu and NaPr. Differ from the patterns within the as-received NaOc. In summary, the ternary systems composed of cast NaAc-NaPr-NaBu and NaPr-NaBu-NaOc seems to have unlikely glass-forming potential based on the XRD patterns that show clear strong crystalline peaks of phases forming under the conditions evaluated.
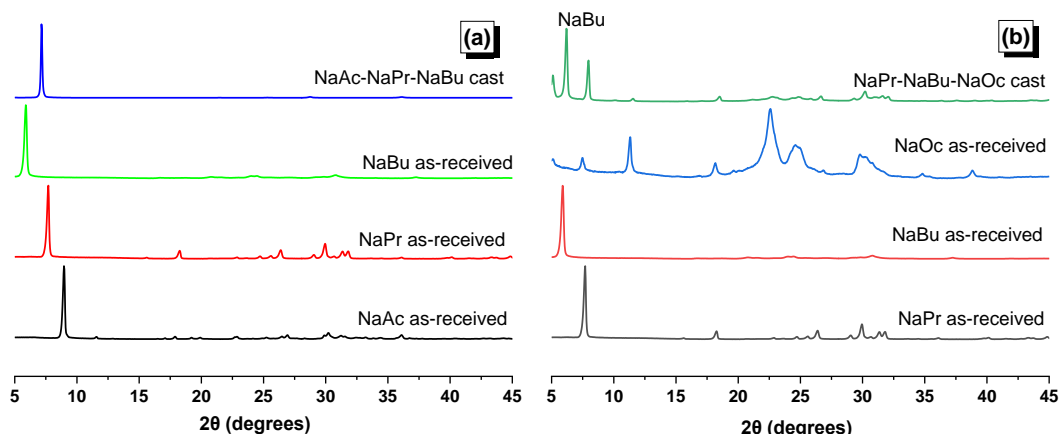
Figure 4.34 XRD patterns of NaAc-NaPr-NaBu and NaPr-NaBu-NaOc

For the cast CaAc-MgAc-KAc-NaAc sample, an X-ray amorphous hump was observed in the XRD pattern in the range of 7-10° shown in Figure 4.35. This indicates that the composition may have high potential glass-forming ability based on the quenching conditions used here. Still same questions rising regarding whether the X-ray amorphous hump could present no crystalline phases existed which indicated high potential of glass-forming ability similar to the former mentioned in the ternary system composed of the cast MgAc-KAc-NaAc and CaAc-KAc-NaAc.
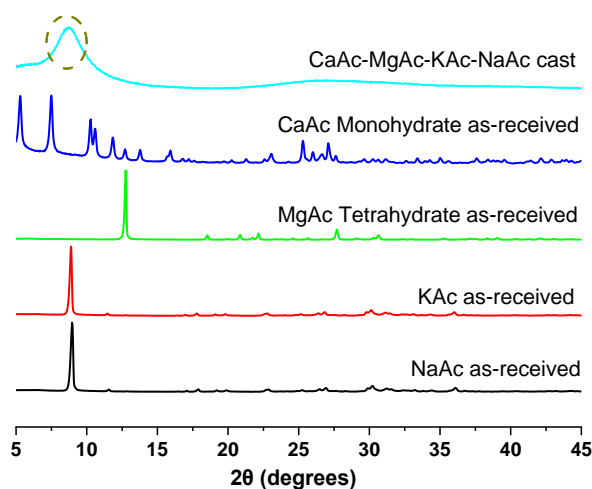
Figure 4.35 XRD patterns of CaAc-MgAc-KAc-NaAc (The dashed area represents the X-ray amorphous hump).

The ternary systems of MgAc-KAc-NaAc and CaAc -KAc-NaAc may have high glass-forming potential. The quarternary system of CaAc-MgAc-KAc-NaAc may also have high glass-forming potential under the used quenching conditions, according to the XRD analysis. However, the ternary systems composed of sodium carboxylates including the NaAc-NaPr-NaBu and NaPr-NaBu-NaOc have relatively low glass-forming potential.

4.3.3 Investigation on potential glass-forming ability

Figure 4.36 shows a summary of the criteria used in this study to identify the glass-forming potential of the evaluated systems manufactured in the used conditions. Table 4.12 summarize the glass-formation ability of all the assessed systems starting from a single component system, towards ternary and quaternary systems which have high potential of glass-forming ability and other systems on the basis of the results obtained in this study.
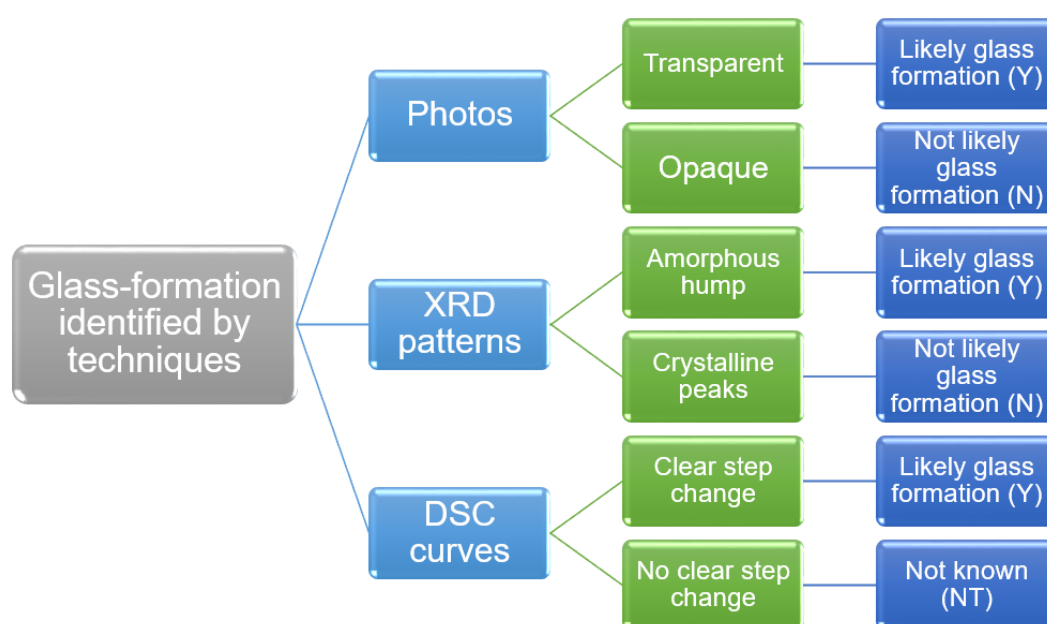
Figure 4.36 A diagram of the techniques for identifying the glass-forming ability

Table 4.2 Glass-forming ability of the evaluated systems (NC-Not applicable)

	Single system		Ternary system		Quaternary system	Other systems
Composition of the system	NaAc cast	KAc cast	MgAc-KAc-NaAc	CaAc-KAc-NaAc	CaAc-MgAc-KAc-NaAc	
Photos	N	N	Y	Y	Y	N
XRD	N	N	Y	Y	Y	N
DSC	NC	NC	NT	Y	NC	NT or NC
Potential of glass-formation ability	Unlikely	Unlikely	High	High	High	Unlikely

A schematic diagram describing the glass-forming ability of the evaluated systems after thermal treatment as a function of the composition, presented as single system, binary system, ternary system and quaternary system shown in Figure 4.36.
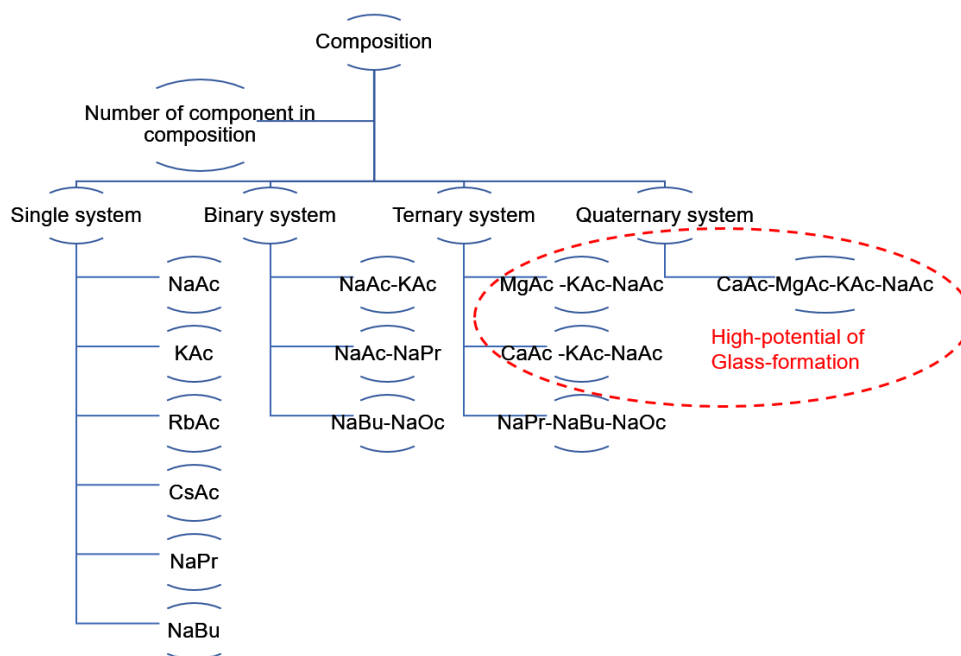
Figure 4.37 Schematic diagram of glass-forming ability for the evaluated systems after thermal treatment changed as the composition

The fundamental understanding of glass formation composition was derived from the aspect of the eutectic composition. Whereas there is a deviation between the best glass-forming composition and eutectics ($X_e \neq 0.5$ in Figure 4.38) existed. It may imply that the eutectic composition for complicated systems differ from systems with multiple components. The thermodynamics in systems including more components is more complicated compared to the single system. The similar deviation was found in more complex systems, which infer that maybe a common behavior, without considering the dynamic aspect [Wang et al., 2010, Zanotto and Mauro, 2017]. The optimal composition for glass formation is typically found in the vicinity of the eutectic composition X_e and a medium point $X_{0.5}$ suggested by other studies [Lu and Mauro, 2017, Lu and Liu, 2003]. $X_{0.5}$ means the average of the two highest solubilities (X_1, X_2), which $X_{0.5} = (X_1 + X_2)/2$ [Wang et al., 2010]. Figure 4.38 illustrated the optimal location with high potential on glass-forming ability. The area represented by shadow in Figure 4.38 presented the possible composition range favor the glass formation, seen off-eutectic [Wang et al., 2010, Lu and Liu, 2003, Lu and Mauro, 2017]. This is consistent with the findings of no glass formed in cast binary system composed of NaAc-KAc with equimolar ratio, which means $X_{1, 2} = 0.5$. It would suggest that the best glass

formation composition is near $X_{0.5}$ but not occurred at this point [Wang et al., 2010]. Confirmed by the study of [Wang et al., 2010, Halmos et al., 1970], binary system composed of NaAc-KAc (40:60) could from glasses, either. However, as different quenching process was used compared to the quenching process used in this chapter, thus it is not clear to know the exact eutectic composition for NaAc-KAc.
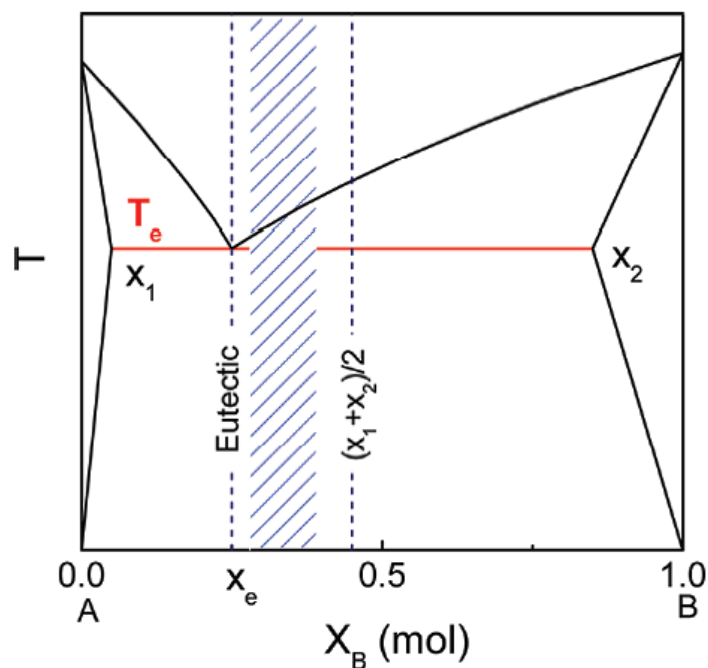
Figure 4.38 Schematic diagram of the position of best glass-forming composition. Where T_e=the temperature of the eutectic point, X_e=the composition of the mixture when temperature reached the eutectic point [Wang et al., 2010].

Though the discussions were about the basic binary system, it facilitates the understanding of glass-forming composition because it would be the primary unit for more complicated systems. According to this, it could be indicated that glass will be easier to form in the systems with more components. It is clear that the glass-forming ability was increased from binary systems to ternary systems composed of metal carboxylates, detected by the XRD and DSC results illustrated in Figure 4.27-Figure 4.33. However, this trend was not applied for the evaluated systems made up of sodium carboxylates, where the glass-formation is unlikely in both binary systems and ternary systems containing sodium carboxylates. Due to the limited knowledge on the role of the composition influence glass-forming ability, it is difficult to tell confidently why and how metal acetates and sodium carboxylates plays a different role on affecting the glass-forming ability as no existing literature focus on this.

4.3.4 pH measurements

The pH measurements were conducted using the method previously described in Chapter 3 and the molality of the evaluated systems was listed in Table 4.13. The details of calculation were listed in Appendix A.

Table 4.3 The molality of the evaluated systems for pH measurements.

Composition of solids	Mass of solid activator (g)	Mass of distilled water (g)	Molality (moles/kg)
NaOH	5.16	31.55	4.09
KOH	7.22	32.17	4.01
NaAc cast	10.58	33.17	3.89
KAc cast	8.34	32.50	2.62
NaAc-KAc-cast	11.59	33.48	1.92
MgAc-NaAc-KAc-cast	25.64	37.69	2.37
CaAc-NaAc-KAc-cast	17.39	35.22	2.42
CaAc-MgAc-NaAc-KAc-cast	23.18	36.95	1.63
NaPr cast	12.39	33.72	3.01
NaBu cast	14.19	34.26	2.56
NaAc-NaPr-cast	11.49	33.45	1.64
NaBu-NaOc-cast	17.82	35.35	1.38
NaAc-NaPr-NaBu-cast	12.39	33.72	1.00
NaPr-NaBu-NaOc-cast	16.01	34.80	0.95

The references were NaOH and KOH solutions for the NaAc and KAc based activators respectively, and all the solids were fully dissolved in 30 minutes. The results of pH measurement up to 30 minutes for single component systems are shown in Figure 4.39 and 4.40, and for multiple component systems in Figure 4.42 and 4.43. The pH value of all the solutions composed of various component of metal carboxylates become stable during the 30-minute period.

The pH values of alkaline solution formed by single acetate systems are shown in Figure 4.39, the solution made with cast KAc has the highest pH value of 13.0 up to 30 minutes, except for the NaOH and KOH solution. The pH value of the alkaline solution formed by as received KAc was 12.71 up to 30 minutes, lower than that of the KAc-cast solution. The pH value of cast NaAc solution was only 11.8, while as received NaAc solution had a pH value of 10.8. It could be clearly seen that the solution made of a single acetate system after casting had a higher pH than the as-received form. Another observation was that the solutions containing K^+ had a higher pH value than those with Na^+, which applied in all solutions composed of hydroxides (KOH/NaOH), cast acetates (KAc-cast/NaAc-cast) and as-received acetates (KAc-as received/NaAc-

as received).

Solutions formed by NaAc and KAc, which are both acetate salts, possess a higher pH value compared to the thermal-treated NaAc and KAc. This characteristic makes them particularly intriguing for potential applications in alkali-activation processes. The higher pH of these acetate salts provides a distinct advantage in alkaline activation reactions by contributing hydroxide ions to the solution, effectively elevating the alkalinity of the medium. This can promote silicate or aluminosilicate precursors dissolved, which is a fundamental step in many alkali-activation applications. As a result, sodium acetate and potassium acetate hold promise for being versatile alkali activators in the synthesis of materials with tailored properties, whether in the realm of cementitious systems, alkali-activated cements technology, or other innovative materials science applications.
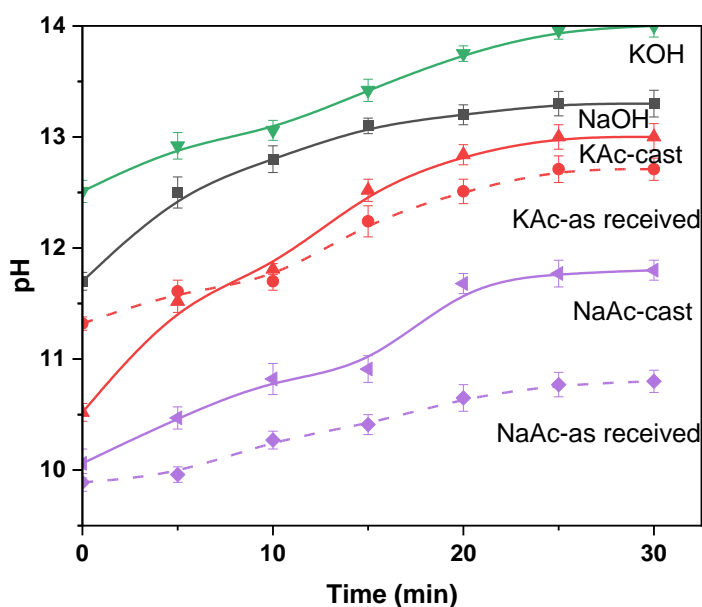
Figure 4.39 pH value of different solutions changed with time up to 30 minutes

Figure 4.40 illustrated the pH values up to 30 minutes varied with different sodium carboxylates. NaOc was not included in Figure 4.39 as NaOc could not be melted at the conditions used. During the first 30 minutes of dissolution, lower pH values were recorded for the solutions made of sodium carboxylates containing the cast and as-received ones compared to NaOH solution, which had a pH of 13.3. It was noticed that the pH value decreased in NaAc-cast and NaBu-cast, from 11.8 to 10.77, respectively. A similar trend was observed in the solutions produced with the received sodium carboxylates, where the pH value of the solution formed by NaAc-as received was 10.8 while the solution formed by NaBu-as received has a pH value of 9.95. Demonstrating that the carboxylate chain length can affect the pH values during the first 30 minutes of the produced solution as shown in Figure 4.41. Therefore, varying the carboxylate chain

length has a role on the solubility of the solid sodium carboxylates.
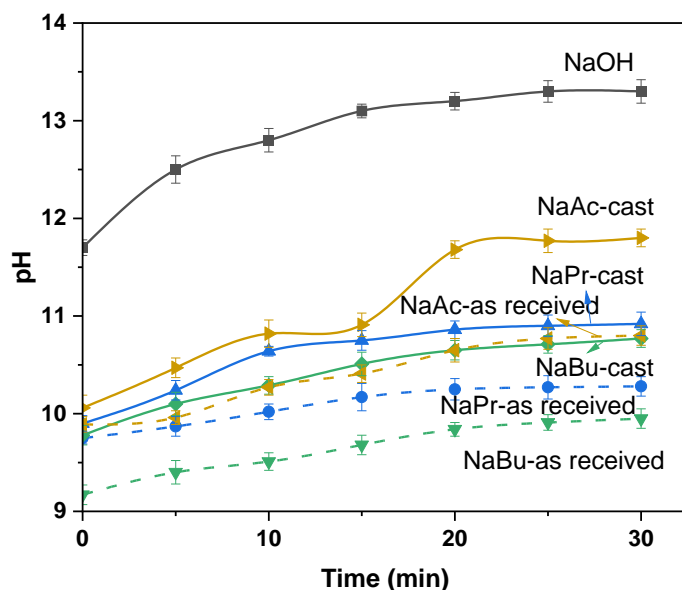
Figure 4.40 pH value of the solution by the formation of single sodium carboxylates
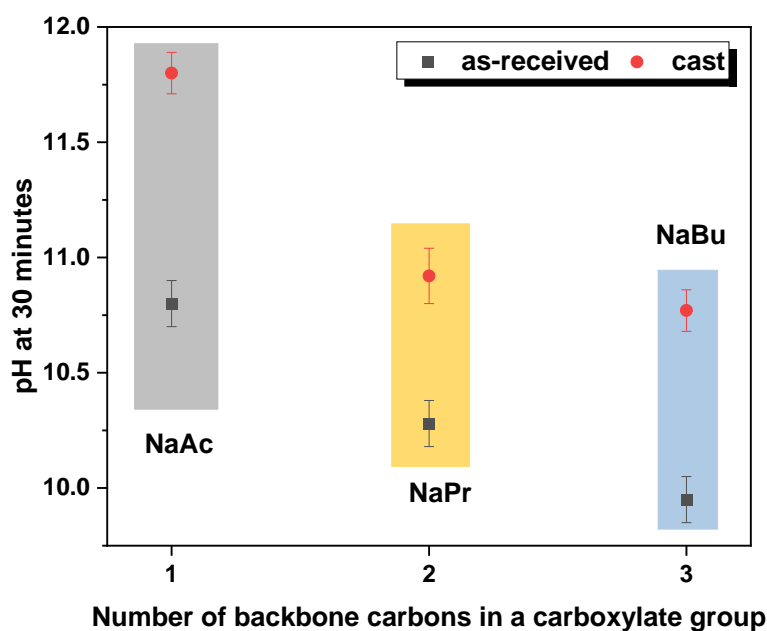
Figure 4.41 pH at 30 minutes as a function of the number of backbone carbons in a carboxylate group

The generally high level of solubility of NaAc [Schmitz, 2002] in distilled water is related to the dissociation of sodium carboxylates. For the dissociation of sodium carboxylates, NaAc is described below for example.

$$CH_3COONa \rightleftharpoons Na^+ + CH_3COO^- \qquad \text{Equation. 4-5}$$

$$CH_3COO^- + H_2O \rightleftharpoons CH_3COOH + OH^- \qquad \text{Equation 4-6}$$
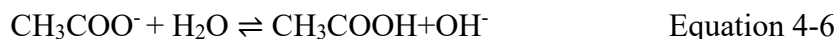
The pH of the formed solution from metal carboxylates is controlled by the degree of the dissociation reaction (Equation. 4-4). It is unclear of why the solubility of metal carboxylates before and after thermal treatment is different because there is quite limited literature on the dissociation of metal carboxylates. The pH value of sodium acetate solutions was reported by [Schmitz, 2002]. However, sodium acetate could be used as buffer solution [Schmitz, 2002]. In general, it is difficult to tell confidently why the solubility behavior is different after thermal treatment of metal carboxylates.

The pH values of the alkaline solution formed by the multi-component cast acetates were shown in Figure 4.42. The number of the components ranged from two to four, which not only included K^+ and Na^+ (Group I) but also Mg^{2+} and Ca^{2+} (Group II). The alkaline solution containing the CaAc-KAc-NaAc-cast developed a pH value of 10.9, 0.2 higher than that of the solution containing CaAc-MgAc-KAc-NaAc-cast. The pH value of the NaAc-KAc-cast solution was 10.5, slightly higher than the MgAc-KAc-NaAc-cast solution (10.4). There is no obvious trend in the pH values formed by the cast acetates owing various number of acetates in the multiple system.

Based on the results reported in previous sections, ternary systems including CaAc-KAc-NaAc-cast and MgAc-KAc-NaAc-cast, as well as quaternary system CaAc-MgAc-KAc-NaAc-cast have high potential of glass-formation. However, the glass formation potential it is not an indicative of high pH values development. In addition, the rate of released alkalinity (the gradient of these curves illustrated in Figure 4.43) have no clear difference in trend compared to non-glassy systems which was unexpected. This was beyond expectation that the rate of dissolution could be control by tailoring the composition of metal carboxylates, and it could be reduced in systems reduced potential of glass-formation.
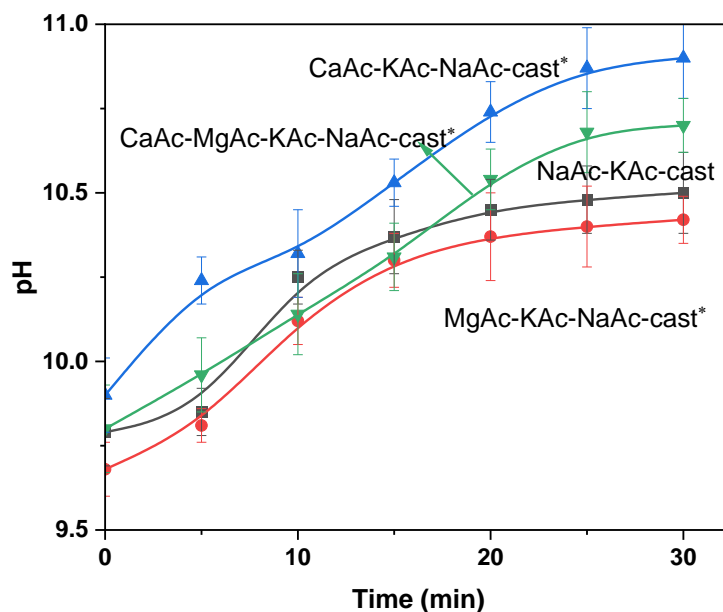
Figure 4.42 pH values of alkaline solution composed of multi-cast metal acetates (* symbol after the labels of the systems represents acetates has high potential of glass-formation)

The pH values of alkaline solution composed of binary and ternary-cast sodium carboxylates were described in Figure 4.43. In the alkaline solution composed of the binary and ternary system, NaBu-NaOc-cast solution has a higher pH value of 10.98. The pH value of NaPr-NaBu-NaOc-cast solution followed, which was 10.75. The pH value of the solution made of NaAc-NaPr-cast and NaAc-NaPr-NaBu-cast were much lower, shown 10.69 and 10.32 respectively. It is evident that the pH value decreased in solutions with NaAc-NaPr-cast or NaAc-NaPr-NaBu-cast. This might be a consequence of introducing NaBu which as long carboxylate chain length and potential lower solubility. Similar results were also observed when comparing NaBu-NaOc-cast solution and NaPr-NaBu-NaOc-cast solution.

Additionally, the pH value of NaBu-NaOc-cast solution is higher than that of NaAc-NaPr-cast solution in binary systems. A similar trend was observed in the solution produced with NaPr-NaBu-NaOc-cast, which has a higher pH value compared to that of NaAc-NaPr-NaBu-cast solution. Since the pH value of solution produced with NaBu-NaOc-cast is higher than that of solution formed of NaPr-NaBu-NaOc-cast, it is clear that the length chain of the acetate used has an influence in the dissolution kinetics of the produced combined material.
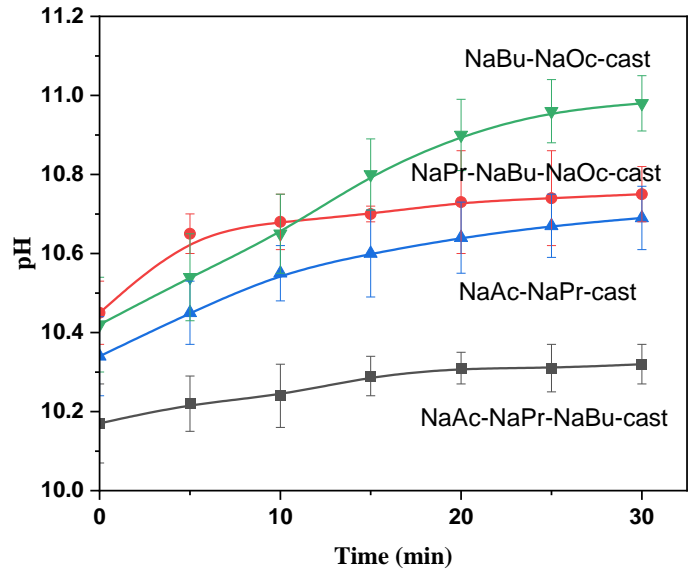
Figure 4.43 pH values of alkaline solution composed of binary and ternary-cast sodium carboxylates

In general, the alkaline solutions produced with the acetates produced in this study (Figure 4.39 to Figure 4.43) can be classified as alkaline, solutions produced with KAc and NaAc present higher pH value than all the other systems evaluated in this study (Figure 4.44). The results indicate that glass-formability is not directly connected to high pH development in the system, consistent with a reduced availability of alkalis in ternary and quaternary systems composed of different metal acetates. Glass formability is more likely linked to rate of dissolution of the thermal treated solid metal acetates, which could potentially provide a novel approach of modifying composition of the overall cementitious system, when using such glasses as potential alkali-activators.
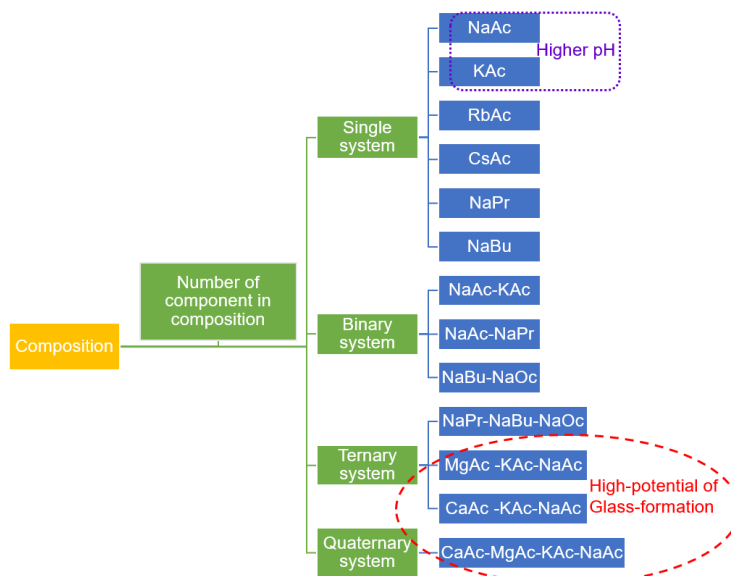
Figure 4.44 Schematic diagram for describing the evaluated systems on pH values and glass-

formation ability. Higher pH means pH >11.5.

The criteria for being activators entail two key requirements. Firstly, the substance must be capable of providing metal cations to balance charges within the system. Secondly, there is a need for sufficient alkalinity to facilitate the dissolution of precursors [Luukkonen et al., 2018]. All the evaluated metal carboxylates after thermal treatment fulfill the first requirement. While for the second requirement, it depends on the activator type used which results different nature of the anion or anion group. For example in NaOH-activated GGBFS, the initial pH of NaOH solution need to exceed 11.5 for effectively activating GGBFS [Song et al., 2000]. Only solution produced with NaAc or KAc after thermal treatment achieved pH values higher than 11.5, and thus NaAc and KAc after thermal treatment are being selected as alkaline activators for producing AAS cements.

GGBFS is regarded as one of the most preferred precursors for producing AACs, and its chemical activation process is thoroughly comprehended. Given that metal carboxylates, after undergoing thermal treatment, hold promise as alternative alkaline activators, the subsequent chapters will delve into their feasibility in AAS cements. It is worth noting that unfortunately none of the evaluated systems exhibiting high glass-forming potential, at the adopted melting and quenching conditions evaluated in this study, developed a sufficiently high pH to promote sufficient slag dissolution. Therefore, sodium acetate and potassium acetate systems after thermal treatment will not be studied any further.

4.4 Conclusions

In this chapter, the potential of metal carboxylates to form glassy activators is being investigated by series of single, binary, ternary and quaternary systems, to identify a treatment that enable to control their dissolution rate. Charring behavior was identified during the thermal treatment process of NaOc, CaAc and MgAc, under the evaluated testing conditions. For single component systems of thermal treated NaAc, KAc, NaPr and NaBu, relatively low glass-forming ability was identified. In binary system composed of the thermal treated NaAc-KAc, NaAc-NaPr and NaBu-NaOc, strong crystalline peaks were identified in their XRD patterns indicated relatively low glass-forming ability. Ternary systems composed of thermally treated MgAc-KAc-NaAc, CaAc-KAc-NaAc and quaternary system composed of thermally treated CaAc-MgAc-KAc-NaAc have high glass-forming potential based on the XRD results. However, the ternary systems composed of thermal treated NaAc-NaPr-NaBu and NaPr-NaBu-NaOc have relatively low glass-forming ability.

The pH measurements were undertaken to assess solubility behavior and the potential of using the cast acetates as alternative activators for producing AACs. The pH of the solution produced with thermally treated KAc reached a value of 13, being the highest among all alkaline solutions produced. Solutions composed of single thermally treated sodium carboxylates; the pH value decreased as the carboxylate chain length increased. No evident trend was identified in solutions produced with binary, ternary and quaternary acetate systems, including thermal treated metal acetates and sodium carboxylates. The lower pH value was recorded in the solutions produced with metal carboxylates after thermal treatment that showed the highest potential of glass-forming.

Whilst the ternary and quaternary compositions showed the highest glass-forming potential, only the NaAc and KAc single component after thermal treatment yielded high enough pH solutions, and therefore NaAc and KAc after thermal treatment that will be further investigated as alternative activators in the production of AACs.

Chapter 5 – Alkali metal acetate-activated ground granulated blast furnace slag cements

5.1 Introduction

The use of conventional activators including sodium hydroxide (NaOH), and sodium silicates (Na$_2$SiO$_3$) come with certain limitations. Their high alkalinity can be corrosive to equipment and limit the use of certain additives [Amer et al., 2021a, Wang et al., 1995]. To address these issues, researchers have explored alternative activators. Existing alternative activators in alkali-activated materials present both advantages and disadvantages [Gu et al., 2014]. Common alternatives such as sodium carbonate sodium carbonate (Na$_2$CO$_3$) offer [Kovtun et al., 2015, Ellis, 2016] and sodium sulfate (Na$_2$SO$_4$) contribute to early strength development and improved workability but may lead to challenges such as delayed setting times and increased drying shrinkage, while its effectiveness can vary depending on slag composition [Adesina and Rodrigue Kaze, 2021]. Potassium-based activators can mitigate these issues to some extent but may pose challenges related to cost and potential efflorescence [Richardson and Li, 2018]. Amidst these considerations, metal acetates emerge as promising candidates for alternative activation. Metal acetates, including sodium acetate, potassium acetate exhibit the potential to produce AAS ccement associated with conventional activators. Their unique properties offer advantages such as controlled setting times and moderated durability. As the exploration of metal acetates as alternative activators gains interest, the motivation lies in harnessing their benefits to provide a more versatile and sustainable solution for alkali-activated materials, thereby contributing to the evolution of advanced and high-performance concrete technologies.

This chapter systematically investigates the feasibility of employing sodium acetate (NaAc) or potassium acetate (KAc) solutions as alkaline activators to produce AAS cement. Throughout the chapter, the resulting binders are referred to as alkali acetate-activated slag cements. Conventional sodium hydroxide (NaOH) and potassium hydroxide (KOH)-activated slag cements are also prepared as reference systems to determine the efficacy of the metal alkaline solutions as alternative activators. Isothermal calorimetry is employed to elucidate the reaction kinetics of the produced AAS cements. The chapter further assesses the type and amount of reaction products evolving in these innovative cements over curing time, utilizing various analytical characterization techniques. Compressive strength, porosity, and water contact angle

(wettability) of the produced cements are determined. The comprehensive results presented in this chapter offer a thorough understanding of the microstructure of the novel alkali-acetate activated slag cements and the properties they can attain.

5.2 Sample preparation and mix design of the evaluated cements

A commercial slag 1 was used in this study, supplied by ECOCEM®. The detailed characterization of slag 1 is reported in Chapter 3, Section 3.1.1. In Table 5.1, the mix design of the evaluated AAS cements is reported. Concluded from Chapter 4, NaAc and KAc were used as alkaline activators to produce AAS cement. The effectiveness of NaAc and KAc as activators will be compared to conventional alkaline activators, which are NaOH and KOH as reference systems. The concentration of activation at 4% Na_2O dose was stable, with respect to the mass of slag. The details of the calculation of using acetates as activators to produce AAS cements are presented in Appendix A.

Table 5.1 Mix proportions of produced alkali-acetate activated slag, and reference cement samples

Mix ID	Activator type	GGBFS (g)	Activator (g)	water (g)	water/binder ratio	pH activating solution
NN	NaOH	100	5.16	31.55	0.3	13.3
NC	NaAc	100	10.58	33.17	0.3	11.8
KH	KOH	100	7.22	32.17	0.3	14.0
KC	KAc	100	8.34	32.50	0.3	13.2

5.3 Reaction kinetics and workability

5.3.1 Workability-Mini-slump test

The AAS activated with acetates demonstrated marginally increased fluidity compared to AAS activated with hydroxides across various w/b ratios. Notably, at a w/b ratio of 0.3, the hydroxide-activated AAS pastes exhibited no fluidity, while measurable fluidity was observed in the acetate-activated AAS pastes. Within both hydroxide- and acetate-activated AAS systems, the sodium-based activators consistently resulted in higher fluidity when compared to their potassium-based counterparts. This observation aligns with findings from prior studies that reported a similar trend in the relative fluidity of potassium hydroxide (KOH)-activated AAS and sodium hydroxide (NaOH)-activated AAS systems [Yousefi Oderji et al., 2019, Kong and Kurumisawa, 2023].
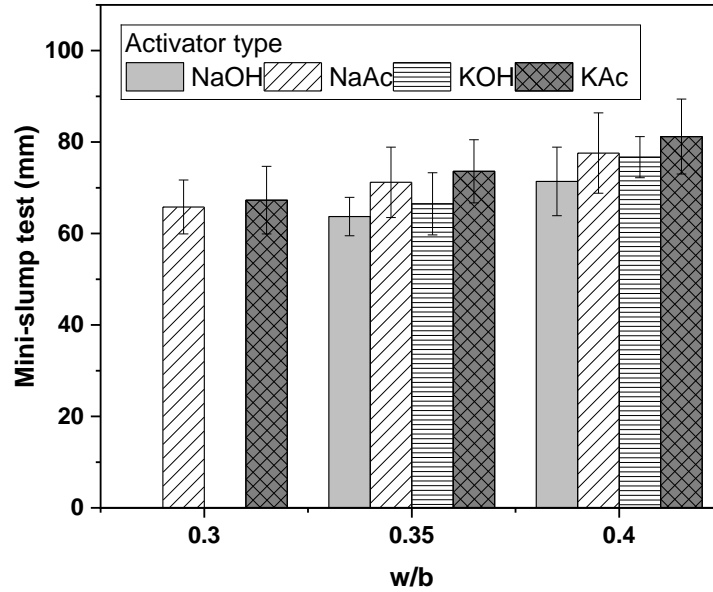
Figure 5.1 Effect of w/b ratio on mini-slump results of AAS produced with different activators. Results for NaOH/KOH-AAS with a w/b=0.3 is not reported as the pastes were not fluid

5.3.2 Setting time

Setting time was tested through the Vicat method depicted in Table 5.2. The initial setting time for NaOH-AAS is 30 minutes, consistent with previous studies analyzing samples produced with a similar activator [Jiao et al., 2018b, Duran Atiş et al., 2009], while the initial setting time for NaAc-AAS is extended to 3 hours. In contrast, KOH-AAS exhibits a slightly faster initial setting time than NaOH-AAS, reduced to 14 minutes. KAc-AAS reacts somewhat more swiftly than NaAc-AAS, with an initial setting time of 1.5 hours. It is worth noting that hydroxide-activated slag cement generally undergoes rapid setting and hardening within a few hours. Table 5.2 clearly indicates that NaOH-AAS requires 3 hours for final setting, while KOH-AAS takes 4 hours. In contrast, alkali metal acetate-AAS exhibit longer setting times. NaAc-AAS necessitates a total of 230 hours for final setting, whereas KAc-AAS requires 129 hours. The setting time results for both hydroxide-activated AAS and acetate-activated AAS align with the heat release rate data from calorimetry results, as depicted in Figure 5.4 (A)-(D). The reaction process in acetate-activated AAS is considerably slower than in hydroxide-activated AAS, owing to their lower alkalinity. This suggests that the reaction mechanism for acetates-activated AAS may differ from that of hydroxides-activated AAS.

Table 5.2 Setting time of AAS cements produced by various activators

Mix ID	Activator type	Initial setting time (hours)	Final setting time (hours)
NN	NaOH	0.5	3
NC	NaAc	3.0	230
KH	KOH	0.2	4.5
KC	KAc	1.5	129

5.3.3 Reaction kinetics

The cumulative heat release curves for the four cementitious systems evaluated are shown in Figure 5.2 (A)-(B). For NaOH/KOH-activated AAS (shown in Figure 5.2 (A) and (B), the used activator led to higher cumulative heat release during the first 250 hours of reaction, suggesting a greater degree of reaction compared to acetate-activated AAS. The initial peak in Figure 5.2 (A) and (B) occurred rapidly after mixing is related to the wetting of GGBFS. This also applied in both sodium/potassium acetate-AAS, demonstrating that the alkalinity reached when using acetate activators is sufficient in both cases to promote dissolution of GGBFS to trigger polycondensation and precipitation of reaction products. In the acetate-activated AAS, a period of limited heat release is observed, consistent with what is understood for conventional Portland cements as the induction period [Singh, 2023]. A more comprehensive analysis of this will follow in the upcoming sections.

In the sodium/potassium hydroxide AAS cement, only one exothermic peak is identifiable, and associated with the acceleration period, due to the reaction products formed and precipitated [Sun and Vollpracht, 2018b, Liu et al., 2019]. It can be seen in the results that when using NaOH, the accelerated period onset occurs after 1 hour, showing with a maximum at 3 hours (Figure 5.2 (A)). The values of the final setting time of the above AAS listed in Table 5.2. Subsequently, an asymmetric deceleration phase manifested, characterized by a substantial volume of heat flow observed until the time reached 24 hours. This was succeeded by a protracted period of low heat release extending beyond 300 hours after the initiation of mixing. It is known that when using NaOH as the alkaline activator, solution exhibit a remarkably higher pH value and C-(A)-S-H type gel faster forms. The initial pre-induction peak and the subsequent acceleration peak overlapped in the NaOH-activated alkali-activated slag (NaOH-AAS) system, resulting in an expedited condensation rate for silicon (Si) and aluminum (Al) species [Sun and Vollpracht, 2018b, Deir et al., 2014]. Similarly in KOH-AAS, the acceleration period in Figure 5.2 (B) showed an onset after 1 hour and the maximum values occurred at 4 hours.

It is believed that similar to what has been speculated for OPC, during the alkali-

activation reaction, GGBFS particles act as nucleation points, where both dissolution and precipitation owing by the reaction products occurs during the commencing hours [Gebregziabiher et al., 2016, Gebregziabiher et al., 2015a, Gebregziabiher et al., 2015b]. The activation process is affected by the alkalinity owing by the activator, because the OH^- promotes more GGBFS dissolved, accelerates the dissolution of Si and Al species [Bernal et al., 2014a, Provis and Van Deventer, 2013, Provis, 2018]. Therefore, it could be demonstrated that the activators exhibit high pH enable a higher dissolution of GGBFS. Introducing NaOH/KOH boosts the OH^- concentration, thus a quick reaction process, which needs less than 1 hour to initial set reported in Table 5.2. Other studies using similar OH^- containing activators where setting time in the range of 28–59 min have been reported agreed with this finding [Duran Atiş et al., 2009, Jiao et al., 2018b].

In NaAc-AAS (Figure 5.2(A)), a pre-induction peak was first observed for the first hours of reaction, then an induction (dormant) period occurred after nearly 50 hours. The maximum heat released in the acceleration period was observed after 228 hrs. In KAc-AAS (Figure 5.2(B)), similar trend occurred as the induction period of about 40 hours, and the time of the maximum heat released was a bit earlier after 128 hours in the acceleration period compared to that of sodium-acetate AAS cement. The possible reasons for a long induction period existed may according to: the reaction products precipitates on the surface of unreacted GGBFS, thus inhibiting the reaction [Kang and Ye, 2022, Bernal et al., 2011, Tänzer et al., 2015] or the ion concentration is too low thus it takes longer time to reach the critical concentration of ionic species in the system to establish the aim of forming reaction products [Zuo et al., 2018]. The induction period in acetate-activated AAS systems is appeared after 40-50 hours, and the time when the acceleration stage began aligns with the final setting started of AAS cements produced by acetates shown in Table 5.2. Compared with hydroxide-activated AAS cement, the acetate-activated AAS cement have a long induction period of nearly 50 hours, suggesting that a lower pH of the activator may delayed the reaction kinetics.
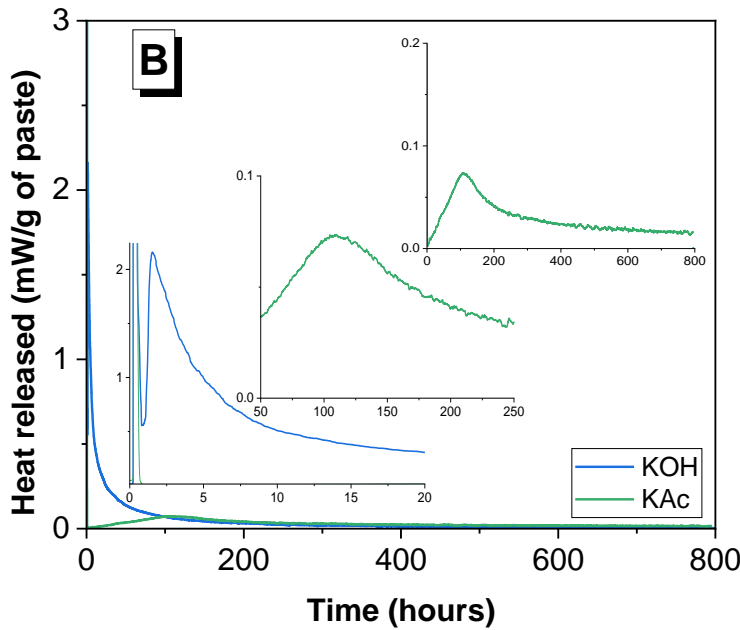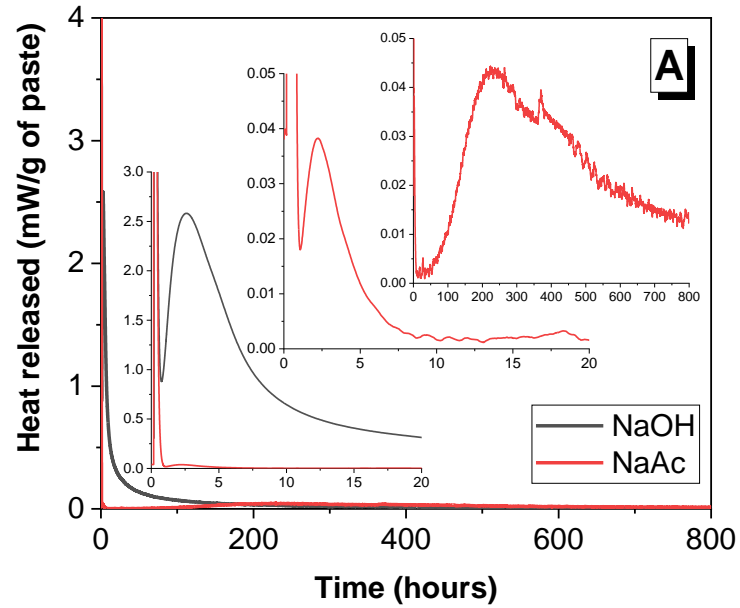
Figure 5.2 Heat release rate of AAS produced with different activator including (A) NaOH/NaAc-AAS and (B) KOH/ KAc-AAS (relative to mass of mixed paste). Time is after mixing time.

Figure 5.3 depicts the released heat during the reaction of hydroxide/acetate-activated AAS after 28 days. The induction period is appeared between the first and second peak. The final gradually stable cumulative heat curve is due to the long dormancy period of the AAS, which leads to an obvious plateau in the cumulative heat curve. However, the cumulative heat release curve depicted a lower value as the activator type was changed from hydroxide to acetate, like the starting-time data belong to the acceleration (Figure 5.2 (A)-(B)) were not sensitive to activator type.

The cumulative heat values recorded for these samples were significantly smaller than those recorded for the NaOH/KOH-AAS cement. These results indicate that the mechanism of reaction in these two systems are completely different. Longer induction period coupled with a slower acceleration period appeared in acetate-activated AAS can be partially related to the lower pH owing by activating solution. Thus, the dissolution of GGBFS activated by acetates were slower, and a reduction on compressive strength of the produced AAS cement were observed.
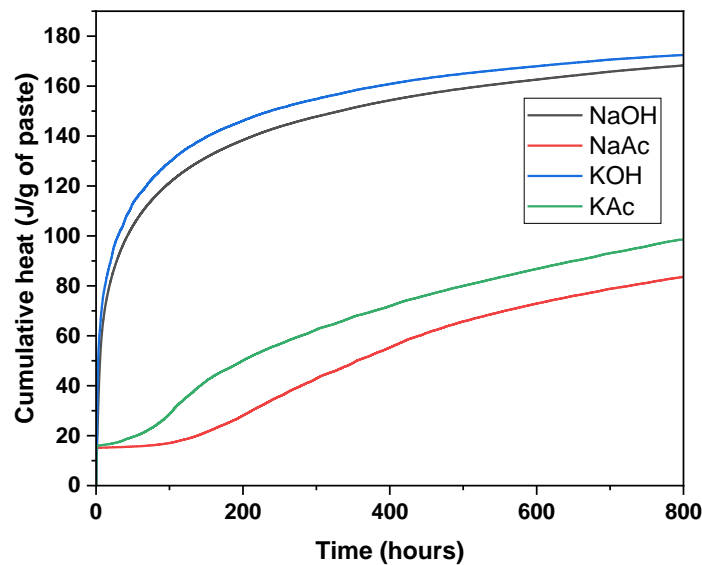
Figure 5.3 Cumulative heat among reaction of AAS produced with different activator.

5.4 Phase assemblage evolution

5.4.1 Mineralogical analysis

The X-ray patterns of the AAS produced with various activators, and cured at different ages until 180 days are shown in Figure 5.4 (a)-(d). Two crystalline reaction products are identified: A calcium silicate hydrate (powder diffraction file (PDF) #029-0329) (C-(A)-S-H type gel) and hydrotalcite (PDF # 01-089-0460) in Figure 5.4 (a) at all curing ages, consistent with documents reported for NaOH-AAS systems [Bernal et al., 2014a]. For KOH-AAS systems as seen from Figure 5.4 (c), the main crystalline reaction products are also a C-(A)-S-H type gel and hydrotalcite at all curing ages, similarly to NaOH-AAS systems. As curing time become longer (Figure 5.4 (a) and (c)), the peak related to the C-(A)-S-H type gels (29.5° 2θ) is sharper and more intense consistent with the activation continued.

In the NaAc-AAS and KAc-AAS systems recorded in Figure 5.4 (b) and (d), the presence of hydrotalcite traces and the calcium carbonate polymorph vaterite (PDF # 01-074-1867) after 7 days of curing was identified. Notably, in the potassium acetate-activated AAS cement cured for 7 days (Figure 5.4 (d)) only shows formation of vaterite. The occurrence of vaterite peaks can be attributed to the weathering of unreacted slag [Ravikumar and Neithalath, 2012], and these peaks evolve with curing time, but do not reappear at advanced curing ages. This observation is consistent with the outcomes obtained from isothermal calorimetry analyses of acetate-activated AAS systems. These systems demonstrate longer induction periods, indicative of a more slower reaction process. Furthermore, in both sodium and potassium acetate-activated AAS systems, the main crystalline reaction product observed is a C-(A)-S-H type gel, as depicted in Figure 5.4 (b) and Figure 5.4 (d) for the KAc-activated system after both 7 and 28 days of curing. No notable distinctions were highlighted between hydroxide-activated AAS systems and acetate-activated AAS systems after 180 days of curing. A noteworthy observation is that a higher amount of hydrotalcite was evident in KAc-AAS compared to NaAc-AAS, as indicated by the XRD patterns displayed in Figure 5.5 (b) and Figure 5.5 (d), even up to the 180-day curing time.
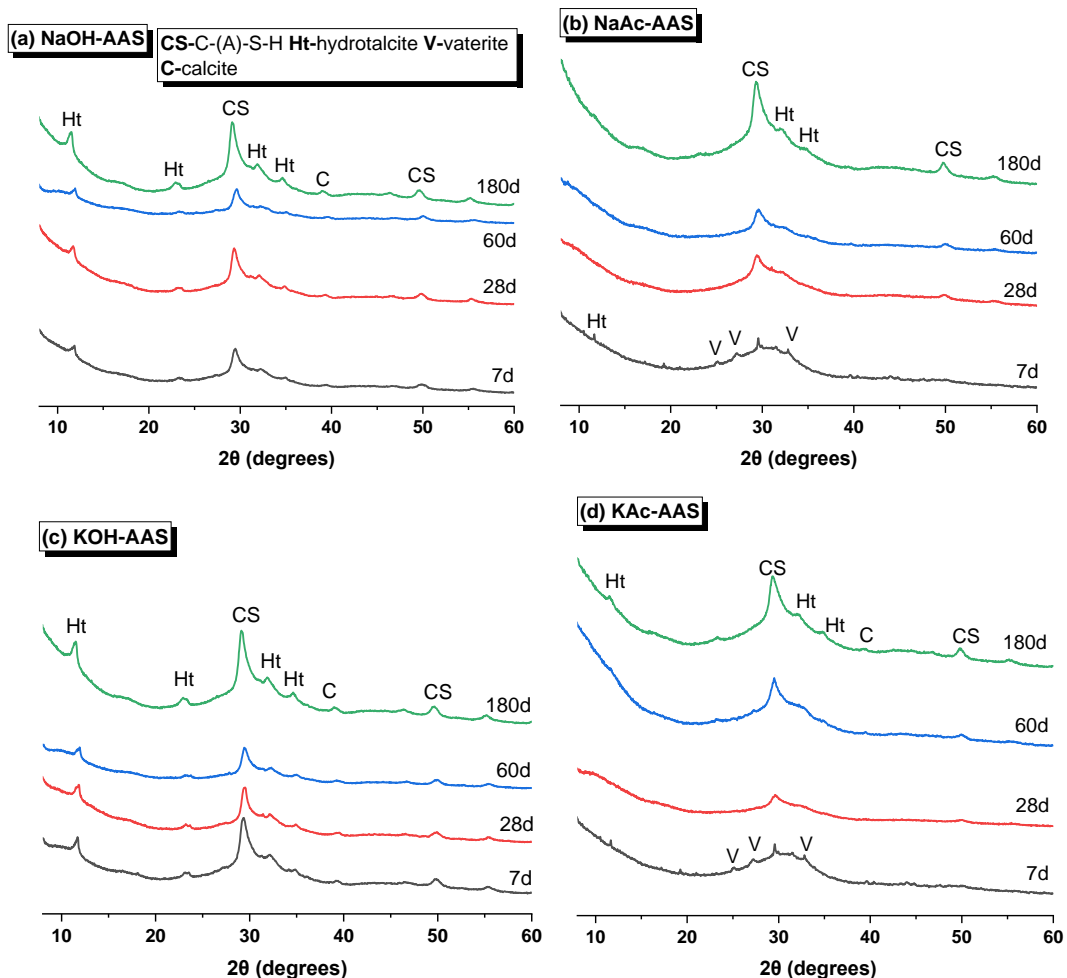
Figure 5.4 XRD pattern of AAS produced with different activator of (a) NaOH, (b) NaAc, (c) KOH, and (d) KAc curing at various days (relative to mass of mixed paste). CS-C-(A)-S-H, Ht-hydrotalcite, V-vaterite, C-calcite.

5.4.2 Spectroscopic analysis of reaction products forming

In Figure 5.5 (a)-(d), infrared spectra are illustrated for AAS cements activated with both hydroxides and acetates, providing a comprehensive depiction of the material's evolution over distinct curing periods extending up to 180 days. The bonds situated among the wavenumber range of 1661-1655 cm^{-1} are consistently observed in all the examined AAS cements, and are due to the symmetric bending vibrations of v_2[OH], which result from the reaction products formed [Gómez-Casero et al., 2022]. This observation aligns with the XRD findings depicted in Figure 5.5, providing clear confirmation of hydrotalcite formation. In hydroxides-activated AAS, bonds in the range of 960-971 cm^{-1}, and in acetates-activated AAS, in the range of 951-969 cm^{-1}, are attributed to v_3(Si–O) asymmetric stretching of C-(A)-S-H type gels [Cao et al., 2020a]. This observation is in coherence with the Si-O-T stretch bands typically reported at the wavenumber range of 958-1050 cm^{-1} in hydroxides-activated AAS [Cao et al., 2020a, Gómez-Casero et al., 2022], which are associated with C-(A)-S–H type gels. This bond was observed at 951 cm^{-1} in NaAc-AAS and 958 cm^{-1} in KAc-AAS after cured 7 days, respectively. The Si-O-T bond with asymmetric stretched in C-(A)-S–H type gels corresponds to a higher polymerization degree occurred in represent of a shift to the high wavenumber [Puertas and Fernández-Jiménez, 2003]. Consequently, the bonds shift to higher wavenumbers as the curing time progresses from 7 days to 180 days. The alterations in Si-O bonds, situated around 663-662 cm^{-1}, displayed no notable distinctions between slag cements activated with hydroxides and those activated with acetates [Puertas et al., 2011, Gong et al., 2019].

In hydroxides-activated slag cements, two bonds associated with the anti-asymmetric stretching vibration v_3[CO$_3$]$^{2-}$ [Cao et al., 2020b] were identified in the wavenumber of 1394-1498 cm^{-1}. Conversely, in acetates-activated slag cements, a similar bond was observed at approximately 1420-1418 cm^{-1}. This finding is consistent with the detection of carbonates in the evaluated AAS cements, as confirmed by the XRD patterns presented in Figure 5.4. In acetate-activated slag cements, distinct bands were identified within the 1350-1570 cm^{-1} region, albeit with differing positions compared to bands in hydroxide-activated samples: one at 1411-1414 cm^{-1} and another at 1558-1563 cm^{-1}. These bands were assigned to symmetric and anti-symmetric stretching vibrations v[CO$_2$], respectively, and were attributed to acetate anions [Pang et al., 2015]. Notably, XRD patterns (Figure 5.4) did not reveal characteristic peaks corresponding to sodium or potassium acetates, suggesting the possible presence of

acetate anions in a solid phase.

In general, Figure 5.5 (a)-(d) illustrate that there are no significant distinctions evident in the IR spectra of AAS cements when transitioning from hydroxide activators to acetates. This suggests that the utilization of sodium/potassium acetates does not induce structural modifications in the reaction products of AAS cements, in comparison to traditional sodium/potassium hydroxides.
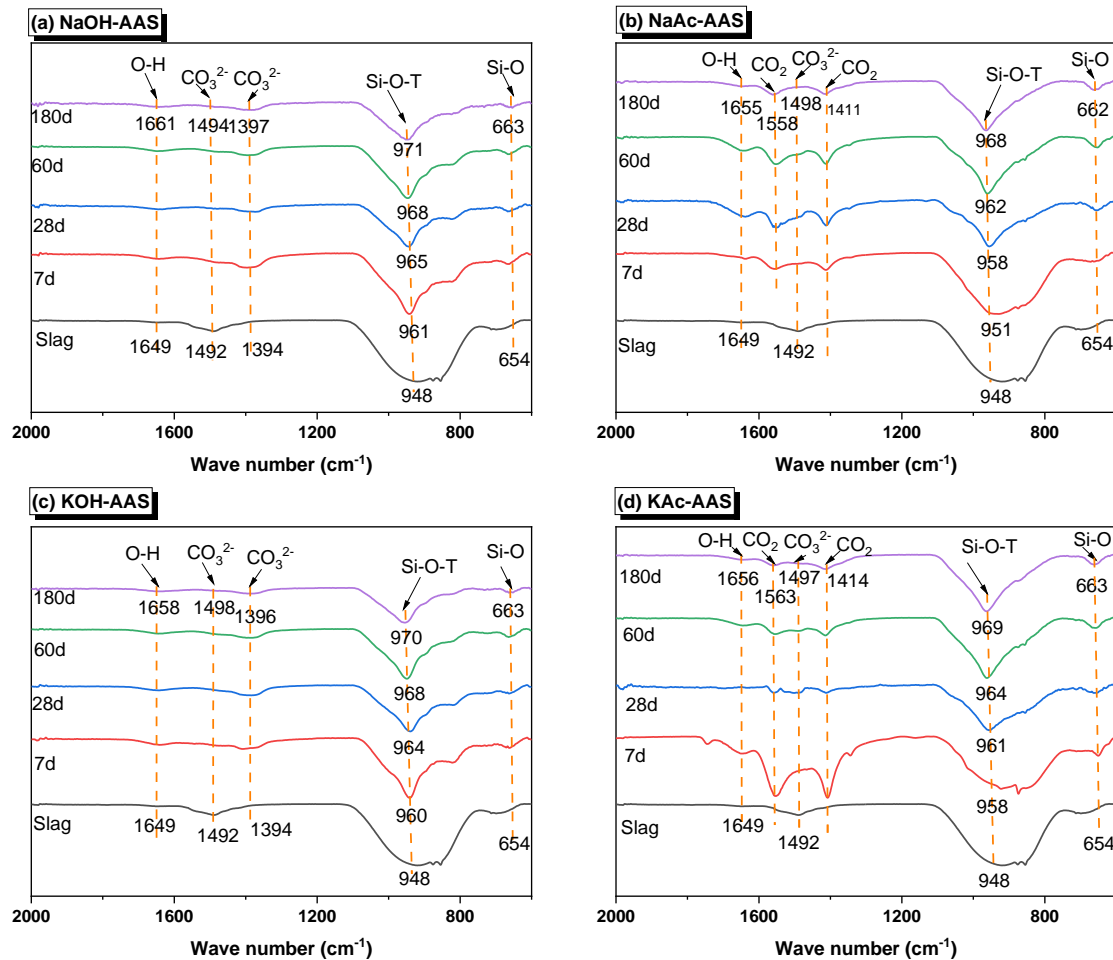
Figure 5.6 FTIR spectrum of AAS produced with different activator of (a) NaOH, (b) NaAc, (c) KOH, and (d) KAc curing up to 180 days as a function of the curing ages (relative to mass of mixed paste).

5.4.3 Thermogravimetry analysis

Figure 5.7 (A) and (B) present the distinct thermogravimetry results for the four AAS cement pastes activated by NaOH, NaAc, KOH, and KAc after 28 days of curing. Thermogravimetric analysis offers a means to semi-quantify the reaction products, encompassing amorphous binding gels like C-(A)-S-H type gels and crystalline phases

like hydrotalcite-like phases [Ben Haha et al., 2011b]. Examining the DTG (first derivative of TG data) curves as shown in Figure 5.7 (B), multiple peaks are evident across different temperature ranges. The entire temperature range can be categorized into three primary groups corresponding to potential reaction occurrences: 30°C-200°C, 200°C-400°C and 600°C-800°C [Ben Haha et al., 2011b, Kim et al., 2013]. Within the first temperature range below 200°C, as illustrated in Figure 5.7 (B), it mainly involves two stages: the first stage was up to 150°C resulted by the loss of free water. The second stage in the DTG curve aligns with the decomposition of the binding phase present in AAS systems, identified as the C-(A)-S-H type gel [Nunes et al., 2022]. This observation aligned with XRD results depicted in Figure 5.4 (a)-(d) for both alkali hydroxide-activated AAS and alkali acetate-activated AAS systems, where formation of this phase was identified. While for C-(A)-S-H type gels, the highest mass loss corresponds to the release of structural water molecules in this temperature range, up to 200°C [Kim et al., 2013]. The mass loss observed within the 200-400°C temperature range is as a result of the decomposition of hydrotalcite-like phases [Rozov et al., 2010], while peaks observed in the 600-800°C temperature range primarily result from the decomposition of calcium carbonates, such as calcite [Kim et al., 2013, Zhang et al., 2021].

In general, significant differences were identified between hydroxide-activated slag and acetate-activated slag systems as depicted in Figure 5.7 (A)-(B).
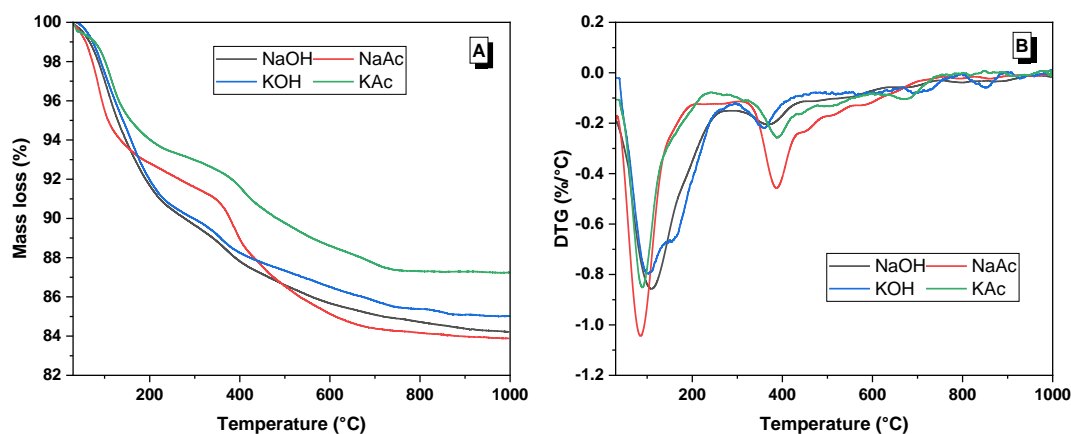
Figure 5.6 Thermogravimetric results of AAS pastes produced by various activators after 28 days of curing, where (A) TG curves, (B) DTG curves.

The degree of reaction in the produced AAS was determined by quantifying the mass loss associated with water molecules linked to binding gels decomposed, primarily C-(A)-S-H type gels, within the temperature range of 30-200°C as the maximum loss occurred at this range and the remaining could be ignored [Gruyaert et al., 2010, Ben Haha et al., 2011a]. Table 5.3 provides a total mass loss until 600°C after

28 days of curing, offering insights into the reaction degree (indicated by the total mass loss) of the four examined AAS cement pastes. These are ranked as follows: NaAc>NaOH>KOH>KAc. While different reaction kinetics are observed when employing acetates, these compounds have proven to be effective activators. The TGA analysis suggests that comparable degrees of slag reaction can be achieved after 28 days of curing. However, it's important to note that isothermal calorimetry results may indicate otherwise. This seeming contradiction can be elucidated through a more detailed examination of the distinct features present in the mass loss curves of each respective.

If the presence of these peaks in the 30-600°C range in the DTG curve of acetate-activated AAS is attributed to the hydrotalcite-like phases decomposition, then it may be that different hydrotalcite-like phases owing higher decomposition temperature was formed in the acetate-activated systems compared to the hydroxide-activated systems. However, due to the weak intensity of the hydrotalcite-like phase peaks in the XRD pattern, this possibility could not be further investigated. Another possibility is that a large amount of hydrotalcite is formed, but XRD shows that the intensity of the hydrotalcite peak is weak (undetectable at 28 days), and the accumulated heat of acetate-activated AAS at 28 days is much lower, so this is also ruled out. It is mostly likely that the thermal decomposition of residual acetate in the system. Thermal decomposition of sodium acetate and potassium acetate forms sodium carbonate and potassium carbonate respectively, releasing acetone ((CH_3)$_2$CO) with traces of CO_2 [Judd et al., 1974] - the reaction does not start before 400°C, indicating that acetate-activated AAS is not produced by the decomposition of sodium acetate and potassium acetate starting at approximately 300°C. Although the XRD pattern shows the absence of crystalline sodium acetate or potassium acetate. However, FTIR spectra indicate that acetate anions are still present in the system. Therefore, the mass loss event corresponding to the DTG peak centered at 380°C in acetate-activated AAS may be the result of decomposition of the acetate anion at lower temperatures.

Table 5.3 Mass loss calculated from TG up to 600°C, the mass loss according to C-(A)-S-H gel was calculated up to 200°C

Sample	Mass loss (%)	
	28-day	
	C-(A)-S-H	Total mass loss
NaOH	8.31	14.33
NaAc	7.18	14.87
KOH	8.03	13.49
KAc	5.97	11.40

5.4.4 Nanostructure of the evaluated AAS cement

Solid state NMR offers insights into the poorly crystalline structures that may not be readily discernible through XRD. This technique provides unique information by clarifying the presented specific atoms and their structural arrangements [Walkley and Provis, 2019]. In solid state NMR, the conventional Q^n (NAl) notation is employed to describe Si bonding, where 'n' denotes the number of -O-Si 'bridges' to the closest neighboring sites, and 'N' indicates the number of Al next-nearest-neighbor sites [Oestrike et al., 1987, Brouwer et al., 2020]. In addition, deconvolution was not performed on the ^{29}Si MAS NMR spectra throughout the study because the not highly initial pH values of acetates, so congruent dissolution of the slag cannot be assumed.

Figure 5.7 shows the ^{29}Si MAS NMR spectra for AAS pastes produced with various activators including NaOH, NaAc, KOH and KAc after 180 days of curing. The spectrum of NaOH-AAS (Figure 5.8) shows peaks at -79.03 ppm assigned to Q^1 along with sites corresponding to Q^2(1Al) (-81.47 ppm) and Q^2(0Al) (-84.17 ppm), respectively. This aligns with the findings previously documented in the case of NaOH-AAS [Wang and Scrivener, 2003, Myers et al., 2015]. The spectra of KOH-AAS which also showed three main peaks at -79.14 ppm for Q^1 sites, -81.25 ppm for Q^2(1Al) sites and -84.35 ppm for Q^2(0Al). These spectra contain similar features to those observed by Richardson et al. [Richardson and Li, 2018] on KOH-activated slag pastes samples after hydration at 60 °C for 1 week. In addition, the absence of a broad shoulder at around -74 ppm, resulted by the appearance of residual anhydrous slag (Q^0) means that GGBFS has reached a high degree of reaction when using NaOH and KOH after cured 180 days. A shoulder Q^2(0Al) appeared indicates that there are also Si ions occupying these bridging positions [Tänzer et al., 2015, Ben Haha et al., 2012]. The presence of Q^1 sites in the C-(A)-S-H type gels occurred in hydroxides-AAS systems, where it can be bonded with Si, Al, Ca^{2+}, as well as H^+ and linked with other alkali charge-balancing species [Wang and Scrivener, 2003, Le Saoût et al., 2011].

There seem to be significant differences in the intensity of the different Q sites when using sodium acetate or sodium hydroxide, which indicates C-(A)-S-H type gels with alternated structure. Similar differences are observed in the KOH-AAS and KAc-AAS. It is clear that neither the Q^1 or Q^2(1Al) sites are clearly distinguishable in the acetate-activated AAS, as it is the case for the hydroxide-activated AAS, which might indicate lower Al substitutions in the C-(A)-S-H type gel phases formed as adding acetates. Also, the fact that the region from -60 to -80 ppm where contributions from unreacted slag are more noticeable is indicating that a potentially lower reaction degree of GGBFS is achieved.

The results obtained from ^{29}Si MAS NMR emphasize substantial differences in the structure of C-(A)-S-H type gels formed in both hydroxides-activated and acetates-

activated slag cement systems. The transition from hydroxides to acetates as activators may result in substantial structural alterations in the reaction product of C-(A)-S-H type gels.
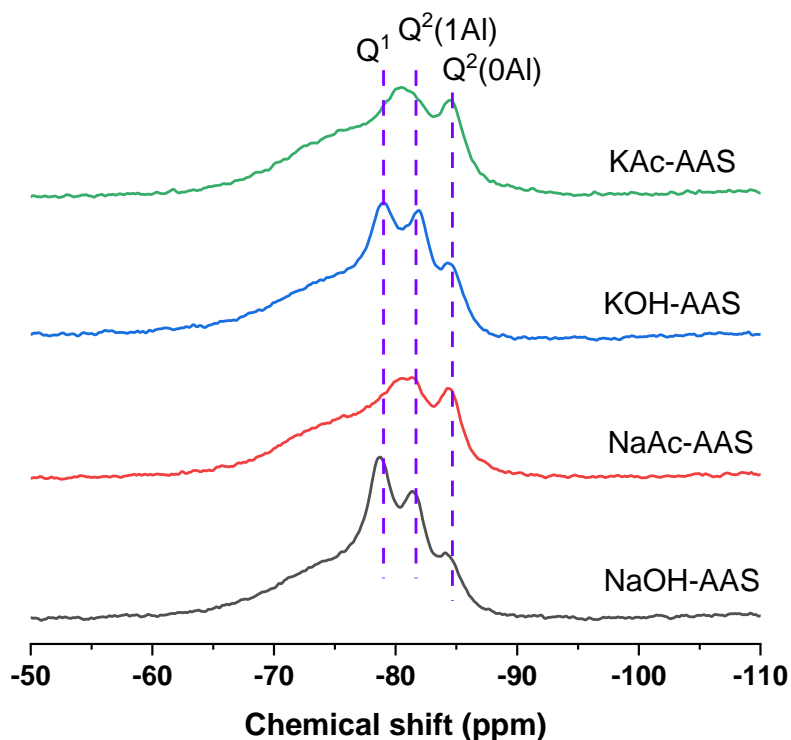
Figure 5.7 ^{29}Si MAS NMR spectra of 180-day AAS with various activators

5.4.5 Microstructure analysis

Figure 5.8 (a)-(d) displays BSE images of the four examined AAS cements after a 180-day curing period, captured at various magnifications. Different elemental compositions are represented by distinct colors, facilitating clear differentiation. In the micrographs from Figure 5.8, unreacted slag particles are identifiable by their light grey color. Meanwhile, the grey areas surrounding the remaining slag particles correspond to binding phases, primarily comprising C-(A)-S-H type gels along with secondary reaction products like hydrotalcite-like phases and carbonates, as detected through XRD analysis (see Figure 5.4). Minimal differences in the micrographs (Figure 5.8 (a) and (c)) are evident between slag cements activated with NaOH and those activated with KOH, indicating their comparable microstructures. This observation aligns with the XRD pattern findings (refer to Figure 5.4 (a) and (c)), consistent with prior research on NaOH-activated slag cements [Ben Haha et al., 2011b] and KOH-activated slag cements [Richardson et al., 1994, Richardson and Li, 2018]. In contrast, Figure 5.8 (b) and (d) reveal that acetate-activated slag cements contain more unreacted slag particles, a significant and clearly observable difference when compared to hydroxide-activated

slag cements. This indicates that acetate-AAS exhibited a lower reaction degree in comparation to hydroxide-AAS. These findings correlate with the mass loss results caused by C-(A)-S-H type gels decomposed, as presented in Table 5.3, providing a rough indicator of the reaction degree in the examined AAS cements.
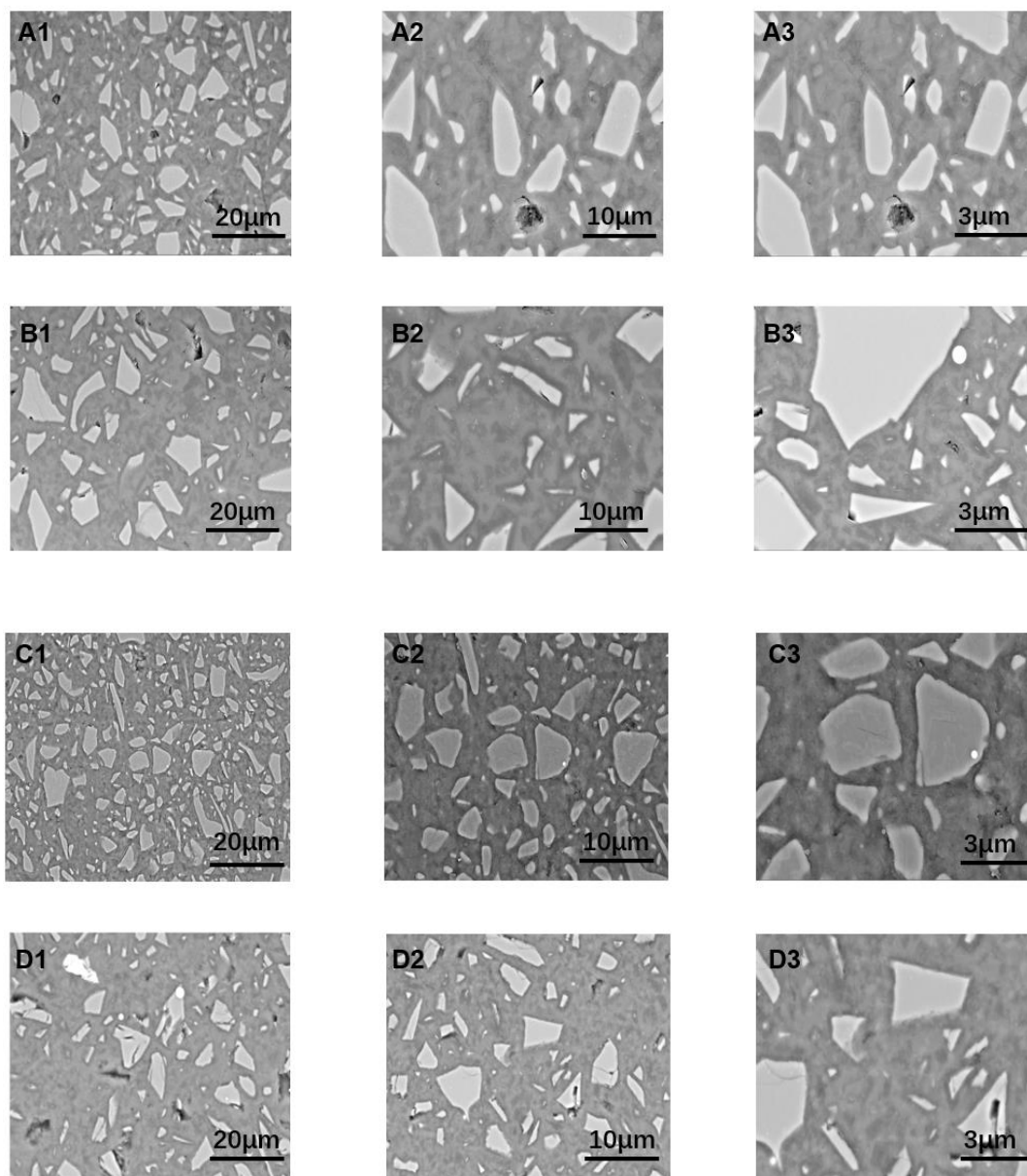
Figure 5.8 BSE images of the evaluated AAS cement at different magnification, where (A) NaOH-AAS, (B) NaAc-AAS, (C) KOH-AAS and (D) KAc-AAS.

Figures 5. 9 (a)-(f) present Energy-Dispersive X-ray Spectroscopy (EDS) maps and atomic ratio plots obtained from EDS spots on the four assessed AAS samples. The atomic ratios are depicted herein for comprehensive analysis. Notably, the Ca/Si ratios (Figure 5.9 (e)) for NaOH-AAS reach a maximum of 2.42, a considerable elevation

compared to NaAc-AAS, which attains a maximum of 1.42. Similar trends are observed for KOH-AAS and KAc-AAS, registering maximum values of 1.47 and 1.44, respectively. These variations in Ca/Si ratios may be attributed to discrepancies in dissolved silicate contents, influenced by the varying degrees of reaction attributed to the pH of the alkaline solutions. Remarkably, the data suggests that NaAc/KAc, acting as activators compared to NaOH/KOH, did not induce substantial alterations in the composition of the formed C-(A)-S-H type gels, aligning with the XRD results depicted in Figure 5.4 [Wang et al., 2022, Ben Haha et al., 2011a]. The Al/Si ratios remain consistently below 0.8 across all AAS pastes, demonstrating no discernible distinctions between different formulations, in line with findings reported in previous studies [Kapeluszna et al., 2017, Wang et al., 2022]. Additionally, the absence of detected carbon within NaAc-AAS in the element maps (Figure 5.9 (b)) suggests that carbon, potentially originating from acetates, has undergone a reactive process.

In Figure 5. 9 (f), the presented data points illustrate the correlation between Mg/Si and Al/Si, providing robust evidence for the formation of hydrotalcite-like phases [Yi et al., 2014, Ben Haha et al., 2011b]. The appearance of hydrotalcite-like phases is characterized by Mg/Al ratios of 2.4 in NaOH-AAS, 1.4 in NaAc-AAS, 1.1 in Sample KOH-AAS, and 0.4 in KAc-AAS, respectively. The observed Mg/Al ratio of 2.4 in NaOH-AAS is consistent with prior investigations on NaOH-activated alkali-activated slag (AAS) systems, where a ratio of approximately 2 was reported [Lee et al., 2016, Fernandez et al., 2005]. Notably, the influence of NaAc is evident in its role of diminishing the Mg/Al ratio in comparison to NaOH throughout the reaction processes. The observed disparity in Mg/Al ratios signifies variations in aluminum uptake within the C-(A)-S-H gels [Myers et al., 2015]. KOH-AAS exhibits a Mg/Al ratio of 1.1, aligning with the previously reported range of 0.1-1.0 in similar systems [Richardson and Li, 2018]. A discernible decreasing trend is also noted from KAc-AAS to KOH-AAS, indicating that acetate ions exert a similar effect on the incorporation of aluminum into C-(A)-S-H type gels.

To conclude, no significant differences were observed in the morphology between hydroxides-activated slag cements and acetates-activated slag cements. Highly dense and homogeneous specimens are observed in both cases, which further demonstrate the effectiveness of acetates as potential activators to produce alkali-activated cements.
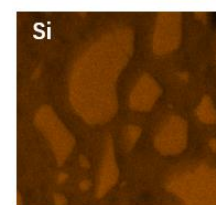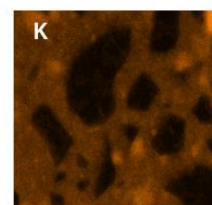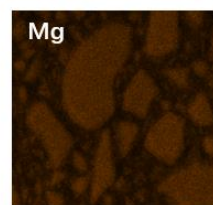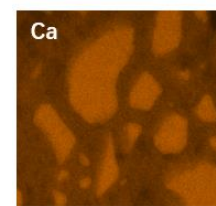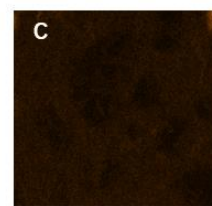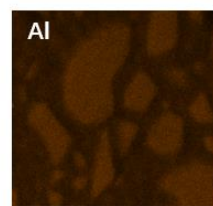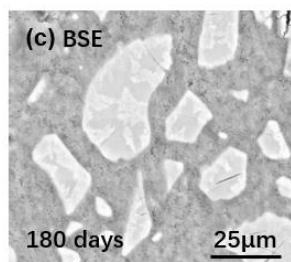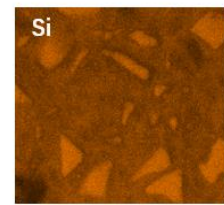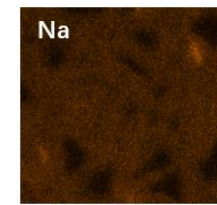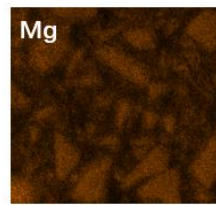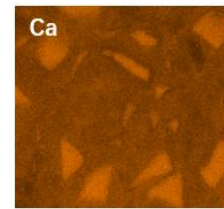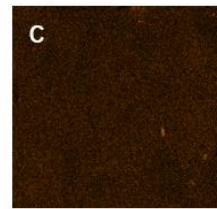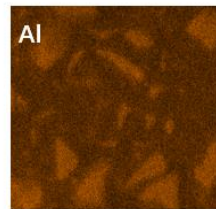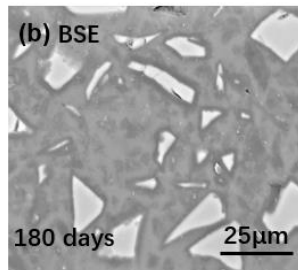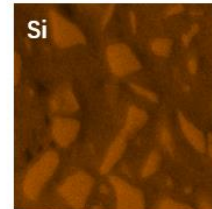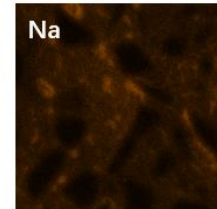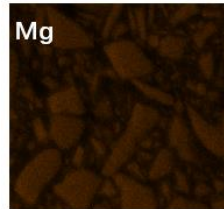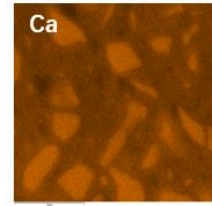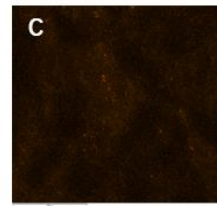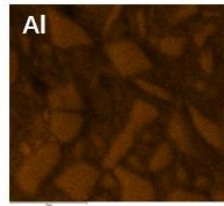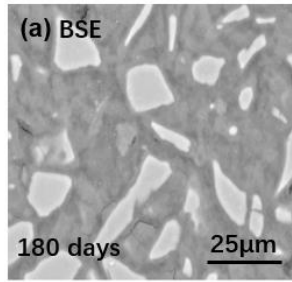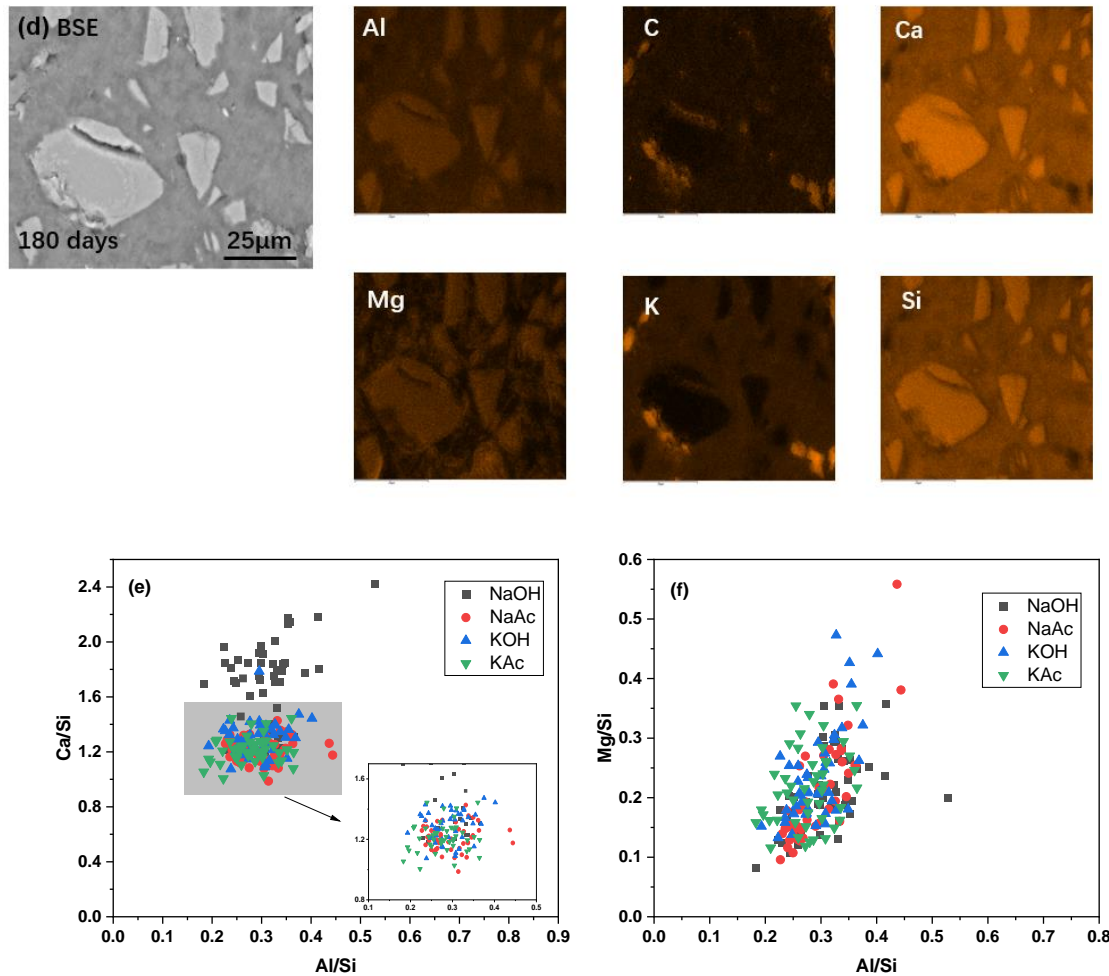
Figure 5.9 BSE images and EDS maps of the assessed AAS, where (a) NaOH-AAS, (b) NaAc-AAS, (c) KOH-AAS, (d) KAc-AAS, (e) atomic ratios from the EDS maps Ca/Si vs Al/Si, and (f) Mg/Si vs Al/Si of AAS pastes

5.5 Mechanical and physical properties

5.5.1 Compressive strength

Figure 5.10 illustrates the compressive strength owing by GGBFS activated with four different activators over a curing period of up to 180 days. It is evident that both NaAc-AAS and KAc-AAS fail to achieve adequate hardening within the initial 7 days of curing, conversely to hydroxide-activated slag cement. Therefore, the compressive strength results after 7 days of curing were not existed. This finding aligns with the results from calorimetry shown in Figure 5.2, where the peaks with maximum values, attributed to NaAc-AAS and KAc-AAS, exhibit significant delays compared to those of NaOH-AAS and KOH-AAS. The compressive strength for NaOH-AAS and KOH-AAS after 28 days of curing were notably higher, reaching 32.59 MPa and 29.91 MPa,

respectively shown in Figure 5.10. Conversely, NaAc-AAS exhibited a lower 28-day compressive strength value of 25.3 MPa. In contrast to findings presented in [Al-Kheetan et al., 2020a], where the addition of NaAc significantly bolstered concrete strength development after cured 7 and 28 days under severe conditions ranging from -25°C to 60°C, differ from the results in this study, consistent with the differences in chemistry of the systems evaluated. However, results reported in [Al-Kheetan and Rahman, 2019] exhibit partial alignment with the findings of this study, as a lower compressive strength was obtained when NaAc was employed to concrete during the short curing periods of 7-14 days. Nevertheless, it is noticeable that the concrete in their study still achieved high strength values.

The compressive strength of KAc-AAS paste samples was nearly 20 MPa lower than that of KOH-AAS after cured 28 days. This finding aligns with the results reported in [Xie et al., 2017], where KAc solution was utilized as a deicer. The study demonstrated that KAc has a detrimental effect on compressive strength development, although the resulting strength values still exceeded 20 MPa. Similarly, another investigation [Zhang et al., 2018b] focusing on the mechanical properties of concrete subjected to freeze-thaw cycles in the KAc solution corresponds with the observations regarding acetate-activated slag cements. The freeze-thaw cycle in KAc solution caused a lower 28-day compressive strength, possibly attributable to water expansion within the concrete during the cycling process [Zhang et al., 2018b, Zhang et al., 2018a].

After 60 days of curing, the compressive strength of NaAc-AAS was 32.47 MPa, marking an approximate decrease of 35 MPa in comparison to NaOH-AAS. Similarly, in the case of KOH-AAS and KAc-AAS, KOH-AAS exhibited a compressive strength value of 64.75 MPa, which was nearly 34 MPa higher than that of KAc-AAS at the same 60-day curing time. Notably, NaOH-AAS achieved the highest compressive strength of 82.31 MPa after a 180-day curing period, and this trend was consistent for KOH-AAS, which attained a compressive strength value of 78.56 MPa. It is evident that compressive strength increased with longer curing times, both in hydroxide-AAS cements and acetate-AAS cements.

Compressive strength evaluations revealed that NaAc- AAS exhibited marginally higher strength than KAc-AAS at and beyond 28 days of curing. This outcome contrasts with the anticipation, given that the cumulative heat generated in KAc-AAS was slightly higher than that in NaAc-AAS up to 28 days, suggesting a seemingly higher degree of reaction in NaAc-AAS than in KAc-AAS. Notably, a similar phenomenon was observed in hydroxide-activated systems: despite the cumulative heat of KOH-AAS being slightly higher up to 28 days, NaOH-AAS consistently demonstrated slightly higher compressive strength at all curing times. Additionally, K-based AAS exhibited a faster initial setting time compared to Na-based AAS, a characteristic attributed to the larger ionic size of potassium or its strong alkalinity[Richardson and Li, 2018], facilitating quicker penetration into slag particles and, consequently, a more

rapid reaction. However, it is crucial to underscore that the influence of cation type is considerably smaller compared to the effect of anion type.

In general, the compressive strength of alkali metal acetates-AAS cements was lower when compared to that of alkali hydroxides-AAS cements across all curing ages, ranging from 7 days to 180 days. While it remains challenging to precisely elucidate the mechanism underlying the notable differences in reaction kinetics for alkali-acetate AAS cements, it is worthy noticeable that the compressive strength of acetates-activated AAS exceeded 20 MPa after cured 28 days. This underscores the feasibility of employing NaAc and KAc as alkaline activators for the production of AAS. In the context of non-structural or general construction applications, alkali-activated slag cements are commonly expected to attain a compressive strength ranging between 40-50 MPa after 180 days of curing [Batuecas et al., 2021]. The compressive strength exhibited by acetates-activated slag cements aligns with these requirements, rendering them suitable for applications such as pavements, non-load-bearing structures, and various general construction projects [Terry et al., 2020]. Conversely, for structural applications with elevated strength prerequisites, alkali-activated slag cements may be mandated to achieve compressive strengths surpassing 50 MPa after 180 days [Awoyera and Adesina, 2019]. Specifications in structural projects often necessitate compressive strengths within the range of 50 MPa to 80 MPa or higher [Amer et al., 2021a, Tuyan et al., 2020, Singh et al., 2015], contingent upon specific design criteria and safety considerations.
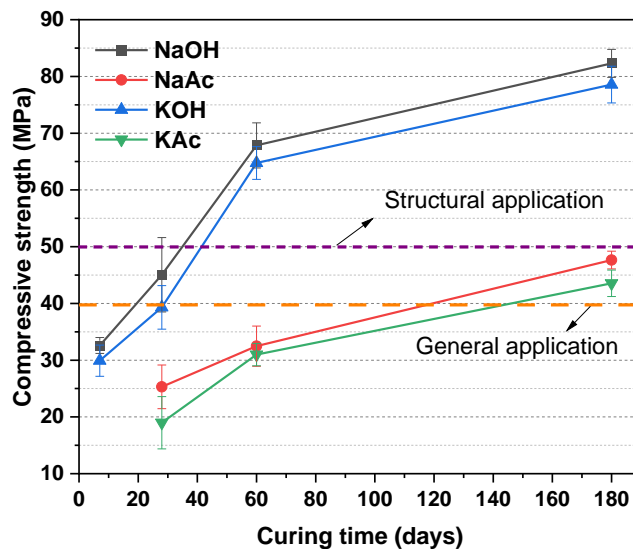
Figure 5.10 Compressive strength results of AAS pastes with different activators changed with curing time

5.5.2 Pore size distribution

Figures 5.11 (A) and (B) depict the results of mercury intrusion porosimetry conducted on alkali-activated slag cements utilizing various activators, including hydroxides and acetates. The cumulative volumes of mercury intrusion vary based on the type of activator uses, as evident in Figures 5.11 (A) and (B). NaAc-AAS exhibits lower cumulative intrusion volumes compared to that of NaOH-AAS, while KAc-AAS exhibits higher cumulative porosity volumes compared to KOH-AAS. This higher cumulative porosity in KAc-AAS indicates a less efficient filling of the available space by the reaction products, consequently contributing to a raise in the total pore volume within the solid paste [Zajac et al., 2018]. However, this trend does not hold for NaOH/NaAc-AAS systems. Figure 5.11 (A) highlights that the pore size distribution in NaAc-AAS is primarily concentrated in the range of 0.008-0.01 μm, whereas in NaOH-AAS, it predominantly exists in the 0.01-0.02 μm range. Conversely, for KOH-AAS, the pore size distribution is mainly within the 0.003-0.005 μm range, while KAc-AAS displays a pore size distribution range around 0.008-0.01μm, additionally around 0.04-0.06 μm and 0.08-0.1 μm.
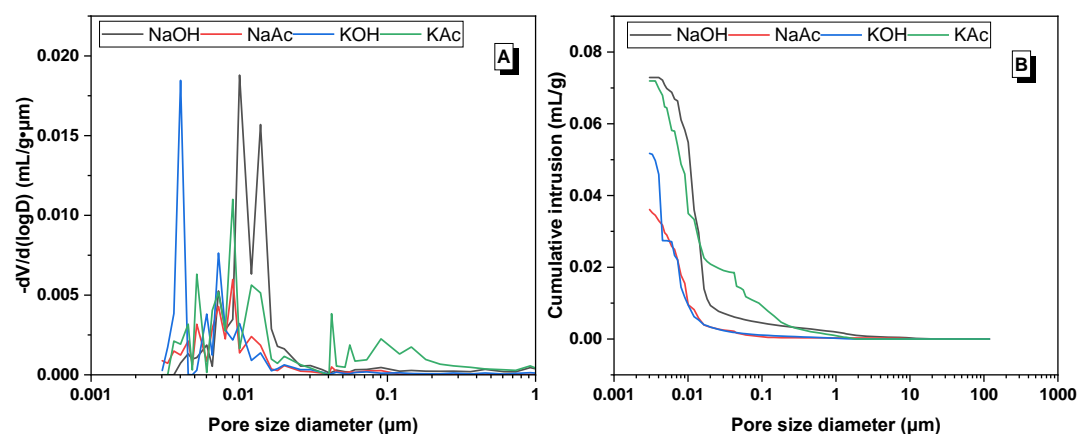
Figure 5.11 Pore size distribution of alkali-activated slag pastes at 28 days as a function of different activators. (A) differential pore volume and (B) cumulative pore volume

Table 5.4 listed the critical pore entry size diameter of the AAS cements produced with various activators. The critical pore size pertains to the maximum value observed in the differential distribution curves, as well as the pore size occurred in most frequency in the interconnected pores [Zajac et al., 2018]. A comparable critical pore size is identified slag cements activated by with activators including hydroxides and acetates, with the exception of the KAc-AAS, which presents a significantly lower critical pore size compared with all the other samples evaluated here. The critical pore size diameter of NaAc-AAS was a bit lower than that of NaOH-AAS, while it was opposite in KAc-AAS which is more than twice of the value in KOH-AAS. The total

porosity of AAS produced by various activators determined from MIP is listed in Table 5.4. NaAc-AAS presented the lowest total porosity of the samples tested. NaOH-AAS reported comparable porosity to samples produced with KAc, while KOH-AAS exhibited a slightly lower porosity compared with the other activators used.

Table 5.4 Core pore diameter and total porosity of 28d AAS cements

Paste type	Critical pore size diameter (µm)	Total porosity (%)
NaOH-AAS	0.010	14.0
NaAc-AAS	0.009	8.5
KOH-AAS	0.004	10.9
KAc-AAS	0.009	14.8

In Figure 5.12, the relationship between the compressive strength changed with various porosity of the produced AAS cements following a 28-day curing time is shown. NaOH-AAS cement exhibits higher total porosity and compressive strength. In contrast, NaAc-AAS cements demonstrate lower total porosity and reduced compressive strength when compared to NaOH-AAS cement, consistent with the data from literature presented in the color of light-yellow area. As for KOH-AAS, it exhibits a total porosity of 10.9% alongside a notable compressive strength of 39.31 MPa. However, this is accompanied by a reduced total porosity of 3.1% and a decreased compressive strength of 5.74 MPa compared to NaOH-AAS. A bit lower total porosity than that of the data range recorded in Figure 5.12. KAc-AAS cements show a higher total porosity of 14.8%, which aligns with their lower compressive strengths. There seems to not be a correlation between compressive strength and the total porosity.
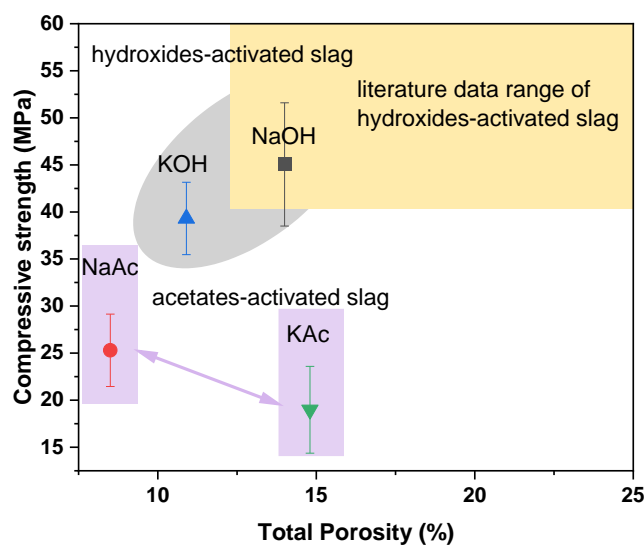
Figure 5. 12 28-day compressive strengths as a function of the total porosity in AAS cements, the literature data range were from [Zhang et al., 2021, Zuo and Ye, 2018]

The correlation between compressive strength and porosity of AAS paste can be ascribed to the volume fractions of different pore sizes, which are presented in Figure 5.13. The pores were quantitively classified into size categories < 10 nm, 10–100 nm and > 100 nm according to [Chen et al., 2022, Zhan et al., 2022]. The pores of the NaOH-AAS were mainly distributed in the range of 10 nm–100 nm with a volume fraction of 71%, represented the micropores. A higher intruded volume below 10 nm was identified in KOH-AAS, consistent with the reduced critical pore size (Table 4) and thus a higher compressive strength was obtained. In addition, pores with a diameter lower than 10 nm (gel pores) could possibly affect the shrinkage [Chen et al., 2022]. A volume fraction of 13% (pore size diameter >100 nm) was observed in KAc-AAS, the diameter range corresponds to the capillary pores and macropores [Chen et al., 2022]. Considering the critical pore size diameter of KAc-AAS is not higher compared to other AAS systems, the highest total porosity of 14.8% possibly due to the macropores existed, thus a compressive strength of < 20 MPa was obtained. For NaAc-AAS, it has a 74% volume fraction of pores which diameter range <10 nm and only 1% volume fraction of pores with diameter >100 nm, thus a lower total porosity was obtained. However, the compressive strength of NaAc-AAS was lower compared to NaOH-AAS, which may need further investigation.
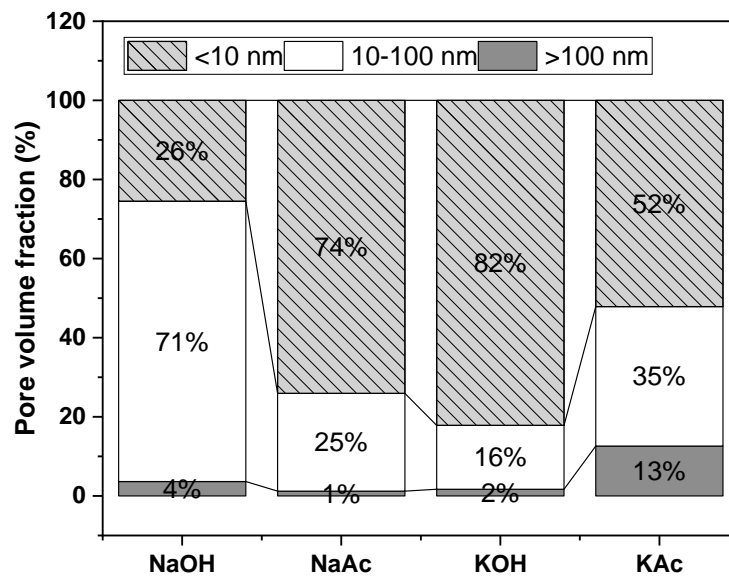
Figure 5. 13 Pore size fraction of the evaluated AAS cements

5.5.3 Water contact angle (wettability)

Wettability is a concern for alkali-activated slag cements due to its direct impact

on the interaction between the material and fluids, particularly water [Zhao et al., 2022]. The wettability of alkali-activated slag cements is closely linked to their durability, controlling wettability helps enhance the material's resistance to environmental factors, contributing to long-term durability.

As described in section 3.4.9, conducting water contact angle measurements on evaluating the potential hydrophobicity owing by AAS produced with acetate-based activators. The photographs taken during the water contact angle experiments are shown in the Table 5.6.

After 28 days of curing, the water contact angle could not be obtained for the NaOH-AAS and KOH-AAS pastes, which indicated wetting and water absorption of these materials. Conversely for alkali metal acetates-activated slag cements, a clear water contact angle is observed for both NaAc-AAS and KAc-AAS. At extended curing durations (180 days), the water contact angle measurement could be obtained in all the evaluated AAS slag cements, demonstrating that some degree of hydrophobicity potential occurred. Comparing NaOH-AAS with NaAc-AAS, it is clear that the latter is more impermeable. These results are consistent with reports for Portland cement concrete added with sodium acetate [Kushartomo and Prabowo, 2019] with a significant reduction in permeability, which is observed with the addition of this chemical compound. Similar trend was observed for KOH-AAS when compared to KAc-AAS. The findings of this study exhibit a degree of consistency with the results obtained when KAc was utilized as an admixture in concrete production [Abed et al., 2023]. While the study did not include an assessment of water permeability, the improvements in workability and compressive strength resulting from the addition of KAc offer compelling evidence of its potential in reducing concrete permeability. Concerning acetate-based cements, negligible changes were observed at different curing times.

The contact angle values in AAS cement demonstrate that acetates-activated slag cement has a reduced permeability compared to hydroxides-activated cement. Furthermore, the impact of curing time on acetate-based cement properties remained relatively stable, whereas a noticeable increase was observed in hydroxide-based cement. The enhancement of using acetates on reducing impermeability of cementitious materials would possibly suggest the application as coating materials.

Table 5.6 Photograph for water contact angle determination of the evaluated AAS cements

Activator type	Contact angle at different curing time (days)	
	28	180

NaOH — ✗ — 34.33±0.14°

NaAc — 44.21±0.01° — 43.09±0.11°

KOH — ✗ — 42.17±0.01°

KAc — 49.95±0.07° — 46.12±0.02°
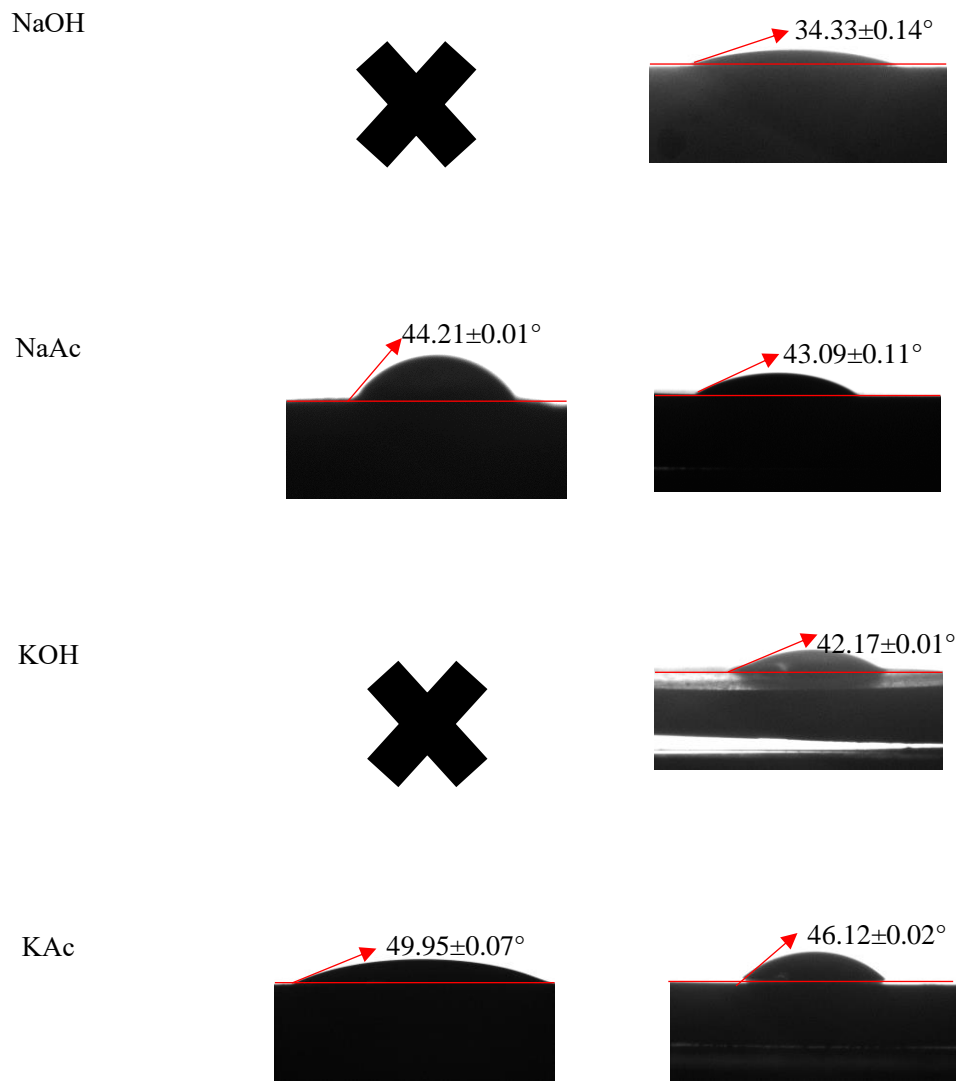
5.6 Discussions on proposed reaction mechanism of alkali-acetate activated slag cements

Figure 5.14 includes a schematic diagram depicting the potential reaction process of hydroxides-activated AAS, particularly NaOH-AAS. In comparison to NaAc and KAc as activators, at the same alkaline concentration, hydroxides solutions exhibit higher pH values. Consequently, when using hydroxide solutions as alkaline activators for dissolving GGBFS, the dissolution of Ca^{2+} and Mg^{2+} occurs rapidly [Ben Haha et al., 2011a, Wang and Scrivener, 1995]. Initially, the Ca^{2+} ions dissolved in the

NaOH/KOH solution in an ionic form since the solution lacks silicate ions [Jiao et al., 2018a, Fernández-Jiménez and Puertas, 1997]. As the reaction progressed, more dissolved Ca^{2+} generated and thus resulted an enhanced concentration. The increase in Ca^{2+} concentration resulted in supersaturation, leading to the precipitation of Ca^{2+} [Li et al., 2019a]. Therefore, the initial stage of the reaction mechanism for hydroxides-activated AAS is characterized by a dissolution-precipitation reaction [Li et al., 2019a, Fu et al., 2023]. Furthermore, other elements such as Al and Si also dissolved at the same time and react with Ca^{2+} to form C-(A)-S-H type gels [Ben Haha et al., 2011a]. The silicate ion has a low diffusion coefficient together with the C-(A)-S-H type gels with limited solubility, resulting the reaction products in hydroxides-AAS tend to continuously cover the GGBFS particles. Once reaction products totally covered the GGBFS particles, the subsequent reaction mechanism shifts to a solid-phase reaction [Li et al., 2019a].
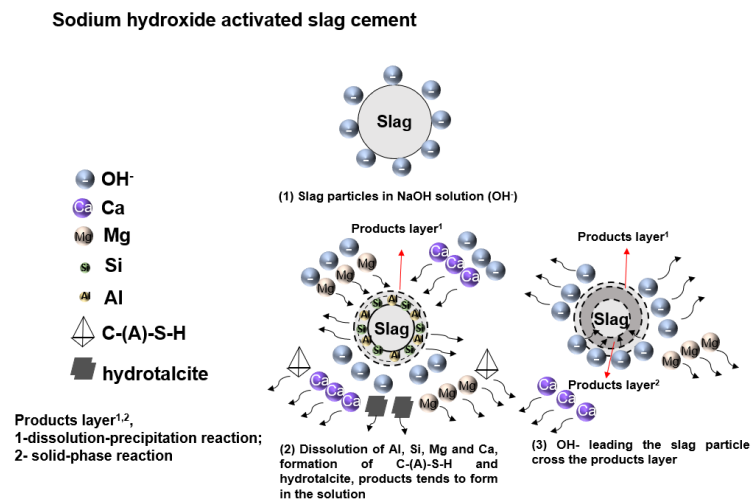
Figure 5.14 Reaction mechanism of NaOH-AAS (some information from [Li et al., 2019a] and [Jiang et al., 2022a])

Figure 5.15 illustrates the proposed hypothesis for the reaction process in alkali metal acetates-activated slag cements. To exemplify the presence of hydroxides and acetates in solutions, the dissociation processes of NaOH and NaAc are represented by Eq. 5.1 to 5.3.

$$NaOH \rightleftharpoons Na^+ + OH^- \qquad\qquad Eq. 5.1$$

$$CH_3COONa \rightleftharpoons Na^+ + CH_3COO^- \qquad\qquad Eq. 5.2$$

$$CH_3COO^- + H_2O \rightleftharpoons CH_3COOH + OH^- \qquad\qquad Eq. 5.3$$

Likewise, the dissociation of NaAc, as represented in Eq. 5.2 to 5.3, in solutions produces OH^- ions, serving as the source of alkalinity for NaAc. However, the suggested hypothesis for acetates-activated slag proposes that the Ca^{2+} ions escaped from the dissolved GGBFS particles initially meet with the CH_3COO^- ions dissociated

from NaAc in the solution, resulting the formation of calcium acetate as depicted in Eq. 5.4 below.

$$CaSiO_3 + 2CH_3COONa \rightarrow Ca(CH3COO)_2 + Na_2SiO_3 \qquad Eq. 5.4$$
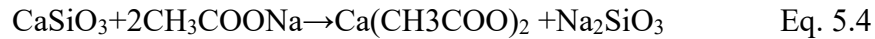
Because calcium acetate is initially generated before the appearance of C-(A)-S-H gels, the Ca^{2+} ions origin from GGBFS particles are consumed. This leads to a lower initial pH in the acetate activator and consequently a slower dissolution of silicate species. This phenomenon explains the longer induction period observed in the calorimetry results of NaAc/KAc-AAS, where the cement cannot harden for up to 7 days. The surplus CH_3COO^- ions present in the system then proceed to form calcium acetate until all the CH_3COO^- ions are depleted illustrated in Figure 5.15. This could also explain the relatively lower formation of hydrotalcite in acetates-activated AAS systems. In the later stages, the reaction mechanism bears similarity to that of silicate-activated AAS.
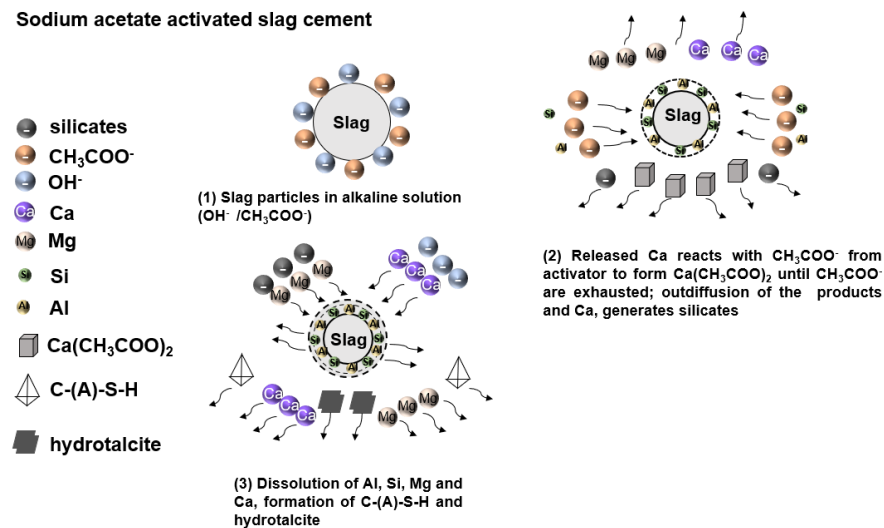
Figure 5.15 A schematic diagram illustrated the reaction mechanism of NaAc-AAS.

5.7 Conclusions

The feasibility of using NaAc and KAc as alternative activators for the production of AAS cements was examined, and the properties of the resulting AAS cements were evaluated. Several conclusions were drawn from the study:

Acetate-activated slag cements exhibited a much longer induction period in the initial hours after mixing. Consequently, the initial and final setting times were extended for acetate-activated AAS than those observed for hydroxide-activated AAS.

The XRD patterns of hydroxide and acetate-activated slag cements showed no significant differences in the type of reaction products forming during the curing period

of up to 180 days. In both cases, the main reaction products identified were hydrotalcite-like phases, C-(A)-S-H type gels, along with calcium carbonates, corroborated by ATR-FTIR. Thermogravimetry analysis revealed a notably lower reaction degree in acetates-activated slag cements compared to hydroxides-activated slag cements. ^{29}Si MAS NMR spectroscopy identified remarkable differences in the spectra corresponded to C-(A)-S-H type gels. C-(A)-S-H type gels with different Mg/Al ratio was quantitively detected by SEM-EDS analysis, similar features (a highly dense, and homogeneous binding phase) were observed in all the AAS evaluated.

The compressive strength of hydroxides-activated AAS consistently exceeded that of acetates-activated AAS at all curing ages. Moreover, acetates-AAS exhibited lower compressive strength despite having lower total porosity could attribute to the volume fraction of different pores. However, no clear trend correlation between the compressive strength and porosity can be drawn. The water contact angle measurements exhibited marked differences between hydroxides-AAS and acetates-activated AAS, indicating that acetates have the potential to reduce permeability at longer curing ages and remained unchanged from 28 days to 180 days, whereas in hydroxide-based cement, it was significantly enhanced at extended curing times.

The results corroborate that acetates can be used as effective activators for producing AAS cements with comparable microstructure properties to hydroxide-activated systems with potential lower shrinkage. Therefore, a novel route for producing alkali-activated cements has been discovered and demonstrated. It is determined that the alkali acetate-activated slag cements under investigation may not be suitable for on-site concrete casting. Nevertheless, the hydrophobic characteristics render them appealing for potential applications in the development of coatings aimed at reducing permeability.

Chapter 6 – Blended (NaOH-NaAc) acetate-activated GGBFS cements

6.1 Introduction

Conventional sodium hydroxide-activated slag cements have long been recognized for their numerous advantages, including high early strength development and excellent durability [Bernal et al., 2014a, Provis and Bernal, 2014a]. However, they also exhibit a significant drawback: a rapid reaction process [Xiang et al., 2022, Ben Haha et al., 2011a]. This rapidity means that these cements often necessitate the addition of retarders to control the setting time [Tong et al., 2021, Xiang et al., 2022], posing challenges for its use for the construction industry. Moreover, the speedy reaction limits the workability of the cement mixture, making it less suitable for certain applications where extended working times are essential.

Chapter 5 delves into the viability of sodium acetate as an alternative alkaline activator. The expeditious reactivity characteristic of sodium hydroxide-activated cements, known to constrain workability [Tong et al., 2021], prompted an examination of sodium acetate-activated slag cements. These cements demonstrate an extended reaction duration, offering a pragmatic resolution to the workability limitation associated with rapid reactions. This finding presents a viable option for construction professionals seeking enhanced flexibility and control over the setting time of such cementitious blends. The concept of employing blended systems, wherein sodium acetate is incorporated with the substitution of sodium hydroxide as the alkaline activator, stems from these insights. Furthermore, the utilization of acetates in concrete has garnered significant attention due to their remarkable impermeabilization properties of cementitious materials containing such admixtures [Al-Kheetan et al., 2020a, Al-Kheetan et al., 2019]. Their use can also contribute to a longer service life for concrete structures, achieving a reduction on maintenance costs and environmental impact [Al-Kheetan et al., 2020a, Luo et al., 2022]. As sustainable construction practices gain prominence, the impermeabilization properties of acetates offer a valuable tool in achieving durable and resilient concrete infrastructure while minimizing the environmental footprint of maintenance and repair activities.

The study aims to examine the modification of the reaction process in AAS cements by substituting sodium acetate for sodium hydroxide in the activator composition. The produced AAS cements were assessed through a comprehensive analysis encompassing fresh state properties, mechanical properties, microstructure, and impermeabilization properties. The findings promise to not only enhance the

understanding of using sodium acetate in AAS production but also contribute to the development of more resilient and sustainable construction practices.

6.2 Mix design and sample preparation of the evaluated cements

The properties of GGBFS used in this chapter are detailed within the confines of Section 3.1.1 of Chapter 3. The blended activator composition varying from Sample 0NA to Sample 100NA according to NaAc with substitution to NaOH. Similar activating conditions, to those used in Chapter 5, were adopted in this study. A summary of AAS produced and analyzed in this chapter is shown in Table 6.2. The details of the calculation of using blended activators to produce AAS cements are presented in Appendix B. Sample preparation was presented in Section 3.2.2 of Chapter 3.

Table 6.2 Mix design of AAS pastes evaluated

Mix ID	Activator type	Mass of individual component in activator (g)		GGBFS (g)	Water (g)	w/b	pH value of the activating solution
		NaAc	NaOH				
100NA	NaAc	10.58		100	33.17	0.3	11.8
75NA	75% NaAc-25% NaOH	7.94	1.29	100	32.77	0.3	12.0
50NA	50% NaAc-50% NaOH	5.29	2.58	100	32.36	0.3	12.5
25NA	25% NaAc-75% NaOH	2.64	3.87	100	31.95	0.3	13.0
0NA	NaOH		5.16	100	31.55	0.3	13.3

The explanation of the calculation for the mass of individual components in the materials mix design is provided in detail in Appendix B.

6.3 Reaction kinetics

Heat released and cumulative heat curves of alkali-activated slag cements produced with different activator compositions were presented in Figure 6.1 (A) and (B) respectively. Figure 6.1 (A) illustrated the heat released of the AAS activated by various percentage of NaAc. The sample solely produced with sodium hydroxide (0NA) reacted rapidly, only showing one exothermic peak and no pre-induction period, consistent with the observations reported in Chapter 5. As NaOH is partially replaced

by sodium acetate (25NA), the time at which the peak with the highest value occurred was found to be comparable to that of the 0NA sample, at approximately 2.7 hours. However, the 25NA Sample exhibited a slightly higher heat release during this period.

When the NaAc content increased to 50% (referred to as 50NA), the time at which the highest peak corresponding to the acceleration period occurred was slightly delayed compared to both 25NA and 0NA, manifesting at 4 hours, with a noticeable reduction in heat release at this point. In the case of Sample 75NA, the time at which the highest peak was observed was 11 hours later than that of Sample 0NA. This suggests that the reaction process extended significantly as the NaAc content increased. Notably, the peak associated with the maximum value, characteristic of the acceleration period in NaAc-AAS, appeared markedly slower than in other systems, emerging at 261 hours. This observation aligns with the results in Chapter 5, which indicated that NaAc-activated slag reaction process differs to that of NaOH-AAS, so that heat released does not seem to truly indicate the reaction degree of GGBFS in the assessed systems. The shifting of the reaction mechanism is also consistent with the acceleration period being identified at prolonged times with an increasing NaAc content in the activator. The findings presented in Figure 6.1 (A) provide confirmation of the hypothesis that the reaction process of slag can indeed be altered by adjusting the activator's composition, specifically the NaAc content in this study.

Figure 6.1 (B) illustrates the cumulative heat release of the blended (hydroxide+acetate)-activated slag for over a 28-day reaction period. A distinct pattern in the cumulative heat release curve emerged for AAS cement when NaAc content was altered, leading changes in the activator composition, with the exception of Sample 25NA. The cumulative heat released decreased as the activator type transitioned from Sample 0NA to 100NA, with the exclusion of Sample 25NA. However, Sample 25NA stood out due to its higher peak value and greater cumulative heat release, as evident in Figure 6.1 (A) and (B). Notably, the cumulative heat values recorded for Sample 100NA were considerably lower compared to those observed for the other AAS cement samples, including 0NA-75NA. While a detailed discussion of the comparison between Sample 0NA and 100NA was provided in Chapter 5, it is worth exploring blended systems based on the existing limited knowledge. The NaOH-AAS reaction process (Sample 0NA) exhibited rapid kinetics, whereas the inclusion of NaAc (Sample 100NA) with its lower pH led to a notably slower reaction process. However, when the activator composition was a blend of NaOH and NaAc, the situation is more complex, given that the mechanism of NaAc-activated AAS remains less understood, and it doesnot seem to be driven by an exothermic reaction. The reason for mentioning this is because isothermal calorimetry results, interpretated considering conventional knowledge of AAS, will indicate that the slag is not reacting as the NaAc activator is used, which was demonstrated in Chapter 5 not to be the case, and as it will be shown in the following sections.
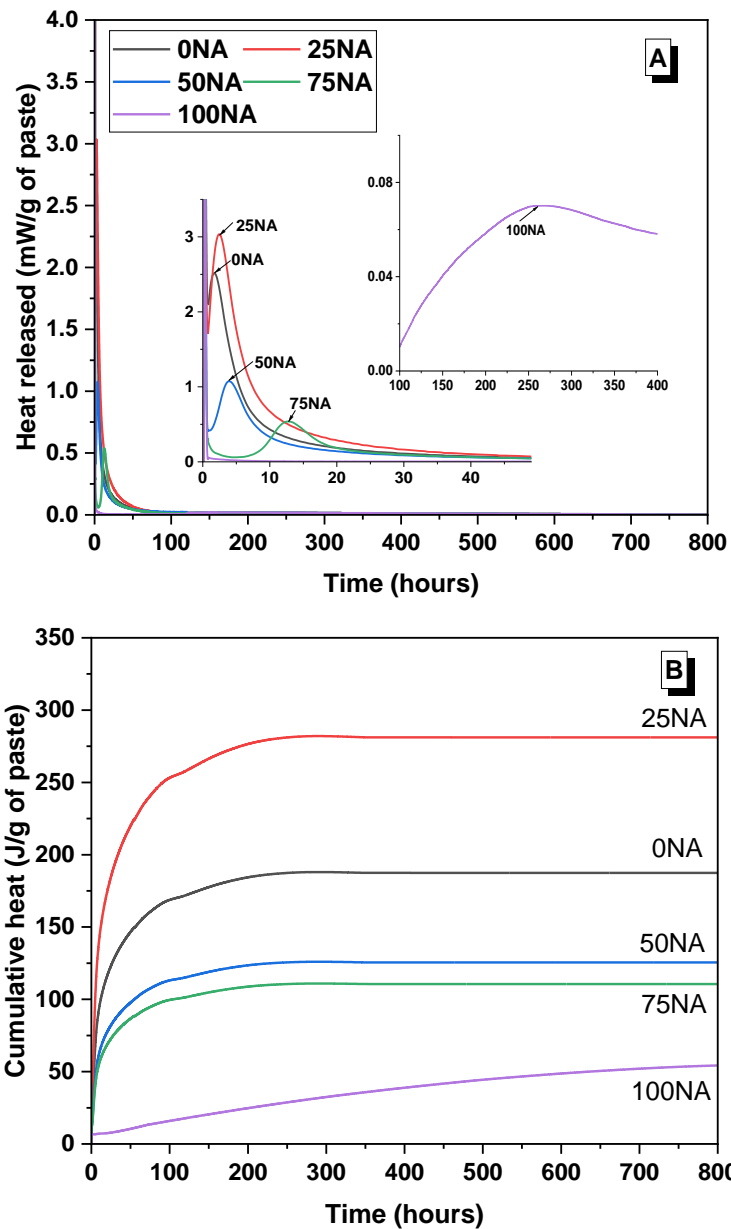
Figure 6.1 Alkali- activated slag cements produced with different activators of (A) heat release rate and (B) cumulative heat of reaction

6.4 Phase assemblage evolution

6.4.1 Mineralogical analysis

XRD results of the evaluated AAS pastes produced using different activators, changed with curing time are reported in Figure 6.2 (a)-(e). In the assessed AAS cement pastes at all curing ages, a crystalline peak occurring at around 29.5° in the 2θ position

was identified, and assigned to C-(A)-S-H type gel ($Ca_5Si_6O_{16}(OH)_2$; PDF# 00-029-0329), which is one of the main reaction crystalline products formed in AAS cements. These findings align closely with observations from previous studies conducted under similar alkaline conditions [Fernández-Jiménez et al., 2003, Escalante-García et al., 2003], as well as with the results discussed in Chapter 5. Traces of hydrotalcite ($Mg_6Al_2CO_3(OH)_{16}\cdot4H_2O$; PDF#01-089-0460) were observed at 2θ position around 11.6° in Figure 6.2 (a)-(e), recorded as the secondary reaction products in AAS systems. A peak attributable to this phase was not clearly identified in the paste solely produced with NaAc (100NA) after 3 and 7 days of curing, but it was evidently present at advanced curing times. Additionally, crystalline peaks identified at the 2θ position around 45° were assigned to calcium carbonates calcite (PDF# 01-083-0577) [Jin et al., 2015], as detected by XRD analysis. Furthermore, peaks corresponding to various calcium carbonate polymorphs, such as vaterite (PDF# 01-074-1867) was also identified.

In Figure 6.2 (a), it is evident that there were no notable changes observed from Sample 0NA to 75NA after a 3-day curing period. However, for the sample solely produced with NaAc (100NA), presented a considerably slower reaction process, as indicated by calorimetry results, and consequently crystalline reaction products were not observed at this early reaction time. After cured 7 days (Figure 6.2 (b), only a reflection of C-(A)-S-H type gel were identified in Sample 100NA system. By contrast, the other four AAS cement samples evaluated, produced with activators ranging from 100% NaOH to 25% NaOH (0NA to 75NA), did not display significant differences in their phase assemblages. Upon extending the curing period to 28 days, Figure 6.2 (c) shows that C-(A)-S-H type gels and hydrotalcite were both recognized as the main reaction products in all assessed AAS. This held true regardless of variations in the activator composition, as illustrated from curing times of 250 days to 360 days. This demonstrate that despite the pessimistic cumulative heat released results from isothermal calorimetry (Fig 6.2 (b)) the slag is indeed reacting, and therefore such results cannot be interpreted as an indirect measure of the slag degree of reaction in the cements studied here.

In Chapter 5, a hypothesis was formulated to gain insights into the impact of NaAc on the reaction process and mechanism of NaAc-AAS. However, the situation is complex due to the blending of NaOH and NaAc in varying molar ratios to create the blended activators. Furthermore, modifying the reaction process through changes in activator composition, where NaOH reacts rapidly and NaAc exhibits a much longer induction period of over 200 hours, adds to the complexity. Sample 25NA displayed the highest peak release rate in the blended composition, as recorded by calorimetry results in Figure 6.1. However, XRD results for Sample 25NA did not reveal any significant differences compared to other blended AAS cements. Notably, the pH value of the activator used for producing the 25NA cement was 13, which is slightly lower

than that of Sample 0NA. This suggests that the pH value may not be the sole factor contributing to the highest heat release rate observed in Sample 25NA. Understanding the functioning of blended AAS systems is a complex challenge. Numerous factors can influence the resulting AAS cements, making it difficult to pinpoint specific causal relationships.
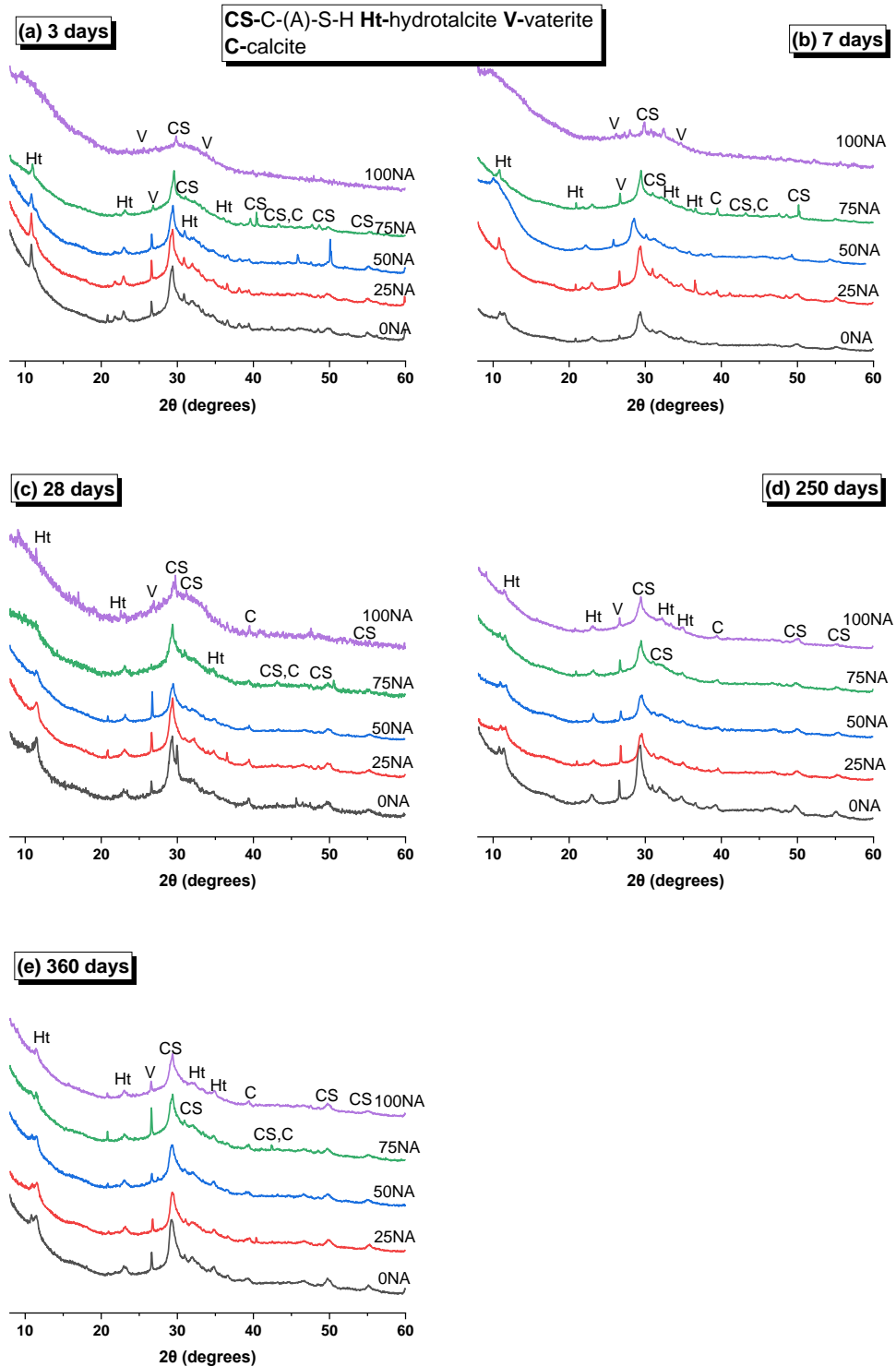
Figure 6.2 XRD patterns of the evaluated AAS cements changed with curing time, where (a) 3 days, (b) 7 days, (c) 28 days, (d) 250 days and (e) 360 days of curing.

6.4.2 Spectroscopic analysis of reaction products forming

The FTIR spectra associated with the AAS cement after cured 3 days, 7 days, 28 days, 250 days and 360 days is presented in Figure 6.3 (a)-(e). Also, similar vibration bands to those observed in the NaOH-AAS cement were detected in Sample 25NA to Sample 100NA. The bands at the wavenumber range of 941-978 cm^{-1}, according to the Si-O-T, presented as v_3(Si-O) asymmetric stretching vibrations of C-(A)-S-H type gel [Puertas et al., 2011, Puertas et al., 2004], indicate that the reaction of slag is occurring during the initial time of reaction. This somehow agrees with the calorimetry results, where it was observed that the addition of NaAc prolonged the appearance of the acceleration period, but a cumulative heat release was still recorded as shown in Figure 6.1. This band also shifts to a higher wavenumber when curing time prolonged from 3 days to 28 days. The band attributed to the Si-O band owing the stretching vibration was also observed around 649-666 cm^{-1}, with no significant difference from that in NaOH-AAS [Puertas et al., 2011, Gong et al., 2019]. The v_2[OH] symmetric bending vibrations was observed at 1662-1649 cm^{-1} [Wiyantoko et al., 2015]. This indicates the presence of hydrotalcite formation in the systems [Wiyantoko et al., 2015]. These results align with the XRD results illustrated in Figure 6.2, where hydrotalcite was clearly identified.

There are two bands identified in these pastes corresponding to the anti-asymmetric stretching vibration v_3[CO$_3$]$^{2-}$ located at around 1414-1420 cm^{-1} indicating that some carbonation has happened to these pastes [Cao et al., 2020b, Puertas et al., 2011], in coherence with the carbonate polymorphs detected by XRD (Fig 6.2). Distinctive bands were existed within the 1340-1560 cm^{-1} region in all the evaluated AAS samples except Sample 0NA which is NaOH-AAS: one at 1341-1348 cm^{-1} and another at 1546-1559 cm^{-1}. These bands were separately corresponded to symmetric and anti-symmetric stretching vibrations v[CO$_2$], and were associated with acetate anions [Pang et al., 2015]. Although no crystalline phases assigned to NaAc was detected in the XRD patterns, which could possibly due to the acetate anions was presented in the solid phase.

The IR spectra of AAS cement pastes produced with various activators, featuring different compositions regarding the substitution of NaAc for NaOH, did not exhibit any noticeable variations, as depicted in Figure 6.3 (a)-(e). This observation emphasizes that changes in the NaAc content did not result in structural modifications in the produced AAS cements, as evidenced by FTIR characteristics. The XRD results in Figure 6.2 further corroborate this finding. Overall, even in the case of Sample 100NA, varying the replacement ratios of NaAc for NaOH in the activator composition did not result in any detectable significant alterations.
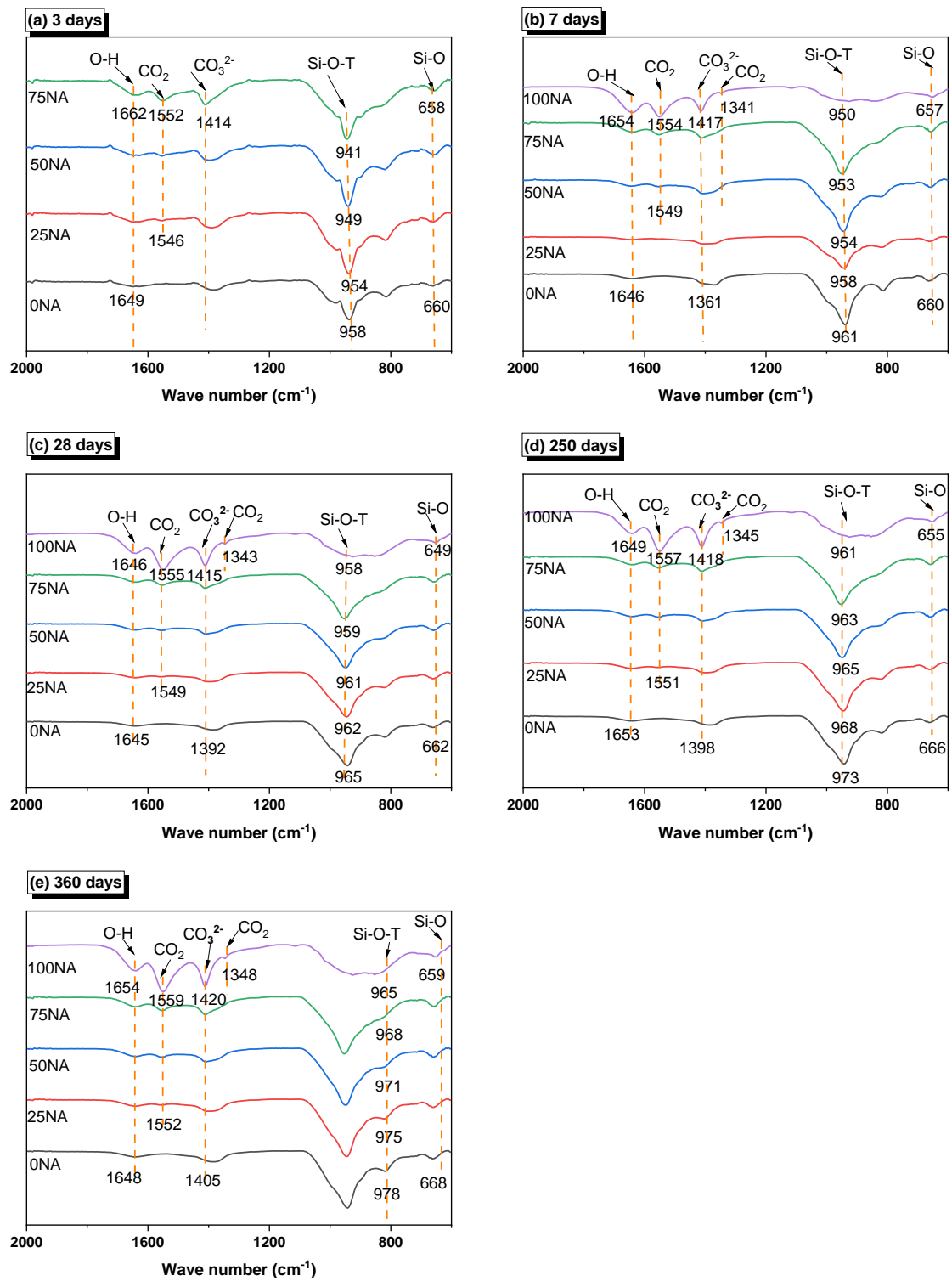
Figure 6.3 FTIR spectra of the AAS paste produced by blended activators curing after, (a) 3 days. (b)7 days, (c) 28days, (d) 250 days and (e) 360 days.

6.4.3 Thermogravimetry analysis

The mass loss due to potential reactions during temperature variation, influenced by the activator composition featuring varying NaAc content, has been documented in Figure 6.4 (A). Figure 6.4 (B) presents the first derivative of the TG data, depicted as DTG curves.

Figure 6.4 (A) reveals that cements produced with NaAc (100NA) exhibited the lowest mass loss, suggesting a lower degree of slag reaction within the same temperature range when compared to the other samples. This finding aligns with the observations in the NaAc-AAS cement presented in Chapter 5. The DTG curves depicted in Figure 6.4 (B) reveal the presence of several peaks, each corresponding to potential reactions occurring within different temperature ranges. Notably, the mass loss occurring below 200°C is attributed to binding gels decomposed, specifically C-(A)-S-H type gel [Ben Haha et al., 2011a, Kim et al., 2013], as illustrated in Figure 6.4 (B). The mass loss below 200°C exhibited a decline with the increased inclusion of NaAc in the activator composition. This decline suggests a reduction on the amounts of C-(A)-S-H gels present in AAS cements when the substitution ratio of NaAc for NaOH increased. The second temperature range of 200-400°C was associated with the decomposition of the crystalline products, such as hydrotalcite-like phases [Rozov et al., 2010, Kim et al., 2013]. The temperature range of 600-800°C was mainly assigned to the decomposition of calcium carbonates (i.e. calcite) [Kim et al., 2013, Ben Haha et al., 2011b].

As extensively discussed in Chapter 5, NaOH-AAS initiates a rapid reaction process, whereas the introduction of NaAc notably delays this reaction. The total mass loss results, ranging from 16.16% for Sample 0NA to 6.25% for Sample 100NA, align with this finding. Interestingly, the total mass loss with different levels of NaOH substitution by NaAc, were quite small, indicating that comparable degrees of reaction are achieved in the cements evaluated. This once again corroborates the hypothesis that the isothermal calorimetry results cannot be used as an indirect indicative of the degree of reaction in NaAc-AAS.

The paste 25NA exhibited the highest mass loss at 16.4%, which is similar to that recorded for the NaOH-AAS, consistent with the highest heat release rate observed in isothermal calorimetry results (Figure 6.1). A definitive explanation for the unique properties of Sample 25NA remains elusive, but results seem to indicate that 25 % NaAc replacement seems to be an optimum replacement value. No significant distinctions are evident among AAS cements generated using various activators, even when the replacement ratio of NaAc for NaOH is altered.
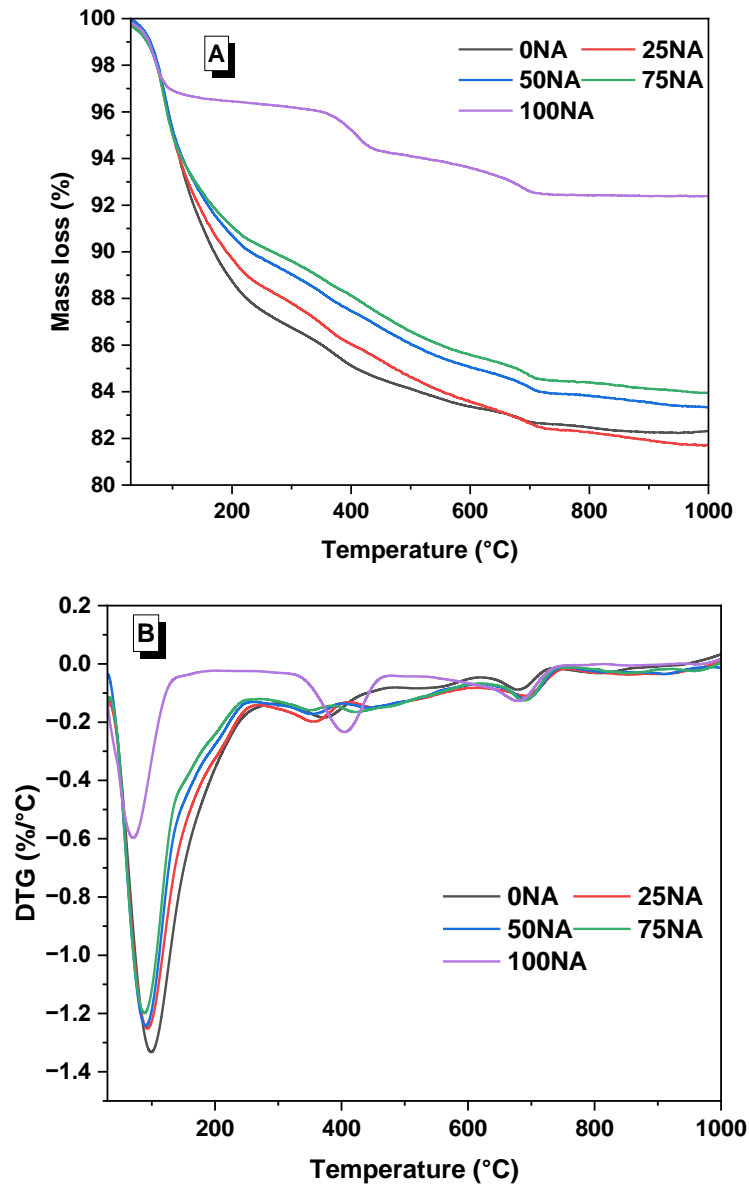
Figure 6.4 Thermogravimetric curves of AAS pastes with different composition after 28 days of curing, where (A) TG curves of the evaluated AAS pastes (B) DTG curves of the assessed AAS pastes.

Table 6.3 presents the mass loss values calculated from TG curves for various AAS cement pastes, which were produced using different NaAc/ NaOH blends, and these measurements were conducted up to 600°C. The reaction degree of AAS pastes can be assessed by examining the mass loss resulted by the occurred reaction of C-(A)-S-H gels decomposed within 30-200°C, where water loss has occurred. The rationale for selecting the temperature range for total mass loss up to 600°C was detailed in Chapter 5. The mass loss values related to the C-(A)-S-H gels cured after 28 days are summarized in Table 6.3.

As observed in Chapter 5, Sample 0NA demonstrated a slightly higher reaction degree in comparison to Sample 100NA. The reaction degree of the assessed AAS

cement pastes can be listed as follows: Sample 25NA> 0NA > 50NA > 75NA > 100NA. The decrease in the reaction degree is noticeable with the increased incorporation of NaAc, which partly consistent with the observations made for Sample 25NA in the calorimetry results presented in Figure 6.1.

Table 6.3 Mass loss calculated from TG up to 600°C, the mass loss according to C-(A)-S-H was calculated up to 200°C

Sample	Mass loss (%)	
	28-day	
	C-(A)-S-H	Total mass loss
0NA	11.01	16.16
25NA	10.03	16.40
50NA	9.27	14.93
75NA	8.65	14.16
100NA	3.39	6.25

6.4.4 Microstructure analysis

Figure 6.5 (A)-(E) shows BSE images at various magnification of AAS produced by different activators after cured 360 days. In the micrographs, the light grey in represent of the slag particles which were not reacted persisted in Sample A-E. Areas printed in grey situated among these residual GGBFS particles represent the main binding phase, comprises the C-(A)-S-H gel, traces of LDHs as well as carbonates appeared [Ben Haha et al., 2011a, Ke et al., 2016, Ke et al., 2017], as determined by XRD analysis (refer to Figure 6.2 (a)-(e)), similar like that observed in Section 5.6.5 of Chapter 5. The presence of light grey particles, as evident in Figure 6.5 A1-E1 at the same magnification, aligns with unreacted slag particles. This observation indicates a discernible decrease in the reaction degree as the NaAc content in the activator boosted from 0 to 100%, moving from Sample 0NA to 100NA. In coherence with the isothermal results shown in Figure 6.1 and Figure 6.2, observations were made that the augmentation of NaAc content extended the reaction process.
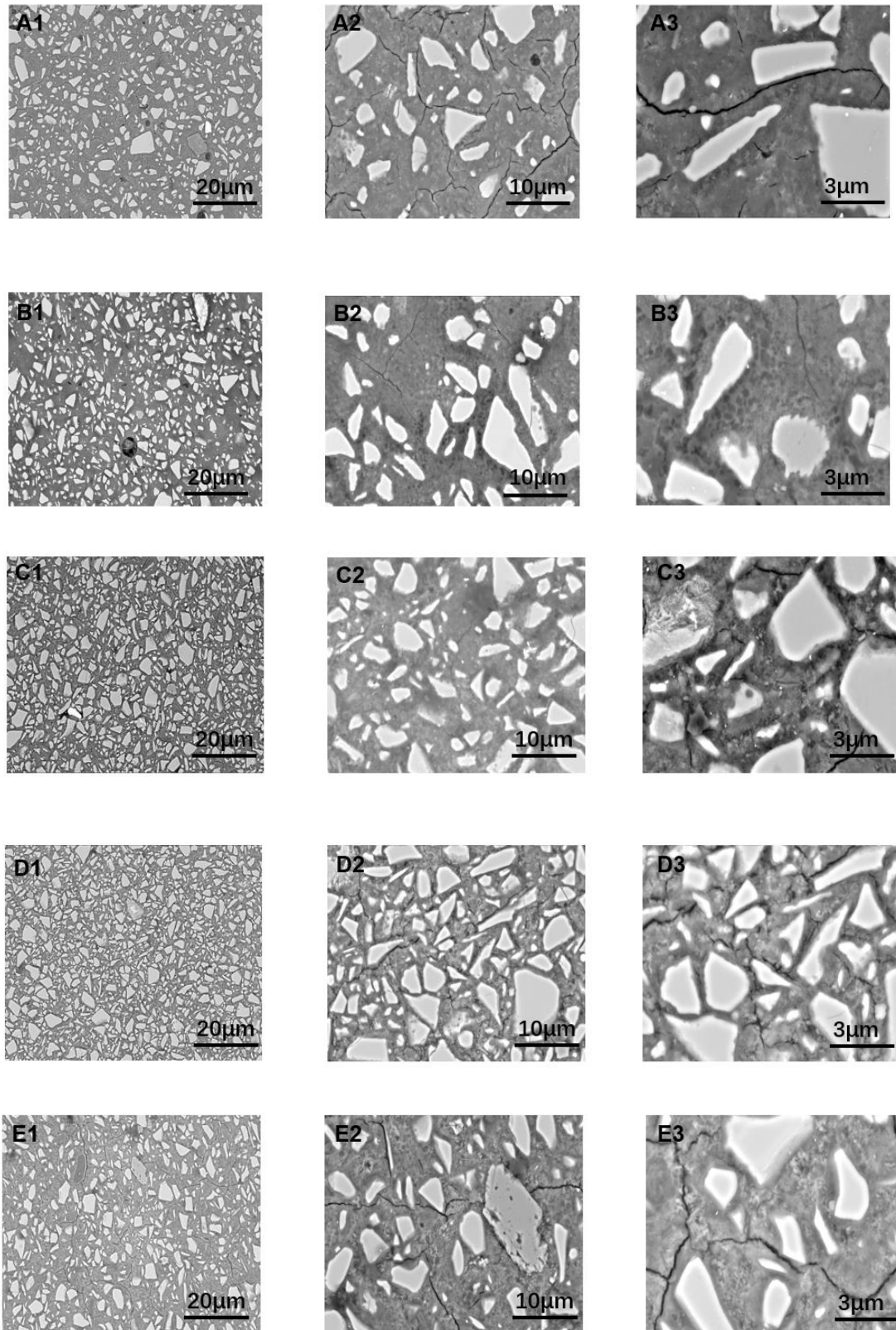
Figure 6.5 BSE images at different magnification of (A) 0NA, (B) 25NA.(C) 50NA, (D) 75NA and (E) 100NA after cured 360 days.

Figure 6.6 (A)-(B) illustrates correlation plots of atomic ratios generated from EDS spot analyses conducted on AAS samples prepared with varying activators containing 0 % to 100% of NaAc substitution. Each sample formulation underwent sampling procedures outlined in Chapter 3, resulting in the acquisition of over 60 data points for analysis. The reaction product, comprising the C-(A)-S-H type gel together with gels mixed with LDHs within GGBFS [Wang et al., 2022, Ben Haha et al., 2011a] are displayed in the data provided here in the form of atomic ratios. Data points exhibiting Al/Si ratios lower than 0.8 (as depicted) are selected for exploring the chemical composition of the formed hydrotalcite-like phase, as well as C-(A)-S-H type gels, consistent with the similar data reported in other studies [Kapeluszna et al., 2017, Wang et al., 2022].

Figure 6.6 (A) displays the data points illustrating the relationship between Ca/Si and Al/Si ratios. The range of Ca/Si ratios exhibited a notable shift, primarily from 0.3-1.5 to 0.4-2, as the NaAc content was incrementally increased from 0% to 100%. It is evident that the Ca/Si ratios experienced a slight increase from 1.5 to 2, corresponding to the progression from Sample 0NA to 100NA, mirroring the NaAc content increment in the activators. Notably, there were no significant variations in the Ca/Si ratios, with the exception of Sample 100NA, which utilized 100% NaAc. In this case, the Ca/Si ratios reached up to 5, in contrast to the 1.5 ratio observed in NaOH-AAS. This observation suggests that the incorporation of NaAc as a replacement for NaOH in the activator design did not induce substantial arrangements in the formed C-(A)-S-H type gels' composition. The findings align with those obtained through XRD analysis, as presented in Figure 6.2. The dashed line in Figure 6.6 (A) represents a Ca/Al ratio of 1.4, related to the regions associated with C-(A)-S-H gels.

Figure 6.6 (B) depicts plots of data points featuring Mg/Si versus Al/Si. The observed correlation between Mg/Si and Al/Si strongly suggests hydrotalcite-like phases appeared [Yi et al., 2014, Ben Haha et al., 2011b]. In Figure 6.6 (B), the dashed lines represent hydrotalcite-like phases with Mg/Al ratios of 2.4 in Sample 0NA, 1.9 in Sample 25NA, 2.1 in Sample 50NA, 1.8 in Sample 75NA and 1.4 in Sample 100NA, respectively. The Mg/Al=2.4 aligns with previous findings on NaOH-activated slag cements, where hydrotalcite-like phases with an approximate ratio of Mg/Al = 2 are typically identified [Lee et al., 2016, Fernandez et al., 2005]. It is noteworthy that a reduction in the Mg/Al ratio, shifting from 2.4 to 1.4, is observed in the hydrotalcite-like phases with the increase of NaAc content. It is important to highlight that there is a decrease in the Mg/Al ratio, transitioning from 2.4 to 1.4, with the progressive addition of NaAc. Conversely, the Mg/Al ratio experiences a slight increase from 1.9 to 2.1, followed by a subsequent decrease to 1.8 as the NaAc content increases from 25% to 50% and then to 75%. The variation in the Mg/Al ratio suggests the potential differences in the extent of aluminum substitution inside C-(A)-S-H gels [Myers et al., 2015]. The intercepts at approximately 0.46, 0.33, 0.40, 0.29, and 0.07 on the Al/Si axis

corresponding to Mg/Al ratios of 2.4, 1.9, 2.1, 1.8, and 1.4, respectively, indicative of the incorporation of aluminum into C-(A)-S-H type gel. This demonstrates that incorporate aluminum into C-(A)-S-H type gels fluctuates with the NaAc content, and the formed hydrotalcite-like phases undergoes changes as well.
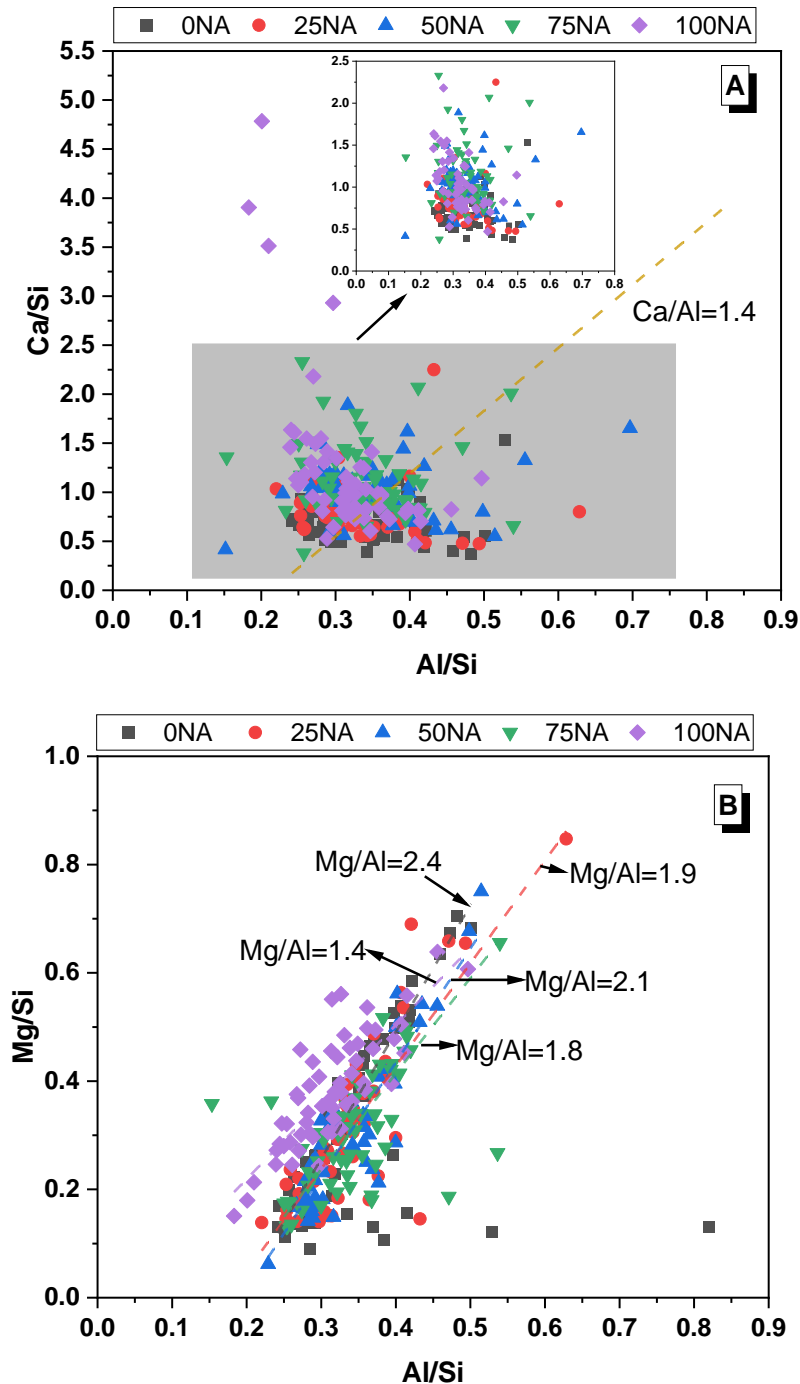
Figure 6.6 Plots of EDS spot map atomic ratios comparing for AAS cement produced by different activators with NaAc replacement to NaOH from 0-100% curing after 360 days, (A) Ca/Si vs Al/Si and (B) Mg/Si vs Al/Si

6.5 Mechanical and physical properties

6.5.1 Compressive strength

The compressive strength of the evaluated AAS cements prepared by different activators varied as curing time up to 28 days was presented in Figure 6.7. Sample 100NA did not harden after 7 days of curing and thus only 28-day compressive strength of Sample 100NA is reported and compared to other blended system. This observation aligns with the compressive strength findings presented in Chapter 5, which further corroborated by calorimetry results that Sample 100NA requires at least 261 hours to reach its maximum heat release rate, as illustrated in Figure 6.1. For the remaining cement pastes evaluated, following 3 days of curing, the compressive strength exhibited a consistent decrease as the NaAc content increased, ranging from 16.89 MPa for 25NA to 12.67 MPa for 75NA. This trend persisted across all curing times up to 28 days for the AAS cements. Sample 0NA displayed a notably higher compressive strength after cured 7 days, reaching 29.16 MPa. It is worth noting that not a higher compressive strength owing by Sample 25NA compared to Sample 0NA, inconsistent with the trends observed in the calorimetry results and the higher mass loss reported in Table 6.3. As the curing time progressed, the compressive strength of the AAS cements increased. After cured 28 days, the Sample 0NA maintained the highest compressive strength up to 43.23 MPa among all the blended samples. the Sample 25NA achieved a compressive strength value of 37.42 MPa, representing a 13.4% reduction compared to Sample 0NA. The subsequent compressive strength values decreased in the following order: 33.57 MPa for Sample 50NA, 28.73 MPa for Sample 75NA, and finally, 26.16 MPa for Sample 100NA. These results are differ from those reported in [Al-Kheetan et al., 2020c] where NaAc was used in Portland cement systems as an admixture of reducing concrete permeability. The inclusion of 2% or 4% NaAc (relative to the cement mass) led to an enhancement in the compressive strength of the resulting concrete, even under extremely low-temperature conditions of -25°C [Al-Kheetan et al., 2020a]. While NaAc exerts a distinct influence on AAS cement, the compressive strength values observed after 28 days of curing are comparable to those in the aforementioned concrete. However, a remarkable rise occurred on the compressive strength exhibited by concrete incorporating 4% NaAc at a w/c ratio of 0.37, this could attain approximately 52MPa at a temperature of 21°C [Al-Kheetan and Rahman, 2019]. Results primarily differ from the variations in chemistry between OPC and AAS systems, and the fact that the acetates added are serving different purposes in each study.

In summary, the compressive strength of blended AAS cements exhibited a consistent decrease with an increasing NaAc content at all curing ages, ranging from 3 days to 28 days. The common strength requirements of alkali-activated slag cements is

at the range of 40-60 MPa after 28 days [Awoyera and Adesina, 2019] of curing for structural applications. However, all the cementitious systems evaluated exhibited the compressive strength > 20MPa after cured 28 days, even those solely produced with NaAc. This corroborates that the compound is an effective activator for producing slag-based cements.
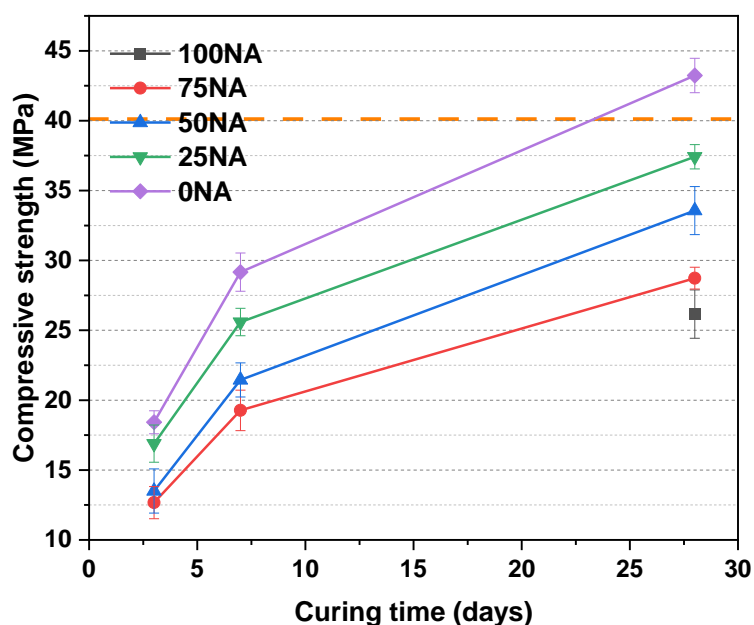
Figure 6.7 Compressive strength as a function of curing ages

6.5.2 Water contact angle (wettability)

Water contact angle representing the wettability of AAS cement produced with blended alkaline activators after cured 28 days was listed in Table 6.4. As discussed in Chapter 5, as acetates are often used to impermeabilize concretes, wettability was evaluated to determine if using such compounds as activators for producing AAS might have a similar effect. A detailed discussion is reported in Chapter 5 about the wettability of the AAS named Sample 0NA and 100NA after cured 28 days. It was then concluded that the sample 0NA is completely wetting, and although the wettability changes with the inclusion on NaAc, the behavior of AAS cements produced with NaAc cannot be classified as hydrophobic, as the water contact angle recorded do not exceed 90° [Yao et al., 2021]. It is worth noting that the water contact angle values recorded in this study are consistent with those reported by Al-Kheetan [Al-Kheetan et al., 2020b] evaluating the effect of different hydrophobic commercial substances in pavements, which

indicates that the wettability of the cements studied here is promising, and these materials might present unique impermeabilizing properties.

When the ratio of NaAc with substitute NaOH in the composition was increased from 0 to 25%, the water contact angle could be measured for Sample 25NA as shown in Table 6.4. As the NaAc substitution was continuously increased, the water contact angle value for Sample 50NA was higher than that of Sample 25NA. This suggested that water contact angle (<90°) increased in the 50NaAc/50NaOH activated slag cement system, followed this by a significant decrease of the contact angle at higher NaOH replacement levels. This indicates that there is an optimal value of the blended activator composition reducing the wettability of activated slag cement. It is difficult to explain why the water contact angle was suddenly reduced from Sample 50NA to Sample 75NA, as there are many factors which could influence the water contact angle including the physical aspects and chemical aspects [Yao et al., 2021]. Nevertheless, the water contact angle has an obviously increase from Sample 75NA to Sample 100NA, demonstrating that the wettability reduced.

Although it is unclear how NaAc affect the wettability in present of contact angle changed, it was confirmed that the blended activators are pivotal in on moderate the hydrophobicity potential of these novel activated slag cements. It is feasible that the hydrophobic property could be modified by changing the composition of activators in the blended AAS system especially the molar ratio of NaAc. This would be beneficial for the application of these materials, which could potentially be used as coating materials for impermeabilization of concrete structures. Further investigation is required to help understand how NaAc affect the hydrophobic property of the AAS cements produced by the blended activators.

Table 6.4 Water contact angle development as a function of the composition of the activators

Activator type	Water contact angle after 28 days of curing
0NA (NaOH-AAS)	✘

25NA
(25NaAc-75NaOH-AAS)

50NA
(50NaAc-50NaOH-AAS)
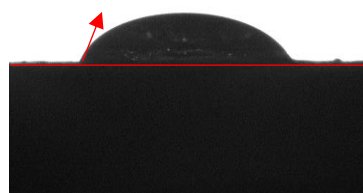
75NA
(75NaAc-25NaOH-AAS)
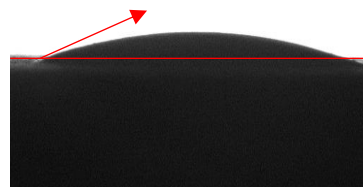
100NA
(NaAc-AAS)
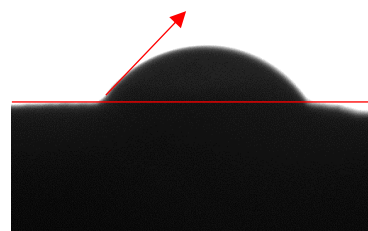
6.6 Conclusions

Ground granulated blast furnace slag cements were manufactured using blended activators, wherein the molar ratio of NaAc is varied as a substitute for NaOH within the activator composition. The characteristics of the resulting cement pastes were evaluated using a variety of techniques drawing to the following conclusions:

The incorporation of 25% NaAc as a substitute for NaOH resulted in a notably higher heat release rate and a slightly greater cumulative heat release when compared to NaOH-AAS. As the replacement of NaOH with NaAc was increased from 50% to 100%, there was an extension in the heat release rate of the reaction. Simultaneously, the cumulative heat released during the reaction significantly decreased with the higher NaAc content in the blended activator composition.

X-ray diffraction analysis revealed the presence of hydrotalcite and C-(A)-S-H type gel in represent of the main reaction products among all AAS samples assessed, independently of the NaAc content in the activator. These findings were further corroborated by ATR-FTIR results. Thermogravimetry results indicated that the mass loss observed in NaAc-AAS was notably lower compared to that in NaOH-AAS. The amounts regarding the formed C-(A)-S-H type gels among various systems, independently of the NaAc content (up to 75%) are comparable. This indicates a similar degree of reaction in the evaluated AAS cements, despite contrasting isothermal calorimetry results. Hence, it is suggested that isothermal calorimetry results cannot serve as an indirect indicator of the reaction degree in AAS cements produced by blended activators that incorporate NaAc as a substitute for NaOH. Additionally, hydrotalcite-like phases exhibit with varying Mg/Al ratios corresponding to the NaAc content within the activator composition.

Substituting NaAc for NaOH in the activator composition had the consequence of diminishing compressive strength, with this decline persisting as greater amounts of NaAc were integrated, even after 28 days of curing. However, even in samples produced solely with NaAc as an activator, compressive strength of >20MPa are recorded after 28 days, making the material suitable for use when moderated strength is required.

The impermeability level, as indicated by the water contact angle, exhibited enhancement upon the introduction of NaAc to the activator composition. Furthermore, a 50% replacement of NaAc for NaOH appears to be the optimum activator composition, as it enhances on reducing permeability of the produced AAS cement.

Chapter 7 – Effect of magnesium acetate addition in the phase assemblage of alkali-activated GGBFS cements pastes

7.1 Introduction

The effectiveness of using sodium acetate and potassium acetate as alternative activators for producing alkali acetate-AAS was evaluated in previous chapters. The blast furnace slag chemistry, which can be described in the four-component oxide system: $CaO–SiO_2–Al_2O_3–MgO$ strongly influences the type and amount of the formed reaction products in AAS [Bernal et al., 2014c, Liao et al., 2023]. Previous research has validated that the amount of MgO in GGBFS can notably influence the chemical composition and structure of the binder phase, as well as the nature of secondary reaction products that develop [Zhang et al., 2022, Bernal et al., 2014c]. In systems produced with conventional activators such as NaOH or Na_2SiO_3, the amount of MgO in GGBFS determines the type of the formed hydrotalcite-like phase (Ht) [Walkley et al., 2021, Ben Haha et al., 2011b]. It has also been demonstrated in some AAS, that an increased formation of hydrotalcite increases the CO_2 binding capacity of these cements which leads to higher carbonation resistance of these materials [Bernal et al., 2014c, Ke et al., 2018b]. Therefore, the variation of different methods of increasing the MgO content in the system is of interest, including choosing various GGBFS with different MgO content, and adding additional external MgO into the system. MgAc is one of metal acetates that include magnesium thus could be treated as alternative MgO-source.

The majority of European and North American slags used for manufacturing AAS exhibit the MgO content among the range 7-10%. According to the literature [Ben Haha et al., 2011b], an MgO content in the slag between 7% to above 10% can effectively induce the increase of the quantities of hydrotalcite-like phase forming when using conventional activators. Few studies have evaluated the effect of adding different magnesium sources to alkali-activated cements. Jin et al. [Jin et al., 2015] produced the AAS pastes with a content of 2.5-7.5% of MgO by adding different reactive MgO and found that more Ht was formed in the AAS pastes with adding an external MgO source increased. Moreover, when the content of MgO was exceeded above 7.5% it resulted a remarkable enhancement of Mg/Al in the Ht, and Al replacement in the C-(A)-S-H type gels forming, compared with that Mg/Al identified in cements produced with addition of 5% of MgO. The resulted increase in the amount of Ht forming in AAS, and the rise of Al incorporation in the C-(A)-S-H type gels, was attributed to the acceleration of slag

reaction, in coherence with the observation by Hwang et al. [Hwang et al., 2018]. He et al. [He et al., 2021] investigated four different AAS cements with MgO contents varying from 0 to 10%. For conventional NaOH-activated slag, more Ht was formed than that of waterglass due to the high pH resulted in a rapid reaction. However, the introduction of Mg from MgO benefits formation of more hydrotalcite in Na_2CO_3-activated AAS and more AFt in Na_2SO_4-activated AAS. It was concluded that the optimal content of MgO is 4-6% for AAS cement produced with Na_2CO_3 and Na_2SO_4. Hydrotalcite formation seem to be also favored when the magnesium to aluminum and silica (Mg/(Si + Al)) ratio was over 0.58, in alkali-activated binders cured under hydrothermal conditions [Wang et al., 2021]. It is worth noting that all these studies were conducted in cements produced with conventional activators, and no studies have been found using magnesium acetates (MgAc).

Therefore, the aim of this study was to determine the feasibility of using magnesium acetate as a suitable source of MgO for inducing changes in phase assemblage of NaOH-activated slag cements, particularly evaluating the formation of the secondary phase hydrotalcite-type phase. Using magnesium acetate has a great advantage, as it eliminates the potential risk of conversion of MgO to $Mg(OH)_2$, and the associated damage it can cause, which is the main concern when adding MgO in Portland cement materials.

7.2 Mix design and sample preparation of the evaluated cements

MgO content was varied by adding MgAc powder. The quantity of magnesium acetate was first determined considering the solubility of magnesium acetate in water at 20°C (53.4 g/100 mL [Williams, 1996]), so such value was not exceeded in this study. The dose of MgAc was determined to ensure the total MgO content (from GGBFS+ MgAc) in the cementitious system was above 10 wt.% of the dry mix, this meets the needs for monitoring the potential adjustments in the phase assemblage evolution of AAS cement. The dosage of MgAc in this study was 12g listed in Table 7.1. The mix design of the evaluated AAS systems were also included. The procedure of AAS pastes preparation was described in details in Chapter 3.

Table 7.1 Mix design of NaOH-AAS added with MgAc

Mix ID	Activator dose Na_2O (wt.%))	Activator type	individual component in activator (g)		GGBFS (g)	water(g)	w/b	MgO from MgAc (g)	Total MgO (g)
			MgAc	NaOH					
NN	4	NaOH	0	5.16	100	31.55	0.3	0	7.25

12NM	4	NaOH-MgAc	12	5.16	100	35.14	0.3	3.38	10.63

7.3 Reaction kinetics

The effect of MgAc (NaOH-MgAc) addition in the heat flows during the reaction of NaOH-activated slag cement (NaOH-AAS) is shown in Figure 7.1. Independently of the addition of MgAc, two distinctive exothermic peaks are identified in the evaluated paste. The initial peak in the NaOH-AAS and NaOH-MgAc AAS in Figure 7.1 (A) quickly appeared at only serval minutes after mixing, as a result of the pre-induction step. This could be formed by wetting occurred on GGBFS particles, an on-set of GGBFS dissolution [Ben Haha et al., 2011b].

In the absence of MgAc a higher cumulative heat release (Figure 7.1(B)) is identified during the first 300 h of reaction in NaOH-AAS, which was resulted by a higher reaction degree owing by GGBFS. However, considering the results from Chapter 5 and Chapter 6, where it was identified that the reaction of slag with acetates is not exothermic, it can be argued that the reduced heat release is perhaps only showing that the addition of the MgAc is changing how the reaction proceeds.

After a reduced induction period, a second exothermic region is observable in the calorimetry curves of the NaOH-AAS system, which is assigned to the acceleration period resulting by the reaction products formed and precipitated [Burciaga-Díaz and Betancourt-Castillo, 2018, Gijbels et al., 2020]. This was then followed by an asymmetric deceleration period, showing a high heat release for the first 40h followed for a low heat release for over 300 hours after mixing. In the absence of MgAc, a pre-induction peak and the acceleration peak are coincided, while for conventional AAS has been associated with a fast condensation of silica and alumina species [Sun and Vollpracht, 2018b]. The intensity of the acceleration peak is related to the composition of slag, and the setting time and strength of AAS is influenced by the reaction process and reaction products [Burciaga-Díaz and Betancourt-Castillo, 2018, Song et al., 2000].

The addition of MgAc lead to a significant difference in the acceleration period, which reached a maximum value at 7 hours, being slightly slower than that observed in NaOH-AAS paste. This indicated that a slower reaction process is occurring in the NaOH-MgAc AAS consistent to what was observed in Chapter 6, where addition of NaAc also impacted the kinetics of reaction of NaOH-AAS systems. However, this is somehow inconsistent with the observations by He et al. [He et al., 2021], which NaOH activated slag containing higher MgO content shown a quick reaction, indicating that more MgO accelerate the reaction process. The incorporation of MgAc was initially considered as an additional Mg-source in the system. However, distinctions exist

between MgAc and MgO. MgAc does not straightforwardly emulate the role of MgO, particularly its ability to facilitate the enhanced formation of hydrotalcite-like phases.
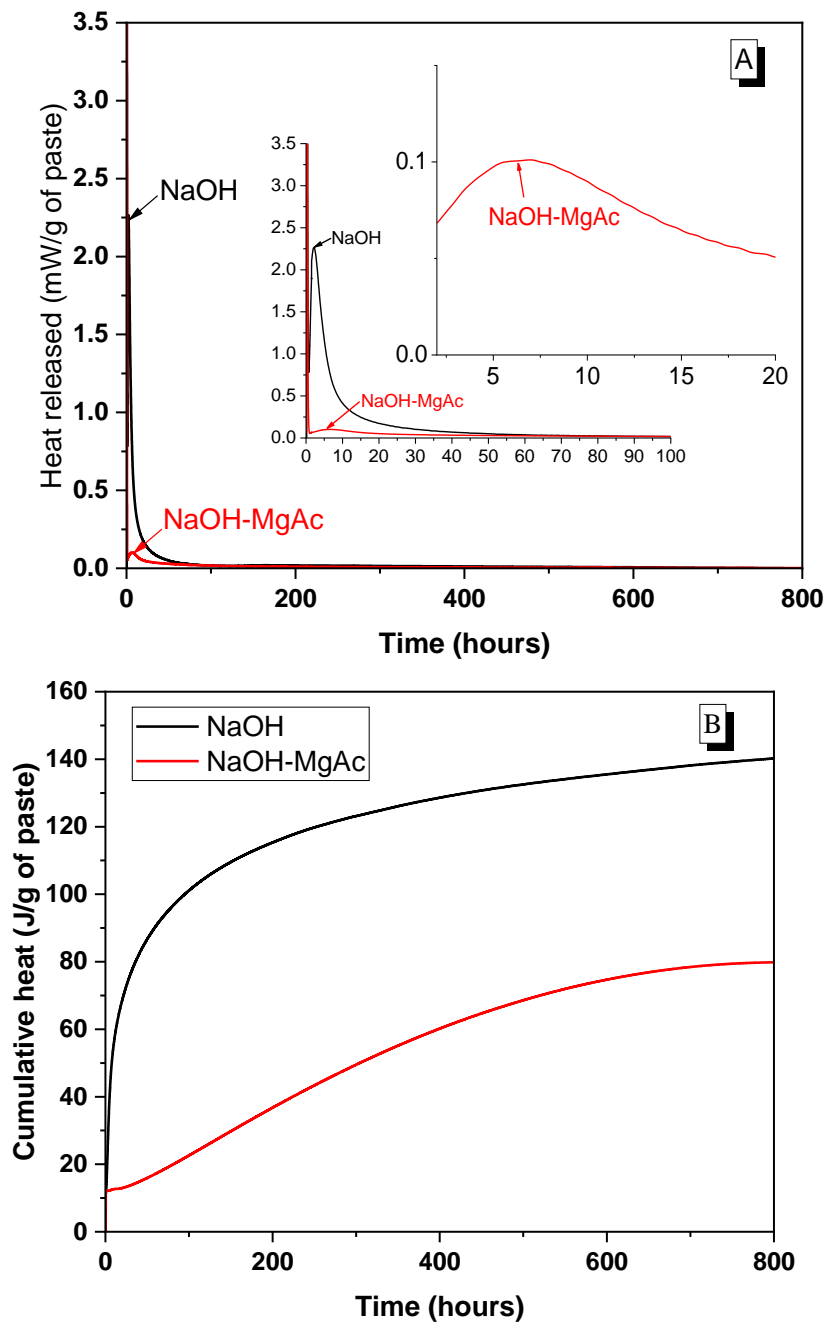
Figure 7.1 Isothermal calorimetry results for NaOH-AAS with or without MgAc, showing (A) Heat release rate curves, including inserts to show features a short testing durations, and (B) Cumulative heat of reaction (relative to mass of mixed paste). The time reported does not account for mixing time

7.4 Phase assemblage evolution

7.4.1 Mineralogical analysis

Figure 7.2 (a) and (b) depicts the XRD results of the NaOH-AAS with and without adding MgAc, respectively. The broad band identified between 25°-35° 2θ correspond to the CaO–Al_2O_3–MgO–SiO_2 glassy component of GGBFS with a short order [Bernal et al., 2014c]. In both evaluated slag pastes the following crystalline phase were identified: a calcium silicate hydrate (C-S-H; $Ca_5Si_6O_{16}$ (OH)$_2$; Powder diffraction file (PDF) # 00-029-0329)) centred at 2θ 29.5°, in line with findings previously documented for NaOH-AAS at similar concentrations. [Sun and Vollpracht, 2018a, Ben Haha et al., 2011b]. Traces of hydrotalcite ($Mg_6Al_2CO_3$ (OH)$_{16}$·$4H_2O$; PDF#01-089-0460) [Jin et al., 2015] were observed around 11.6°, 23°, 33°and 37° in Figure 7.2 (a) and around 23° and 33° in Figure 7.2 (b). The peaks assigned to AFm phases such as monocarbonate ($Ca_4Al_2O_6$·CO_3·$11H_2O$, PDF# 00-036-0377) is only identifiable in NaOH-AAS after cured 28 days. This agreed with previous studies that report formation of an Al-substituted C-(A)-S-H and hydrotalcite as the main crystalline reaction products in AAS, when MgO content (in the system) were > 5wt.% [Ke et al., 2016]. In addition, peaks corresponding to calcium carbonate polymorphs such as vaterite (PDF# 01-074-1867) and calcite (PDF# 01-083-0577) were detected [Bernal et al., 2014c].

Conversely to what was expected in this study with the addition of MgAc, the diffractogram of the NaOH-MgAc AAS (Figure 7.2 (b)), does not show the main reflection attributed to hydrotalcite, which is located at 11.6° 2θ, however secondary peaks associated with this phase were observed. Hwang et al. [Hwang et al., 2018] found the optimal content of MgO for two different fineness of slag was 7.5 and 5% respectively, and the effect of MgO was to promote more hydrotalcite-type phases formed. This consistent with a study reported by He et al. [He et al., 2021], which shown that the diffraction peak of hydrotalcite becomes more prominent as more MgO is added. A content of 2.5-7.5% of MgO with different reactivities were added to NaOH-AAS and the results confirmed that both reactivity and the content of MgO influence the hydrotalcite-phase formation. For MgO-activated slag, higher dosage of MgO (up to 20%) has a beneficial effect on promoting secondary reaction products formed and the reaction degree [Park et al., 2020].

As reported in Table 7.1, the addition of MgAc introduced approximately 3 wt.% MgO in the system. Considering the slag composition included 7.25% MgO, it is estimated that the total MgO content in the cements produced was 10.63 wt.%. When the total MgO is above 10%, system may become more prone to the formation of expansive phases, such as brucite ($Mg(OH)_2$). Moreover, the formation of expansive phases competes with the development of desired hydrotalcite-like binding phases [Ben

Haha et al., 2011b]. Therefore, the MgAc addition is hindering the formation of ordered hydrotalcite similarly to what has been observed in Chapter 5 and 6 when adding NaAc or KAc acetates.
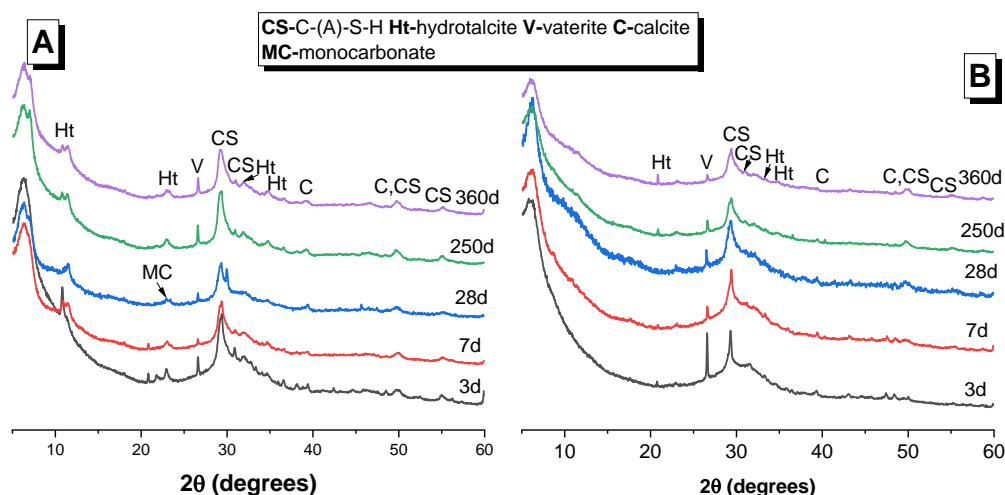
Figure 7.2 XRD patterns of the evaluated slag pastes, where (A) NaOH-AAS, (B) NaOH-MgAc AAS as a function of curing time

7.4.2 Structural features of reaction products forming

Figure 7.4 (a)-(c) show the infrared spectra of the evaluated AAS pastes after 3, 7, 28, 250 days and 360 days of curing. Both NaOH-AAS and NaOH-MgAc AAS pastes cured for 3 days (Figure 7.4 (a)), show the symmetric bending vibrations of v_2[OH] at 1649 cm^{-1} for NaOH-MgAc AAS, and at 1652 cm^{-1} for NaOH-AAS respectively, corresponding to the reaction products forming in AAS cements [Wiyantoko et al., 2015]. The main band assigned to the T-O-T band designated for an Al replaced C-S-H gel was centred at 958 cm^{-1} in NaOH-AAS, and at 951 cm^{-1} for NaOH-MgAc AAS [Cao et al., 2020b]. As discussed in previous Chapters, the move to higher wavenumber is likely associated with a higher crosslinked C-(A)-S-H type gels formed [García Lodeiro et al., 2010, Puertas et al., 2011]. The wavenumber assigned to the Si-O-T increased at longer curing durations (see Figure 7.4 (a) to Figure 7.4 (c)). Another band appeared at around 654 cm^{-1} to 662 cm^{-1} seen from Figure 7.4 (a)-(c) corresponded to the Si-O bonds owing stretching vibration in both NaOH-AAS and NaOH-MgAc AAS [Puertas et al., 2011]. In addition, peaks at around 1361-1415 cm^{-1} were observed and assigned to v_3[CO$_3$]$^{2-}$ vibration bonds [Puertas et al., 2011, Cao et al., 2020b], consistent with the calcium carbonate polymorphs identified by XRD in these samples (Figure 7.2) that showed that even at very early times of reaction some carbonation has occurred in

the samples. In NaOH-AAS with the addition of MgAc, a new position compared to bands in hydroxide-activated samples occurred at 1546-1563 cm^{-1}, attributed to stretching vibrations $v[CO_2]$ and was resulted by acetate anions [Pang et al., 2015]. However, no crystalline peaks assigned to MgAc was observed in XRD pattern results, suggesting that the acetate anions were presented within a solid phase.

No significant differences were founded in the IR spectra of NaOH-AAS and NaOH-MgAc AAS cement pastes as shown in Figure 7.3 (a)-(e), despite the remarkable differences observed in their kinetics of reaction when determined by isothermal calorimetry (Section 7.2.1). This demonstrates that the reaction products forming in the presence of MgAc have a similar structure to those identified in NaOH-AAS, in coherence with the XRD patterns as shown from Figure 7.2 (a)-(b).
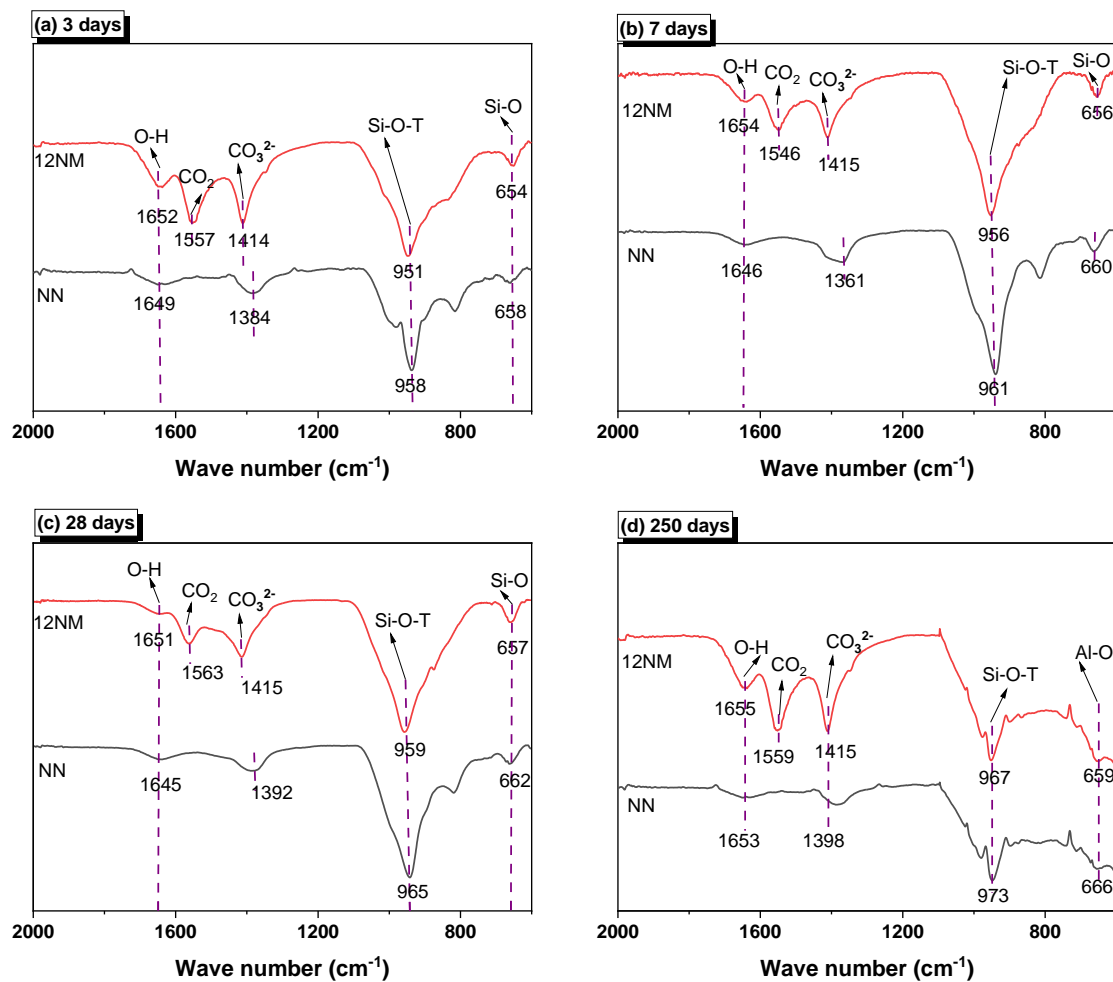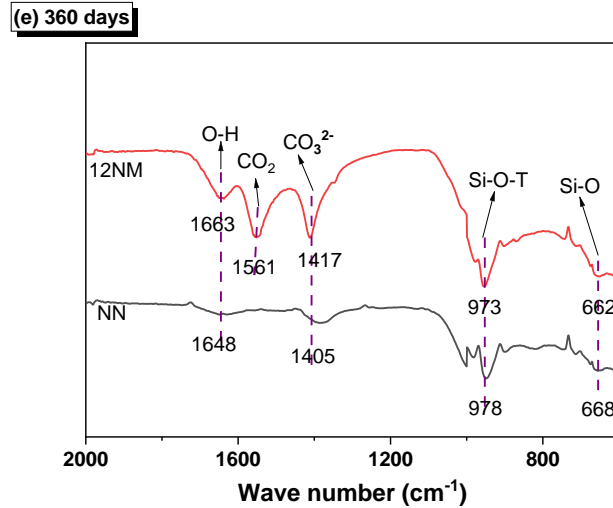
Figure 7.3 ATR FTIR spectra of the NaOH-AAS and NaOH-MgAc AAS after (a) 3 days of curing, (b) 7 days of curing, (c) 28 days of curing, (d) 250 days of curing and (e) 360 days of curing, NN-NaOH-AAS, 12NM- NaOH-MgAc AAS.

7.4.3 Thermogravimetry analysis

Thermogravimetry curves and derivative curves of the 28 days cured NaOH-AAS, with and without the addition of MgAc, are depicted in Figure 7.4 (A) and (B) respectively. At temperatures up to 200 °C, there was a weight loss resulted by C-(A)-S-H gel dehydrated [Hwang et al., 2018, Kim et al., 2017]. Mass loss occurred during this temperature range was slightly higher for NaOH-AAS paste compared with that of NaOH-MgAc, potentially indicating MgAc has a negative effect on the reaction degree. The mass loss recorded between 200-500°C range is mainly attributed to the hydrotalcite-like phase decomposed [Ben Haha et al., 2011a, Rozov et al., 2010]. Compared with NaOH-AAS, a mass loss occurring between 250-350°C in also detected for the NaOH-MgAc pastes. This was possibly corresponded to the remaining MgAc at this temperature. In addition, the acetate ions could possibly intercalate with Mg-Al layered double hydroxides at appropriate condition [Manohara et al., 2021]. The XRD results illustrated in Figure 7.2 confirmed the existence of Mg-Al LDH and also identified in FTIR results in Figure 7.3, but it was still not known whether acetate ions intercalated with LDH based from XRD and FTIR results. A mass loss at 600-800°C is allocated to calcium carbonates like calcite decomposed [Maciejewski et al., 1994, Karunadasa et al., 2019]. In general, there is no significant differences on the main reaction products in the pastes with or without MgAc addition as shown in Figure 7.3 despite the significant differences in reaction kinetics recorded at early ages. This would be attributed to the MgAc, which is not reactively acted in the AAS pastes due to the insufficient dissolution of MgAc.
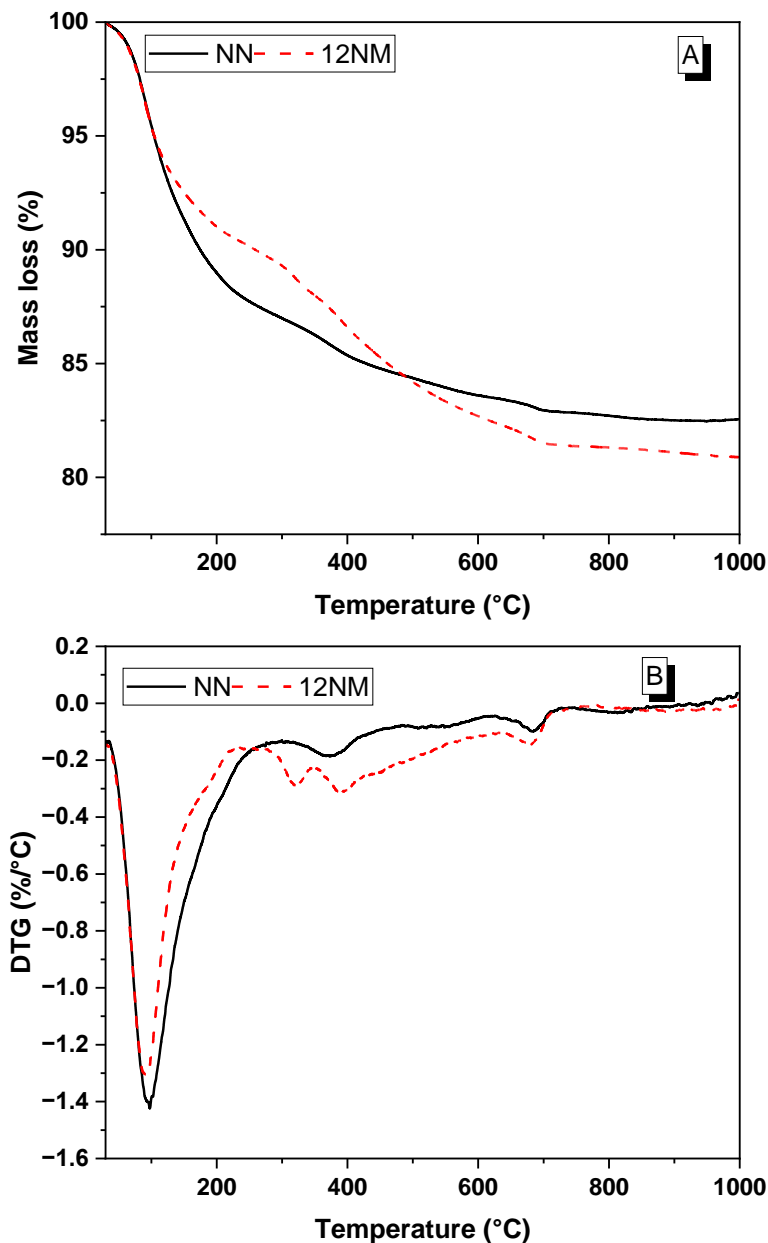
Figure 7.4 (A) Thermogravimetry curves and (B) Differential thermograms of NaOH-AAS cements produced without MgAc and with the addition of MgAc, changed as curing time.

The total mass loss and the amount of bound water in C-(A)-S-H type gels are often treated to be an indicative of the reaction degree in AAS. Table 7.2 listed the mass loss from TG data up to 650°C. Suggesting that the reaction degree (indicated by the total mass loss) of NaOH-AAS is slightly lower than that of NaOH-MgAc AAS, but the differences are not as marked as identified in the calorimetry results (Figure 7.1 (A)). This demonstrates that solid MgAc is unlikely to be acting as an additional reactive MgO source in these systems, possibly acting as a filler in AAS pastes.

Table 7.2 Mass loss calculated from thermogravimetry until 650°C, the mass loss according to C-

	(A)-S-H was calculated until 200°C	
Sample	Mass loss (%)	
	28-day	
	C-(A)-S-H	Total mass loss
NaOH	11.01	16.65
NaOH-MgAc	8.98	17.85

7.4.4 Microstructure features of hardened pastes

BSE images at different magnification of AAS cement pastes activated by NaOH and NaOH with the addition of MgAc curing at 360 days are presented in Figure 7.5. As the grey level is determined by the atomic number in the compound [Yi et al., 2014], it is then possible to distinguish the not-reacted GGBFS (isolated particles) together with reaction products. The cementitious matrix, which would be the continues phase identified in the micrographs, is much darker than the unreacted slag grains [Famy et al., 2002].

The morphology of NaOH-AAS and NaOH-MgAc AAS seen from Figure 7.5 is quite similar, demonstrating that the addition of MgAc in these cements does not have a negative impact in the microstructure of NaOH-AAS cements in the longer term. Equally these results are indicating that the addition of MgAc at the dosage evaluated do not induce significant changes consistent with the XRD results recorded in Figure 7.2. Figure 7.5 B1-B3 depicted that NaOH-MgAc AAS has a lower reaction degree and less reaction product is formed, compared to NaOH-AAS shown in Figure 7.5 A1-A3. Demonstrating a larger fraction of unreacted slag particles is existed in the MgAc containing cement. However, this is only an observation, and further analysis of the results will be needed (e.g. image segmentation) to determine the proportion of unreacted GGBFS in each of the cement evaluated. Unfortunately, such analysis could not be conducted in this study, as only a very limited number of images for the systems evaluated were collected.

The chemical component of the matrices forming in NaOH-AAS and NaOH-MgAc AAS systems curing at 360 days were analyzed through the EDS analysis. Because the formed reaction product phases are highly intermixed, it is impossible to do discrete analysis on them. However, it is achievable to obtain the plots of normalized elemental ratios [Ben Haha et al., 2011b, San Nicolas et al., 2014]. EDS were performed on 60 points selected in each AAS sample at a magnification of 1000.

Figure 7.6 (A) shows the plots of data points for the Ca/Si vs Al/Si ratios of the two cement systems evaluated. The Ca/Si ratio of the main binding gel in both NaOH-AAS and NaOH-MgAc AAS matrices, mostly ranges from 1.13 to 1.14. The plot of

Figure 7.6 (A) depicts data points regarding Al/Si ratios range from 0.1 to 0.8, demonstrating that an Al substituted C-S-H type gel formed in AAS systems [Wang et al., 2022, Kapeluszna et al., 2017]. The dash line in Figure 7.6 (A) showing Ca/Al =1.4 included to visualize the regions of C-(A)-S-H type gels composition. Considering findings from Figure 7.6 (A), the Ca/Si ratios in NaOH-AAS with and without MgAc addition are similar, however, the addition of MgAc seems to induce a slight decreased in the Ca/Si ratios compared to that of NaOH-AAS. Ca/Si ratio may lead to the formation of C-(A)-S-H type gels, a key binding phase in cementitious materials. It contributes to the development of a denser microstructure and the formation of additional binding phases, thereby enhancing the overall strength of the AAS paste.

Figure 7.6 (B) depicted Mg/Si versus Al/Si, as this relationship demonstrates the potential creation of Mg-Al LDH phases in these cements [Yi et al., 2014, Ben Haha et al., 2011b]. The dashed lines in Figure 7.6 (B) shown the compositions of the LDH forming, with a ratio of Mg/Al =2.4 in NaOH-AAS and Mg/Al =1.9 in NaOH-MgAc AAS, respectively. This is consistent with the previous investigations in NaOH-activated slag cements that usually the hydrotalcite-like LDH phases with the ratio of Mg/Al approximately 2 [Lee et al., 2016, Fernandez et al., 2005]. It is clear that a reduction was observed in the Mg/Al ratio from 2.4 to 1.9 of the hydrotalcite-like phases with the addition of MgAc. A crystalline reflection assigned to hydrotalcite was not observed in the MgAc containing cements by XRD even after 360 days of curing (Fig 7.2), however, the EDS results are demonstrated that the formation of such phase is likely occurring, and it must have a very disordered structure.

The trends of the composition of the LDH forming in the presence of MgAc is inconsistent with the results reported by Jin et al [Jin et al., 2015]. The results from their study reported that Mg/Al increased with the addition of MgO when using MgO as main additional magnesium source. The intercept at nearly 0.46, 0.37 of Mg/Al=2.4 and 1.9, respectively in Al/Si axis indicated the Al uptake in C-(A)-S-H gels. Demonstrating that C-(A)-S-H type gels exhibit approximately similar Al uptake proportions, but the formed hydrotalcite-like phases contained less MgO.
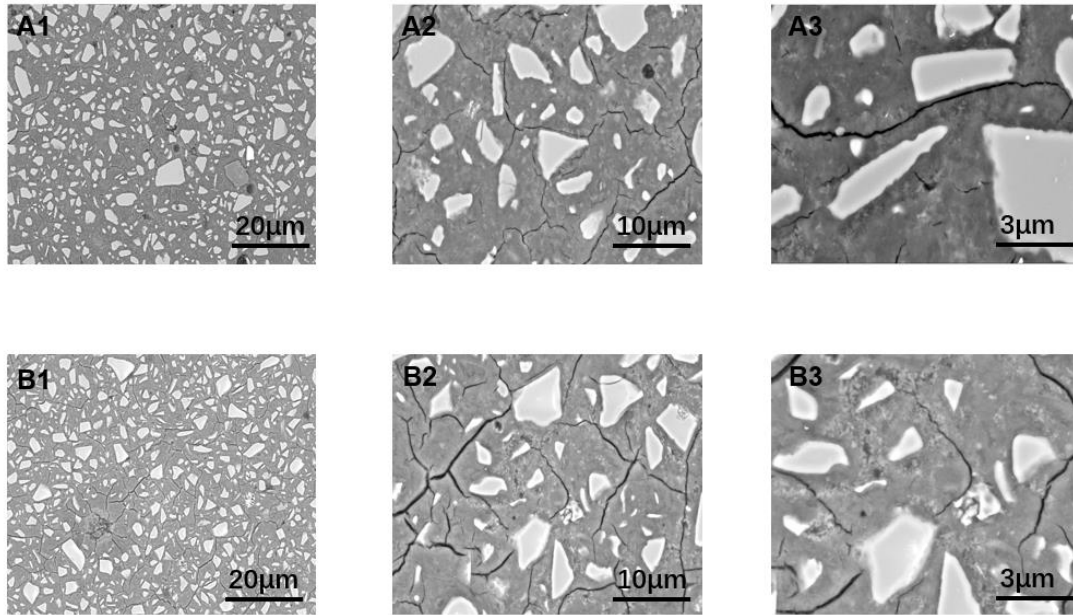
Figure 7.5 BSE images at different magnification of (A) NaOH-AAS and (B) NaOH-MgAc-AAS. (Cracking in the images is due to the over-polishing during BSE samples preparation as samples were weaker)
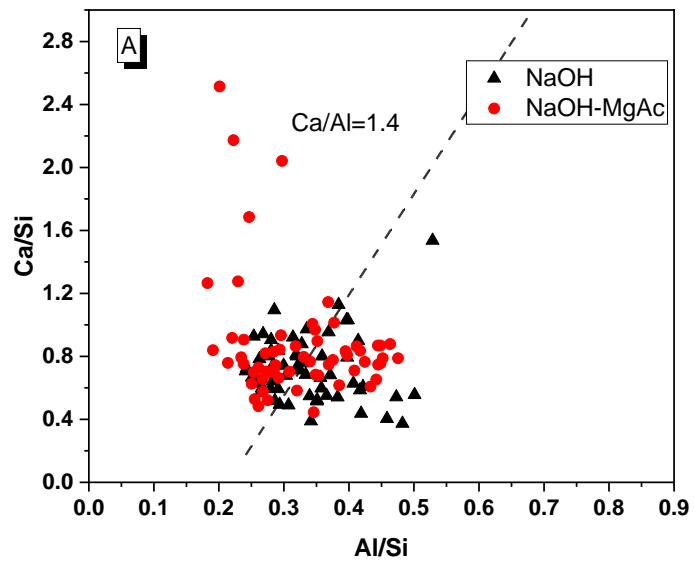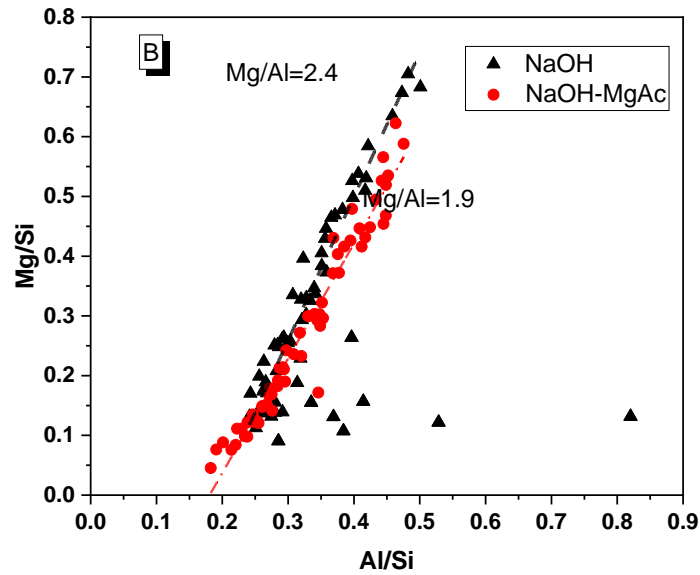
Figure 7.6 Plots of EDS data map comparing (A) Ca/Si vs Al/Si and (B) Mg/Si vs Al/Si in the matrices

7.5 Compressive strength

The compressive strength of the evaluated NaOH-AAS with and without adding MgAc (12NM) is shown in Figure 7.8. The NaOH-AAS paste (without the addition of MgAc, abbreviated as NN) develops a high compressive strength after 3 days, and exhibits a raising strength growth at extended curing durations. The addition of MgAc led to a significant reduction in the compressive strength, however, samples developed acceptable strength at early curing ages (7.42 MPa) after cured 3 days, which is less than half of that recorded for NaOH-AAS specimens. After 7 days, of curing, NaOH-AAS cement pastes with the addition of MgAc developed a compressive strength of 14.5 MPa, approximately double of that curing recorded after 3 days. NaOH-AAS added with MgAc reported a strength of 30.3 MPa, almost 10 MPa lower compared to that of NaOH-AAS after curing of 28 days.

The NaOH-AAS with MgAc added showed a gradual growth in strength as the curing period extended, achieving a compressive strength of 30.3 MPa after cured 28 days. In contrast, NaOH-AAS exhibited a higher 28-day compressive strength, exceeding 40 MPa. The compressive strength development was not increased as expected when additional MgO was introduced, significantly different to previously documented by Hwang et al.[Hwang et al., 2018]. They found that the compressive strength increased in all samples with addition of MgO and could reach to 65.3 MPa after 28 days of curing. This compressive strength value is almost twice than that recorded in the system with MgAc added. Park et al. [Park et al., 2020] also evaluated how the MgO amount affected the compressive strength of AAS cements. It was

noticeable that the increase from 0% MgO content to 5% MgO content could lead the compressive strength boosted from almost 20 MPa to 30 MPa. This is comparable to the compressive strength values of NaOH-MgAc AAS similarly cured after 28 days.

He et al. [He et al., 2021] investigated that the NaOH-AAS cement when adding reactive MgO (prepared by burning magnesite) content of 0, 2%, 4%, 6%, 8% and 10% (calculated as a proportion of the total mass of binder). The compressive strength of NaOH-AAS directly reduced as reactive MgO content increased from 0 to 10% in all curing ages from 3 days to 56 days, and the reduction decreased at later curing ages. Similar observation of NaOH-AAS adding MgAc was identified in this study, indicating that sufficient dissolution of MgAc might have not been achieved, and the effect of MgAc is comparable to that of adding MgO in the system.

Consequently, additional magnesium is unlikely to be released soon enough to participate actively in the reaction with other species dissolving in the slag, under the activation conditions evaluated here.
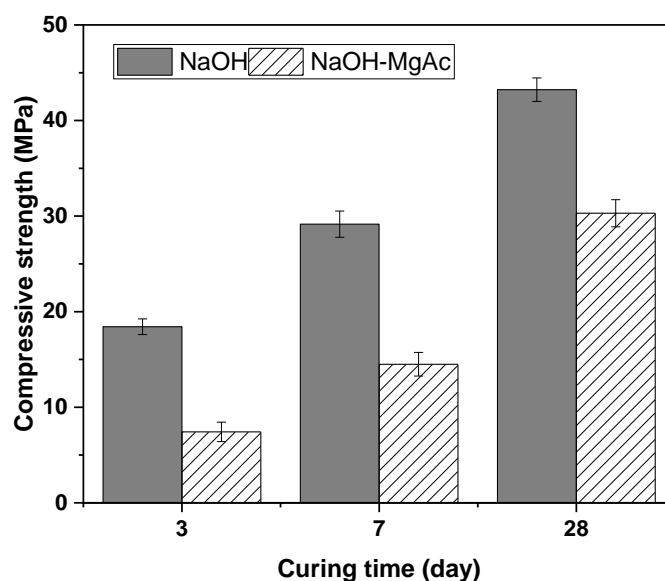
Figure 7.7 Compressive strength of the NaOH-AAS and NaOH-MgAc AAS changed with curing time.

7.6 Conclusions

NaOH-AAS cements added with MgAc were produced and the properties of the assessed cement pastes were discussed. Some conclusions are included as followed:

The addition of MgAc changes the reaction kinetics of NaOH-AAS system,

leading to a slower acceleration period. Moreover, the cumulative heat of reaction of NaOH-MgAc AAS was significantly lower than that of NaOH-AAS, which could be associated with a reduced degree of reaction.

No significant differences in the type of reaction products forming with the addition of MgAc were identified by X-ray diffraction. An aluminium substituted C-S-H was discovered as the main reaction product, coupled with calcium carbonates attributed to weathering of the sample. ATR-FTIR results of hardened pastes, corroborated the formation of such phases. The main X-ray diffraction reflection associated with hydrotalcite was not observed upon MgAc addition, however other secondary peaks assigned to this phase were identified in the XRD pattern. Formation of this phase in MgAc containing pastes was also observed by thermogravimetry and BSE-EDS analysis of aged samples. These results might suggest that potential intercalation of the acetate in the layered double hydroxide structure are leading to forming a disordered structure, but this needs to be further investigated. Thermogravimetry results indicated a neglectable increase on the degree of reaction in NaOH-AAS with the addition of MgAc cured after 28 days. An observation of considerable reduced compressive strength in MgAc added pastes was identified. The addition of MgAc do not induce significant changes to the composition of the main reaction product C-(A)-S-H type gels, but the hydrotalcite-like phases were formed with a decreased Mg/Al ratio.

Considering MgAc was added to these binders with the aim of promoting formation of Mg-rich phases, it is concluded that this is not achievable for the activation conditions adopted and the way how MgAc was added to the binder (as a powder), mainly due to potential dissolution issues of this compound when added in a powdered form to the cement systems evaluated. Additional research is necessitated to understand potential changes in chemical composition in the reaction products formed with the addition of solid MgAc, and the possible interaction between NaOH and MgAc.

Chapter 8 – Conclusions and future work

8.1 Conclusions

The preceding chapters have presented results indicating the effective use of organic sodium/potassium acetates as alternative activators for producing alkali-activated slag (AAS) cements. While it was observed that alkali acetates-activated slag cements undergo a more extended reaction process compared to hydroxides-activated slag cements, the compressive strength achieved by alkali acetates-activated slag cements is on par with that of hydroxides-activated slag cements. To further tailor the reaction process, blended activators containing sodium acetate with substitute to sodium hydroxide were explored. Furthermore, an innovative approach was introduced, involving the use of magnesium acetate as a viable source of magnesium to induce alterations in the phase assemblage of NaOH-AAS cements. The main findings in individual systems are summarized as follows:

For manufacturing organic alkaline activators:

A systematic exploration of various metal carboxylate systems was conducted, encompassing single, binary, ternary, and quaternary combinations.

- In single systems, including NaAc, KAc, NaPr, and NaBu, a relatively low glass-forming potential was identified after thermal treatment, while others exhibited charring during the thermal process under the given conditions.

- Binary systems, such as NaAc-KAc, NaAc-NaPr, and NaBu-NaOc, displayed strong crystalline peaks in XRD patterns, indicating a relatively low glass-forming potential.

- Ternary systems, including thermal treated NaAc-NaPr-NaBu and NaPr-NaBu-NaOc, were found to have relatively low glass-forming potential. However, high glass-forming potential was observed in ternary systems, such as MgAc-KAc-NaAc, CaAc-KAc-NaAc, and the quaternary system CaAc-MgAc-KAc-NaAc.

It can be determined that NaAc and KAc after thermal treatment, can be considered as suitable alternative activators due to their formed solutions yield high pH for producing AAS due to their higher pH values.

For producing alkali acetates-activated slag cements:

Acetates-activated slag cements exhibit a longer reaction process compared to that in hydroxides-activated slag cements.
- Acetates-activated slag cements has a prolonged reaction process compared to hydroxides-activated slag cements.

- X-ray diffraction results illustrated no remarkable differences in the type of main crystalline reaction products forming up to 180 curing days between hydroxides and acetates-activated slag cements. The main reaction products identified were C-(A)-S-H type gels, hydrotalcite-like phases, along with calcium carbonates, corroborated by IR spectra. A notably lower reaction degree was observed in acetates-activated slag cements detected by thermogravimetry analysis in comparation to hydroxides-activated slag cements. Additionally, remarkable structural differences were founded in the C-(A)-S-H type phases from acetates-activated slag cement to hydroxides-activated slag cements through ^{29}Si MAS NMR spectroscopy. A highly dense, and homogeneous binding phase was formed.
- Acetates-activated slag cements hold a lower compressive strength in comparation to hydroxides-activated slag cements, but exhibit lower total porosity. No evident connection was found between the 28d-compressive strength and porosity in acetates-activated slag cements and hydroxides-activated slag cements. Acetates have the potential to reduce permeability after 28 days, compared to hydroxides-activated slag cements. The impermeability level remains relatively constant from 28 to 180 days in acetates-activated slag cements, while significant improvements are noted in the hydroxides-activated slag cements over the same curing period.

The results presented above provide confirmation of the feasibility of using acetates as alternative activators to produce alkali-activated slag cements. Additionally, the acetates-activated AAS cements have approximating properties like hydroxide-activated systems. In conclusion, these findings open up an alternative pathway for the production of alkali-activated cements.

For blended (NaOH-NaAc) acetate-activated slag cements:

Ground granulated blast furnace slag cements were produced using blended activators, with varying molar ratios of NaAc to NaOH, ranging from 0% to 100% as a replacement in the composition.
- A 25% replacement ratio of NaAc to NaOH in the activator composition led to a significantly higher heat release rate and slightly greater cumulative heat release compared to NaOH-AAS. But when the replacement raised from 50% to 100%, the reaction process was significantly prolonged, and the cumulative heat released decreased.
- The NaAc content change did not affect the types of the main crystalline reaction products, as hydrotalcite-like phases and C-(A)-S-H type gels While the amounts of C-(A)-S-H type gels formed exhibit subtle variations, up to 75% NaAc content. The variation in NaAc content resulted the hydrotalcite-like phases with varying Mg/Al ratios occurred.

- The substitution of NaAc for NaOH in the activator composition had a noticeable impact on the compressive strength of the AAS cements, with a persistent negative effect as more NaAc was introduced. However, even when NaAc was the sole activator, the AAS cement still owing compressive strengths that exceeded 20 MPa

after cured 28 days.

This illustrates that NaAc is a suitable activator when a moderate strength is required. Increasing the NaAc content in the activator composition improved the impermeability of the resulting AAS cement, as indicated by the water contact angle. Furthermore, it appeared that a composition with 50% NaAc substituting for NaOH in the activator represented the optimal balance for enhancing the impermeability of the AAS cement.

For NaOH-activated slag cements with the addition of MgAc:

Sodium hydroxide-activated ground granulated blast furnace slag (NaOH-AAS) cements were produced with the inclusion of MgAc.

- The addition of MgAc resulted in changes to the reaction kinetics of the NaOH-AAS system, resulting a slower acceleration period, which cumulative heat release was significantly lower suggesting a reduced reaction degree.

- MgAc did not induce notable changes in the types of reaction products identified through XRD results. The main products were consistent with those found in the absence of MgAc. The incorporation of MgAc did not lead to an increase in the amounts of hydrotalcite-like phases. A slightly higher reaction degree was indicated by thermogravimetry results in NaOH-AAS when MgAc was introduced, after cured 28 days.

- No substantial alterations in the composition of the main reaction product C-(A)-S-H type gels were detected, with the addition of MgAc, after varying curing time from 250 to 360 days. However, the hydrotalcite-like phases exhibit a reduced Mg/Al ratio. This observation raises the possibility of a disordered structure formation, potentially due to the intercalation of acetates within layered double hydroxides. Further investigations are required to elucidate this phenomenon.

- The significantly reduced compressive strength observed in pastes containing MgAc is consistent with the lower degree of reaction.

It could be concluded that the aim of utilizing MgAc as additional Mg source to promote the formation of Mg-rich phases is not achievable under the adopted activation conditions evaluated, and the method of incorporating MgAc in powdered form. This is primarily attributed to potential dissolution issues arising when adding MgAc as a powder in the examined systems.

8.2 Directions for future work

This study offers a promising solution for producing alkali-activated slag cement using organic acetates in comparison to conventional hydroxides-activated slag systems. While this research has evaluated the properties of AAS cements produced with sodium and potassium acetates, several critical aspects remain unexplored. With the goal of improving the production of environmentally responsible and sustainable alkali-activated slag cement, intended to replace OPC, and to acquire a more comprehensive grasp of the resilience of alkali-activated slag cement manufactured with acetates during its operational life. There remain several unresolved inquiries that necessitate additional exploration.

- Life cycle analysis can also be conducted to indicate how much cheaper and more sustainable of the proposed AAS compared to those made from conventional alkaline activators.

- The effect of activator concentration on the properties of produced AAS is also of interest to be investigated the reaction process, enhance the compressive strength of the AAS cements, and potentially influence their resistance to carbonation.

- It is worth evaluating the properties of AAS cements produced using activators composed of potassium acetate with varying replacement ratios for potassium hydroxide.

- It would be advantageous to employ Dynamic Vapor Sorption (DVS) to study the complete absorption-desorption cycle of the resulting AAS cements, to gain a comprehensive understanding of impermeability level of acetates-activated slag cement.

- Different dosage levels of MgAc or using a solution of MgAc (by dissolving MgAc in distilled water) are also needed to evaluate the phase assemblage evolution. Furthermore, additional techniques, such as ^{24}Mg MAS NMR, can be employed to assess whether magnesium from magnesium acetate participates in the formation of the reaction products or not.

In summary, this study represents a pioneering effort in the utilization of organic metal acetates as alternative activators for the production of alkali-activated slag cements. While the results obtained in this research are promising, there are important areas that require further investigation and questions that need to be addressed to ensure the large-scale production of alkali acetate-activated slag concrete with secure in-use reliability. Discoveries from this research have unveiled a promising path forward and are expected to stimulate greater interest in exploring the potential of organic metal acetates as alternative activators. Certainly, as the utilization of GGBFS faces potential

limitations or scarcity, especially in developed nations, the abundance of steel slag in developing countries emerges as a promising alternative. The prevalence of steel production in these regions generates substantial quantities of steel slag, making it a viable and readily available precursor for alkali-activated materials. This shift in focus from GGBFS to steel slag aligns with the need for sustainable and locally sourced materials, addressing the challenges posed by the diminishing availability of traditional precursors. Consequently, exploring the use of steel slag in alkali-activated materials not only provides a solution to potential shortages but also aligns with the principles of environmental sustainability and resource efficiency.

References

2016. BS EN 196-1:2016, Methods of testing cement. Determination of strength. British Standard.

ABDOLLAHNEJAD, Z., MASTALI, M., WOOF, B. & ILLIKAINEN, M. 2020. High strength fiber reinforced one-part alkali activated slag/fly ash binders with ceramic aggregates: Microscopic analysis, mechanical properties, drying shrinkage, and freeze-thaw resistance. *Construction and Building Materials,* 241**,** 118129.

ABED, A. A., MOJTAHEDI, A. & LOTFOLLAHI YAGHIN, M. A. 2023. Factorial Mixture Design for Properties Optimization and Modeling of Concrete Composites Incorporated with Acetates as Admixtures. *Sustainability* [Online], 15.

ADESINA, A. & RODRIGUE KAZE, C. 2021. Physico-mechanical and microstructural properties of sodium sulfate activated materials: A review. *Construction and Building Materials,* 295**,** 123668.

AKANNI, M. S., BURROWS, H. D., ELLIS, H. A., ASONWED, D. N., BABALOLA, H. B. & OJO, P. O. 1984. Solution behaviour of some divalent metal carboxylates in organic solvents. *Journal of Chemical Technology and Biotechnology. Chemical Technology,* 34**,** 127-135.

AKITT, J. W. & MANN, B. E. 2017. *NMR and Chemistry: An introduction to modern NMR spectroscopy*, Crc Press.

AKTURK, B., NAYAK, S., DAS, S. & KIZILKANAT, A. B. 2019. Microstructure and Strength Development of Sodium Carbonate–Activated Blast Furnace Slags. *Journal of Materials in Civil Engineering,* 31**,** 04019283.

AL-KHEETAN, M. J., GHAFFAR, S. H., AWAD, S., CHOUGAN, M., BYZYKA, J. & RAHMAN, M. M. 2021. Microstructural, Mechanical and Physical Assessment of Portland Cement Concrete Pavement Modified by Sodium Acetate under Various Curing Conditions. *Infrastructures* [Online], 6.

AL-KHEETAN, M. J., GHAFFAR, S. H., MADYAN, O. A. & RAHMAN, M. M. 2020a. Development of low absorption and high-resistant sodium acetate concrete for severe environmental conditions. *Construction and Building Materials,* 230**,** 117057.

AL-KHEETAN, M. J. & RAHMAN, M. M. 2019. Integration of Anhydrous Sodium Acetate (ASAc) into Concrete Pavement for Protection against Harmful Impact of Deicing Salt. *JOM,* 71**,** 4899-4909.

AL-KHEETAN, M. J., RAHMAN, M. M. & CHAMBERLAIN, D. A. 2019. Fundamental interaction of hydrophobic materials in concrete with different moisture contents in saline environment. *Construction and Building Materials,* 207**,** 122-135.

AL-KHEETAN, M. J., RAHMAN, M. M. & CHAMBERLAIN, D. A. 2020b. Moisture evaluation of concrete pavement treated with hydrophobic surface impregnants. *International Journal of Pavement Engineering,* 21**,** 1746-1754.

AL-KHEETAN, M. J., RAHMAN, M. M., GHAFFAR, S. H., AL-TARAWNEH, M. A. & JWEIHAN, Y. S. 2020c. Comprehensive investigation of the long-term performance of internally integrated concrete pavement with sodium acetate. *Results in Engineering,* 6**,** 100110.

AL-OTOOM, A., AL-KHLAIFA, A. & SHAWAQFEH, A. 2007. Crystallization Technology for Reducing Water Permeability into Concrete. *Industrial & Engineering Chemistry*

Research, 46, 5463-5467.

ALEIXO, A. I., OLIVEIRA, P. H., DIOGO, H. P. & MINAS DA PIEDADE, M. E. 2005. Enthalpies of formation and lattice enthalpies of alkaline metal acetates. *Thermochimica Acta,* 428, 131-136.

ALHARBI, N., VARELA, B. & HAILSTONE, R. 2020. Alkali-activated slag characterization by scanning electron microscopy, X-ray microanalysis and nuclear magnetic resonance spectroscopy. *Materials Characterization,* 168, 110504.

ALHAWAT, M., ASHOUR, A., YILDIRIM, G., ALDEMIR, A. & SAHMARAN, M. 2022. Properties of geopolymers sourced from construction and demolition waste: A review. *Journal of Building Engineering,* 50, 104104.

ALMALKAWI, A. T., BALCHANDRA, A. & SOROUSHIAN, P. 2019. Potential of Using Industrial Wastes for Production of Geopolymer Binder as Green Construction Materials. *Construction and Building Materials,* 220, 516-524.

ALONSO, M. M., GASCó, C., MORALES, M. M., SUáREZ-NAVARRO, J. A., ZAMORANO, M. & PUERTAS, F. 2019. Olive biomass ash as an alternative activator in geopolymer formation: A study of strength, radiology and leaching behaviour. *Cement and Concrete Composites,* 104, 103384.

AMER, I., KOHAIL, M., EL-FEKY, M. S., RASHAD, A. & KHALAF, M. A. 2021a. Characterization of alkali-activated hybrid slag/cement concrete. *Ain Shams Engineering Journal,* 12, 135-144.

AMER, I., KOHAIL, M., EL-FEKY, M. S., RASHAD, A. & KHALAF, M. A. 2021b. A review on alkali-activated slag concrete. *Ain Shams Engineering Journal,* 12, 1475-1499.

ANDREW, R. M. J. E. S. S. D. 2018. Global CO 2 emissions from cement production. 10, 195.

ANGELL, C. 1968. Oxide glasses in light of the "Ideal Glass" concept: I, ideal and nonideal transitions, and departures from ideality. *Journal of the American Ceramic Society,* 51, 117-124.

ANGELL, C. A. 1990. Dynamic processes in ionic glasses. *Chemical Reviews,* 90, 523-542.

ANTOLIK, A., JóŹWIAK-NIEDŹWIEDZKA, D., DZIEDZIC, K. & LISOWSKI, P. 2023. Effect of Potassium Formate on Alkali–Silica Reaction in Aggregates with Different Categories of Reactivity. *Materials Proceedings* [Online], 13.

AWAD, W. H., GILMAN, J. W., NYDEN, M., HARRIS, R. H., SUTTO, T. E., CALLAHAN, J., TRULOVE, P. C., DELONG, H. C. & FOX, D. M. 2004. Thermal degradation studies of alkyl-imidazolium salts and their application in nanocomposites. *Thermochimica Acta,* 409, 3-11.

AWOYERA, P. & ADESINA, A. 2019. A critical review on application of alkali activated slag as a sustainable composite binder. *Case Studies in Construction Materials,* 11, e00268.

AXINTE, E., BOFU, A., WANG, Y., ABDUL-RANI, A. M. & ALIYU, A. A. A. An overview on the conventional and nonconventional methods for manufacturing the metallic glasses. MATEC Web of Conferences, 2017. EDP Sciences, 03003.

BAKHAREV, T., SANJAYAN, J. G. & CHENG, Y.-B. 1999. Alkali activation of Australian slag cements. *Cement and Concrete Research,* 29, 113-120.

BAKHAREV, T., SANJAYAN, J. G. & CHENG, Y. B. 2000. Effect of admixtures on properties of alkali-activated slag concrete. *Cement and Concrete Research,* 30, 1367-1374.

BARTHOLOMEW, R. F. & LEWEK, S. S. 1970. Glasses Formed from Molten Acetates. *Journal of the*

American Ceramic Society, 53**,** 445-447.

BATUECAS, E., RAMóN-ÁLVAREZ, I., SáNCHEZ-DELGADO, S. & TORRES-CARRASCO, M. 2021. Carbon footprint and water use of alkali-activated and hybrid cement mortars. *Journal of Cleaner Production,* 319**,** 128653.

BELL, J. L. S., PALMER, D. A., BARNES, H. L. & DRUMMOND, S. E. 1994a. Thermal decomposition of acetate: III. Catalysis by mineral surfaces. *Geochimica et Cosmochimica Acta,* 58**,** 4155-4177.

BELL, M. D., LYSAKER, P. H., MILSTEIN, R. M. & BEAM-GOULET, J. L. 1994b. Concurrent validity of the cognitive component of schizophrenia: Relationship of PANSS scores to neuropsychological assessments. *Psychiatry Research,* 54**,** 51-58.

BEN HAHA, M., LE SAOUT, G., WINNEFELD, F. & LOTHENBACH, B. 2011a. Influence of activator type on hydration kinetics, hydrate assemblage and microstructural development of alkali activated blast-furnace slags. *Cement and Concrete Research,* 41**,** 301-310.

BEN HAHA, M., LOTHENBACH, B., LE SAOUT, G. & WINNEFELD, F. 2011b. Influence of slag chemistry on the hydration of alkali-activated blast-furnace slag — Part I: Effect of MgO. *Cement and Concrete Research,* 41**,** 955-963.

BEN HAHA, M., LOTHENBACH, B., LE SAOUT, G. & WINNEFELD, F. 2012. Influence of slag chemistry on the hydration of alkali-activated blast-furnace slag — Part II: Effect of Al2O3. *Cement and Concrete Research,* 42**,** 74-83.

BENNETT, T. D., YUE, Y., LI, P., QIAO, A., TAO, H., GREAVES, N. G., RICHARDS, T., LAMPRONTI, G. I., REDFERN, S. A. T., BLANC, F., FARHA, O. K., HUPP, J. T., CHEETHAM, A. K. & KEEN, D. A. 2016. Melt-Quenched Glasses of Metal–Organic Frameworks. *Journal of the American Chemical Society,* 138**,** 3484-3492.

BENTZ, D. P. 2007. Transient plane source measurements of the thermal properties of hydrating cement pastes. *Materials and Structures,* 40**,** 1073-1080.

BERNAL, S., RODRíGUEZ, E., MEJíA DE GUTIéRREZ, R. & PROVIS, J. L. 2015a. Performance at high temperature of alkali-activated slag pastes produced with silica fume and rice husk ash based activators. *Materiales de construcción,* 65.

BERNAL, S. A. 2016. Advances in near-neutral salts activation of blast furnace slags. *RILEM technical letters,* 1**,** 39-44.

BERNAL, S. A., DE GUTIERREZ, R. M., PROVIS, J. L. & ROSE, V. 2010. Effect of silicate modulus and metakaolin incorporation on the carbonation of alkali silicate-activated slags. *Cement and Concrete Research,* 40**,** 898-907.

BERNAL, S. A., MEJíA DE GUTIéRREZ, R. & PROVIS, J. L. 2012. Engineering and durability properties of concretes based on alkali-activated granulated blast furnace slag/metakaolin blends. *Construction and Building Materials,* 33**,** 99-108.

BERNAL, S. A., PROVIS, J. L., FERNáNDEZ-JIMéNEZ, A., KRIVENKO, P. V., KAVALEROVA, E., PALACIOS, M. & SHI, C. 2014a. Binder chemistry–high-calcium alkali-activated materials. *Alkali activated materials.* Springer.

BERNAL, S. A., PROVIS, J. L., FERNáNDEZ-JIMéNEZ, A., KRIVENKO, P. V., KAVALEROVA, E., PALACIOS, M. & SHI, C. 2014b. Binder Chemistry – High-Calcium Alkali-Activated Materials. *In:* PROVIS, J. L. & VAN DEVENTER, J. S. J. (eds.) *Alkali Activated Materials: State-of-the-Art Report, RILEM TC 224-AAM.* Dordrecht: Springer Netherlands.

BERNAL, S. A., PROVIS, J. L., MYERS, R. J., SAN NICOLAS, R. & VAN DEVENTER, J. S. 2015b. Role

of carbonates in the chemical evolution of sodium carbonate-activated slag binders. *Materials and Structures,* 48, 517-529.

BERNAL, S. A., PROVIS, J. L., MYERS, R. J., SAN NICOLAS, R. & VAN DEVENTER, J. S. J. 2015c. Role of carbonates in the chemical evolution of sodium carbonate-activated slag binders. *Materials and Structures,* 48, 517-529.

BERNAL, S. A., PROVIS, J. L., ROSE, V. & MEJíA DE GUTIERREZ, R. 2011. Evolution of binder structure in sodium silicate-activated slag-metakaolin blends. *Cement and Concrete Composites,* 33, 46-54.

BERNAL, S. A., RODRíGUEZ, E. D., KIRCHHEIM, A. P. & PROVIS, J. L. 2016. Management and valorisation of wastes through use in producing alkali-activated cement materials. *Journal of Chemical Technology & Biotechnology,* 91, 2365-2388.

BERNAL, S. A., SAN NICOLAS, R., MYERS, R. J., MEJíA DE GUTIéRREZ, R., PUERTAS, F., VAN DEVENTER, J. S. J. & PROVIS, J. L. 2014c. MgO content of slag controls phase evolution and structural changes induced by accelerated carbonation in alkali-activated binders. *Cement and Concrete Research,* 57, 33-43.

BERODIER, E., BIZZOZERO, J. & MULLER, A. C. 2016. Mercury intrusion porosimetry. *A practical guide to microstructural analysis of cementitious materials,* 419.

BINNEMANS, K. 2005. Ionic Liquid Crystals. *Chemical Reviews,* 105, 4148-4204.

BLAIR, J. A., DUFFY, J. A. & WARDELL, J. L. 1992. A refractivity study of metal carboxylate glasses. *Journal of Non-Crystalline Solids,* 146, 159-164.

BLAKE, P. G. & JACKSON, G. E. 1968. The thermal decomposition of acetic acid. *Journal of the Chemical Society B: Physical Organic,* 1153-1155.

BROUWER, D. H., BROUWER, C. C., MESA, S., SEMELHAGO, C. A., STECKLEY, E. E., SUN, M. P. Y., MIKOLAJEWSKI, J. G. & BAERLOCHER, C. 2020. Solid-state 29Si NMR spectra of pure silica zeolites for the International Zeolite Association Database of Zeolite Structures. *Microporous and Mesoporous Materials,* 297, 110000.

BURCIAGA-DíAZ, O. & BETANCOURT-CASTILLO, I. 2018. Characterization of novel blast-furnace slag cement pastes and mortars activated with a reactive mixture of MgO-NaOH. *Cement and Concrete Research,* 105, 54-63.

CALAHOO, C. & WONDRACZEK, L. 2020. Ionic glasses: Structure, properties and classification. *Journal of Non-Crystalline Solids: X,* 8, 100054.

CAMERON, J. 2012. *Principles of physiological measurement,* Elsevier.

CAO, K., WANG, L., XU, Y., SHEN, W. & WANG, H. 2021. The Hydration and Compressive Strength of Cement Mortar Prepared by Calcium Acetate Solution. *Advances in Civil Engineering,* 2021, 8817725.

CAO, R., ZHANG, S., BANTHIA, N., ZHANG, Y. & ZHANG, Z. 2020a. Interpreting the early-age reaction process of alkali-activated slag by using combined embedded ultrasonic measurement, thermal analysis, XRD, FTIR and SEM. *Composites Part B: Engineering,* 186, 107840.

CAO, R., ZHANG, S., BANTHIA, N., ZHANG, Y. & ZHANG, Z. J. C. P. B. E. 2020b. Interpreting the early-age reaction process of alkali-activated slag by using combined embedded ultrasonic measurement, thermal analysis, XRD, FTIR and SEM. 186, 107840.

CAVAGNA, A. 2009. Supercooled liquids for pedestrians. *Physics Reports,* 476, 51-124.

CHEN, C.-M., XU, X., JI, H.-Y., WANG, B., PAN, L., LUO, Y. & LI, Y.-S. 2021. Alkali Metal

Carboxylates: Simple and Versatile Initiators for Ring-Opening Alternating Copolymerization of Cyclic Anhydrides/Epoxides. *Macromolecules,* 54**,** 713-724.

CHEN, C. & TURNER, J. 1980. Crystallization in a double-diffusive system. *Journal of Geophysical Research: Solid Earth,* 85**,** 2573-2593.

CHEN, H. S. 1976. Correlation between the thermal stability and activation energy of crystallization in metallic glasses. 29**,** 12-14.

CHEN, S., RUAN, S., ZENG, Q., LIU, Y., ZHANG, M., TIAN, Y. & YAN, D. 2022. Pore structure of geopolymer materials and its correlations to engineering properties: A review. *Construction and Building Materials,* 328**,** 127064.

CHEN, X., OU, J., WEI, Y., HUANG, Z., KANG, Y. & YIN, G. 2010. Effect of MgO contents on the mechanical properties and biological performances of bioceramics in the MgO-CaO-SiO2 system. *J Mater Sci Mater Med,* 21**,** 1463-71.

CHERKI EL IDRISSI, A., PARIS, M., ROZIèRE, E., DENEELE, D., DARSON, S. & LOUKILI, A. 2018. Alkali-activated grouts with incorporated fly ash: From NMR analysis to mechanical properties. *Materials Today Communications,* 14**,** 225-232.

CHOO, H., LIM, S., LEE, W. & LEE, C. 2016. Compressive strength of one-part alkali activated fly ash using red mud as alkali supplier. *Construction and Building Materials,* 125**,** 21-28.

CLARK, B. & BROWN, P. 2000. The formation of calcium sulfoaluminate hydrate compounds: Part II. *Cement and Concrete Research,* 30**,** 233-240.

CONG, X., ZHOU, W., GENG, X. & ELCHALAKANI, M. 2019. Low field NMR relaxation as a probe to study the effect of activators and retarders on the alkali-activated GGBFS setting process. *Cement and Concrete Composites,* 104**,** 103399.

COUDERT, E., DENEELE, D., RUSSO, G., VITALE, E. & TARANTINO, A. 2021. Microstructural evolution and mechanical behaviour of alkali activated fly ash binder treated clay. *Construction and Building Materials,* 285**,** 122917.

CRIADO, M., WALKLEY, B., KE, X., PROVIS, J. L. & BERNAL, S. A. 2018. Slag and activator chemistry control the reaction kinetics of sodium metasilicate-activated slag cements. *Sustainability,* 10**,** 4709.

DE MORAES PINHEIRO, S. M., FONT, A., SORIANO, L., TASHIMA, M. M., MONZó, J., BORRACHERO, M. V. & PAYá, J. 2018. Olive-stone biomass ash (OBA): An alternative alkaline source for the blast furnace slag activation. *Construction and Building Materials,* 178**,** 327-338.

DEIR, E., GEBREGZIABIHER, B. S. & PEETHAMPARAN, S. 2014. Influence of starting material on the early age hydration kinetics, microstructure and composition of binding gel in alkali activated binder systems. *Cement and Concrete Composites,* 48**,** 108-117.

DIVVALA, S. & M, S. R. 2021. Early strength properties of geopolymer concrete composites: An experimental study. *Materials Today: Proceedings,* 47**,** 3770-3777.

DU, X., SI, Z., QI, D., LI, Y., HUANG, L., ZHANG, Y. & GAO, Y. 2023. Optimization of spore production and activation conditions of concrete crack healing bacteria and research on crack repair effect. *Construction and Building Materials,* 394**,** 132140.

DUFFY, J. & INGRAM, M. 1969. Formation of Acetate Glasses. *Journal of the American Ceramic Society,* 52**,** 224-225.

DUNG, N. T. & UNLUER, C. 2017. Carbonated MgO concrete with improved performance: The influence of temperature and hydration agent on hydration, carbonation and strength

gain. *Cement and Concrete Composites,* 82**,** 152-164.

DUNN, S. A. & SCHENK, R. J. T. R. R. 1980a. Alternatives to sodium chloride for highway deicing. 776**,** 12-15.

DUNN, S. A. & SCHENK, R. U. 1980b. Alternatives to sodium chloride for highway deicing. *Transportation research record,* 776**,** 12-15.

DURAN ATIŞ, C., BILIM, C., ÇELIK, Ö. & KARAHAN, O. 2009. Influence of activator on the strength and drying shrinkage of alkali-activated slag mortar. *Construction and Building Materials,* 23**,** 548-555.

DURUZ, J. J., MICHELS, H. J. & UBBELOHDE, A. R. 1971. Decomposition reactions of sodium propionate. *Journal of the Chemical Society B: Physical Organic***,** 1505-1509.

DUXSON, P., PROVIS, J. L., LUKEY, G. C., MALLICOAT, S. W., KRIVEN, W. M. & VAN DEVENTER, J. S. J. 2005. Understanding the relationship between geopolymer composition, microstructure and mechanical properties. *Colloids and Surfaces A: Physicochemical and Engineering Aspects,* 269**,** 47-58.

ELLIS, K. 2016. *Mechanical, environmental and economic feasibility analysis of sodium carbonate activated blast furnace slag*, Rochester Institute of Technology.

ESCALANTE-GARCíA, J. I., FUENTES, A. F., GOROKHOVSKY, A., FRAIRE-LUNA, P. E. & MENDOZA-SUAREZ, G. 2003. Hydration Products and Reactivity of Blast-Furnace Slag Activated by Various Alkalis. *Journal of the American Ceramic Society,* 86**,** 2148-2153.

FAMY, C., SCRIVENER, K. L. & CRUMBIE, A. K. 2002. What causes differences of C-S-H gel grey levels in backscattered electron images? *Cement and Concrete Research,* 32**,** 1465-1471.

FENG, L., ZHANG, Y., WANG, X., MERY, S., AKIN, M., LI, M., XIE, N., LI, Z. & SHI, X. 2023. Impact of deicing salts on pervious concrete pavement. *Frontiers in Materials,* 10.

FERNáNDEZ-JIMéNEZ, A. & PUERTAS, F. 1997. Alkali-activated slag cements: Kinetic studies. *Cement and Concrete Research,* 27**,** 359-368.

FERNáNDEZ-JIMéNEZ, A., PUERTAS, F., SOBRADOS, I. & SANZ, J. 2003. Structure of Calcium Silicate Hydrates Formed in Alkaline-Activated Slag: Influence of the Type of Alkaline Activator. *Journal of the American Ceramic Society,* 86**,** 1389-1394.

FERNáNDEZ-JIMéNEZ, A. & PUERTAS, F. J. A. I. C. R. 2001. Setting of alkali-activated slag cement. Influence of activator nature. *Advances in Cement Research,* 13**,** 115-121.

FERNANDEZ, L., ALONSO, C., HIDALGO, A. & ANDRADE, C. 2005. The role of magnesium during the hydration of C3S and C-S-H formation. Scanning electron microscopy and mid-infrared studies. *Advances in Cement Research,* 17**,** 9-21.

FONT, A., SORIANO, L., MORAES, J. C. B., TASHIMA, M. M., MONZó, J., BORRACHERO, M. V. & PAYá, J. 2017. A 100% waste-based alkali-activated material by using olive-stone biomass ash (OBA) and blast furnace slag (BFS). *Materials Letters,* 203**,** 46-49.

FRIESNER, R. A., MURPHY, R. B., REPASKY, M. P., FRYE, L. L., GREENWOOD, J. R., HALGREN, T. A., SANSCHAGRIN, P. C. & MAINZ, D. T. 2006. Extra Precision Glide: Docking and Scoring Incorporating a Model of Hydrophobic Enclosure for Protein−Ligand Complexes. *Journal of Medicinal Chemistry,* 49**,** 6177-6196.

FU, Q., BU, M., ZHANG, Z., XU, W., YUAN, Q. & NIU, D. 2023. Hydration Characteristics and Microstructure of Alkali-Activated Slag Concrete: A Review. *Engineering,* 20**,** 162-179.

GAO, J., JIN, P., ZHANG, Y., DONG, H. & WANG, R. 2022. Fast-responsive capsule based on two soluble components for self-healing concrete. *Cement and Concrete Composites,* 133, 104711.

GAO, X., YU, Q. L. & BROUWERS, H. J. H. 2017. Apply 29Si, 27Al MAS NMR and selective dissolution in identifying the reaction degree of alkali activated slag-fly ash composites. *Ceramics International,* 43, 12408-12419.

GARCIA-LODEIRO, I., PALOMO, A. & FERNáNDEZ-JIMéNEZ, A. 2015. 2 - An overview of the chemistry of alkali-activated cement-based binders. *In:* PACHECO-TORGAL, F., LABRINCHA, J. A., LEONELLI, C., PALOMO, A. & CHINDAPRASIRT, P. (eds.) *Handbook of Alkali-Activated Cements, Mortars and Concretes.* Oxford: Woodhead Publishing.

GARCIA-LODEIRO, I., PALOMO, A., FERNáNDEZ-JIMéNEZ, A. & MACPHEE, D. E. 2011. Compatibility studies between N-A-S-H and C-A-S-H gels. Study in the ternary diagram Na2O–CaO–Al2O3–SiO2–H2O. *Cement and Concrete Research,* 41, 923-931.

GARCíA LODEIRO, I., FERNáNDEZ-JIMENEZ, A., PALOMO, A. & MACPHEE, D. E. 2010. Effect on fresh C-S-H gels of the simultaneous addition of alkali and aluminium. *Cement and Concrete Research,* 40, 27-32.

GEBREGZIABIHER, B. S., THOMAS, R. & PEETHAMPARAN, S. 2015a. Very early-age reaction kinetics and microstructural development in alkali-activated slag. 55, 91-102.

GEBREGZIABIHER, B. S., THOMAS, R. & PEETHAMPARAN, S. 2015b. Very early-age reaction kinetics and microstructural development in alkali-activated slag. *Cement and Concrete Composites,* 55, 91-102.

GEBREGZIABIHER, B. S., THOMAS, R. J. & PEETHAMPARAN, S. 2016. Temperature and activator effect on early-age reaction kinetics of alkali-activated slag binders. *Construction and Building Materials,* 113, 783-793.

GIEBSON, C., SEYFARTH, K. & STARK, J. 2010. Influence of acetate and formate-based deicers on ASR in airfield concrete pavements. *Cement and Concrete Research,* 40, 537-545.

GIJBELS, K., PONTIKES, Y., SAMYN, P., SCHREURS, S. & SCHROEYERS, W. 2020. Effect of NaOH content on hydration, mineralogy, porosity and strength in alkali/sulfate-activated binders from ground granulated blast furnace slag and phosphogypsum. *Cement and Concrete Research,* 132, 106054.

GóMEZ-CASERO, M. A., PéREZ-VILLAREJO, L., SáNCHEZ-SOTO, P. J. & ELICHE-QUESADA, D. 2022. Comparative study of alkali activated cements based on metallurgical slags, in terms of technological properties developed. *Sustainable Chemistry and Pharmacy,* 29, 100746.

GONG, K., CHENG, Y., DAEMEN, L. L. & WHITE, C. E. 2019. In situ quasi-elastic neutron scattering study on the water dynamics and reaction mechanisms in alkali-activated slags. *Physical Chemistry Chemical Physics,* 21, 10277-10292.

GRUYAERT, E., ROBEYST, N. & DE, B. N. 2010. Study of the hydration of Portland cement blended with blast-furnace slag by calorimetry and thermogravimetry. *Journal of Thermal Analysis and Calorimetry J Therm Anal Calorim,* 102, 941-951.

GU, K., JIN, F., AL-TABBAA, A., SHI, B. & LIU, J. 2014. Mechanical and hydration properties of ground granulated blastfurnace slag pastes activated with MgO–CaO mixtures. *Construction and Building Materials,* 69, 101-108.

GUO, S., WU, Y., JIA, Z., QI, X. & WANG, W. 2023. Sodium-based activators in alkali-activated

materials: Classification and comparison. *Journal of Building Engineering,* 70**,** 106397.

HADJIIVANOV, K. I., PANAYOTOV, D. A., MIHAYLOV, M. Y., IVANOVA, E. Z., CHAKAROVA, K. K., ANDONOVA, S. M. & DRENCHEV, N. L. 2021. Power of Infrared and Raman Spectroscopies to Characterize Metal-Organic Frameworks and Investigate Their Interaction with Guest Molecules. *Chemical Reviews,* 121**,** 1286-1424.

HALASZ, I., AGARWAL, M., LI, R. & MILLER, N. 2007. Monitoring the structure of water soluble silicates. *Catalysis Today,* 126**,** 196-202.

HALMOS, Z., MEISEL, T., SEYBOLD, K. & ERDEY, L. 1970. Studies on the melts of alkali metal acetates. *Talanta,* 17**,** 1191-9.

HAN, J., MARIANI, A., PASSERINI, S., VARZI, A. J. E. & SCIENCE, E. 2023. A perspective on the role of anions in highly concentrated aqueous electrolytes. *Energy & Environmental Science,* 16**,** 1480-1501.

HAYES, R., WARR, G. G. & ATKIN, R. 2015. Structure and Nanostructure in Ionic Liquids. *Chemical Reviews,* 115**,** 6357-6426.

HE, J., ZHENG, W., BAI, W., HU, T., HE, J. & SONG, X. 2021. Effect of reactive MgO on hydration and properties of alkali-activated slag pastes with different activators. *Construction and Building Materials,* 271**,** 121608.

HERTEL, T. & PONTIKES, Y. 2020. Geopolymers, inorganic polymers, alkali-activated materials and hybrid binders from bauxite residue (red mud) – Putting things in perspective. *Journal of Cleaner Production,* 258**,** 120610.

HTTPS://ANALYZING-TESTING.NETZSCH.COM. [Accessed].

HTTPS://WWW.ELEVISE.CO.UK/GACC4A.HTML. [Accessed].

HTTPS://WWW.PARTICLETECHLABS.COM/ANALYTICAL-TESTING/GAS-ADSORPTION-AND-POROSIMETRY/MERCURY-INTRUSION. [Accessed].

HTTPS://WWW.PERKINELMER.COM/UK/. [Accessed].

HURST, M. O. & FORTENBERRY, R. C. 2015. Factors affecting the solubility of ionic compounds. *Computational and Theoretical Chemistry,* 1069**,** 132-137.

HWANG, C.-L., VO, D.-H., TRAN, V.-A. & YEHUALAW, M. D. 2018. Effect of high MgO content on the performance of alkali-activated fine slag under water and air curing conditions. *Construction and Building Materials,* 186**,** 503-513.

IMEN YAMINA, O., ZINE EL ABIDINE, R. & NADIA, T. 2021. Review about the effect of chemical activation of industrials waste which is rich by SiO2 and CaO. *Materials Today: Proceedings.*

INFORMATION Safety data sheet of Cesium Acetate. *CAS number 3396-11-0.*

INFORMATION Safety data sheet of Magnesium Acetate. *CAS number 16674-78-5.*

INFORMATION Safety data sheet of Sodium Butyrate. *CAS number 156-54-7.*

INFORMATION Safety data sheet of Sodium Octanote. *CAS number 1984-06-01.*

INFORMATION， Safety data sheet of Rubidium Acetate. *CAS number 563-67-7.*

INGRAM, M. D., LEWIS, G. G. & DUFFY, J. A. 1972. Ionic-covalent interactions and glass formation in molten acetates. Cobalt(II) as a spectroscopic probe. *The Journal of Physical Chemistry,* 76**,** 1035-1040.

ISMAIL, I., BERNAL, S. A., PROVIS, J. L., HAMDAN, S. & VAN DEVENTER, J. S. J. 2013. Drying-induced changes in the structure of alkali-activated pastes. *Journal of Materials Science,* 48**,** 3566-3577.

JAHANDARI, S., TAO, Z., ALIM, M. A. & LI, W. 2023. Integral waterproof concrete: A comprehensive review. *Journal of Building Engineering,* 78, 107718.

JANKOVIĆ, M., JANKOVIĆ, B., MARINOVIĆ-CINCOVIĆ, M., POROBIĆ, S., NIKOLIĆ, J. K. & SARAP, N. 2020. Experimental study of low-rank coals using simultaneous thermal analysis (TG–DTA) techniques under air conditions and radiation level characterization. *Journal of Thermal Analysis and Calorimetry,* 142, 547-564.

JIANG, D., SHI, C. & ZHANG, Z. 2022a. Recent progress in understanding setting and hardening of alkali-activated slag (AAS) materials. *Cement and Concrete Composites,* 134, 104795.

JIANG, L., NIU, Y., JIN, W., GAO, H. & CHEN, L. 2022b. Influence of chloride salt type on chloride ion diffusion performance of alkali-activated slag mortar. *Construction and Building Materials,* 351, 128930.

JIANG, Z.-H. & ZHANG, Q.-Y. 2014. The structure of glass: A phase equilibrium diagram approach. *Progress in Materials Science,* 61, 144-215.

JIAO, Z., WANG, Y., ZHENG, W. & HUANG, W. 2018a. Effect of Dosage of Alkaline Activator on the Properties of Alkali-Activated Slag Pastes. *Advances in Materials Science and Engineering,* 2018, 8407380.

JIAO, Z., WANG, Y., ZHENG, W. & HUANG, W. 2018b. Effect of dosage of sodium carbonate on the strength and drying shrinkage of sodium hydroxide based alkali-activated slag paste. *Construction and Building Materials,* 179, 11-24.

JIN, F., GU, K. & AL-TABBAA, A. 2015. Strength and hydration properties of reactive MgO-activated ground granulated blastfurnace slag paste. *Cement and Concrete Composites,* 57, 8-16.

JUDD, M. D., PLUNKETT, B. A. & POPE, M. I. 1974. The thermal decomposition of calcium, sodium, silver and copper(II) acetates. *Journal of thermal analysis,* 6, 555-563.

JUENGER, M. C. G., WINNEFELD, F., PROVIS, J. L. & IDEKER, J. H. 2011. Advances in alternative cementitious binders. *Cement and Concrete Research,* 41, 1232-1243.

JUN, Y., HAN, S. H. & KIM, J. H. 2023. Performance of CO2-Cured Alkali-Activated Slag Pastes During Curing and Exposure. *International Journal of Concrete Structures and Materials,* 17, 3.

JUN, Y., KIM, T. & KIM, J. H. 2020. Chloride-bearing characteristics of alkali-activated slag mixed with seawater: Effect of different salinity levels. *Cement and Concrete Composites,* 112, 103680.

KANG, X. & YE, H. 2022. Antimicrobial alkali-activated slag through self-intercalation of benzoate in layered double hydroxides. *Cement and Concrete Composites,* 130, 104533.

KAPELUSZNA, E., KOTWICA, Ł., RóŻYCKA, A. & GOŁEK, Ł. 2017. Incorporation of Al in C-A-S-H gels with various Ca/Si and Al/Si ratio: Microstructural and structural characteristics with DTA/TG, XRD, FTIR and TEM analysis. *Construction and Building Materials,* 155, 643-653.

KARASTOGIANNI, S., GIROUSI, S. & SOTIROPOULOS, S. 2016. pH: Principles and measurement. *Encyclopedia of Food and Health,* 4, 333-338.

KARUNADASA, K. S. P., MANORATNE, C. H., PITAWALA, H. M. T. G. A. & RAJAPAKSE, R. M. G. 2019. Thermal decomposition of calcium carbonate (calcite polymorph) as examined by in-situ high-temperature X-ray powder diffraction. *Journal of Physics and Chemistry of Solids,* 134, 21-28.

KE, X., BERNAL, S. A. & PROVIS, J. L. 2016. Controlling the reaction kinetics of sodium carbonate-

activated slag cements using calcined layered double hydroxides. *Cement and Concrete Research,* 81, 24-37.

KE, X., BERNAL, S. A. & PROVIS, J. L. 2017. Uptake of chloride and carbonate by Mg-Al and Ca-Al layered double hydroxides in simulated pore solutions of alkali-activated slag cement. *Cement and Concrete Research,* 100, 1-13.

KE, X., BERNAL, S. A. & PROVIS, J. L. 2018a. Layered double hydroxides modify the reaction of sodium silicate-activated slag cements. *Green Materials,* 7, 52-60.

KE, X., CRIADO, M., PROVIS, J. L. & BERNAL, S. A. 2018b. Slag-Based Cements That Resist Damage Induced by Carbon Dioxide. *ACS Sustainable Chemistry & Engineering,* 6, 5067-5075.

KHALE, D. & CHAUDHARY, R. 2007. Mechanism of geopolymerization and factors influencing its development: a review. *Journal of Materials Science,* 42, 729-746.

KIM, G. M., KHALID, H. R., KIM, H. J. & LEE, H. K. 2017. Alkali activated slag pastes with surface-modified blast furnace slag. *Cement and Concrete Composites,* 76, 39-47.

KIM, M. S., JUN, Y., LEE, C. & OH, J. E. 2013. Use of CaO as an activator for producing a price-competitive non-cement structural binder using ground granulated blast furnace slag. *Cement and Concrete Research,* 54, 208-214.

KOCKAL, N. U. 2016. Investigation about the effect of different fine aggregates on physical, mechanical and thermal properties of mortars. *Construction and Building Materials,* 124, 816-825.

KONG, Y. K. & KURUMISAWA, K. 2023. Fresh properties and characteristic testing methods for alkali-activated materials: A review. *Journal of Building Engineering,* 75, 106830.

KOTWICA, Ł. & MALICH, M. 2021. Alkali-silica reaction in calcium aluminate cement mortars induced by deicing salts solutions. *Road Materials and Pavement Design*, 1-24.

KOVTUN, M., KEARSLEY, E. P. & SHEKHOVTSOVA, J. 2015. Chemical acceleration of a neutral granulated blast-furnace slag activated by sodium carbonate. *Cement and Concrete Research,* 72, 1-9.

KURTULDU, G. & LöFFLER, J. F. 2020. Multistep Crystallization and Melting Pathways in the Free-Energy Landscape of a Au–Si Eutectic Alloy. 7, 1903544.

KUSHARTOMO, W. & PRABOWO, A. 2019. The Application of Sodium Acetate as Concrete Permeability-Reducing Admixtures. *IOP Conference Series: Materials Science and Engineering,* 508, 012009.

L'HôPITAL, E., LOTHENBACH, B., LE SAOUT, G., KULIK, D. & SCRIVENER, K. 2015. Incorporation of aluminium in calcium-silicate-hydrates. *Cement and Concrete Research,* 75, 91-103.

LANDOLL, M. P. & HOLTZAPPLE, M. T. 2013. Kinetics study of thermal decomposition of calcium carboxylate salts. *Biomass and Bioenergy,* 57, 205-214.

LE SAOûT, G., BEN HAHA, M., WINNEFELD, F. & LOTHENBACH, B. 2011. Hydration Degree of Alkali-Activated Slags: A 29Si NMR Study. *Journal of the American Ceramic Society,* 94, 4541-4547.

LEE, H., CODY, R. D., CODY, A. M. & SPRY, P. G. Effects of various deicing chemicals on pavement concrete deterioration.   Mid-continent transportation symposium proceedings, 2000. 151-155.

LEE, J.-Y., GWAK, G.-H., KIM, H.-M., KIM, T.-I., LEE, G. J. & OH, J.-M. 2016. Synthesis of hydrotalcite type layered double hydroxide with various Mg/Al ratio and surface charge

under controlled reaction condition. *Applied Clay Science,* 134**,** 44-49.

LEISEROWITZ 1976. Molecular packing modes. Carboxylic acids. *Acta Crystallographica Section B,* 32**,** 775--802.

LI, J., YU, Q., HUANG, H. & YIN, S. 2019a. Difference in the reaction process of slag activated by waterglass solution and NaOH solution. *Structural Concrete,* 20**,** 1528-1540.

LI, Q., YANG, K. & YANG, C. 2019b. An alternative admixture to reduce sorptivity of alkali-activated slag cement by optimising pore structure and introducing hydrophobic film. *Cement and Concrete Composites,* 95**,** 183-192.

LI, S., PAN, J., ZHU, D., GUO, Z., SHI, Y., DONG, T., LU, S. & TIAN, H. 2021. A new route for separation and recovery of Fe, Al and Ti from red mud. *Resources, Conservation and Recycling,* 168**,** 105314.

LI, Y. 2005. Bulk metallic glasses: Eutectic coupled zone and amorphous formation. *JOM,* 57**,** 60-63.

LIANG, G. & YAO, W. 2023. Effect of diatomite on the reaction kinetics, early-age chemical shrinkage and microstructure of alkali-activated slag cements. *Construction and Building Materials,* 376**,** 131026.

LIAO, J., QING, G. & ZHAO, B. 2023. Phase Equilibrium Studies in the CaO–SiO2–Al2O3–MgO System with MgO/CaO Ratio of 0.2. *Metallurgical and Materials Transactions B,* 54**,** 793-806.

LIN, H., YANG, Y., HSU, Y.-C., ZHANG, J., WELTON, C., AFOLABI, I., LOO, M. & ZHOU, H.-C. 2023. Metal-Organic Frameworks for Water Harvesting and Concurrent Carbon Capture: A Review for Hygroscopic Materials. *Advanced Materials,* n/a**,** 2209073.

LITTLE, E. J., JR. & JONES, M. M. 1960. A complete table of electronegativities. *Journal of Chemical Education,* 37**,** 231.

LIU, Z., ZHANG, D.-W., LI, L., WANG, J.-X., SHAO, N.-N. & WANG, D.-M. 2019. Microstructure and phase evolution of alkali-activated steel slag during early age. *Construction and Building Materials,* 204**,** 158-165.

LONGHI, M. A., ZHANG, Z., RODRíGUEZ, E. D., KIRCHHEIM, A. P. & WANG, H. 2019. Efflorescence of alkali-activated cements (geopolymers) and the impacts on material structures: A critical analysis. *Frontiers in Materials,* 6**,** 89.

LU, C., LI, Z., WANG, J., ZHENG, Y. & CHENG, L. 2023. An approach of repairing concrete vertical cracks using microbially induced carbonate precipitation driven by ion diffusion. *Journal of Building Engineering,* 73**,** 106798.

LU, J.-X. & POON, C. S. 2018. Use of waste glass in alkali activated cement mortar. *Construction and Building Materials,* 160**,** 399-407.

LU, Z. P. & LIU, C. T. 2003. Glass Formation Criterion for Various Glass-Forming Systems. *Physical Review Letters,* 91**,** 115505.

LU, Z. P. & MAURO, J. C. 2017. The glassy state of matter: Its definition and ultimate fate. *Journal of Non-Crystalline Solids,* 471**,** 490-495.

LUO, S., BAI, T., GUO, M., WEI, Y. & MA, W. 2022. Impact of Freeze–Thaw Cycles on the Long-Term Performance of Concrete Pavement and Related Improvement Measures: A Review. *Materials* [Online], 15.

LUUKKONEN, T., ABDOLLAHNEJAD, Z., YLINIEMI, J., KINNUNEN, P. & ILLIKAINEN, M. 2018. One-part alkali-activated materials: A review. *Cement and Concrete Research,* 103**,** 21-34.

LUUKKONEN, T., YLINIEMI, J. & ABDOLLAHNEJAD, Z. 2022. 4 - Alkali-activated dry-mix concretes. *In:* PACHECO-TORGAL, F., CHINDAPRASIRT, P. & OZBAKKALOGLU, T. (eds.) *Handbook of Advances in Alkali-Activated Concrete.* Woodhead Publishing.

LYU, B.-C., GUO, L.-P., WU, J.-D., FEI, X.-P. & BIAN, R.-S. 2022. The impacts of calcium acetate on reaction process, mechanical strength and microstructure of ordinary Portland cement paste and alkali-activated cementitious paste. *Construction and Building Materials,* 359**,** 129492.

MACIEJEWSKI, M., OSWALD, H.-R. & RELLER, A. 1994. Thermal transformations of vaterite and calcite. *Thermochimica Acta,* 234**,** 315-328.

MACPHEE, D. E. & HANSEN, H. R. 2011. The alkali activation of aluminosilicate materials: mechanisms and practical implementation. University of Abeerdeen.

MALIEKKAL, B. P., KAKKASSERY, J. T. & PALAYOOR, V. R. 2018. Efficacies of sodium nitrite and sodium citrate–zinc acetate mixture to inhibit steel rebar corrosion in simulated concrete interstitial solution contaminated with NaCl. *International Journal of Industrial Chemistry,* 9**,** 105-114.

MANJUNATH, R., NARASIMHAN, M. C., UMESH, K. M., SHIVAM, K. & BALA BHARATHI, U. K. 2019. Studies on development of high performance, self-compacting alkali activated slag concrete mixes using industrial wastes. *Construction and Building Materials,* 198**,** 133-147.

MANOHARA, G. V., NORRIS, D., MAROTO-VALER, M. M. & GARCIA, S. 2021. Acetate intercalated Mg–Al layered double hydroxides (LDHs) through modified amide hydrolysis: a new route to synthesize novel mixed metal oxides (MMOs) for CO2 capture. *Dalton Transactions,* 50**,** 7474-7483.

MARTINEZ-LOPEZ, R. & IVAN ESCALANTE-GARCIA, J. 2016. Alkali activated composite binders of waste silica soda lime glass and blast furnace slag: Strength as a function of the composition. *Construction and Building Materials,* 119**,** 119-129.

MASŁOWSKA, J. & WIĘDŁOCHA, M. 2000. Thermal Decomposition of Some Chemical Compounds Used As Food Preservatives and Kinetic Parameters of This Process. *Journal of Thermal Analysis and Calorimetry,* 60**,** 305-312.

MASSAROTTI, V. & SPINOLO, G. 1979. Crystal data for sodium propanoate: C2H5COONa. *Journal of Applied Crystallography,* 12**,** 613-614.

MCADIE, H. G. & JERVIS, J. M. 1970. The pyrolysis of metal acetates: Part I. Some group II acetates. *Thermochimica Acta,* 1**,** 19-28.

MCLEAN, A. J. 2017. pH Meter. *Academic Psychiatry,* 41**,** 769-769.

MEJíA, J., MEJíA DE GUTIéRREZ, R. & PUERTAS, F. 2014. Rice husk ash as a source of silica in alkali-activated fly ash and granulated blast furnace slag systems.

MENDES, B. C., PEDROTI, L. G., VIEIRA, C. M. F., MARVILA, M., AZEVEDO, A. R. G., FRANCO DE CARVALHO, J. M. & RIBEIRO, J. C. L. 2021. Application of eco-friendly alternative activators in alkali-activated materials: A review. *Journal of Building Engineering,* 35**,** 102010.

MICHELS, H. J. & UBBELOHDE, A. R. 1972. Melting mechanisms of n-alkanecarboxylates (CH2+1CO2–; n⩽ 6). *Journal of the Chemical Society, Perkin Transactions 2,* 1879-1881.

MIRZABABAEI, P., MOGHADAS NEJAD, F. & HAJIKARIMI, P. 2023. Accelerated laboratory evaluation of the effect of deicing condition on fracture characteristics of Silane-based

modified asphalt mixtures. *Theoretical and Applied Fracture Mechanics,* 125, 103855.

MOBASHER, N., BERNAL, S. A., HUSSAIN, O. H., APPERLEY, D. C., KINOSHITA, H. & PROVIS, J. L. 2014a. Characterisation of Ba (OH) 2–Na2SO4–blast furnace slag cement-like composites for the immobilisation of sulfate bearing nuclear wastes. *Cement and Concrete Research,* 66, 64-74.

MOBASHER, N., BERNAL, S. A., HUSSAIN, O. H., APPERLEY, D. C., KINOSHITA, H. & PROVIS, J. L. 2014b. Characterisation of Ba(OH)2–Na2SO4–blast furnace slag cement-like composites for the immobilisation of sulfate bearing nuclear wastes. *Cement and Concrete Research,* 66, 64-74.

MOBASHER, N., BERNAL, S. A. & PROVIS, J. L. 2016. Structural evolution of an alkali sulfate activated slag cement. *Journal of Nuclear Materials,* 468, 97-104.

MYERS, R. J., BERNAL, S. A., GEHMAN, J. D., VAN DEVENTER, J. S. J. & PROVIS, J. L. 2015. The Role of Al in Cross-Linking of Alkali-Activated Slag Cements. *Journal of the American Ceramic Society,* 98, 996-1004.

NARASIMHAM, P. S. L. & RAO, K. J. 1978. Phase diagram and glass formation in the K2SO4 ZnSO4 system. *Journal of Non-Crystalline Solids,* 27, 225-246.

NAZABAL, V., POULAIN, M., OLIVIER, M., PIRASTEH, P., CAMY, P., DOUALAN, J. L., GUY, S., DJOUAMA, T., BOUTARFAIA, A. & ADAM, J. L. 2012. Fluoride and oxyfluoride glasses for optical applications. *Journal of Fluorine Chemistry,* 134, 18-23.

NAZARI, A. & SANJAYAN, J. G. 2015. Synthesis of geopolymer from industrial wastes. *Journal of Cleaner Production,* 99, 297-304.

NGUYEN, H., SANTOS, H., SREENIVASAN, H., KUNTHER, W., CARVELLI, V., ILLIKAINEN, M. & KINNUNEN, P. 2022. On the carbonation of brucite: Effects of Mg-acetate on the precipitation of hydrated magnesium carbonates in aqueous environment. *Cement and Concrete Research,* 153, 106696.

NIU, S., HAN, K., LU, C. & SUN, R. 2010. Thermogravimetric analysis of the relationship among calcium magnesium acetate, calcium acetate and magnesium acetate. *Applied Energy,* 87, 2237-2242.

NUNES, V. A., BORGES, P. H. R. & ZANOTTI, C. 2019. Mechanical compatibility and adhesion between alkali-activated repair mortars and Portland cement concrete substrate. *Construction and Building Materials,* 215, 569-581.

NUNES, V. A., SURANENI, P., BEZERRA, A. C. S., THOMAS, C. & BORGES, P. H. R. 2022. Influence of Activation Parameters on the Mechanical and Microstructure Properties of an Alkali-Activated BOF Steel Slag. *Applied Sciences,* 12.

OESTRIKE, R., YANG, W.-H., KIRKPATRICK, R. J., HERVIG, R. L., NAVROTSKY, A. & MONTEZ, B. 1987. High-resolution 23Na, 27Al and 29Si NMR spectroscopy of framework Aluminosilicate glasses. *Geochimica et Cosmochimica Acta,* 51, 2199-2209.

OMAR, O., MOUSA, M. R., HASSAN, M., HUNGRIA, R., GAVILANES, A., ARCE, G., MILLA, J. & RUPNOW, T. 2022. Optimization of the Self-Healing Efficiency of Bacterial Concrete Using Impregnation of Three Different Precursors into Lightweight Aggregate. *Transportation Research Record,* 2677, 1611-1624.

OMUR, T., KABAY, N., MIYAN, N., ÖZKAN, H. & ÖZKAN, Ç. 2022. The effect of alkaline activators and sand ratio on the physico-mechanical properties of blast furnace slag based mortars. *Journal of Building Engineering,* 58, 104998.

OUELLETTE, R. J. & RAWN, J. D. 2015. 1 - Structure of Organic Compounds. *In:* OUELLETTE, R. J. & RAWN, J. D. (eds.) *Principles of Organic Chemistry.* Boston: Elsevier.

PACHECO-TORGAL, F. 2014. 1 - Introduction to the environmental impact of construction and building materials. *In:* PACHECO-TORGAL, F., CABEZA, L. F., LABRINCHA, J. & DE MAGALHãES, A. (eds.) *Eco-efficient Construction and Building Materials.* Woodhead Publishing.

PALOMO, á., ALONSO, S., FERNANDEZ-JIMéNEZ, A., SOBRADOS, I. & SANZ, J. 2004. Alkaline Activation of Fly Ashes: NMR Study of the Reaction Products. *Journal of the American Ceramic Society,* 87, 1141-1145.

PALOMO, A., GRUTZECK, M. W. & BLANCO, M. T. 1999. Alkali-activated fly ashes: A cement for the future. *Cement and Concrete Research,* 29, 1323-1329.

PANG, S.-F., WU, C.-Q., ZHANG, Q.-N. & ZHANG, Y.-H. 2015. The structural evolution of magnesium acetate complex in aerosols by FTIR–ATR spectra. *Journal of Molecular Structure,* 1087, 46-50.

PARK, S., PARK, H. M., YOON, H. N., SEO, J., YANG, C.-M., PROVIS, J. L. & YANG, B. 2020. Hydration kinetics and products of MgO-activated blast furnace slag. *Construction and Building Materials,* 249, 118700.

PASSUELLO, A., RODRíGUEZ, E. D., HIRT, E., LONGHI, M., BERNAL, S. A., PROVIS, J. L. & KIRCHHEIM, A. P. 2017. Evaluation of the potential improvement in the environmental footprint of geopolymers using waste-derived activators. *Journal of Cleaner Production,* 166, 680-689.

PATIL, K. C., CHANDRASHEKHAR, G. V., GEORGE, M. V. & RAO, C. N. R. 1968. Infrared spectra and thermal decompositions of metal acetates and dicarboxylates. *Canadian Journal of Chemistry,* 46, 257-265.

PETERSON, O. 1996. "Chemical effects on cement mortar of calcium magnesium acetate as a deicing agent". *Cement and Concrete Research,* 26, 637-639.

PORTIER, J. 1989. Halogenide, chalcogenide and chalcohalogenide glasses: materials, models, applications. *Journal of Non-Crystalline Solids,* 112, 15-22.

PROVIS, J. L. 2018. Alkali-activated materials. *Cement and Concrete Research,* 114, 40-48.

PROVIS, J. L. & BERNAL, S. A. 2014a. Geopolymers and Related Alkali-Activated Materials. 44, 299-327.

PROVIS, J. L. & BERNAL, S. A. 2014b. Geopolymers and Related Alkali-Activated Materials. *Annual Review of Materials Research,* 44, 299-327.

PROVIS, J. L., PALOMO, A. & SHI, C. 2015. Advances in understanding alkali-activated materials. *Cement and Concrete Research,* 78, 110-125.

PROVIS, J. L. & VAN DEVENTER, J. S. 2013. *Alkali activated materials: state-of-the-art report, RILEM TC 224-AAM,* Springer Science & Business Media.

PROVIS, J. L., YONG, C. Z., DUXSON, P. & VAN DEVENTER, J. S. J. 2009. Correlating mechanical and thermal properties of sodium silicate-fly ash geopolymers. *Colloids and Surfaces A: Physicochemical and Engineering Aspects,* 336, 57-63.

PUERTAS, F. & FERNáNDEZ-JIMéNEZ, A. 2003. Mineralogical and microstructural characterisation of alkali-activated fly ash/slag pastes. *Cement and Concrete Composites,* 25, 287-292.

PUERTAS, F., FERNáNDEZ-JIMéNEZ, A. & BLANCO-VARELA, M. T. 2004. Pore solution in alkali-

activated slag cement pastes. Relation to the composition and structure of calcium silicate hydrate. *Cement and Concrete Research,* 34**,** 139-148.

PUERTAS, F., PALACIOS, M., MANZANO, H., DOLADO, J. S., RICO, A. & RODRíGUEZ, J. 2011. A model for the C-A-S-H gel formed in alkali-activated slag cements. *Journal of the European Ceramic Society,* 31**,** 2043-2056.

QAIDI, S. M. A., TAYEH, B. A., AHMED, H. U. & EMAD, W. 2022. A review of the sustainable utilisation of red mud and fly ash for the production of geopolymer composites. *Construction and Building Materials,* 350**,** 128892.

RAMER, G. & LENDL, B. 2006. Attenuated Total Reflection F ourier Transform Infrared Spectroscopy. *Encyclopedia of analytical chemistry: applications, theory and instrumentation.*

RASHAD, A., BAI, Y., BASHEER, P., MILESTONE, N. & COLLIER, N. 2013a. Hydration and properties of sodium sulfate activated slag. *Cement and Concrete Composites,* 37**,** 20-29.

RASHAD, A. M., BAI, Y., BASHEER, P. A. M., MILESTONE, N. B. & COLLIER, N. C. 2013b. Hydration and properties of sodium sulfate activated slag. *Cement and Concrete Composites,* 37**,** 20-29.

RAVIKUMAR, D. & NEITHALATH, N. 2012. Effects of activator characteristics on the reaction product formation in slag binders activated using alkali silicate powder and NaOH. *Cement and Concrete Composites,* 34**,** 809-818.

RAWSON, H. 1967. *Inorganic glass-forming systems*, Academic press.

REDDEN, R. & NEITHALATH, N. 2014. Microstructure, strength, and moisture stability of alkali activated glass powder-based binders. *Cement and Concrete Composites,* 45**,** 46-56.

RICH, P. R. & MARéCHAL, A. 2008. Carboxyl group functions in the heme-copper oxidases: Information from mid-IR vibrational spectroscopy. *Biochimica et Biophysica Acta (BBA) - Bioenergetics,* 1777**,** 912-918.

RICHARDSON, I. G., BROUGH, A. R., GROVES, G. W. & DOBSON, C. M. 1994. The characterization of hardened alkali-activated blast-furnace slag pastes and the nature of the calcium silicate hydrate (C-S-H) phase. *Cement and Concrete Research,* 24**,** 813-829.

RICHARDSON, I. G. & LI, S. 2018. Composition and structure of an 18-year-old 5M KOH-activated ground granulated blast-furnace slag paste. *Construction and Building Materials,* 168**,** 404-411.

ROZOV, K., BERNER, U., TAVIOT-GUEHO, C., LEROUX, F., RENAUDIN, G., KULIK, D. & DIAMOND, L. W. 2010. Synthesis and characterization of the LDH hydrotalcite–pyroaurite solid-solution series. *Cement and Concrete Research,* 40**,** 1248-1254.

SAJID, H. U., JALAL, A., KIRAN, R. & AL-RAHIM, A. 2022. A survey on the effects of deicing materials on properties of Cement-based materials. *Construction and Building Materials,* 319**,** 126062.

SAN NICOLAS, R., BERNAL, S. A., MEJíA DE GUTIéRREZ, R., VAN DEVENTER, J. S. J. & PROVIS, J. L. 2014. Distinctive microstructural features of aged sodium silicate-activated slag concretes. *Cement and Concrete Research,* 65**,** 41-51.

SCHMITZ, G. 2002. pH of Sodium Acetate Solutions. *Journal of Chemical Education,* 79**,** 29.

SCHNEIDER, J., CINCOTTO, M. A. & PANEPUCCI, H. 2001. 29Si and 27Al high-resolution NMR characterization of calcium silicate hydrate phases in activated blast-furnace slag pastes.

Cement and Concrete Research, 31**,** 993-1001.

SCRIVENER, K., MARTIRENA, F., BISHNOI, S. & MAITY, S. 2018a. Calcined clay limestone cements (LC3). *Cement and Concrete Research,* 114**,** 49-56.

SCRIVENER, K., SNELLINGS, R. & LOTHENBACH, B. 2018b. *A practical guide to microstructural analysis of cementitious materials*, Crc Press.

SCRIVENER, K. L. 2004. Backscattered electron imaging of cementitious microstructures: understanding and quantification. *Cement and Concrete Composites,* 26**,** 935-945.

SHI, C., QU, B. & PROVIS, J. L. 2019. Recent progress in low-carbon binders. *Cement and Concrete Research,* 122**,** 227-250.

SHI, X., AKIN, M., PAN, T., FAY, L., LIU, Y. & YANG, Z. 2009. Deicer Impacts on Pavement Materials: Introduction and Recent Developments. *The open civil engineering journal,* 3**,** 16-27.

SHI, Z., SHI, C., WAN, S., LI, N. & ZHANG, Z. 2018. Effect of alkali dosage and silicate modulus on carbonation of alkali-activated slag mortars. *Cement and Concrete Research,* 113**,** 55-64.

SILVA, J. M. S., CRAMER, S. M., ANDERSON, M. A., TEJEDOR, M. I. & MUñOZ, J. F. 2014. Concrete microstructural responses to the interaction of natural microfines and potassium acetate based deicer. *Cement and Concrete Research,* 55**,** 69-78.

SILVA, P. D., SAGOE-CRENSTIL, K. & SIRIVIVATNANON, V. 2007. Kinetics of geopolymerization: Role of Al2O3 and SiO2. *Cement and Concrete Research,* 37**,** 512-518.

SINGH, B., ISHWARYA, G., GUPTA, M. & BHATTACHARYYA, S. K. 2015. Geopolymer concrete: A review of some recent developments. *Construction and Building Materials,* 85**,** 78-90.

SINGH, V. K. 2023. 12 - Hydration and setting of Portland cement. *In:* SINGH, V. K. (ed.) *The Science and Technology of Cement and Other Hydraulic Binders.* Woodhead Publishing.

SONG, S., SOHN, D., JENNINGS, H. M. & MASON, T. O. 2000. Hydration of alkali-activated ground granulated blast furnace slag. *Journal of Materials Science,* 35**,** 249-257.

SORIANO, L., FONT, A., TASHIMA, M. M., MONZó, J., BORRACHERO, M. V. & PAYá, J. 2020. One-part blast furnace slag mortars activated with almond-shell biomass ash: A new 100% waste-based material. *Materials Letters,* 272**,** 127882.

STEINHAUSER, G. 2008. Cleaner production in the Solvay Process: general strategies and recent developments. *Journal of Cleaner Production,* 16**,** 833-841.

SUN, B., SUN, Y., YE, G. & DE SCHUTTER, G. 2022. A mix design methodology of slag and fly ash-based alkali-activated paste. *Cement and Concrete Composites,* 126**,** 104368.

SUN, Z. & VOLLPRACHT, A. 2018a. Isothermal calorimetry and in-situ XRD study of the NaOH activated fly ash, metakaolin and slag. 103**,** 110-122.

SUN, Z. & VOLLPRACHT, A. 2018b. Isothermal calorimetry and in-situ XRD study of the NaOH activated fly ash, metakaolin and slag. *Cement and Concrete Research,* 103**,** 110-122.

TAN, H., ZHANG, Y., MA, D., FENG, Y. P. & LI, Y. 2003. Optimum glass formation at off-eutectic composition and its relation to skewed eutectic coupled zone in the La based La–Al–(Cu,Ni) pseudo ternary system. *Acta Materialia,* 51**,** 4551-4561.

TAN, Z., BERNAL, S. A. & PROVIS, J. L. 2017. Reproducible mini-slump test procedure for measuring the yield stress of cementitious pastes. *Materials and Structures,* 50**,** 235.

TANAKA, H., TONG, H., SHI, R. & RUSSO, J. 2019. Revealing key structural features hidden in liquids and glasses. *Nature Reviews Physics,* 1**,** 333-348.

TäNZER, R., BUCHWALD, A. & STEPHAN, D. 2015. Effect of slag chemistry on the hydration of alkali-activated blast-furnace slag. *Materials and Structures,* 48**,** 629-641.

TCHAKOUTé, H. K., RüSCHER, C. H., HINSCH, M., DJOBO, J. N. Y., KAMSEU, E. & LEONELLI, C. 2017. Utilization of sodium waterglass from sugar cane bagasse ash as a new alternative hardener for producing metakaolin-based geopolymer cement. *Geochemistry,* 77**,** 257-266.

TCHAKOUTé, H. K., RüSCHER, C. H., KONG, S., KAMSEU, E. & LEONELLI, C. 2016. Geopolymer binders from metakaolin using sodium waterglass from waste glass and rice husk ash as alternative activators: A comparative study. *Construction and Building Materials,* 114**,** 276-289.

TENG, L.-W., HUANG, R., CHEN, J., CHENG, A. & HSU, H.-M. 2014. A Study of Crystalline Mechanism of Penetration Sealer Materials. *Materials,* 7**,** 399-412.

TERNSTROM, T. 1964. A periodic table. *Journal of Chemical Education,* 41**,** 190.

TERRY, L. G., CONAWAY, K., REBAR, J. & GRAETTINGER, A. J. 2020. Alternative Deicers for Winter Road Maintenance—A Review. *Water, Air, & Soil Pollution,* 231**,** 394.

TOBóN-ZAPATA, G. E., FERRER, E. G., ETCHEVERRY, S. B. & BARAN, E. J. 2000. Thermal Behaviour of Pharmacologically Active Lithium Compounds. *Journal of Thermal Analysis and Calorimetry,* 61**,** 29-35.

TONG, K. T., VINAI, R. & SOUTSOS, M. N. 2018. Use of Vietnamese rice husk ash for the production of sodium silicate as the activator for alkali-activated binders. *Journal of Cleaner Production,* 201**,** 272-286.

TONG, S., YUQI, Z. & QIANG, W. 2021. Recent advances in chemical admixtures for improving the workability of alkali-activated slag-based material systems. *Construction and Building Materials,* 272**,** 121647.

TSANG, C., SHEHATA, M. H. & LOTFY, A. 2016. Optimizing a Test Method to Evaluate Resistance of Pervious Concrete to Cycles of Freezing and Thawing in the Presence of Different Deicing Salts. *Materials,* 9.

TURNER, L. K. & COLLINS, F. G. 2013. Carbon dioxide equivalent (CO2-e) emissions: A comparison between geopolymer and OPC cement concrete. *Construction and Building Materials,* 43**,** 125-130.

TUYAN, M., ZHANG, L. V. & NEHDI, M. L. 2020. Development of sustainable alkali-activated slag grout for preplaced aggregate concrete. *Journal of Cleaner Production,* 277**,** 123488.

VAN DEVENTER, J. S. J., PROVIS, J. L., DUXSON, P. & BRICE, D. G. 2010. Chemical Research and Climate Change as Drivers in the Commercial Adoption of Alkali Activated Materials. *Waste and Biomass Valorization,* 1**,** 145-155.

VAN HUMBEECK, J. 1998. Chapter 11 - Simultaneous Thermal Analysis. *In:* BROWN, M. E. (ed.) *Handbook of Thermal Analysis and Calorimetry.* Elsevier Science B.V.

VAN UITERT, L. G., BONNER, W. A. & GRODKIEWICZ, W. H. 1971. Acetate glasses. *Materials Research Bulletin,* 6**,** 513-517.

VILLAQUIRáN-CAICEDO, M. A. 2019. Studying different silica sources for preparation of alternative waterglass used in preparation of binary geopolymer binders from metakaolin/boiler slag. *Construction and Building Materials,* 227**,** 116621.

WADSö, L. 2010. Operational issues in isothermal calorimetry. *Cement and Concrete Research,* 40**,** 1129-1137.

WALKLEY, B., KE, X., PROVIS, J. L. & BERNAL, S. A. 2021. Activator Anion Influences the Nanostructure of Alkali-Activated Slag Cements. *The Journal of Physical Chemistry C,* 125, 20727-20739.

WALKLEY, B. & PROVIS, J. L. 2019. Solid-state nuclear magnetic resonance spectroscopy of cements. *Materials Today Advances,* 1, 100007.

WANG, J., HU, Z., CHEN, Y., HUANG, J., MA, Y., ZHU, W. & LIU, J. 2022. Effect of Ca/Si and Al/Si on micromechanical properties of C(-A)-S-H. *Cement and Concrete Research,* 157, 106811.

WANG, K., NELSEN, D. E. & NIXON, W. A. 2006. Damaging effects of deicing chemicals on concrete materials. *Cement and Concrete Composites,* 28, 173-188.

WANG, L.-M., LI, Z., CHEN, Z., ZHAO, Y., LIU, R. & TIAN, Y. 2010. Glass Transition in Binary Eutectic Systems: Best Glass-Forming Composition. *The Journal of Physical Chemistry B,* 114, 12080-12084.

WANG, S.-D., PU, X.-C., SCRIVENER, K. & PRATT, P. 1995. Alkali-activated slag cement and concrete: a review of properties and problems. *Advances in cement research* 7, 93-102.

WANG, S.-D. & SCRIVENER, K. L. 1995. Hydration products of alkali activated slag cement. *Cement and Concrete Research,* 25, 561-571.

WANG, S.-D. & SCRIVENER, K. L. 2003. 29Si and 27Al NMR study of alkali-activated slag. *Cement and Concrete Research,* 33, 769-774.

WANG, Z., KHALID, H. R., PARK, S. M., BAE, S. J. & LEE, H. K. 2021. MgO-induced phase variation in alkali-activated binders synthesized under hydrothermal conditions. *Materials and Structures,* 54, 111.

WILLIAMS, M. L. 1996. *CRC Handbook of Chemistry and Physics, 76th edition*, Occup Environ Med. 1996 Jul;53(7):504.

WIYANTOKO, B., KURNIAWATI, P., PURBANINGTIAS, T. E. & FATIMAH, I. 2015. Synthesis and Characterization of Hydrotalcite at Different Mg/Al Molar Ratios. *Procedia Chemistry,* 17, 21-26.

XIANG, J., HE, Y., CUI, X. & LIU, L. 2022. Enhancement of setting times and hardening of alkali-activated slag binder using CO2-modified slag. *Cement and Concrete Composites,* 134, 104797.

XIE, N., SHI, X. & ZHANG, Y. 2017. Impacts of Potassium Acetate and Sodium-Chloride Deicers on Concrete. *Journal of Materials in Civil Engineering,* 29, 04016229.

XIE, T., VISINTIN, P., ZHAO, X. & GRAVINA, R. 2020. Mix design and mechanical properties of geopolymer and alkali activated concrete: Review of the state-of-the-art and the development of a new unified approach. *Construction and Building Materials,* 256, 119380.

XUE, C., LI, W., LUO, Z., WANG, K. & CASTEL, A. 2021. Effect of chloride ingress on self-healing recovery of smart cementitious composite incorporating crystalline admixture and MgO expansive agent. *Cement and Concrete Research,* 139, 106252.

YANG, K.-H., CHO, A.-R., SONG, J.-K. & NAM, S.-H. 2012. Hydration products and strength development of calcium hydroxide-based alkali-activated slag mortars. *Construction and Building Materials,* 29, 410-419.

YAO, H., XIE, Z., HUANG, C., YUAN, Q. & YU, Z. 2021. Recent progress of hydrophobic cement-

based materials: Preparation, characterization and properties. *Construction and Building Materials,* 299**,** 124255.

YE, N., YANG, J., LIANG, S., HU, Y., HU, J., XIAO, B. & HUANG, Q. 2016. Synthesis and strength optimization of one-part geopolymer based on red mud. *Construction and Building Materials,* 111**,** 317-325.

YI, Y., LISKA, M. & AL-TABBAA, A. 2014. Properties and microstructure of GGBS–magnesia pastes. *Advances in Cement Research,* 26**,** 114-122.

YLINIEMI, J., PESONEN, J., TIAINEN, M. & ILLIKAINEN, M. 2015. Alkali activation of recovered fuel–biofuel fly ash from fluidised-bed combustion: Stabilisation/solidification of heavy metals. *Waste Management,* 43**,** 273-282.

YOUSEFI ODERJI, S., CHEN, B., AHMAD, M. R. & SHAH, S. F. A. 2019. Fresh and hardened properties of one-part fly ash-based geopolymer binders cured at room temperature: Effect of slag and alkali activators. *Journal of Cleaner Production,* 225**,** 1-10.

ZAHARAKI, D., GALETAKIS, M. & KOMNITSAS, K. 2016. Valorization of construction and demolition (C&D) and industrial wastes through alkali activation. *Construction and Building Materials,* 121**,** 686-693.

ZAINUL ARMIR, N. A., ZULKIFLI, A., GUNASEELAN, S., PALANIVELU, S. D., SALLEH, K. M., CHE OTHMAN, M. H. & ZAKARIA, S. 2021. Regenerated Cellulose Products for Agricultural and Their Potential: A Review. *Polymers (Basel),* 13.

ZAJAC, M., SKOCEK, J., ADU-AMANKWAH, S., BLACK, L. & BEN HAHA, M. 2018. Impact of microstructure on the performance of composite cements: Why higher total porosity can result in higher strength. *Cement and Concrete Composites,* 90**,** 178-192.

ZANOTTO, E. D. & MAURO, J. C. 2017. The glassy state of matter: Its definition and ultimate fate. *Journal of Non-Crystalline Solids,* 471**,** 490-495.

ZAWRAH, M. F., GADO, R. A., FELTIN, N., DUCOURTIEUX, S. & DEVOILLE, L. 2016. Recycling and utilization assessment of waste fired clay bricks (Grog) with granulated blast-furnace slag for geopolymer production. *Process Safety and Environmental Protection,* 103**,** 237-251.

ZHAN, J., FU, B. & CHENG, Z. 2022. Macroscopic Properties and Pore Structure Fractal Characteristics of Alkali-Activated Metakaolin–Slag Composite Cementitious Materials. *Polymers* [Online], 14.

ZHANG, H., AI, J., REN, Q., ZHU, X., HE, B. & JIANG, Z. 2023. Understanding the strength evolution of alkali-activated slag pastes cured at subzero temperature. *Cement and Concrete Composites,* 138**,** 104993.

ZHANG, J. 2022. Research on the Correlation Between the Lattice Enthalpy of Ionic Compounds and Melting Points. *Academic Journal of Science and Technology,* 3**,** 52-59.

ZHANG, J., SHI, C. & ZHANG, Z. 2021. Effect of Na2O concentration and water/binder ratio on carbonation of alkali-activated slag/fly ash cements. *Construction and Building Materials,* 269**,** 121258.

ZHANG, S., KEULEN, A., ARBI, K. & YE, G. 2017. Waste glass as partial mineral precursor in alkali-activated slag/fly ash system. *Cement and Concrete Research,* 102**,** 29-40.

ZHANG, W., GONG, S. & ZHANG, J. 2018a. Effect of rubber particles and steel fibers on frost resistance of roller compacted concrete in potassium acetate solution. *Construction and Building Materials,* 187**,** 752-759.

ZHANG, W., ZHANG, J., CHEN, S. & GONG, S. 2018b. Degradation of Roller-Compacted Concrete Subjected to Freeze-Thaw Cycles and Immersion in Potassium Acetate Solution. *Advances in Materials Science and Engineering,* 2018**,** 4282181.

ZHANG, Y., LIANG, M., GAN, Y. & ÇOPUROĞLU, O. 2022. Effect of MgO content on the quantitative role of hydrotalcite-like phase in a cement-slag system during carbonation. *Cement and Concrete Composites,* 134**,** 104765.

ZHAO, J., GAO, X., CHEN, S., LIN, H., LI, Z. & LIN, X. 2022. Hydrophobic or superhydrophobic modification of cement-based materials: A systematic review. *Composites Part B: Engineering,* 243**,** 110104.

ZHENG, Q., ZHANG, Y., MONTAZERIAN, M., GULBITEN, O., MAURO, J. C., ZANOTTO, E. D. & YUE, Y. 2019. Understanding Glass through Differential Scanning Calorimetry. *Chemical Reviews,* 119**,** 7848-7939.

ZHU, X., ZHANG, M., YANG, K., YU, L. & YANG, C. 2020. Setting behaviours and early-age microstructures of alkali-activated ground granulated blast furnace slag (GGBS) from different regions in China. *Cement and Concrete Composites,* 114**,** 103782.

ZUO, Y., NEDELJKOVIĆ, M. & YE, G. 2018. Coupled thermodynamic modelling and experimental study of sodium hydroxide activated slag. *Construction and Building Materials,* 188**,** 262-279.

ZUO, Y. & YE, G. 2018. Pore Structure Characterization of Sodium Hydroxide Activated Slag Using Mercury Intrusion Porosimetry, Nitrogen Adsorption, and Image Analysis. *Materials* [Online], 11.

Appendixes

Appendix A.

The solution prepared for the pH measurement was determined by the activation for producing alkali-activated slag cements (AAS). Therefore, the concentration of activation is 4 g M_2O (M = Na^+ or K^+) per 100 g of slag, consistent with the activation conditions used in producing AAS. In addition, the same water to binder ratio (w/b) of 0.3 was used.

The calculation of the needed quantities of alkalis is 4 g M_2O (M = Na^+ or K^+) listed below, which means 4 g Na_2O/K_2O per 100 g slag.

For NaAc (cast solids) as an example:
Molar mass (Na_2O) = 62 $gmol^{-1}$

The moles of Na_2O in 4 g of Na_2O should be:

$$\frac{4\ g}{62\ gmol^{-1}} = 0.0645\ mol\ (Na_2O)$$

0.0645 moles of Na_2O contains 0.129 moles of Na.

Thus, to make the fixed property of 0.129 moles of Na, following calculations of the needed mass of metal carboxylates are presented.

1) Starting point = 0.129 moles of Na per 100g slag,

Chemical formula of NaAc = $C_2H_3O_2Na$, Molar mass of NaOH refer to $M_{(NaOH)}$= 40 gmol⁻¹, Molar mass of NaAc presented as $M_{(NaAc)}$ = 82 gmol⁻¹, Number of Na atoms in one molecule of NaAc = 1

To provided 0.129 moles of Na, 0.129 moles of NaAc was needed.

2) Work out the mass of NaAc for providing 0.129 moles of NaAc:

$$0.129 \; mol \times 82 \; gmol^{-1} = 10.58 \; g$$

Mass of NaAc to provide 0.13 moles of per 100 g of slag = 10.58g

Therefore, the required mass of the distilled water should be:

w/b= mass of distilled water/ mass of (slag + solid activator)

$$\frac{Mass \; of \; distilled \; water}{100g + 10.58g} = 0.3$$

mass of distilled water=33.17g

Additionally,

$$Molality = \frac{Moles \; of \; solute}{Mass \; of \; solvent \; (in \; kg)}$$

Therefore, the molality of NaAc is calculated as below:

$$\frac{0.129}{33.17/1000} = 3.89 \; moles/kg$$

Appendix B.

For blended (NaOH-NaAc) systems, 25% NaAc-75% NaOH as an example:

1) 4 g of Na_2O is included as a summary providing from both in NaOH and NaAc. The mass of Na_2O provided from NaOH is represented as m $(Na_2O)_{NaOH}$, the mass of of Na_2O provided from NaAc is shown as m $(Na_2O)_{NaAc}$.

2) Supposing the moles of NaOH represented as X, and similarly Y revealed the moles of NaAc.

X=$n_{(NaOH)}$, Y= $n_{(NaAc)}$,

3) Then m $(Na_2O)_{NaOH}$=62× $\frac{X}{2}$, m $(Na_2O)_{NaAc}$= 62× $\frac{Y}{2}$,

4) Finally,

$$62\times \frac{X}{2} + 62\times \frac{Y}{2}= 4$$

$$\frac{X}{Y} = \frac{75\%}{25\%}$$

X=0.09677, Y=0.03225

$m_{(NaOH)}$= $n_{(NaOH)}$ × M(NaOH)= 0.09677× 40 = 3.87 g

$m_{(NaAc)}$= $n_{(NaAc)}$ × M(NaAc)= 0.0325× 82 = 2.64 g

Thus, the needed quantities in the composition of 25 NaAc-75 NaOH is 2.64g of NaAc and 3.87g of NaOH, respectively.